Cardiff School of Biosciences

Exploring the use of Quantum dots as quantitative model delivery agents for small molecules, peptides and proteins

Thesis presented to Cardiff University for the degree of Doctor of Philosophy

Author: Kez Cleal

September 1, 2015

Supervisors:
Prof. A. T. Jones,
Prof. P. Borri,
Prof. W. W. Langbein,
Dr. P. D. Watson

Summary

Progress in the biological sciences is leading to the characterization of a wide range of disease processes in molecular detail. However overriding or intervening in these processes in a controlled fashion remains a great challenge and many researchers are now looking beyond the use of individual small molecule inhibitors to the realm of macromolecules and nanoparticle complexes. For small molecules, the lack of cell-specific targeting often limits their reach and they are inherently limited in the scope of their interaction with cells. In contrast, biological macromolecules which comprise of peptide, protein or nucleic acid derived constructs can interface with cellular processes in a broader range of contexts with the potential to confer new paradigms in disease treatment. However, several challenges exist for utilizing macromolecules as therapies including compliance with the immune system and targeting to a site of interest which may be the cell surface or a site within the cell interior. To address these problems recent years have seen an explosion of interest in utilizing nanoparticles as drug delivery systems which exploit the principle that multiple functionalities can be grouped into a single entity to tackle distinct biological barriers. Whilst nanoparticles offer great hope for disease management, there is considerable difficulty in fabricating at the nanoscale and our understanding of the factors which influence nanoparticle cell uptake and processing remains limited. As such there is considerable scope for exploring novel methods for both assembling cargoes into nanoparticle complexes and quantifying their uptake and trafficking in cells. In this work, luminescent nanoparticles known as Quantum dots (QDs) were utilized as a model system for the delivery of peptide, protein and small molecule cargoes. Characterization of QDs in biological media (Chapter 3) revealed that these particles are sensitive to the adsorption of serum proteins to the particle surface in a process known as protein corona formation. This observation inspired an approach to exploit non-covalent association to assemble a hydrophobic small molecule (Chapter 4), and cationic peptide and protein (Chapter 5) cargoes into nanoparticle complexes. In line with recent reports, a recurrent finding from this work identifies the serum protein concentration as a critical factor in determining the performance of these non-covalent nanoparticle complexes in terms of their ability to bind to cells and withstand cargo dissociation. Currently, there are few methods which aim to quantifying intracellular particle trafficking at a single particle level. Here a novel computational method was developed (Chapter 6) based on single particle tracking microscopy to allow the study of individual particles as they undergo transit between cellular compartments. The method demonstrated high specificity and event detection scores using simulated data and the impact of this work relates to the potential to perform high throughput quantification of nanoparticle trafficking at the single particle level.

DECLARATION

This work has not been submitted in substance for any other degree or award at this or any other university or place of learning, nor is being submitted concurrently in candidature for any degree or other award.

Signed  (candidate) Date 06/03/2016

STATEMENT 1

This thesis is being submitted in partial fulfillment of the requirements for the degree of PhD.

Signed 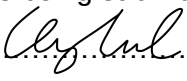 (candidate) Date 06/03/2016

STATEMENT 2

This thesis is the result of my own independent work/investigation, except where otherwise stated.

Other sources are acknowledged by explicit references. The views expressed are my own.

Signed  (candidate) Date 06/03/2016

STATEMENT 3

I hereby give consent for my thesis, if accepted, to be available online in the University's Open Access repository and for inter-library loan, and for the title and summary to be made available to outside organisations.

Signed  (candidate) Date 06/03/2016

Table of Contents

Table of Figures

Introduction

Table of abbreviations

2D	Two dimensional
3D	Three dimensional
AAV1	Adeno-associated virus serotype 1
AAV2	Adeno-associated virus serotype 2
ADP	Adenosine diphosphate
ADSCs	Adipocyte derived stem cells
AGT	Adaptive Gaussian thresholding
aQDs	Amine functionalized QDs
Arf1	ADP-ribosylation factor 1
AUC	Area under the curve
B_{max}	Maximum number of binding sites
BSA	Bovine serum albumin
Cdc42	Cell division control protein 42 homolog
CI	Confidence interval
CLIC/GEEC	Clathrin Independent Carriers/GPI-Anchored Proteins Enriched Early Endosomal Compartments
ConA	Concanavalin A
CPPs	Cell penetrating peptides
cRGD	Cyclic RGD
CXCR4	C-X-C Chemokine receptor 4
DDS	Drug delivery system
DLS	Dynamic light scattering
DMEM	Dulbecco's Modified Eagle Medium
DMSO	Dimethyl sulfoxide
DNA	Deoxyribonucleic acid
DOPE	Dioleoylphosphatidyl-ethanolamine
EDC	1-ethyl-3-(3-dimethylaminopropyl) carbodi-imide hydrochloride
EDX	Energy-dispersive X-ray spectroscopy
EGF	Epidermal growth factor
EGFR	Epidermal growth factor receptor
EPR	Enhanced permeability and retention
ER	Endoplasmic reticulum
ESCRT	Endosomal sorting complex required for transport
FBS	Fetal bovine serum
FDA	Food and drug Administration
FITC	Fluorescein isothiocyanate
GFP	Green fluorescent protein
GFPR8	Green fluorescent protein - r8
GPI	Glycophosphatidylinositol
GRAF1	GTPase regulator associated with focal adhesion kinase-1
GTPase	Guanosine triphosphatase
HA	Haemagglutinin
HSA	Human serum albumin

HDGF	Hepatoma-derived growth factor
HIV	Human immunodeficiency virus
HO-1	Heme-oxygenase 1
IgG	Immunoglobulin G
IL-8	Interleukin - 8
Keap1	Kelch-like ECH-associated protein 1
LAMPs	Lysosome-associated membrane glycoproteins
LC3-II	Microtubule-associated protein 1A/1B-light chain 3 - phosphatidylethanolamine conjugate
LDL	Low density lipoprotein
LDLD	Lipoprotein lipase deficiency
MHC	Major histocompatibility complex
mins	Minutes
miRNA	micro ribonucleic acid
MPS	Mononuclear macrophage system
MRI	Magnetic resonance imaging
mRNA	Messenger ribonucleic acid
MSCs	Mesenchymal stem cells
MSD	Mean squared displacement
NA	Numerical aperture
NHS	National health service
NICE	National Institute for Clinical Excellence
Nrf2	Nuclear factor (erythroid-derived 2)-like 2
OTC	Ornithine transcarbamylase deficiency
pak-1	p21 activated kinase
PAMAM	cationic poly(amido amine)
PBS	Phosphate buffered saline
PCL	poly(-ε- aprolactone)
PDF	Probability density function
PDGF	Platelet derived growth factor
PDI	Polydispersity index
PEG	Polyethylene glycol
PEI	Polyethyleneimine
PGLA	poly (lactic-*co*-glycolic acid)
PI3K	Phosphatidylinositol 3-kinase
PLA	poly(lactic acid)
PM	Plasma membrane
POD	Polyethylene glycol–diortho ester–distearoyl glycerol
p-value	Probability of rejecting the null hypothesis
px	Pixel
QDs	Quantum dots
R^2	Coefficient of determination
RNA	Ribonucleic acid
RT	Room temperature
sCMOS	Scientific complementary metal oxide semiconductor
SDS	sodium dodecyl sulphate

siRNA	Small interfering ribonucleic acid
SNR	Signal to noise ratio
SPIONs	Super paramagnetic iron oxide nanoparticles
SPT	Single particle tracking
STF	Spatial temporal filter
Sulfo-SMCC	Sulfosuccinimidyl 4-(N-maleimidomethyl) cyclohexane-1-carboxylate
TAE	Tris acetic acid
TAT	Trans activator gene product
TEM	Transmission electron microscopy
TGFa	Transforming growth factor alpha
TGN	Trans Golgi network
TrIC	Tracking Image Correlation
UV-vis	Ultraviolet–visible

1 Introduction

Over recent decades there has been a great deal of progress in uncovering the basic mechanisms of disease at the cellular level, however our ability to intervene in or override these processes often lags far behind. A large part of this disconnect stems from the difficulty in developing medicines which can target a specific compartment or cell within the body to uncouple a particular molecular defect. There have of course been a number of stunning successes in disrupting the molecular basis of a disease, with an early example being the pioneering small molecule drug Gleevec (Imatinib) which has afforded chronic myeloid leukaemia patients 10 year survival odds of 84 % (Kalmanti et al., 2015). However small molecule inhibitors are limited in their biological reach and in order to tackle the most intractable of human diseases the domain of macromolecules is currently being explored. In the main these are compounds composed of biological precursors and constitute peptides or proteins which interact with receptors or effect protein-protein interactions, or nucleic acids such as short interfering ribonucleic acids (siRNAs) which regulate transcription, or even entire genes.

1.1 The rise of biologicals

Indeed, eleven new drugs classified as 'biologicals' were approved by the FDA in 2014 alone with expected annual sales of several billion (FDA, 2014; Mullard, 2015). However, the vast majority of these compounds target receptors on the exterior leaflet of cell membranes which comprise the plasma membrane or the luminal side of the endomembrane system following endocytosis. Many more targets await in the cell interior although in order to reach the cytosolic compartment a cellular membrane must be breached. By themselves, macromolecular entities are generally too large and hydrophilic to overcome this barrier and require an additional mechanism or drug delivery system (DDS) which enables them to gain entry. Additionally many cargo molecules of interest commonly lack a cell targeting mechanism. For this reason grouping of distinct functionalities into nanoparticle entities which range in size from roughly 5 – 250 nm is currently being explored where each component is designed to address a specific challenge. Nanoparticles over this size-range may permit the incorporation of large numbers of cargo molecules into the nanoparticle system, so for each complex reaching its target site potentially hundreds to cargo molecules may be released which may increase drug efficacy. It is also hoped that sequestering components into nanoparticle complexes may also reduce the biological stress to the system potentially resulting in diminished side effects and improved patient compliance (Alexis et al., 2008; Safra et al., 2000).

1.2 Nanoparticles as delivery devices

Utilizing nanoparticles as delivery devices has drawn interest from nearly every branch of medicine with the hope of overcome long standing bottle necks in drug delivery for macromolecules as well as

small molecules that suffer from poor pharmacodynamics (Cho et al., 2008; Schütz et al., 2013; Thukral et al., 2014). A few early successes of non-targeted nanoparticles have already made it into the clinic such as Doxil (James et al., 1994) and Daunoxome (Petre and Dittmer, 2007) among others, mainly for delivery of small molecules in cancer patients (Allen and Cullis, 2013). However delivery of macromolecular components to a specific cell type in vivo is a considerably more challenging problem and involves the surmounting of multiple biological barriers relating to the survival of the nanoparticle in the blood stream, targeting of a specific cell type, gaining entry into the cell and finally escape into the cytosol. Despite these many challenges a huge diversity of nanoparticles are currently under investigation for use as novel therapeutic and diagnostic devices.

1.3 The diversity of nanoparticles

A nanoparticle can be defined as a single entity whose average diameter falls within the range of 1 micrometre to 1 nanometre, although most nanoparticles normally fall within the 5-250 nm range which approximates the size of an intracellular protein complex or small organelle such as a peroxisomes (Smith and Aitchison, 2013). Smaller nanoparticles consist of very high surface area to volume ratios and may be ideal for display of surface ligands and cargos whereas larger particles can sequester large volumes of material with their interior structure for release on the appropriate cue. Due to the vast scope of the field and the myriad of devices under development, a brief discussion is given of some of the more auspicious and widespread nanoparticle devices under scrutiny.

1.3.1 Liposomes

Liposomes are comprised of amphiphilic lipids which assemble into nanometer sized vesicles to encapsulate a water soluble payload (Fig.1.1a). The first membrane enclosed vesicles were reported in 1965 (Bangham et al., 1965) and since then considerable effort has been invested in developing these entities for drug delivery purposes culminating in the approval of a range of medicines with many more under clinical trial (Allen and Cullis, 2013). In general, therapeutic liposomes are currently designed to act as small molecule drug reservoirs which demonstrate carefully tuned release kinetics and require an accumulation at disease sites to enhance their efficacy (Allen and Cullis, 2013). A major advantage of liposomes is their biocompatibility as well as the ability to encase large volumes of hydrophilic cargo molecules which place them as promising candidates for non-viral gene therapy. Current research is focused on developing active targeting and release mechanisms to expand beyond the realm of small molecules.

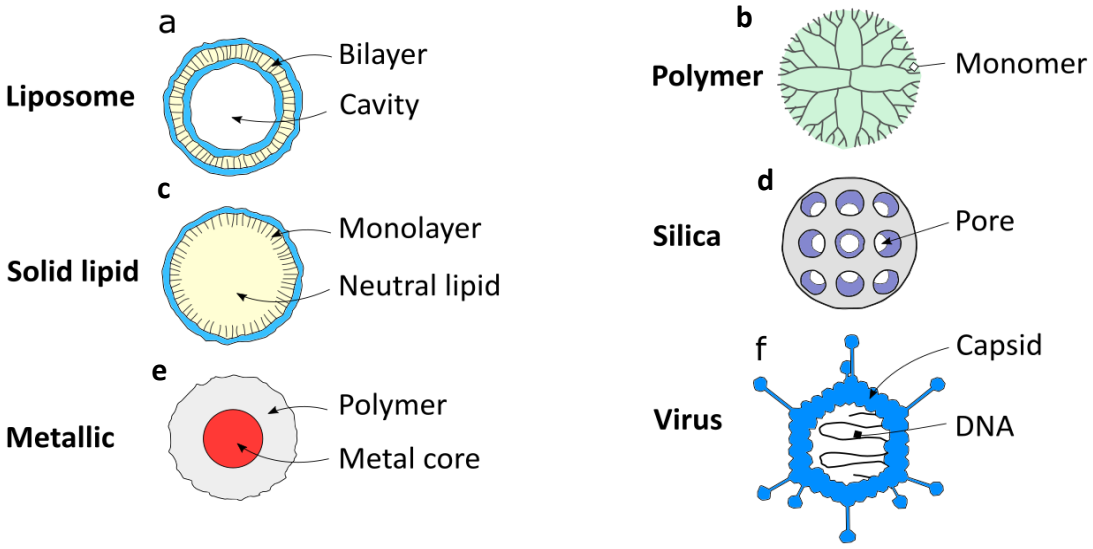

Figure 1.1 The diversity of nanoparticles.

Liposomes (a) consist of a lipid bilayer which encloses a hydrophilic cavity whereas solid lipid particles (b) consist of a lipid monolayer with a neutral lipid core. Metallic nanoparticles (c) consist of a metallic core which is often encased within a polymer to improve water solubility and provide functional groups at the surface for further modification. Polymer based particles can be fabricated in a number of configurations, shown here is a structured arrangement of monomers known as a dendrimer (d). Silica particles (e) are characterized by a large number of pores which provide a high surface area to volume ratio. Viral particles such as Adenovirus (f) are comprised of protein arrays which form the viral capsid to encase the nucleic acid cargo.

1.3.2 Polymeric nanoparticles

Nanoparticles based on the assembly of smaller monomers can take on a variety of shapes, sizes and structures (Fig.1.1b). These particles are often self-assembled or constructed as a series of polymerization steps. For example shell-crosslinked nanoparticles comprised of biodegradable amphiphilic block copolymers (e.g. poly(lactic acid) (PLA), poly (lactic-*co*-glycolic acid) (PGLA), or poly(-ε - aprolactone) (PCL)) form macromolecular aggregates which are then covalently cross-linked to stabilize the structure (Xiong and Lavasanifar, 2011; Zhang et al., 2009). Dendrimers on the other hand are fabricated by step-wise polymerisation of monomers to create tightly controlled tree-like structures (e.g. cationic poly(amido amine) (PAMAM) polymers) (Khandare et al., 2012; Majoros et al., 2005). Polymeric nanoparticles may be loaded with drugs in a non-covalent fashion or chemically conjugated with active compounds following the initial synthesis stage. These particles are generally biodegradable and can be fine-tuned to achieve various loading and release characteristics.

1.3.3 Solid lipid nanoparticles

Introduced in 1991 (Eldem et al., 1991), solid lipid nanoparticles are as their name suggests composed of a neutral lipid core that is delimited by a single phospholipid layer and can be formulated over a wide range of sizes from < 50 – 1000 nm (Fig.1.1c) (Thukral et al., 2014). Solid lipid nanoparticles offer many advantages such as biocompatibility, drug stability, easy of scale-up during manufacturing, high surface area and high loading of lipophilic drugs. Small molecule drugs have been explored as cargo molecules in addition to some proteins, peptides, antigens and siRNA (Almeida and Souto, 2007; Sahay et al., 2013).

1.3.4 Silica based nanoparticles

Mesopourous silica nanoparticles are honeycomb-like materials that have the capacity to absorb or encapsulate large volumes of material owing to their high surface area and pore volume (Fig.1.1d). As such, silica nanoparticles have excellent drug loading characteristics, high chemical stability and are generally biocompatible. An attractive property of silica nanoparticles is the possibility to functionalise the inner pore system and/or particle surface, making them applicable for a range of applications including sensing, diagnostics, catalysis and drug delivery (Argyo et al., 2014). Current challenges focus on creating stimuli responsive particles and understanding the clearance and excretion profiles in vivo (Argyo et al., 2014).

1.3.5 Metallic nanoparticles

Metallic nanoparticles can be composed of a large number of elements and alloys, although the most popular nanoparticles under development are iron oxide, gold and quantum dot nanoparticles (Fig.1.1e). These nanoparticles typically consist of a dense metallic core which is further encased within a polymer shell to provide stability and reactive surface groups for further chemical modification. Super paramagnetic iron oxide nanoparticles (SPIONs) have unique magnetic properties which make them excellent contrast agents in magnetic resonance imaging (MRI) (Gupta and Gupta, 2005). The large magnetic moment of SPIONs affords high MRI imaging sensitivity and enables low doses and toxicity to be achieved in vivo (Gupta and Gupta, 2005; C. Huang et al., 2011). SPIONs appear to be largely biocompatible and are degraded in the body where they feed into standard iron recycling pathways (Weissleder et al., 1989). Gold nanoparticles exhibit a range of desirable properties such as low toxicity, high surface area, ease of functionalization and opportunities for imaging (Raman scattering, electron microscopy) and photothermal therapy (Dreaden et al., 2012; Saha et al., 2012). Quantum dots (QDs) are small crystalline semiconductors which exhibit exceptional spectral properties (Michalet, 2005). Their bright emission profiles permit tracking at the single particle level positioning these particles as intracellular live cell probes for investigating the interaction of nanoparticles with cells. Additionally QDs are also being investigated for in vivo drug delivery and for diagnostic applications (Michalet, 2005).

1.3.6 Viral based nanoparticles

The power of viruses to transfect cells is unrivalled and reflects the vast amount of time they have had to evolve into gene transfer machines. Interest in exploiting these entities for gene therapy has been around for decades, although despite some remarkable preclinical results clinical applications have remained limited (Aghi and Martuza, 2005; Waehler et al., 2007). Viruses come ready equipped with mechanisms to overcome some of the more challenging biological barriers that non-viral vectors are faced with such as highly efficient endocytic escape mechanisms. Furthermore viral particles can also be assembled with small molecule, antigen or protein cargoes (Fig.1.1f) (Garcea and Gissmann, 2004). Nevertheless there remain several key obstacles which relate to the native tropism of viruses which often do not meet clinical standards, the high cost of vector production, concerns over how the virus integrates into the host genome, and the possibility of an immunogenic response in the patient (Waehler et al., 2007). Indeed well publicised adverse drug reactions in some patients have tarnished the field with controversy and spurred interest in the various non-viral alternatives discussed above (Yla-Herttuala et al., 2008). For example, in September 1999, Jesse Gelsinger (age 18) received an

adenovirus treatment for ornithine transcarbamylase deficiency (OTC) which led to a massive inflammatory response and death four days later from multiple organ failure (Thomas et al., 2003).

The challenge for non-viral vectors is to match the high delivery capacities of viruses whilst doing so in a cell specific, safe and affordable way. Collectively this involves overcoming engineering challenges as well as a variety of biological barriers.

1.4 Overcoming biological barriers

1.4.1 Biological environments and the immune system

A DDS may be administered into the body via a number of potential routes such as intravenous or –muscular injection or absorption across the gut epithelia or skin, for example. An initial challenge for a DDS then is to withstand introduction into a biological environment and maintain a functional capacity following interaction with local protein factors within this environment and during distribution throughout the body. Most nanoparticles additionally require colloidal stability to be widely distributed in the body. Colloidal stability refers to the ability of a particle to remain in a colloidal state over an extended timeframe, and the insensitivity of a particle to aggregation as a result of fluctuating conditions in vivo (Wang and Thanou, 2010). Many studies have found that following injection into the bloodstream, DDS are rapidly cleared through interactions with the mononuclear macrophage system (MPS) (Barratt et al., 2001; Stolnik et al., 1995) or complement system (Vonarbourg et al., 2006) preventing them from reaching their target site. Opsonins of the complement system such as immunoglobulins G and M, fibronectin, apolipoproteins and protein C3b, in addition to recognition by scavanger receptors have been implicated in clearance of DDS by macrophages of the mononuclear phagocytic system (Dobrovolskaia and McNeil, 2007; Vonarbourg et al., 2006). This leads to the eventual accumulation of the DDS in the MPS organs such as the liver and spleen with the potential for causing toxicity. Indeed the finding that nanomaterials may stimulate or even supress the immune system depending on their specific surface chemistry and characteristics raises concerns over immunotoxicity and systemic effects which must be addressed for each particle design (Dobrovolskaia and McNeil, 2007). Engineering of nanoparticle surfaces to provide compatibility with the immune system and facilitate a defined clearance profile is an ongoing area of research. For nanoparticles composed of toxic constituents such as QDs, proper clearance is needed to minimize potential toxicity. A recent paper explored the renal clearance of QD nanoparticles as a function of their polymer coatings and size (Soo Choi et al., 2007). Zwitterionic or neutral coatings were reported to reduce adsorption of serum protein components and enhance renal clearance with

particles below 5.5 nm being rapidly cleared by the renal system providing a foundation for further development of biocompatible DDS.

1.4.2 Protein corona formation

Understanding the interactions which occur between nanoparticle surfaces and components found in biological fluids is still in its infancy. Over recent years the interaction of endogenous proteins with nanoparticle surfaces has risen to the forefront of nanoparticle drug design with effects beyond immune recognition. Nanoparticle surfaces may often be charged or harbour hydrophobic domains which can initiate non-specific adsorption of protein components to form a layer known as the nanoparticle protein corona (Monopoli et al., 2012). This process also appears to be almost unavoidable although the extent of protein binding may be modulated depending on the surface characteristics of the particle (Lundqvist et al., 2008; Walczyk et al., 2010; Walkey et al., 2014; Walkey and Chan, 2012). Factors which govern corona formation remain poorly characterized although particle size, texture and surface chemistry have been identified as fundamental constraints (Walkey et al., 2014; Walkey and Chan, 2012). The importance of this process for nanoparticle drug delivery was recently underlined by a study which examined the influence of serum concentration on the ability of a nanoparticle surface ligand to interact with its receptor at cell surfaces (Salvati et al., 2013). In this study, corona formation acutely affected cell targeting with the corona effectively masking the transferrin ligand at high serum concentrations. The nanoparticles utilized in this study were 50 nm silica and were crosslinked to transferrin via a short poly-ethylene linker. Analysis of conjugates in biochemical experiments and cell culture demonstrated that the interaction of transferrin with its receptor was lost with increasing serum concentration and the formation of a protein corona.

1.4.3 Targeting of tissues and cells

Following survival in the circulatory system and immune avoidance a DDS must then facilitate targeting to a defined location which may require extravasation of the DDS from the bloodstream to reach the target cell type. A convenient mechanism for achieving an accumulation of nanoparticles at solid tumour sites is the enhanced permeability and retention effect (EPR) (Cho et al., 2008; Jain and Stylianopoulos, 2010; Matsumura and Maeda, 1986). Angiogenesis at tumour sites often gives rise to vasculature with abnormal structure with wide fenestrations and a deficient lymphatic drainage system. This leads to a progressive accumulation of nano-sized materials in the tumour interstitial matrix relative to healthy tissues and the EPR has served as a key rational for developing DDS which exploit this phenomenon for delivery of chemotherapeutics or contrast agents. However, the heterogeneity of tumour environments ensures that the EPR is generally non-uniform across the

entire tumour which may account for the modest survival benefit offered by many FDA approved DDS which are currently in the clinic or under trial (Jain and Stylianopoulos, 2010; Schütz et al., 2013).

Vascular defects have also been reported in a wider range of conditions such as age-related macular degeneration, asthma, diabetes and multiple sclerosis (Chetta et al., 2007; Folkman, 2003; Lengfeld et al., 2014; Martin et al., 2003). Other tissues may also favour non targeted accumulation of nanoparticles owing to specific morphological features of the tissue or the circulatory system supplying them. For example the discontinuous endothelium of the liver and bone marrow has characteristic fenestrae of 50 – 100 nm and are frequently sites of high nanoparticle accumulation in biodistribution studies (Alexis et al., 2008; Braet et al., 2007). Thus non targeted delivery may have certain merit although the range of tissue compartments accessible via this mode of targeting may be limited.

1.4.3.1 Cell targeting

One challenge of targeting cancer cells is that they are often very similar to the healthy tissues which surround them. To isolate these cells targeting ligands may be used which form the outermost layer of the nanoparticle structure. These molecules are required to display high affinities or avidities to target receptors and are commonly required to induce endocytosis. This is an important consideration as each ligand can display its own uptake characteristics and intracellular localization pattern. Furthermore there is also the concern that the uptake and distribution characteristics of a targeting ligand may be strongly influenced by the nanoparticle to which it is attached, further complicating the development of nanoparticle delivery devices (Jones and Sayers, 2012). An enormous variety of ligands are under investigation and can be broadly divided into small molecules, peptides, proteins and aptamers which are oligonucleotides whose secondary or tertiary structure allows them to recognize and bind specific biomolecules (Reinemann and Strehlitz, 2014; Shan et al., 2015; Yu et al., 2012). Antibodies or antibody fragments have received considerable attention due to their highly specific recognition properties and wide availability (Fay and Scott, 2011). For example the monocloncal antibody Herceptin targets the receptor tyrosine kinase HER2 found overexpressed in up to 30 % breast cancers, and is currently under investigation for nanoparticle targeting (Colombo et al., 2010). Other ligands which have also been employed include transferrin, lactoferrin, transforming growth factor alpha (TGFa), insulin, albumin, cell penetrating peptides, cyclic-RGD and folate (Jones and Sayers, 2012; Ruoslahti et al., 2010; Yu et al., 2012). These ligands are often chemically cross linked to the surface using linkers such as EDC (1-ethyl-3-(3-dimethylaminopropyl) carbodi-imide hydrochloride) or Sulfo-SMCC (sulfosuccinimidyl 4-(N-maleimidomethyl) cyclohexane-1-carboxylate) (Rosenthal et al., 2011). A variety of non-covalent strategies are also being investigated as a means to target specific cell types (Doane and Burda, 2013). As an example human serum albumin has been

used as a scaffold for non-covalent attachment of targeting peptides (Bunschoten et al., 2012). Peptides in this study were also functionalized with a near infrared dye IR783, with the dye itself in this case acting as the albumin binding motif (Bunschoten et al., 2012). The peptide targeting ligands which were displayed on the particle surface demonstrated targeting of the chemokine receptor 4 (CXCR4) in sentinel lymph nodes to allow in vivo imaging of these structures.

1.4.4 Entry into the cell

In some situations, a DDS may aim to directly breach the plasma membrane to gain entry into the cell although with this approach there is the concern that disrupting the integrity of this layer may give rise to off target effects and cytotoxicity. Of course this may be desirable for tumour cell killing although without stringent control and cell-specific targeting of diseased cells, healthy tissues may also be effected. The vast majority of DDS are designed with the intention of gaining entry into the cell by first being taken up into the cellular endomembrane system through the process of endocytosis.

1.4.4.1 Endocytosis

Endocytosis plays a variety of roles in the cell such as the uptake of nutrients, regulation of signalling at the cell surface and antigen processing (Doherty and McMahon, 2009). The influx of membranes must be tightly balanced against the efflux from exocitic pathways in ordered to maintain the structural integrity and composition of the plasma membrane (Doherty and McMahon, 2009). Nanoparticles can gain entry into the cell by exploiting endocytic pathways through receptor ligand interactions or through non-specific uptake as a result of membrane turnover (Akinc and Battaglia, 2013). So far at least six distinct endocytic pathways have been described, with any one cell type typically utilizing several pathways concurrently (Fig.1.2). Important cell type differences have been found in the activity and regulation of these pathways which may serve as a basis for nanoparticle targeting to specific tissue types (Akinc and Battaglia, 2013; Doherty and McMahon, 2009).

In general endocytic pathways have been found to be highly dynamic and complex in terms of their functional and structural organization, how they are linked and separated, and how these pathways interact with other cellular processes such as secretion and autophagy. Even well studied pathways such as the clathrin dependent pathway are still considered poorly characterized which greatly complicates the development of nanoparticles which aim to exploit these pathways for cargo delivery. Historically, endocytosis was initially segregated into cell drinking (pinocytosis) and cell eating (phagocytosis) although now pinocytosis has been recognised as being several distinct pathways which are further categorized into clathrin and calthrin-independent pathways (Doherty and McMahon, 2009). The names of pathways have been derived from regulatory proteins which constitute the pathway, the cargoes involved or the sensitivity of the pathway to specific inhibitors.

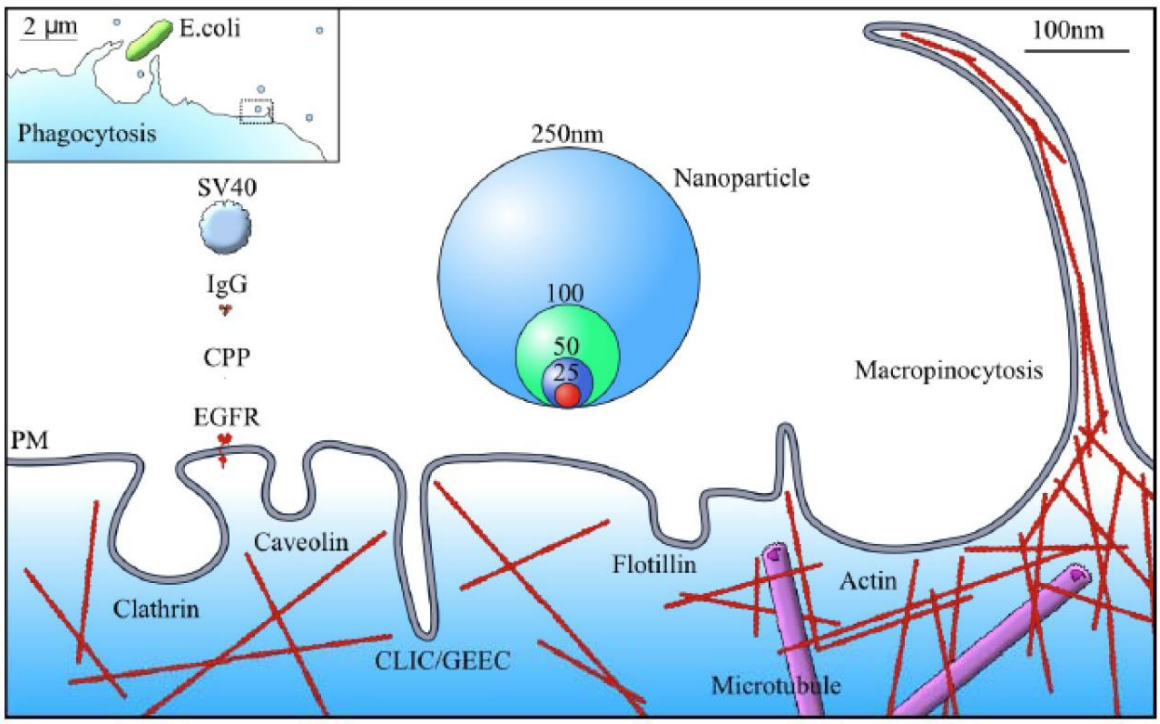

Figure 1.2 Endocytic pathways as routes of nanoparticle entry.

At least six distinct endocytic pathways are thought to exist which may be exploited for uptake of nanoparticle devices. These particles can dwarf individual proteins such as EGFR or IgG and can approach the scale of virus such as SV40 or even entire bacteria. The physical dimensions of a nanoparticle may restrict which pathways can accommodate their uptake irrespective of their surface functionality. Very large cargoes may be engulfed by specialized cells through the receptor driven phagocytic pathway (inset), while others such as the clathrin and caveolae pathways are constrained to cargoes of approximately 150 and 100 nm, respectively. Relatively little is known regarding the size constraints of the CLIC/GEEC and flotillin pathways. Constitutive pathways such as macropinocytosis are frequently implicated in nanoparticle uptake which may be partly a consequence of size considerations. A variety of mechanisms are being explored to facilitate nanoparticle cell uptake and intracellular processing such as antibodies (IgG) and cell penetrating peptides (CPP). PM – plasma membrane. Figure taken from (Cleal et al., 2013).

An overview of the features of these pathways and how they relate to nanoparticle endocytosis are discussed below.

1.4.4.1.1 Clathrin dependent endocytosis

The clathrin pathway is by far the most studied and well characterized endocytic pathway and involves clathrin heavy and light chain triskeleons which form invaginations at the cell membrane that pinch off to form clathrin coated vesicles. These vesicles then lose their coats within 2 mins and are transported to the early endosome compartment which serves as a distribution node to several later compartments including the trans-Golgi network and late endosomes/lysosomes. Recent studies from the Nichols lab using a universal plasma membrane labelling techniques followed by quantitative imaging of endocytosis suggest that as much as 95 % of endogenous protein uptake may be orchestrated by this pathway alone (Bitsikas et al., 2014). The complexity of this pathway was also recently expounded by a genome wide siRNA screen to identify novel regulators of this pathway. Well known proteins were identified such as clathrin and dynamin, although a further 4600 putative factors were identified which await further characterization (Bakal and Perrimon, 2010; Collinet et al., 2010).

Several reports have demonstrated uptake of nanoparticles by the clathrin pathway through both receptor mediated targeting and non-specific uptake (Harush-Frenkel et al., 2007; Rappoport et al., 2012; Salvati et al., 2013; Suresh et al., 2014). In one study, D,L-polylactide (PLA) based nanoparticles were prepared with cationic or anionic surface coatings with particle diameters of around 90 nm, although only the positively charged particles entered the cell by the clathrin pathway (Harush-Frenkel et al., 2007). In contrast, a recent paper investigating carboxyl polystyrene nanoparticles of around 55 nm found that these negatively charged particles did enter via the clathrin pathway underlining the difficulty in generalizing between studies involving even subtly different nanoparticles (Rappoport et al., 2012). Targeting of nanoparticles to the clathrin pathway has also been investigated in a now seminal paper by Salvati et al., who used transferrin functionalized silicon dioxide nanoparticles to target uptake via the transferrin receptor. However, these particles were shown to lose their targeting capabilities when placed in media containing serum proteins as a direct consequence of corona formation emphasising the multiple challenges associated with controlled nanoparticle uptake (Salvati et al., 2013).

1.4.4.1.2 Caveolae mediated endocytosis

Another well studied endocytic pathway involves uptake through structures known as caveolae which are invaginations of the plasma membrane occurring in lipid raft domains (Reeves et al., 2012; Rothberg et al., 1992). Caveolae are enriched in glycophosphatidylinositol (GPI) linked proteins, cholesterol, sphingolipids and the caveolin and cavin proteins (Bastiani et al., 2009; Reeves et al.,

2012). Not all cells express the caveolins with notable exceptions being the blood cell types such as T- and B- lymphocytes indicating that uptake via this pathway is cell type specific to an extent. These structures are enriched in epithelial cells comprising up to 20 % of the surface of microvascular endothelium and are thought to play a role in epithelial transcytosis although the cellular mechanisms are poorly resolved. Caveolae are also implicated in a range of other functions including adipocyte metabolism, cellular mechanosensation, and lipid homeostasis (Hansen et al., 2013; Hansen and Nichols, 2010). There is an increasing interest in caveolae for their additional signalling functions and their roles in the aetiology and progression of diseases such as atherosclerosis and cancer (Parton and del Pozo, 2013; Pavlides et al., 2012; Shatz and Liscovitch, 2008). Caveolae pinch off from the plasma membrane and may deliver material to the Golgi and endoplasmic reticulum raising interest for effecting delivery or transcytosis of DDS via this pathway (Parton and del Pozo, 2013; Parton and Howes, 2010).

Recent studies suggest that nanoparticles functionalized with a polyelectrolyte composed of an aromatic sulfonic backbone may exhibit specificity for caveolae in epithelial cells (Voigt et al., 2014). Receptor mediated nanoparticle targeting has also been achieved by fabricating particles with bovine serum albumin (BSA) appended to the surface. BSA binds the caveolae localized protein gp60 and was shown to facilitate uptake of particles up to 100 nm in diameter (Sleep, 2014; Wang et al., 2009).

1.4.4.1.3 Flotillin mediated uptake

Evidence is accumulating that the flotillin proteins -1 and -2 are involved in uptake and trafficking of membrane components in a cell type specific manner (Stuermer, 2011). These proteins which are also known by the names of Reggie-2 and -1, respectively, were originally described in neuronal axon regeneration in goldfish, but have now been identified in diverse cell types including adipocytes, hepatocytes, epithelial cells, neutrophils and T-lymphocytes (Schulte et al., 1997; Stuermer, 2011). These proteins localize to the cytoplasmic face of lipid microdomains by protein-lipid modifications in the form of palmitoylation and myristoylation, in addition to a stretch of hydrophobic residues along the head domain (Banning et al., 2011). Recent studies suggest that the flotillin pathway functions to regulate the number of plasmalemmal neurotransmitter transports at the cell surface affecting the clearance capacity for neurotransmitters such as dopamine and glutamate at brain synapses (Cremona et al., 2011). In adipocytes, the pathway has been implicated in the trafficking of the Glut4 glucose transporter from intracellular compartments to the cell surface (Baumann et al., 2000) whereas in T cells a role in recruitment of the T cell receptor has been identified (Stuermer et al., 2004). So far evidence indicates that the flottillin pathway therefore functions in a relatively cell-type specific manner with a general function for the pathway currently unknown.

Due to the poorly resolved mechanisms of this pathway, only a few studies have reported uptake via the flotilin pathway and it remains to be seen how efficiently this pathway can be isolated by receptor mediated targeting. Cationic polyplexes comprised of a reducible poly(amido amine) carrier and a DNA cargo were found to enter retinal pigment epithelium cells (RPE) via a flotillin-1-dependent pathway and were capable of effecting gene transfection on a similar level to the commercial reagent Lipofectamine (Vercauteren et al., 2011b). In another study, amoprphous silica nanoparticles of different sizes between 30 and 300 nm showed internalization into flotillin-1 and -2 labelled vesicles in lung and epithelial cell models (Kasper et al., 2013). However, smaller nanoparticles sizes were associated with significant toxicity and interleukin (IL-8) inflammatory marker release. A recent report utilizing poly-L-lysine to create DNA nanoparticle complexes found that these nanoparticles are recognised by the nucleolin cell surface receptor which was found in association with flotillin by co-immunoprecipitation although more work is required to identify this pathway as the principle route of entry (Chen et al., 2011).

1.4.4.1.4 Endocytosis through CLIC-GEEC

The CLIC/GEEC pathway was identified relatively recently by two independent studies investigating the uptake of GPI-linked proteins, toxins and bulk fluid (Kirkham et al., 2005; Sabharanjak et al., 2002). Initially GEECs (GPI- Enriched Early Endocytic Compartments) were identified as tubular structures associated with the plasma membrane whose formation was inhibited by dominant negative cdc42 expression, a protein known to regulate actin dynamics (Sabharanjak et al., 2002). Later on CLICs (Clathrin Independent Carriers) were identified by electron microscopy as prevalent tubules up to 800 nm in length, or bagel shaped structures in mouse embryonic fibroblasts which lack caveolae (Kirkham et al., 2005). CLICs were also found to harbour GPI anchored proteins, bulk fluid and cholera toxin B. The high degree of similarity between these structures has led to the CLIC/GEEC convention to refer to a single pathway. More recent studies have supported a link with the actin associated protein GRAF1 (GTPase regulator associated with focal adhesion kinase-1) required for CLIC formation (Lundmark et al., 2008). CLIC/GEECs are thought to be a major contributor to bulk fluid endocytosis with three times the volume of fluid uptake in fibroblasts compared to the clathrin pathway (Howes et al., 2010). This suggests that this pathway may also be important for non-specific uptake of nanoparticles although this remains to be investigated directly.

The poor understanding of this pathway and the paucity of methodologies to identify trafficking by this route means currently few studies have investigated nanoparticle uptake in this context. A recent study demonstrated that adeno-associated virus 2 (AAV2) is internalized in HeLa and 293T cells via the CLIC/GEEC pathway independently of clathrin, caveolin and micropinocytosis pathways indicating that

this pathway is competent for nanoparticle sized cargoes (Nonnenmacher and Weber, 2011). Furthermore, this route of entry was sensitive to actin and membrane cholesterol disruption, but required cdc42, Arf1 and GRAF1 function, with cargo eventually trafficking to the Golgi apparatus. Future studies may thus aim to specifically target the CLIC/GEEC pathway for nanoparticle uptake.

1.4.4.1.5 Macropinocytosis

Macropinocytosis is thought to occur constitutively at a basal level in most cell types for the uptake of bulk fluids although certain cell types such as immature dendritic cells use it for antigen sampling (Sallusto et al., 1995). The unique sensitivity of macropinocytosis to inhibitors of Na^+/H^+ exchange such as amiloride differentiates this pathway from other types (Koivusalo et al., 2010). This process is thought to originate at sites of membrane ruffling where large protrusions collapse back onto the plasma membrane to engulf fluid into macropinosomes. Circular ruffles (circular dorsal ruffles) or waves have been described resulting in the uptake of growth factor receptors and integrins as well as fluids to form macropinosomes that can be as large as 2 μm in diameter (Gu et al., 2011). Apart from a requirement for the actin cytoskeleton, macropincoytosis is poorly defined, with most studies relying on induction by activating ligands such as epidermal growth factor (EGF) and platelet derived growth factor (PDGF) which initiate a dramatic increase in ruffling (Lim and Gleeson, 2011). The mechanisms relating receptor signalling to the onset of membrane ruffling are also unresolved although the actin regulator p21 activated kinase (pak-1) has been implicated in fluid phase and stimulated uptake (Dharmawardhane et al., 2000) in addition to vaccinia virus entry (Mercer and Helenius, 2008).

Interestingly, large numbers of studies investigating nanoparticle uptake indicate an involvement of macropinocytosis to some extent, although this almost always occurs alongside uptake through additional pathways. This would suggest that macropinocytosis is non-specific in its selectivity although certain physical characteristics of nanoparticles may favour uptake by this pathway. A recent study of interest utilized a library of mesoporous silica nanoparticles comprising of rod-shaped particles with different aspect ratios (lengths) which entered cells by micropinocytosis (Meng et al., 2011). Interestingly, particles with an aspect ratio of 2.1-2.5 were found to be optimal for uptake and delivery of cytotoxic compounds to HeLa cells illustrating that size and shape can influence macropinocytosis selectivity.

1.4.4.1.6 Phagocytosis

Many aspects of phagocytosis bare similarities with macropinocytosis relating to the reorganization of the plasma membrane by the actin cytoskeleton to engulf large volumes of material. However,

phagocytosis primarily occurs in specialized cells of the immune system known as professional phagocytes and include members such as macrophages, neutrophils and dendritic cells. Phagocytosis plays critical roles in organismal defence against infectious agents and even exogenous entities such as DDS (Aderem and Underhill, 1999; Doherty and McMahon, 2009; Hillaireau and Couvreur, 2009). Other cell types such as endothelial, epithelial and fibroblasts also display phagocytic activity but to lesser extents (Rabinovitch, 1995). The phagocytic pathway is initiated by recognition of particle surfaces by opsonins such as IgG and complement factors which then initiate receptor driven uptake to form the phagosome. Various receptors have been described such as the FcγR, mannose/fructose, scavenger and CD44 while more are still being discovered (Aderem and Underhill, 1999; Vachon et al., 2006). Through a series of fusion events with early and late endosomes and eventually lysosomes, the phagosome matures into a phagolysosome over the course of 30 mins to several hours resulting in the enzymatic degradation of the offending particle (Aderem and Underhill, 1999; Janeway and Medzhitov, 2002). In the case of dendritic cells, degradation results in increased presentation of peptide products on major histocompatability complexes class I and II at the cell surface (Savina and Amigorena, 2007). Thus targeting of nanoparticles to the phagocytic pathway in dendritic cells has been explored as a way to achieve antigen presentation in conditions such as infection, cancer and autoimmune diseases (Conniot et al., 2014; Gao et al., 2015; Serra and Santamaria, 2015).

In a recent study, pluronic-stabilized polypropylene sulphide nanoparticles were used to target lymph node dendritic cells (Reddy et al., 2007). This was achieved by essentially exploiting corona formation where the particle surface served to activate the complement system to provide the necessary targeting cues for dendritic cell uptake. Interestingly, 25 nm particles proved to be superior at delivering an antigenic ovalbumin cargo when compared to 100 nm particles. Indeed, utilizing the complement system as a delivery mechanism is an elegant concept which may inspire similar approaches in a wider range of nanoparticle systems owing to the near ubiquity of protein corona formation.

Described above are a collection of endocytic routes which have been at least partially characterized. The likelihood is that additional routes await discovery which may or may not be cell type specific. As a recent example, endophilin which has been previously assigned as a member of the clathrin pathway may in fact function in a distinct pathway involving a fast-acting tubulovesicular carrier (Boucrot et al., 2015). Thus DDS have multiple opportunities to enter cells with the possibility of utilizing many routes at once for particles which lack targeting motifs. For untargeted particles uptake may be influenced by the physical dimensions and charge of the particle and the relative activity of individual endocytic pathways in that cell type. In fact, adhesion of a nanoparticle to the cell surface over an extended time frame may be all that is required to gain entry into the cell as a result of the constant cycling of the

plasma membrane. However, the eventual fate of the particle intracellularly must then be addressed with a variety of mechanisms being explored to drive DDS towards their intracellular targets.

1.4.4.2 Intracellular processing of nanoparticles

1.4.4.2.1 Negotiating the endomembrane system

Although much attention is focused on characterizing cellular uptake of a DDS through a particular endocytic pathway, the performance of the system may often be largely determined by the subsequent intracellular processing and fate of the particle. However, the mechanisms which determine the intracellular fate of a nanoparticle are only beginning to be explored and there is a growing need for further mechanistic studies in this regard. As discussed previously, endocytosis involves the pinching off of vesicles from the plasma membrane which then enter into the endosomal system (Fig.1.3). This system is intertwined with multiple cellular pathways and has critical roles in maintaining cellular homeostasis. From a drug delivery perspective, the key elements of this system consist broadly of a recycling circuit for returning plasma membrane components and ligands to the cell surface, a degradation pathway for breakdown of macromolecules and a connecting, or feeder pathway which directs one-way transport of fluid and membrane components from the recycling circuit to the lysosomal degradation system (Fig.1.3) (Huotari and Helenius, 2011). This feeder pathway is mediated by late endosomes, also known as multi vesicular bodies, which also pose as an intermediary for trafficking of components from the trans-Golgi to the lysosome (Huotari and Helenius, 2011).

Following cargo internalization by endocytosis, the majority of membrane material is recycled back to the plasma membrane via early endosomes, which themselves can be highly heterogeneous and have a complex morphology with tubule and vacuolar regions (Grant and Donaldson, 2009; Jovic et al., 2010). It has been reported that a typical fibroblast may internalize the equivalent of 2 % of its plasma membrane per minute, or 50-180 % of the surface area per hour (Maxfield and McGraw, 2004; Steinman et al., 1983). The volume of fluid ingested by macrophages corresponds to an impressive 30 % of the entire volume of the cell per hour with roughly two thirds of this volume being secreted within 10-15 mins, although other cell types are less prolific (Guillot et al., 1990; Steinman et al., 1976). As a consequence of this active recycling, transport to the late endosome concerns a relatively small fraction of material which will eventually be transported to the lysosome. Bulk fluids and solutes

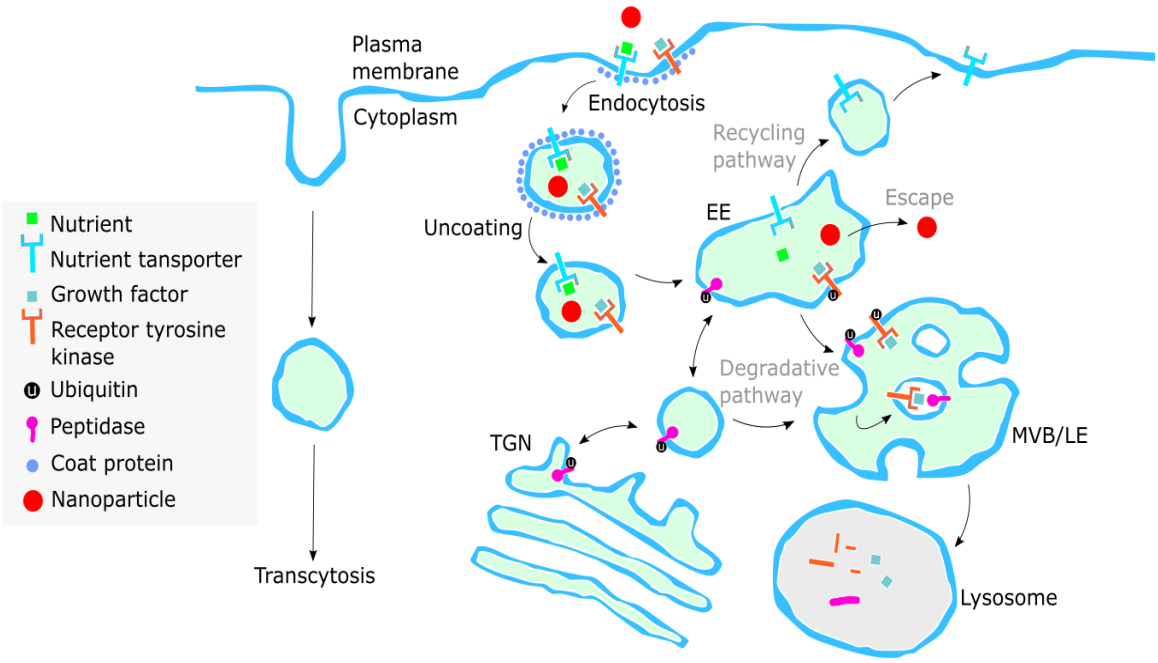

Figure 1.3 Nanoparticle escape from the endomembrane system.

Endocytosis has essential roles in the uptake of nutrients, the regulation of signalling and the transport of cargoes from apical to basolateral surfaces through transcytosis. Nanoparticles can gain entry into cells through various endocytic pathways to enter the endosomal network. In a simplified form this system is composed of a recycling pathway and a degradative pathway. Nutrient transporters entering the early endosomes (EE) are frequently recycled back to the plasma membrane devoid of their cargo. For certain receptor-ligand complexes ubiquitination servers as a signal for egression into the late endosomes (LE) or multi-vesicular bodies (MVB). The LE also serves as a gateway to the lysosome for peptidases and other lysosomal proteins trafficked from the trans Golgi network (TGN). Nanoparticle systems may aim to target these distinct compartments or to escape the endosomal network and reach the cytosol.

do not undergo sorting although larger particles such as viruses and DDS are often selectively directed through this pathway (Huotari and Helenius, 2011).

1.4.4.2.2 Trafficking through early endosomes

Early endosomes receive cargo from multiple pathways such as clathrin, caveolae and CLIC/GEEC for a period of roughly 10 mins during which time fluid and cargo components are recycled away (Huotari and Helenius, 2011). The conversion into late endosomes is dependent on the small GTPase Rab5 and its effector VPS34/p150, a PI3K complex (phosphatidylinositol 3-kinase) which provides the necessary change in identity to drive this process (Behnia and Munro, 2005; Zeigerer et al., 2012). The early endosomes are in bidirectional exchange with the TGN and receive vesicles containing acid hydrolases which give them a degradative capacity (Fig.1.3). The generation of intraluminal vesicles already begins in the early endosome with the formation of protein plaques containing the endosomal sorting complex required for transport (ESCRT) machinery which mediates sorting of ubiquitinated proteins into these vesicles. In some contexts, multivesicular endosomes are responsible for sequestering signalling components, miRNAs, mRNAs and MHC class II molecules into intra luminal vesicles which then undergo fusion with the plasma membrane to release vesicles in the form of exosomes (Théry et al., 2009). Exosomes are now recognised as having essential roles in cell-cell communication and also represent an exciting frontier in nanoparticle drug delivery, diagnostics and prognostics. Although beyond the scope of this brief introduction the reader is referred to several excellent reviews (Andaloussi et al., 2013; Kosaka et al., 2010).

1.4.4.2.3 Trafficking to the Golgi and ER

From the early endosome compartment it may also be possible to target the Golgi and ER compartments with a specific delivery vector (Bexiga and Simpson, 2013; Sandvig et al., 2010; Tekle et al., 2008). Recent studies have attempted to exploit the retrograde trafficking of toxins such as plant derived ricinB or Shiga toxin from Shigella dysenteriae, in order to target nanoparticles to these compartments (Audi et al., 2005; Johannes and Römer, 2010; Tekle et al., 2008). RicinB is the lectin subunit of ricin responsible effecting cell binding and retrograde trafficking in the cell (Doan, 2004). QDs conjugated with these toxins however failed to follow the expected trafficking route instead ending up in late endosomes implying that the protein toxins are processed differently by the cell when conjugated to QDs (Tekle et al., 2008). A further interesting finding from these studies was that the presence of ricinB conjugated QDs in endosomal compartments was found to perturb the endosome to Golgi trafficking of unconjugated ricinB or Shiga toxins. Transport of ricin was inhibited whereas Shiga toxin transport was increased. This is an important finding as the effect of a nanoparticle on the normal trafficking processes of the cell is often overlooked although may potentially be a source of unwanted side effects for nanoparticle therapeutics.

1.4.4.2.4 Late endosomes and lysosomes

During endosome maturation continuous transport with the TGN is responsible for providing a steady influx of acid hydrolases during maturation into late endosomes and removal of early endosomal components through effectors such as Rab7, Rab9 and the retromer complex (Pfeffer, 2009). By the time they are ready to fuse with lysosomes after roughly 10 – 40 mins of maturation, late endosomes have undergone a dramatic transformation in terms of their protein composition, their intracellular location to a perinuclear region, formation of intra luminal vesicles, morphological changes and a drop in pH to around 4.5 - 5.5 (Huotari and Helenius, 2011; Maxfield and McGraw, 2004). The delimiting membrane of the late endosome also becomes enriched in lysosomal glygoproteins such as LAMPS which provide resistance to the degradative hydrolases of the lysosome.

Finally fusion of late endosomes with lysosomes is considered a point of no return for luminal protein components which are then subject to hydrolysis into simple building blocks (Appelqvist et al., 2013). For many DDS intracellular processing leads to the accumulation of the nanoparticle in this compartment. The impact of nanoparticles on the native function of lysosomes is only beginning to be addressed and recent studies using gold nanoparticles suggest that excessive nanoparticle accumulation can lead to alkalization of lysosomal pH and severe impairment of the degradation capacity of this organelle (Ma et al., 2011).

Lysosomes themselves can in fact also undergo secretion with relocation of lysosomes to the cell periphery, homotypic fusion with other lysosomes, and finally lysosomal fusion with the plasma membrane. Lysosomal exocytosis plays important roles in cell signalling, bone resorption, and plasma membrane repair (Andrews, 2005; Appelqvist et al., 2013). This processes has also recently been implicated in regulating the efficacy of a DDS where lysosomal exocytosis reduced the cell killing of mesoporous silica nanoparticles in vitro and inhibition of this process improved the performance of the nanoparticle system (Yanes et al., 2013). In another study, recycling of late endosomes or lysosomes limited siRNA delivery by lipid nanoparticles with 70 % of the internalized siRNA undergoing exocytosis via this pathway (Sahay et al., 2013).

Overall, for a DDS entering the cell there are a variety of possible outcomes which include the recycling of components out of the cell or transport to a defined compartment of the endomembrane system such as the lysosome, Golgi or ER (J. G. Huang et al., 2011). There are of course a great number of potential targets within the endomembrane system and each of these possible fates may be desirable for a DDS in certain instances and for certain applications. For example, secretion of nanoparticles following uptake may be necessary for applications requiring transcytosis across epithelia such as the blood brain barrier. This has been demonstrated with albumin nanoparticles with apolipoprotein E covalently bound as the targeting motif (Zensi et al., 2009). These particles crossed into the central

nervous system and were found in neurons in a mouse model. Alternatively, transport to the lysosomal compartment in a selective manner may be required for treating lysosomal storage diseases for example (Appelqvist et al., 2013; Giannotti et al., 2011). Additionally there is interest in delivering nanoparticles to the lysosome to effect release of cytotoxic compounds or to invoke cytotoxicity (Cho et al., 2008). In a recent study, epidermal growth factor (EGF) was conjugated to iron oxide nanoparticles and these particles were selectively trafficked to lysosomes in EGFR overexpressing cancer cells (Domenech et al., 2013). Application of an alternating magnetic field was then used to permeablize these lysosomes to effect cell killing indicating an additional motivation to target these organelles.

Nevertheless, for most other applications recycling of the DDS out of the cell or delivery through to the lysosome is considered undesirable as the nanoparticle may fail to impart an effect or be subject to degradation by acid hydrolases. Thus optimising the intracellular processing and targeting of a DDS is a key challenge for development of nanomedicines and it remains to be seen how different endocytic pathways can be exploited in different cell types. Owing to the cross talk between endocytic pathways which feed into the endomembrane system there may also be opportunities to target a variety of endomembrane compartments by judicial optimisation of the DDS.

1.4.4.3 Endocytic escape

In order to reach additional cellular compartments the DDS must escape the endomembrane system into the cytosol which inevitably involves overcoming a lipid bilayer. Once free in the cytosol the nanoparticle or its cargo may then pursue additional targets. These may be cellular factors present within the cytosol or further intracellular compartments such as the mitochondria or nucleus which may be reached by exploiting the relevant endogenous import localization sequences of the cell (Marfori et al., 2011; von Heijne, 2005). In particular, for nucleic acid based therapies a significant bottleneck is still an inability to efficiently escape the endosomal system (Tokatlian and Segura, 2010; Varkouhi et al., 2011). The highly specific entry and delivery capabilities of viruses are much to be desired although as discussed the use of viruses can provoke potent immunogenic responses in some patients which has turned focus to developing non-viral vectors which avoid these problems (Yla-Herttuala et al., 2008). To study endocytic escape a few strategies are currently employed. These can be broadly characterised into assays which identify pore formation or membrane rupture relying on the escape of fluorescent membrane impermeable reporters such as dextran into the cytosol (Martens et al., 2014). Membrane fusion can be studied by egress of fluorescent nanoparticle lipids into the endomembrane bilayer system while other methods include cell fractionation, or fluorescence microscopy in an attempt to resolve particle escape on a single particle level (Martens et al., 2014).

Maximising the delivery of cargo to the cytosol is a key constraint and a variety of strategies are under investigation.

1.4.4.3.1 Fusogenic lipids

There exist a class of lipids which are able to destabilize the usual lamella phase or extended lipid bilayer sheets found in cell membranes. These lipids which include members such as the phosphatidylethanolamines (e.g. dioleoylphosphatidyl-ethanolamine – DOPE) can adopt an inverted micelle-like structure of the inverse hexagonal phase which are incompatible with bilayer assembly under normal physiological conditions (Koltover, 1998). Liposomes containing cationic lipids which adopt this phase can be non-covalently conjugated with nucleic acids to form lipoplexes (Tros de Ilarduya et al., 2010). These assemblies can then attach themselves to anionic cell membranes and undergo fusion to release their contents into the cytoplasm (Fig.1.4a – c) (Koltover, 1998). The fusogenicity of lipoplexes has been related to the degree of saturation of the fusogenic lipid tail domain (Heyes et al., 2005). Lipoplexes are sensitive to competitive binding with serum factors and lack inherent targeting. Controlling the point at which a lipoplex undergoes membrane fusion with intracellular membranes rather than the plasma membrane is considered a key factor in minimising off target effects and recent approaches have focused on modifying the lipoplex surface to regulate this process (Schlegel et al., 2011). One such strategy is to employ a pH sensitive coating which breaks down in the low pH environment of the endolysosomal system. This has been performed with a polyethylene glycol-diortho ester-distearoyl glycerol (POD) polymer coat appended to the surface of DOPE liposomes which demonstrated breakdown at low pH (Guo and Szoka, 2001). A number of studies have employed this strategy with impressive results. For example DOPE and aminoxy cholesteryl lipid particles were functionalized with PEG to give rise to pH sensitive oxime bonds. The delivery of siRNA by these particles in a hepatitis B mouse model proved more effective than the licensed drug lamivudine (Carmona et al., 2009).

1.4.4.3.2 Polymers sensitive to pH and the proton sponge effect

Cationic polymers that can be protonated may exert a buffering effect when taken into the endolysosomal system of cells. Such polymers are thought to act as a 'proton sponge' which prevents acidification during endosome maturation. This is thought to result in a greater influx of protons by

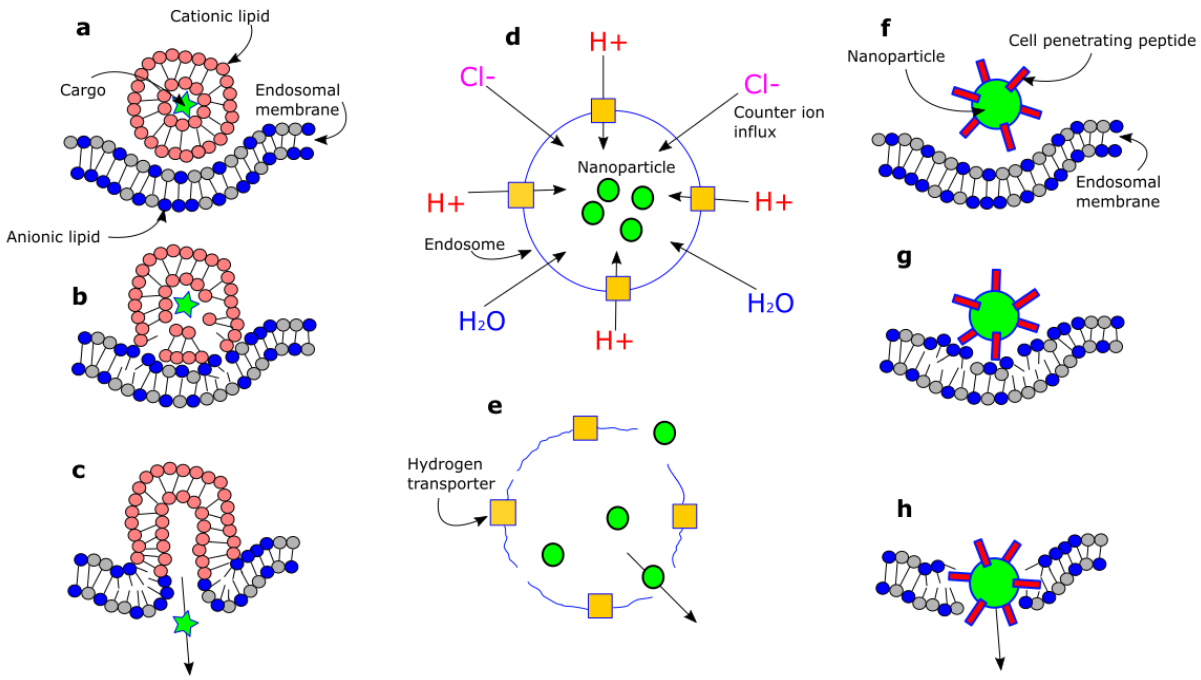

Figure 1.4 Strategies for escaping the endomembrane system.

Liposomes which contain fusogenic lipids may destabilize the bilayer structure of the endosomal membrane and induce a membrane fusion event which expels the associated cargo into the cytosol (a – c). Nanoparticles may also exert a proton sponge effect (d – e) which causes ingress of hydrogen ions and counter ions into the endosomal lumen. This is accompanied by osmotic swelling of the endosome and eventual rupture and escape of the nanoparticle (e). Another strategy is to utilize peptides or proteins with membrane destabilizing activity such as cell penetrating peptides which also disrupt the integrity of the endosomal membrane to promote cargo escape into the cytosol (f – h).

the V-ATPase H^+ pump which occurs alongside inflow of anions from the counter ion pathway to balance the transmembrane voltage difference (Fig.1.4 d – e) (DiCiccio and Steinberg, 2011). Endosomal rupture is then thought to result from a combination of several effects. The increased luminal counter ion concentrations lead to an osmotic gradient and the subsequent swelling of the endosome (Sonawane et al., 2003) and the cationic charge of the polymer may also induce a flip-flop of lipid groups which destabilizes the membrane (Yaroslavov et al., 2006). Polyethyleneimine (PEI) has proven to be a popular choice of polymer in this context owing to its ability to form non-covalent complexes with nuclei acids whilst maintaining an ability to mediate a proton sponge effect (Urban-Klein et al., 2005). Other polymers containing tertiary amine groups such as the imidazole ring of histidine can act as detergents when protonated to induce further membrane destabilization (Miller et al., 1983; Moreira et al., 2009; Pack et al., 2000).

1.4.4.3.3 Fusiogenic peptides and proteins

A variety of endosomal disrupting peptides and proteins have been described in the literature. These entities are often used in combination with other agents or grafted onto nanoparticle surfaces. In the main these have been taken from bacteria, viruses, or eukaryotic sources although others have been engineered or designed from scratch. For viruses or virus derived proteins, the endosomal escape properties can often be reduced to small peptide domains. The HA2 peptide from influenza haemagglutinin protein has been shown to undergo a conformational change at low pH to adopt a helical structure which leads to fusogenic activity and endosomal escape (Subramanian et al., 2002).

The HIV derived protein TAT (Trans activator gene product) is a potent activator of the human integrated HIV-1 genome and interest in this protein was piqued by its ability to enter uninfected cells (Frankel and Pabo, 1988). Subsequent work identified the minimal sequence responsible, a stretch of 12 amino acids (Tat peptide) which gave way to the field of cell penetrating peptides (Vivès et al., 1997). Since then, the number of CPPs has expanded into the hundreds although a poor understanding of their mechanism of entry and lack of cell specificity has hampered their deployment in therapeutics (Gautam et al., 2012). These problems have also been compounded by studies which show that cargo molecules which are appended to the CPP can greatly influence the uptake characteristics of these peptides (Watkins et al., 2011). Nevertheless, there is now a wealth of literature which shows that CPPs can be used as delivery vectors for a range of cargoes including nanoparticles (Fig.1.4 f – h) (Huang et al., 2015; Jones and Sayers, 2012)

Bacterial toxins have also been studied intensely for their abilities to form pores in membranes or disrupt membrane integrity. For example diphtheria toxin from *Corynebacterium diphtheria*

undergoes a conformational change at endosomal pH with the T domain of the toxin inserting into the membrane to act as a fusogenic peptide and allowing the C fragment to escape into the cytosol (Kakimoto et al., 2009; Murphy, 2011). Listeriolysin O from Listeria monocytogenes on the other hand forms pores at acidic pH and has been investigated as an endosomal escape agent for polymeric and liposome nanoparticles (Glomski et al., 2002; Kullberg et al., 2010; Walton et al., 1999). The main disadvantages of toxins for nanoparticle therapeutics involve immunogenic risks and the highly specific mechanism of some toxins which are difficult to preserve when conjugated to nanoparticles (Verkaik et al., 2010).

Protein and peptide factors showing membrane activity have also been derived from eukaryotes such as the melittin protein toxin from bee venom (Tan et al., 2012) or the antennapedia peptide derived from Drosophila (Joliot et al., 1991; Thorén et al., 2000). From humans a peptide derived from human calcitonin has been reported to display CPP behaviour (Rennert et al., 2006). Interestingly, there may even scope for engineering certain proteins of interest to display CPP-like properties whilst preserving the original function of the protein. In particular, a GFP variant has been engineered to display membrane penetrating activity (McNaughton et al., 2009). Here surface residues were modified to produce a highly cationic surface with a net charge of +36 which enabled this protein to enter cells. This supercharged GFP could also be used as a vector for siRNA and gene delivery (McNaughton et al., 2009; Thompson et al., 2012). Studies such as this suggest that there may be great potential for engineering individual components of DDS in ordered to maximise endocytic escape, which could include the cargo itself.

There is still a great deal of scope for designing novel nanoparticle assemblies or engineering of existing motifs and components into efficient delivery agents. In this work, QDs were explored as model semiconductor nanoparticles with the hypothesis that they could be utilized for delivery of small molecules, peptides and proteins in vitro. As discussed, the exceptional luminescent properties of QDs make these particles excellent probes for quantitative methods and for investigating nanoparticle – cell interactions. Following an initial characterization of these particles in biological media (Chapter 1), QDs were then investigated for their ability to deliver a small molecule drug, curcumin (Chapter 2). The binding of macromolecular compounds were also investigated and these consisted of individual CPPs, CPPs with short peptide cargos, or CPPs appended to GFP (Chapter 3). A highlight of these studies was the finding that a single amino acid substitution in the peptide cargo sequence could dramatically influence QD cell binding (Sayers et al., 2014). A final part of this work was concerned with characterizing the intracellular fate of QDs. Capturing the point of endocytic

escape is technically challenging and so a novel computational methodology based on single particle tracking microscopy was developed to allow individual nanoparticles to be studied as they undergo intracellular trafficking between cellular compartments with the aim of capturing endocytic escape (Chapter 5). This method was found to be performant when using simulated data sets in terms of its rate of event detection and low false positive rate, although future studies will allow the method to address biological questions of interest.

2 Materials and methods

2.1 Materials

HeLa cells were obtained from the American Type Culture Collection (Teddington, UK Dulbecco's Modified Eagle Medium (DMEM GlutaMAX^{TM}-I), fetal bovine serum (FBS), Opti-MEM and imaging media RPMI 1640 (GlutaMAX^{TM}) were from Life Technologies (Warrington, UK). Trypsin (0.25%) and phosphate buffered saline (PBS, pH 7.4) were also purchased from Life Technologies. Curcumin (purity ≥ 90 %) was purchased from Caymen Chemical (Cambridge, UK). Dimethyl sulfoxide (DMSO), Mowiol 4-88 for and paraformaldehyde were from Sigma-Aldrich (Gillingham, UK). Paraformaldehyde was used for fixation and Mowiol 4-88 was used for mounting fixed samples on glass slides. Both Mowiol 4-88 and paraformaldehyde stocks were stored at -20 ^{o}C. Agarose, urea, sodium dodecyl sulphate (SDS), NaCl, guanadine, citrate, acetate, ethylene glycol, glycerol, methanol and tris-acetic acid-EDTA (TAE) were from Sigma-Aldrich. Glass coverslips (thickness = 1.5, circular 25mm) were from VWR (Soulbury, UK).

2.1.1 Quantum Dots

Quantum dots (655 ITK-amino PEG and 625 ITK-carboxyl) were purchased from Life Technologies and consisted of cadmium selenide core and zinc sulphide shell (CdSe/ZnS) particles that are encapsulated within a proprietary surface polymer of undisclosed character. Both QDs are coated in the same polymer type although display different reactive surface groups, amino or carboxyl, respectively. Particles were provided as an 8µM suspension in 50mM borate buffer at pH 8.3. QDs were stored at 4^{o}C according to manufacturer's instructions. QD stocks were typically used within 6 months before ordering of new stocks.

2.1.2 Peptides and proteins

Peptides utilized in this study included were R8 and AcR8 which were from Biomatik (Delaware, USA), Cyclic-RGD (cRGD) from Anaspec (Cambridge, UK). G(SG)4-R8, F(SG)4-R8, G(SG)4-Pen, F(SG)4-Pen, G(SG)4-TP10, F(SG)4-TP10 and D-NuBCP-9-r8 were kindly provided by Arwyn Jones, Cardiff School of Pharmacy and Pharmaceutical Sciences. Nrf2-Tat was from Merk-Millipore (Feltham, UK). All peptides were prepared in water and stored at -20^{o}C. Goat anti-Rabbit IgG – Alexa 488 was purchased from Life Technologies. Recombinant proteins eGFPR8 and eGFP (abbreviated as GFPR8 and GFP) were also provided by Arwyn Jones in Tris buffer pH 8.0 and stored at 4^{o}C.

GFPR8

The GFPR8 protein sequence is provided below and consists of a histidine tag which was used for purification purposes, enhanced green fluorescent protein and the peptide R8:

MHHHHHHMVSKGEELFTGVVPILVELDGDVNGHKFSVSGEGEGDATYGKLTLKFICTTGKLPVPWPTLVTTLTYG
VQCFSRYPDHMKQHDFFKSAMPEGYVQERTIFFKDDGNYKTRAEVKFEGDTLVNRIELKGIDFKEDGNILGHKLEY

NYNSHNVYIMADKQKNGIKVNFKIRHNIEDGSVQLADHYQQNTPIGDGPVLLPDNHYLSTQSALSKDPNEKRDH
MVLLEFVTAAGITLGMDELYKRRRRRRRR

GFP

The protein sequence for enhanced green fluorescent protein is given below which additionally contains and N-terminal histidine tag for purification purposes:
MHHHHHHMVSKGEELFTGVVPILVELDGDVNGHKFSVSGEGEGDATYGKLTLKFICTTGKLPVPWPTLVTTLTYG
VQCFSRYPDHMKQHDFFKSAMPEGYVQERTIFFKDDGNYKTRAEVKFEGDTLVNRIELKGIDFKEDGNILGHKLEY
NYNSHNVYIMADKQKNGIKVNFKIRHNIEDGSVQLADHYQQNTPIGDGPVLLPDNHYLSTQSALSKDPNEKRDH
MVLLEFVTAAGITLGMDELYK

2.2 Methods

2.2.1 Cell culture

HeLa cells derived from human cervical carcinoma (EMBL, Heidelberg, Germany) were grown as a subconfluent layer under a humidified 5 % CO_2 environment at 37 ^{o}C using DMEM supplemented with 10 % FBS. Cells were split twice weekly using 0.25% Trypsin for 5 mins to detach cells from the growth plate. Cells were plated in 10 cm plastic dishes (Fisher, Chirchester, UK) at concentrations of 1:5, 1:10 and 1:20 in growth medium. For microscopy experiments cells were grown on glass coverslips in 6 well dishes.

2.2.2 Widefield microscopy setup

Cell and particle tracking images were captured on Olympus IX71 or Olympus IX73 inverted wide field fluorescent microscopes which were equipped with an Exfo X-cite 120 or Prior Proscan 220 light source, respectively, using the HCImage (Hamamatsu) software package. Blue, green and red fluorescence was detected using the Chroma excitation filters ET402/15x, ET490/20 and ET 572/35x, respectively. Due to their unique spectral properties, QDs could be visualised using any one of our excitation filters, however images were acquired using the ET 572/35x filter due to reduced background from autofluorescence. Fluorescence emission was separated by a multiband dichroic emission filter set #69002 (Chroma) and captured using either an Orca-ER CCD camera from Hamamatsu (IX71 microscopy) or an ORCA-Flash4.0 sCMOS camera from Hamamatsu (IX73 microscopy). Unless stated otherwise, red and green channels were acquired with an acquisition time of 200 ms and 400 ms, respectively. For single particle imaging experiments involving only the red channel the acquisition time was dropped to 50 ms.

2.2.3 Cell transfection

Cells grown on glass coverslips were transfected using the FuGENE HD transfection reagent from Promega according to the manufacturer's instructions. Briefly, 2 µg of DNA was complexed with 5 µL of transfection reagent in 100 µL of Opti-MEM for 30 mins. Transfection reagent was added to cells grown on glass coverslips in 6-well plastic dishes. Cells were then grown overnight to form a sub-confluent layer before further experimentation.

2.2.4 Statistical tests

Tests for statistical equality were performed using a two tailed t-test (Student's) assuming unequal variance using the Microsoft Excel 2013 function TTEST. The parameters of the function were the two arrays of data to be compared with the tails parameter set at 2. The standard significance boundary of $p < 0.05$ was used as a cut off.

2.2.5 Fluorescence and absorbance spectroscopy

Emission spectra of QD nanoparticles was acquired in triplicate using a Cary Eclipse (Varian) fluorescence spectrophotometer using black walled 96 well plates (Greiner). A sample volume of 100 µL per well was used and QDs were prepared in PBS buffer at a concentration of 100 nM with brief vortexing. Excitation and emission were analysed using a 10 nm band pass with a scan rate of 600 nm/min. Measurements were acquired using the Carry Eclipse software provided by Varian. For absorbance spectroscopy measurements were taken in triplicate using a Nanodrop ND-1000 (Thermo) using a sample volume of 2 µL. Following each measurement the optical head was cleaned using a soft tissue followed by washing with 5 µL of PBS.

2.2.6 Imaging of carboxyl QDs on a glass surface

Carboxyl QDs were prepared in PBS at a concentration of 1 nM with brief vortexing. 5 µL of QDs were then spotted onto glass coverslips on a horizontal surface and allowed to adhere for 10 mins at room temperature. Free QDs were then gently washed away by running 1 mL of dH_20 (1x wash) over the surface of glass coverslips. QDs were then imaged using a Plan Apo 100x/1.4 numerical aperture objective from Olympus with an exposure time of 50 ms. Time-lapse movies were acquired for at least 500 frames. Imaging was performed by mounting the glass coverslip in a 1.5 mL imaging chamber.

2.2.7 Transmission electron microscopy (TEM) and Energy-dispersive X-ray spectroscopy (EDX)

Electron micrographs were obtained using a JEM-2100 LaB6 transmission electron microscope fitted with a high resolution Gatan digital camera. Transmission electron micrographs and energy-dispersive X-ray spectrographs were acquired using the same system and analysed using the Oxford Instruments AztecTEM software suite. QDs were prepared in PBS at a concentration of 10 nM. QD samples were also prepared with a serum concentration of 10 % FBS by mixing QDs in PBS with undiluted FBS. This

solution was then vortexed for 30 s before imaging by TEM. All QD samples were dryed on a copper grid before mounting and imaging.

2.2.8 Quantification of QD size by TEM

QD dimensions were quantified by using an automated routine to analyse TEM images. Image processing was performed by first applying a Gaussian filter to tiff images using the built-in function found in ImageJ (Schneider et al., 2012) with sigma value of 4. This had the effect of smoothing the image and reducing the noise level. The image was then subjected to a background subtraction using a rolling ball algorithm with radius of 50 pixels which was also provided as a built-in function in ImageJ. The image was then thresholded using the Otsu method also found within the ImageJ library, before quantification of major and minor axis using the 'Measure particles' function in ImageJ. This produced a list of particles and their associated major and minor dimensions.

2.2.9 Gel electrophoresis

Samples were assessed by gel electrophoresis using a horizontal 0.8% agarose gel system (Biorad). Running buffer was 1x TAE pH 8.0 and the sample volume was 7 µL. The contentration of QDs was typically 25 nM unless stated otherwise. Samples were loaded along with 3 µL 30 % glycerol in running buffer. Gels were run for 30 minutes (carboxyl QDs) or 1 hour (amine QDs) under a steady current and 50 V or 5 V per 1 cm of gel. Greyscale images were acquired using a Geneflow gel doc system, whereas colour images were captured using a mounted compact camera (Cannon). Unless stated otherwise, the quantity of QDs loaded into the well was 375 fmol.

2.2.10 Protein corona formation on carboxyl QDs

Carboxyl QDs at 50 nM were prepared with a final concentration of 1, 10 or 99.375 % FBS with PBS pH 7.4 as the buffer. An FBS and buffer solution was first prepared before adding of a separate stock of QDs and vortexing immediately for 30 s. Corona formation proceeded for either 2 or 24 hours before analysis by gel electrophoresis and fluorescence microscopy.

2.2.11 Imaging of QDs in serum on a glass surface

QDs were prepared with a final concentration of 1 nM with PBS as the buffer. Solutions were prepared with or without 10 % FBS by first mixing buffer and PBS followed by addition of a QD stock. Preparations of 5 µL were then spotted onto a glass coverslip for 5 mins before gentle washing with dH_20 (1x wash) to remove excess QDs. Slides were then dried at room temperature and imaging was performed by mounting the glass coverslip in a 1.5 mL imaging chamber and analysing by widefield microscopy using a 100x/1.4 NA objective (Olympus).

2.2.12 Concentration effects on carboxyl QD corona formation

A serial dilution of QDs was prepared over a concentration range of 8 to 8000 nM in PBS before being added straight into 87.5 % FBS to bring the final concentration of QDs to between 1 to 1000 nM final

concentration. A concentration of 87.5 % FBS was used in this experiment as this was the highest achievable concentration of FBS possible using an 8 µM QD stock. Upon addition of QDs, solutions were vortexed for 30 s before incubating at room temperature for 2 hours. QDs were then analysed by gel electrophoresis by loading 15 fmol QDs into each well.

2.2.13 Quantification of carboxyl QD cell binding in presence or absence of serum

QDs were prepared at concentrations ranging from 0.1 to 100 nM with warmed DMEM only or DMEM + 10 % FBS as the buffer system. Following addition of QDs, solutions were vortexed for 30 s and allowed to stabilise at 37 ^{o}C for 10 mins. Preparations were then added onto cells grown on glass coverslips and incubated for 30 mins under tissue culture conditions. Cells were then gently washed twice in warm PBS before fixation in 4 % paraformaldehyde for 10 mins at room temperature and mounting in Mowiol. Cells were imaged by widefield microscopy using a 20x/0.75 NA objective (Olympus). For quantification, the bright-field channel was used to generate a mask for 50 cells. Masks were defined by manually selecting regions of interest using the ImageJ Region-Of-Interest Manager. A very small fraction of cells showed signs of blebbing which could be identified across all samples including the control. These cells were determined to be apoptotic and were discarded from quantification. Finally, the mean fluorescence intensity per cell was quantified using an ImageJ measurement function (Schneider et al., 2012).

2.2.14 Carboxyl QD cell binding with variable serum concentration

To prepare a variable serum concentration, 160 nM QDs were prepared in DMEM before being added to a dilution series of FBS from 0.1 to 99.375 % with DMEM as the buffer. Solutions were immediately vortexed for 30 s giving a final concentration of QDs of 1 nM and a variable serum concentration. QDs were then added to cells at 1 nM giving the same quantity of QDs but variations in the total amount of serum. Cells were incubated for 30 mins before washing twice in warm PBS pH 7.4 and fixing in 4 % paraformaldehyde. Cells were then washed in PBS before counterstaining with 25 µg/mL Concanavalin A-FITC (ConA) for 5 min in PBS to label the plasma membrane. Cells were then washed 2 x in PBS before mounting on glass slides using Mowiol 4-88 as the mounting medium. Imaging was performed on a widefield microscope using 100x/1.4 NA or 20x/0.75 NA objectives (Olympus). For quantification, 30 cells were isolated by using the ConA channel as the cell mask. As described in 2.2.13 masks were manually generated by hand before recording the mean fluorescence intensity per cell using ImageJ (Schneider et al., 2012).

2.2.15 Preparation and characterization of curcumin QD nanoparticles

To prepare QD and curcumin complexes, a QD stock was prepared in PBS pH 7.4 separately with brief vortexing. Curcumin stock was prepared using DMSO as the solvent at a concentration of 50 mM. Curcumin stocks were prepared fresh every 2 weeks and stored at 4 ^{o}C. QD and curcumin complexes

were prepared by adding 98 µL QDs to 2 µL of curcumin solution to bring the final concentration of QDs to 100 nM with 1.95 to 500 µM curcumin. Complexes were immediately vortexed for 30 s with a 15 min incubation at room temperature before further experimentation. For samples containing serum, QDs and serum were prepared separately allowing a further 15 mins to stabilize before addition of curcumin. Complexes were then centrifuged at 5000 g for 5 mins using a fixed angle rotor centrifuge (Eppendorf) and the supernatant (50 µL) was collected for further analysis by UV/vis spectroscopy using a Nanodrop ND-1000. Curcumin QD stability was assessed by maintaining the complexes at room temperature and periodically analysing the collected supernatant fraction by UV/vis spectroscopy up to 48 h after separation. For samples containing QDs, the QD only absorbance was taken as the background.

2.2.16 Dynamic light scattering and zeta sizing

QD and curcumin complexes were prepared as described in Materials and Methods section 2.2.15, above. For dynamic light scattering and zeta size measurements, complexes were first prepared at a concentration of 100 nM QDs with 100 µM curcumin in PBS buffer. Before measurements were taken complexes were diluted in PBS to give a final QD concentration of 15 nM. Measurments were taken using a Zetasizer Nano ZS (Malvern) to quantify the hydrodynamic radius and zeta potential of these complexes.

2.2.17 QD loading capacity and entrapment efficiency

QD loading capacity for curcumin was calculated according to the formula: QD loading capacity = Bound curcumin drug mass / QD particle mass. The curcumin entrapment efficiency was calculated according to: Curcumin entrapment efficiency = Bound curcumin drug mass / Total curcumin drug mass (Zhang et al., 2010). The bound curcumin drug mass was derived from a standard curve of free curcumin dissolved in DMSO. This was achieved by measuring the area under the curve from the UV/Vis spectroscopy binding experiment between 325 and 600 nm. The QD particle mass was quoted at 650 kDa by the manufacturer.

2.2.18 Dissociation of curcumin QDs in serum

To assess the drug dissociation behaviour of QDs in the presence of serum, 98 µL QDs in PBS were mixed with 2 µL curcumin in DMSO with vortexing for 30s to give a concentration of 200 nM QDs and 1 mM curcumin. Samples were incubated at room temperature for 30 mins and then centrifuged at 5000 g for 5 mins before collecting the supernatant. Following complexation, an equal volume of serum was added with brief vortexing to bring the final concentration range to between 1.56 to 50 % serum, 100 nM QDs and 500 µM curcumin. Complexes were incubated for a further 15 mins at room temperature before quantifying the change in the absorbance profile by measuring the absorbance ratio at 385 - 442 nm. In a separate experiment, an attempt was made to quantify the rate of change

in the absorbance ratio by immediately measuring the absorbance profile following mixing of complexes and serum. In this experiment 2 µL aliquots of sample containing QDs was placed on the NanoDrop and periodic measurements were taken as quickly as the instrument would allow.

2.2.19 Quantification of curcumin QDs dissociation in serum

QD and curcumin complexes were prepared as described above (2.2.18). To assess the binding equilibria of curcumin, 50 µL of complexes were further subjected to centrifugation in triplicate at 20,000 g for 30 mins which separated the QD fraction into the sediment. The supernatant fraction (15 µL) was then carefully collected and analysed by UV/vis spectroscopy taking the area under the curve to quantify the curcumin fraction which had disscoated from the QDs and was now associated with the serum fraction. As a control, FBS alone was subjected to centrifugation at 20,000g for 30 mins before analysis by UV/Vis spectroscopy.

2.2.20 Dissociation curve fitting

To calculate the dissociation constant of curcumin complexes as a function of total serum concentration, nonlinear regression curve fitting was performed with the Prism 6 software package from GraphPad Inc. Meausrements were quantified in triplicate using a one site binding – saturation model.

2.2.21 Cell viability assay

Cells were seeded at 4000 cells per well in black walled µClear plastic 96 well plates (Greiner) and grown overnight before further use. Stocks of QDs in DMEM and curcumin in pure DMSO were prepared separately. The curumin in DMSO stock was prepared at 100 x working concentration. Curcumin was added to QDs in DMEM (1% final DMSO concentration) and incubated for 15 mins at room temperature. For samples containing serum, QDs were first added to serum supplemented media for 15 mins at room temperature, before addition of curcumin for a further 15 mins. Samples comprised of 1 to 316 µM curcumin complexed with 1 to 316 nM QDs. Samples were prepared in the presence or absence of 10 % FBS. Media preparations were warmed to 37 ^{o}C and applied to cells which were then incubated for 24 h under tissue culture conditions. Cells were then gently washed twice with 100 µL of 10 % serum supplemented DMEM media. The cell viability assay was then performed using a CellTitre Glo assay kit from Promega according to the manufacturer's instructions. Briefly, 100 µL of CellTitre Glo reagent was added to each well of a 96-well plate for 10 mins with gently agitation. To quantify cell viability, luminescence of samples was recorded immediately using a FLUOstar Optima plate reader (BMG).

2.2.22 Peptide complexation with QDs

All peptides were dissolved in dH_20 at a concentration of 2 mM. For gel electrophoresis experiments, QDs and peptides were combined to bring the final concentration to 25 nM QDs with 0.79 µM to 250 µM peptide. QD and peptide stocks were prepared separately in PBS before mixing and briefly vortexing and incubating for 30 min at room temperature. Products were then assessed by gel electrophoresis on horizontal 0.8 % agarose gels using TAE pH 8.0 as the running buffer. A 10 µL sample volume was loaded with 3 µL of 30 % glycerol in TAE as the loading buffer. Gels were run for 1 hour under a steady current and 100 V (4 V per 1 cm of gel).

2.2.23 Imaging of carboxyl QD aggregation in the presence of CPP

QD and AcR8 complexes were prepared by first making QD and AcR8 stocks separately in PBS. Solutions were then mixed 1:1 with a brief vortexing to bring the final concentration to 1 nM QDs and 10 µM AcR8. 200 µL of sample was then loaded into a 1.5 mL imaging chamber fitted with a glass coverslip. Images were then acquired using a 100x/1.4NA objective (Olympus) with an integration time of 50 ms.

2.2.24 Dissolution of CPP – carboxyl QD aggregates with co-solvents

Carboxyl QDs were prepared in PBS and Ac-R8 was prepared using the stated co-solvent as the buffer. 1 µL of QDs were then added to 39 µL of co-solvent containing Ac-R8 to give a final QD concentration of 25 nM QDs and 6.4 µM of peptide, equivalent to 256 peptides per QD. Solutions were vortexed briefly and incubated at room temperature for 2 hours with gentle agitation on a rotating plate. This peptide concentration was chosen to reflect the point at which QD and peptide aggregation could first be detected when using PBS alone as the buffer in a prior experiment. Co-solvent solutions were prepared prior to experimentation at the following concentrations using PBS pH 7.4 as the primary solvent; Urea (2 M), sodium dodecyl sulphate (0.1 %), Sodium chloride (2 M), Guanadine hydrochloride (2 M), Citrate (0.2 M), Acetate (0.2 M), Ethylene glycol (30 %), Glycerol (30 %), Methanol (30 %). Following incubation samples were analysed by agarose gel electrophoresis using 10 µL as the loading volume.

2.2.25 Aggregation of carboxyl QDs and CPPs in the presence of FBS

QD and Ac-R8 stocks were prepared separately using PBS pH 7.4 as the buffer. Solutions were then mixed 1:1 to bring the QD concentration to 50 nM and the peptide concentration range to 5 – 500 µM. For samples containing FBS, serum was either added concomitantly with peptide and QD solutions to achieve the 10 % FBS final concentration, or alternatively, FBS and QD fractions were pre-prepared together prior to addition of the peptide. In this case, QDs and FBS were vortexed briefly and incubated for 30 mins at room temperature prior to addition of peptide. Following addition of the peptide, solutions were again vortexed briefly before incubating at room temperature for 30 mins.

Samples were analysed by gel electrophoresis using 10 µL loading volume. Alternatively, tubes containing aggregated material were imaged using a compact camera (Canon). To visualize QD fluorescence, tubes were placed on a bench next to a UV light source (415 nm) before imaging.

2.2.26 Live-cell imaging of QD uptake

QD and peptide stocks were prepared separately at 100 × in PBS pH 7.4 before combining in serum free DMEM for 30 min at room temperature, before warming and adding to cells at 37 °C. HeLa cells were seeded at 1×10^4 cells per cm^2 in 96 well black plastic walled dishes (Greiner µclear Bio One), or on glass coverslips in 6 well plastic dishes, and grown for 48 h in complete media before further experimentation. Cells were treated with complexes for 1 h in serum free DMEM using a sample volume of 1 mL (6 well dishes) or 100 µL (96 well plates). Complexes were then removed and cells were counterstained with 25 µg / mL Concanavalin A - FITC (ConA) for 5 min in serum free DMEM to label the plasma membrane. ConA treated cells were then washed a further 3 × in fully supplemented DMEM before immediate analysis as live cells by wide-field fluorescence microscopy or following a further 24 h incubation in complete media under tissue culture conditions. Cells were imaged using a wide-field imaging system (Olympus 20 × 0.75 NA lens).

2.2.27 Quantification of QD uptake and colocalization analysis

Using ImageJ (Schneider et al., 2012) an average of 66 individual cells (minimum of 51) were segmented based on ConA cell-surface stain profiles and analysed. A rolling ball background subtraction was performed (radius = 50) and untreated cells were used as baseline. Apoptotic and dividing cells identified by distinct morphological characteristics such as cellular blebs or the occurrence of a pair of rounded cells in close contact were discarded from analysis. For QD uptake analysis, the integrated intensity per cell was quantified per treatment condition. For colocalization analysis individual cells were analysed to obtain the mean Pearson's coefficient per cell using the ImageJ plugin Coloc 2 (Schneider et al., 2012).

2.2.28 Nrf2-Tat binding to QDs

Amine QDs or carboxyl QDs and Nrf2-Tat peptide were prepared separately in PBS before mixing at a ratio of 1:1 with a brief vortexing to bring the final QD concentration to 25 nM and the Nrf2-Tat concentration range to between 0.62 and 632 µM. Solutions were then incubated for 30 mins at room temperature before analysis by gel electrophoresis. In a separate experiment carboxyl QD and Nrf2-Tat was mixed together as above before the addition of 10 % FBS for a further 30 mins to achieve the same final concentrations of QD (25 nM) and peptide (0.62 - 632 µM). All samples were analysed by gel electrophoresis with a sample volume of 10 µL

2.2.29 GFPR8, GFP and Alexa488-IgG binding to QDs

QDs were complexed with Alexa488-IgG, GFP or GFPR8 by first preparing QD and protein stocks separately in PBS. QD and protein samples were then mixed together at a ratio of 1:1 and briefly vortexed to bring the final concentration of QDs to 25 nM. GFP and GFPR8 were assessed from 0.05 to 12.5 µM whereas IgG-Alexa488 was assessed from 0.125 to 2.5 µM. Samples were incubated for 30 mins at room temperature with gentle agitation on a rotating plate before analysis by gel electrophoresis and light microscopy.

2.2.30 Imaging of carboxyl QD GFPR8 complexes on a glass surface

Carboxyl QD complexes were prepared as above by preparing QD and GFPR8 stocks separately in PBS before combining to achieve a final concentration of 25 nM QDs and 2.5 µM GFPR8 or GFP. Samples were incubated for 30 mins at room temperature. For samples containing serum, complexes underwent a further incubation of 30 mins at room temperature after adding 10 % FBS. In serum containing samples the same final concentration of QDs (25 nM) and protein (2.5 µM) was achieved after the addition of FBS. Complexes were then diluted 1:25 in PBS and 5 µL was spotted onto a glass coverslip for 5 mins. Coverslips were gently washed with 1 mL of dH_20 before mounting in a 1.5 mL imaging chamber and imaging by widefield microscopy using 100 x / 1.4 NA objective (Olympus).

2.2.31 Stability of GFP, GFPR8 or QDs in the presence of serum

The stability of GFP, GFPR8 and QDs alone or in combination was tested using a fluormetric assay. Protein samples and QDs were prepared separately in PBS before combining to a final volume of 50 µL and with final concentrations of 2.5 µM protein and 25 nM QDs. For samples containing serum, stocks were prepared as above before mixing concomitantly with serum to bring the final FBS concentration to 10 %. All samples were loaded into black walled plastic 96 well plates (Greiner, µClear) and the fluorescence of samples was recorded periodically at 15 min intervals using a FLUOstar Optima plate reader (BMG) for up to 45 mins.

2.2.32 Binding saturation of GFPR8 and carboxyl QDs

Separate QD and protein stocks of GFP or GFPR8 were prepared in PBS before combining 1:1 to achieve a final volume of 50 µL and concentrations of 25 nM QDs and 1.25 to 6.25 µM protein with 1.25 µM increments. Complexes were incubated at room temperature with gently agitation on a rotating plate for 30 mins. Complexes were then centrifuged in triplicate at 20,000 g for 30 mins using a fixed angle centrifuge to leave a loose pellet. Aliquots of 25 µL of the supernatant fraction were then carefully removed and analysed in a black walled 96 well plate using a fluorescence plate reader (BMG).

2.2.33 GFPR8 dissociation from carboxyl QDs

QDs, GFPR8 and FBS stocks were prepared separately with PBS as the buffer before combining in a ratio of 1:1:2, respectively to give a final concentration of 10 nM QDs with 1 or 1.5 µM GFPR8, and a variable level of FBS ranging from 0 to 50 % by volume. QDs and GFPR8 were first mixed together and briefly vortexed before incubating at room temperature for 30 mins with gentle agitation on a rotating plate. Finally, FBS was then added with brief vortexing and incubation for a further 30 mins at room temperature. As detailed in 2.2.32 complexes were then centrifuged in triplicate at 20,000 g for 30 mins with a 50 µL sample volume, before the supernatant fraction (25 µL) was analysed in a 96 well plate format using a FLUOstar Optima reader (BMG).

2.2.34 Live cell imaging of GFPR8 QDs binding

Cells were grown on glass coverslips in 6 well plastic dishes. For live cell binding, the carboxyl QD concentration was fixed at 5 nM and the concentration of GFPR8 was varied from 50 to 500 nM. As a control GFP was used at 500 nM. Complexes were prepared as described in 2.2.29, to formulate a 10 x stock concentration with PBS as the buffer. Sample binding was performed at room temperature for 30 min before adding into DMEM only or DMEM and a final concentration of 10 % FBS. Complexes were then left to stabilise for 15 mins at room temperature before warming to 37 ^{o}C and adding to cells for 1 hour under tissue culture conditions. Cells were then washed twice in warm serum supplemented media (10 % FBS) and imaged by widefield microscopy using a 100x/1.4 NA objective (Olympus). Integration time was 100 ms for the red channel and 200 ms for the green channel. For maximum intensity projections, 12 images were acquired with a 0.5 µm offset giving a total image depth of 6 µm and an acquisition time of 3.7 s.

2.2.35 Single particle tracking of carboxyl QDs, image processing and software parameters

Time-lapse image sequences were processed in ImageJ using an optimised processing methodology which was developed to enhance the performance of the tracking algorithm. Images underwent regularisation using a Gaussian filter (sigma = 3) and rolling ball background subtraction (diameter = 50 pixels) before being sharpened and the contrast-enhanced using the built-in functions provided in ImageJ. This resulted in images with a low background and defined point-like QDs. Particle tracking was conducted using the MOSAIC particle tracking plugin (Sbalzarini and Koumoutsakos, 2005). Briefly, this method consists of a feature point tracking algorithm which quantitatively analyses 2D time-lapses to produce particle trajectories. A recent quantitative assessment of available tracking algorithms found this method to score highly in terms of its accuracy and speed (Chenouard et al., 2014). Optimised tracking parameters consisted of radius = 2, cutoff = 3.0, percentile = 2.5 %, link range = 2, and displacement = 3. The particle tracks were saved as a comma-separated-value (.csv) file for further downstream analysis.

2.2.36 Computer programming

All programming was carried out using Python 2.7 and the SciPy ecosystem (Oliphant, 2007). All modules used were open source and are provided as part of the 'scientific-stack' for Python. To obtain all modules used within this project, it is recommended to download the Anaconda Python distribution from Continuum Analytics. Alternatively, modules can be installed individually using the pip Python package manager by entering the command line and typing:

```
$ pip install module_name
```

Where 'module_name' is the name of the required module. For a full list of modules needed to run scripts provided in this work, please refer to the Supplementary Methods.

2.2.37 Particle simulation

A particle simulation program was developed named 'Interaction_simulator' which allowed for an objective investigation of the false positive and detection rates of the filter algorithms discussed in the text, with respect to various image and particle parameters outlined below. The program requires a variety of user defined parameters to generate a simulated 8-bit dual-colour time-lapse consisting of point-like particles moving in the red channel and larger circular objects in the green channel which were intended to model cellular objects such as endosomes. The program also generates complete particle trajectories which removes the uncertainty in particle tracking or allows for comparison with tracking algorithms. The scripts required to run Interaction_simulator are provided in Supplementary Methods 1.

The various parameters which can be set to initialize the simulation are listed in Table 2.1 along with a brief description, an example value and the expected data type in the software, as no user interface is provided.

Parameter name	Description	Example value	Type
vids	The number of time-lapse sequences to generate	10	Integer
outputpath	The destination folder where movies and track data will be saved.	"C:\\Users\\Joe\\Desktop\\SIM"	String
bg	The average pixel intensity of the image background for red and green channels	20	Integer

sigma	The standard deviation of the background noise, used to calculate the signal level.	1	Integer
SNRs	A list defining the signal to noise ratio (SNR) of each movie. Multiple values will generate multiple files of each movie with the corresponding SNRs. The signal is calculated according to: $SNR = \mu_{signal} / \sigma_{background}$ The noise is modelled by a Poisson distribution according to the sigma value provided above.	[20] – A single movie. or [1, 5, 20] – Three identical movies with different SNRs.	List
number_particles	The number of red particles to simulate per movie. Particles are added to frame=0.	100	Integer
frames	The number of frames per movie.	100	Integer
number	The number of green objects to generate at frame=0.	200	Integer
ar_size	The size of the image in pixels. A square movie is generated.	250	Integer
end_size	The radius in pixels of each green object is randomly chosen from this linear range. Object size does not change during the simulation.	(5, 5) – All objects have radius=5 (1, 5) – Object radius falls evenly within the range of 1 – 5 pixels.	Tuple

end_velocity	The maximum displacement of each green object is randomly chosen from this linear range. The maximum displacement of a particle does not change during the simulation.	(5, 5) – All objects have a maximum displacement of 5 px (1, 5) – Object max displacement falls evenly within the range of 1 – 5 pixels.	Tuple
p_fuse	The probability of a fusion event between a colocalized red particle and a green object per frame. The parameter must be > 0.	0.8 – Implies a 20% change of fusion.	Float
p_split	The probability of a split event between a fused red particle and green object per frame. The parameter must be > 0.	0.8 – A 20% change of splitting.	Float
event_gap	The minimum length in frames that an interaction event must last before a chance of splitting can occur.	5	Integer

Table 2.1 Parameters required for particle simulation software.

The parameter name is given as it appears in the software along with a description of the parameter and the expected data type of the parameter.

Using the parameters provided in Table 2.1, the software constructs unique red particles and green objects in the initial (first) frame which each have their own random maximum velocity, position and possibly size according to the parameterized ranges. Particles and objects are then allowed to move randomly within the constraint of their maximum velocity. Any particle which happens to colocalize with an object also has a non-zero probability of fusing with that object. If a fusion event occurs, the particle is confined to the bounds of the object for a set number of frames before a splitting event may happen.

2.2.38 Implementation of the TrIC method

The TrIC method was implemented in 2D as described in detail by (Dupont et al., 2013). Briefly, particle trajectories were generated using the MOSAIC software as described above in 2.2.35. This provided a list of particle trajectories with the image co-ordinates of each particle defined at each step of the time-lapse. This allowed a local image region surrounding each particle to be extracted at each step of the movie consisting of a 21 x 21 pixel region centred on the particle of interest. Having isolated this region the red and green channels were separated and assessed for 2D cross correlation using the Scipy software package. For each step in the particle trajectory this provided a single number describing the correlation between the channels within this local region.

2.2.39 Object proximity over a temporal window

Particles in the red channel were tracked using the MOSAIC algorithm (Sbalzarini and Koumoutsakos, 2005) as described in 2.2.35 which identified the centroid coordinates of these particles with sub pixel accuracy for each step in the time-lapse. For objects in the green channel, their locations were determined by applying a Gaussian fitting procedure. This was achieved by first isolating a region of interest (31 x 31 pixels) from the green channel which was centred on the location of the red particle. This region of interest was fit with an iterative 2D Gaussian function provided as part of the SciPy software package (Oliphant, 2007) to identify the position of nearby green objects. Identifying the locations of red particles and green objects allowed for the Euclidean separation distance to be calculated. This procedure was repeated for every frame to identify red and green particles which remained spatially colocalized for at least three frames.

2.2.40 Adaptive Gaussian thresholding

Adaptive Gaussian thresholding, also known as dynamic thresholding is calculated as the weighted mean of the local neighbourhood of a pixel followed by subtraction of a constant. An efficient implementation of this algorithm from the Scikit-image library was used for analysis (Scikit-image, 2015). Thresholding requires two parameters to be set which are the block size and the offset. Examples of these parameters are block size = 35 and offset = -10.

2.2.41 Calculation of signal to noise ratio

Signal to noise ratio (SNR) was calculated according to the formula:

$$\mathrm{SNR} = \frac{\mu_{\mathrm{sig}}}{\sigma_{\mathrm{bg}}}$$

Here μ_{sig} represents the relative signal value calculated as the signal intensity minus the average background intensity. In real terms, this is taken as the total events detected minus the number of false positives identified. σ_{bg} represents the standard deviation of the background which in this case refers to the standard deviation in the number of false positives identified (Dietrich et al., 2007).

2.2.42 Quantification of transferrin uptake using spatial temporal filter

HeLa cells were grown as a sub confluent layer on glass coverslips in 6 well plastic dishes before transfecting with Rab21-GFP using the transfection protocol outlined in 2.2.3. Transferrin-Alexa 568 from Life Technologies was applied to cells at 50 µg / mL in serum free DMEM for 5 mins before washing 3 x in complete media using 2 mL per wash. Cells were imaged in serum free RMPI 1640 using a 100 x /1.4 NA objective (Olympus) at 37 ^{o}C.

2.2.43 Quacker software implementation

The temporal and spatial filter methods discussed in detail in the text were developed into a program referred to as 'Quacker', the name of which was derived from a combination of Quantum dot and Tracker. The program takes as input a 16-bit dual colour movie in .tiff format and a .csv file containing particle trajectories. The .csv structure is equivalent to the output format from the MOSAIC particle tracking algorithm (Sbalzarini and Koumoutsakos, 2005) consisting of 4 columns of data containing trajectory name, frame number, x and y 2D image co-ordinates. The output of the program is a tri-channel image with thresholded red and green channels which match the input image, along with particle tracks in the blue channel. Interaction events in the blue channel are highlighted with a square box which appears at the location and frame of an identified event. Additionally, the number of events detected and their respective types are printed to the standard output of the computer. The scripts required to run Quacker are provided in Supplementary Methods 2. A description of the parameters available to the user is given below in Table 2.2 with example values and the required data types of each input.

Parameter name	Description	Example value	Type
idir	The input directory	'C:\\Users\\Kez\\Input'	String
Clip_edges	Whether to remove trajectories which approach the edges of the image. Occasionally tracking errors arise at the image edges.	True	Bool
Clip_amount	If a particle is found close than x pixels from the image edge the trajectory is removed from analysis.	10	Integer

col	The input column names as they appear in the .csv file joined with a '_' underscore separator.	'Trajectory_Frame_x_y'	String
multi_process	Whether to use more than one core in processing. If set to True uses the maximum number of cores available.	True	Bool
plots	If set to try, a plot of the thresholded image is generated and the program is terminated. Used to test thresholding parameters.	False	Bool
plot_frame	Which image frame to plot.	0	Integer
Initial_gauss	Sigma value. If set to > 0 a Gaussian filter is applied to the image prior to thresholding.	1	Integer
Gauss_size	The Gaussian size to use for the adaptive Gaussian thresholding step.	5	Integer
Block_size	The block size used for adaptive Gaussian thresholding.	30	Integer
Offset	The offset used for adaptive Gaussian thresholding.	10	Integer
min_track_length	Removes tracks less than x number of frames.	10	Integer
remove_short	Whether to remove short tracks from analysis.	True	Bool
split_variance	Sigma value. Refer to 6.2.4 for a detailed description.	1	Integer

Temporal	Whether to use the temporal filter. Set to True to turn on.	True	Bool
Spatial	Whether to use the spatial filter. Set to True to turn on.	True	Bool
Fuse_length	The length in frames before a split event is identified by the temporal filter.	5	Integer
Split_length	The length in frames before a fuse event is identified by the temporal filter.	5	Integer
Split_p_val	The p-value required before the spatial filter identifies a split event.	0.05	Float
Fuse_score	The p-value required before the spatial filter identifies a fusion event.	0.05	Float

Table 2.2 Parameter options available in Quacker.

The parameter name is given as it appears in the software along with a description of the parameter and the expected data type of the parameter.

Results

3 Characterization of Quantum Dot nanoparticles

3.1 Introduction

Delivery of macromolecules which embrace functionalities beyond those of small molecules to the interior of cells is a major goal in the development of novel medicines, contrast agents and diagnostic tools. Current strategies aim at assembling various functional molecules into nanoparticle vectors which provide targeting capabilities and/or mechanisms to release the payload. Utilizing nano assemblies in this way is anticipated to provide larger doses of therapeutics whilst minimising stress to the biological system (Chen, 2010). The diversity of nanoparticles currently under investigation is large and ranges from polymer assemblies, membrane based liposomes and a variety of metallic nanoparticles.

3.1.1 Quantum dots

Luminescent semiconducting nanocrystals, or Quantum dots (QDs), have been the focus of considerable interest due to their unique spectral and chemical properties. QDs offer many advantages over standard fluorescent proteins and small molecules, such as improved photostability and luminosity, narrow emission spectra, large Stoke's shifts and decay lifetimes of excitons, broad absorption profiles, controllable size range and surface chemistries, and multiplexing capabilities (Petryayeva et al., 2013). The superior luminosity of QDs capacitates long term visualisation of cellular structures and events with prospective tracking at the single particle level (Chien et al., 2011; Pinaud et al., 2010). Accordingly, QDs are currently being investigated as extremely bright and photostable intracellular live-cell probes and are also expected to be used in medical diagnostics.

The exceptional luminescence of QDs stem from their unique electronic properties which are intermediate between those of bulk solid semiconductors and discrete molecules (Wilson et al., 1993). Their small size results in confinement of electrons and electron holes which results in a quantization of energy levels according to Pauli's exclusion principle (Bawendi et al., 1990; Wilson et al., 1993). This quantum mechanical effect occurs when the radii of a semiconductor is smaller than the exciton Bohr radius, a measure of the distance between the electron in the conduction band and the associated electron hole in the valence band. Generally, as the radius of a QD decreases the gap between the highest valence band and the lowest conduction band increases, requiring more energy to excite the nanocrystal, and likewise more energy is released as a photon on a return to the ground state during fluorescence. As a result of this phenomenon the size of a QD directly influences the colour of light

emitted, allowing a wide range of colours to be generated by controlling crystal growth during synthesis (Wilson et al., 1993).

Excitation of QDs, or indeed all emitting dye molecules, also results in a discontinuous emission or blinking behaviour involving random switching between bright fluorescent and dark non-emissive states (Bawendi et al., 1990). The mechanisms which drive QD blinking are still subject to debate although appear to be partly explained by Auger recombination which involves a fast non-radiative charge recombination between a QD and an additional charge carrier, although additional mechanisms are also thought to contribute (Galland et al., 2011; Krauss and Peterson, 2011). The blinking of QDs has been utilized in super-resolution approaches which analyse blinking statistically to localize and resolve QDs precisely with a spacing closer than one-thirtieth of the emission wavelength (Chien et al., 2011; Lidke et al., 2005).

3.1.2 QD composition

In general, QDs are composed of a crystalline semiconducting metal core from groups II-VI, III-V, or IV – VI of the periodic table (Chan et al., 2002). The most common QDs for biological applications consist of a cadmium selenide (CdSe) core which is encased in a zinc sulphide (ZnS) shell and range in size from around 2 to 10 nm (Bruchez et al., 1998; Wagner et al., 2010). The ZnS shell reduces oxidation of the core and improves the quantum yield of the particle by passivizing surface defects which may otherwise act as non-radiative recombination sites for electron-hole pairs. The hydrophobic metal core must then be further capped with an outer polymer shell to facilitate dispersal in aqueous media and provide reactive surface groups for further functionalization with ligands or cargos of interest (Susumu et al., 2011; Tomczak et al., 2013; Walling et al., 2009). The capping stage is critical for minimizing potential toxicity associated with metal ion leaching from the QD core, and also may have a large effect on the biological identity and fate of the particle (Karakoti et al., 2015; Walczyk et al., 2010).

3.1.3 Cellular trafficking of QDs

Considerable effort is being invested in developing facile yet efficient methods for the cytosolic delivery of QDs and their associated cargos ranging from direct electroporation and nucleofection, through to facilitated delivery via attached ligand sequences such as cell penetrating peptides (CPPs) (Delehanty et al., 2010; Yoo et al., 2010). Deciphering the mechanisms of uptake of QDs and nanoparticle vectors in general however is a major challenge owing to the complexity of the endomembrane system and a poor understanding of factors which govern uptake and trafficking within the cell (Akinc and Battaglia, 2013; Cleal et al., 2013). Currently there is a need to define how different cellular pathways can be targeted by the use of ligands attached to the nanoparticle surface or as a result of entry via bulk flow. Evaluating the success of nanoparticle delivery to the cytosol by conventional co-localisation microscopy is also challenging as a result of the difficulty in determining

when a particle has escaped the endomembrane system (Canton and Battaglia, 2012; Martens et al., 2014; Varkouhi et al., 2011; Wohlfart et al., 2012). A common approach is to evaluate the distribution of nanoparticles within live cells by confocal microscopy where a perinuclear distribution is indicative of endocytosis, and a dispersed localisation or presence of material within the nuclear compartment is taken as evidence of endocytic escape and successful delivery. Co-localisation with the endolysosomal compartment is considered undesirable due to the risk of degradation of the vector and/or cargo by acid hydrolases located within this compartment (Settembre et al., 2013; Wang et al., 2013). Interestingly, a recent study using endocytic inhibitors to study the uptake of non-functionalized QDs suggested that carboxyl QDs enter cells via a lipid raft and G protein associated pathway before trafficking to late endosomes and lysosomes (Zhang and Monteiro-Riviere, 2009). Furthermore, low density lipoprotein (LDL) competed with QDs for internalization suggesting the LDL or scavenger receptors may recognize these particles. However, a potential drawback with using endocytic inhibitors relates to possible off target effects (Vercauteren et al., 2010). An emerging technique which offers to shed new light on QD entry is single particle tracking microscopy (SPT).

SPT requires localisation of particles within an image sequence followed by linking of particle co-ordinates into trajectories (Jaqaman et al., 2008; Parthasarathy, 2012; Sergé et al., 2008). SPT can inform on the fast-dynamics of nanoparticle-cell interactions (Clausen and Lagerholm, 2011; Petryayeva et al., 2013; Pierobon and Cappello, 2012), and the characteristics of a particles movement can be modelled to disclose information about its local environment relating to the confinement of the particle and crowding effects (Hall and Hoshino, 2010; Höfling and Franosch, 2013). Commonly, trajectories are analysed in terms of their mean squared displacement (MSD) which for a two dimensional classical diffusion process scales linearly in time (Höfling and Franosch, 2013; Huang et al., 2013). QDs have established themselves at the forefront of single particle applications owing to their exceptional spectral properties, stability, small size and ease of functionalization, and many studies have now employed QDs to investigate biological processes at the single particle level (Arnspang et al., 2012; Liu et al., 2012; S.-L. Liu et al., 2011; Lowe et al., 2010; Z.-G. Wang et al., 2012).

Nanoparticle entry into cells may be facilitated by ligands displayed on the particle surface which initiate active cellular processes (Chen, 2010; Cho et al., 2008). However, when exposed to biological fluids such as serum, nanoparticles dynamically adsorb a large variety of components to form a layer known as the protein corona which can greatly alter the identity of the particle (Fig.3.1) (Mahon et al., 2012; Monopoli et al., 2012; Salvati et al., 2013; Schäffler et al., 2013; Walkey and Chan, 2012). Human serum is reported to contain roughly 3700 individual protein factors from small peptides to macromolecular complexes such as LDL particles highlighting the potential complexity of corona formation (Anderson and Anderson, 2002). The composition of the corona is thought to be influenced

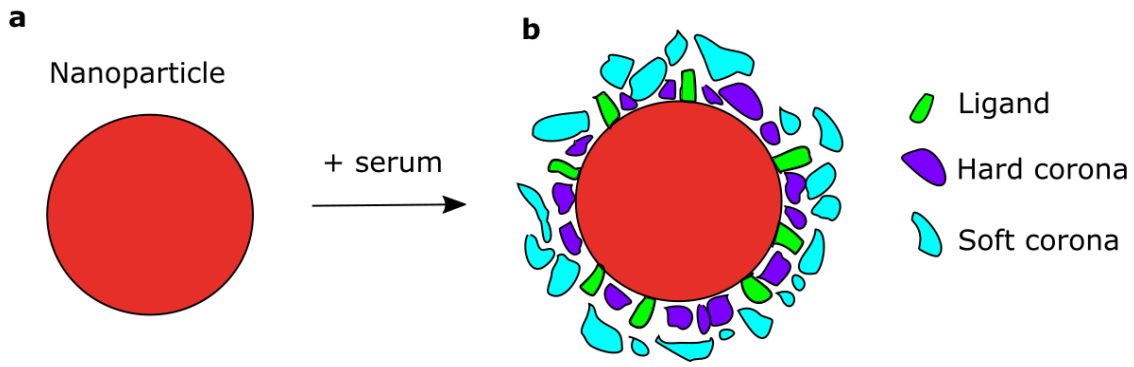

Figure 3.1 Formation of the nanoparticle protein corona.

Adding a nanoparticle (a) into serum or other biological environments results in the absorption of protein components to the particle surface leading to the formation of a protein corona. High affinity binders constitute the hard corona, whereas weaker interactions maintain a loosely bound soft corona (b). Recent studies have demonstrated that the corona can mask a nanoparticle surface ligand (Salvati et al., 2013).

by the surface properties of the particle as well as particle size, morphology and texture (Albanese et al., 2012; Mahon et al., 2012; Monopoli et al., 2012). Pristine nanoparticles are often highly charged following capping with reactive surface groups and may display a high surface energy relative to their environment which can be many times the thermal energy for studied nanoparticles (Mahon et al., 2012; Monopoli et al., 2011). As a consequence, following introduction into biological environments nanoparticles typically absorb a plethora of biomolecules which act to screen charged surface groups found at the particle surface in addition to possible hydrophobic domains which constitute the polymer shell (Casals et al., 2010; Dobrovolskaia et al., 2009; Mahon et al., 2012; Monopoli et al., 2011). Recent studies have shown that a serum corona can completely mask an antibody attached to the surface of model silica nanoparticles, effectively blocking the interaction with its antigen (Salvati et al., 2013). Understanding the factors which govern corona formation has thus become an area of paramount importance in the field of nanoparticle therapeutics and is crucial for predicting the biological response of a nanoparticles therapeutic.

For several nanoparticles including silica (Lesniak et al., 2012; Monopoli et al., 2011; Tenzer et al., 2011; Walczyk et al., 2010), gold (Casals et al., 2010), and polystyrene (Lundqvist et al., 2008; Monopoli et al., 2011; Walczyk et al., 2010) the corona has been reported to comprise of a tightly bound, but not completely irreversible layer termed the hard-corona (Fig.3.1b). On top of this near-monolayer a loosely associated layer forms termed the soft corona, which is thought to exhibit more rapid exchange kinetics and lower binding energy (Milani et al., 2012; Monopoli et al., 2012). Crucially, the proteins identified in the hard corona only ever amount to a few tens of individual factors and these rarely correspond to the most abundant plasma proteins (Capriotti et al., 2013; Casals et al., 2010; Monopoli et al., 2011; Zhang et al., 2011). The total number of factors which comprise a protein corona varies considerably for different nanoparticles although is often reported in the range of 50 - 150 (Monopoli et al., 2012). Quantitative studies which have characterized corona formation using individual factors such as transferrin or human serum albumin (HSA) indicate that these proteins bind with micromolar affinities to form a monolayer of 7 or 3.3 nm, respectively (Jiang et al., 2010; Röcker et al., 2009). The soft corona has been difficult to analyse due to its sensitivity to removal by washing techniques which are used when removing excess serum proteins (Monopoli et al., 2012). Subsequent exposure of the nanoparticle to a new biological environment is thought to lead to a partial exchange of corona components suggesting that that corona may maintain a 'memory' of a particle's transport through various biological compartments which may be particularly important for in vivo applications (Gasser et al., 2010; Lundqvist et al., 2011; Wang et al., 2013).

In this chapter an assessment of commercially available QDs was undertaken to characterize a variety of physicochemical properties of these particles. Additionally the interaction of QDs with biological

media and their uptake in cells was investigated. These studies demonstrate that QDs readily form a dynamic corona which can greatly influence cell binding. These studies provide a context for further development of QDs for biomedical applications.

3.2 Results

3.2.1 Spectroscopic and physiochemical properties of QDs

QDs are small highly fluorescent nanocrystals which show promise for use in imaging applications, therapeutics and diagnostics (Muthu et al., 2012; Pene et al., 2009). A wide range of commercially fabricated QDs are currently available with variations in composition, structure and physicochemical properties. To assess the utility of QD nanoparticles for biological imaging applications, two types of QDs were purchased from a commercial supplier which had 655 nm emission with an amine surface functionality, or 625 nm emission and carboxyl surface groups. Both QDs consisted of a CdSe/ZnS core/shell structure and were encapsulated within a proprietary surface polymer to constitute the carboxyl or amine surface functionality. The absorbance of 100 nM QDs in PBS showed a characteristic broad profile (Fig.3.2a) which tapered with increasing wavelength demonstrating the wide range of excitation wavelengths available for fluorescence applications using these nanoparticles. The emission profiles of these nanoparticles were also assessed using a fluorescence spectrophotometer by measuring 100 µL QDs in 96 well plates. QD were prepared at 100 nM in PBS and showed a fairly narrow with a full width at half maximum of 28.1 and 30.9 nm and emission peaks at 652 and 621 nm for amine and carboxyl QDs respectively (Fig.3.2b). The emission intensity was also assessed as a function of excitation wavelength by scanning between 325 and 600 nm which again illustrated the wide range of excitation wavelengths which generate useful levels of fluorescence for biological applications (Fig.3.2c).

3.2.2 Widefield analysis of QDs

Imaging of carboxyl QDs on a glass surface using a widefield system equipped with a sCMOS (scientific complementary metal oxide semiconductor) camera revealed that isolated particles could be resolved with a good signal to noise ratio using an integration time of only 50 ms (Fig.3.2d). Here, 1 nM QDs were adhered to glass coverslips before washing in dH_20 and imaging. The characteristic blinking behaviour of QDs was also demonstrated by imaging diffraction limited spots over 10 s with the same integration time for 500 frames (Fig.3.2e). The presence of two individual QDs in a diffraction limited spot was often evident by assessing intensity and blinking distributions, although it was difficult to determine higher levels of occupancy without further methods (Fig.3.2d, e).

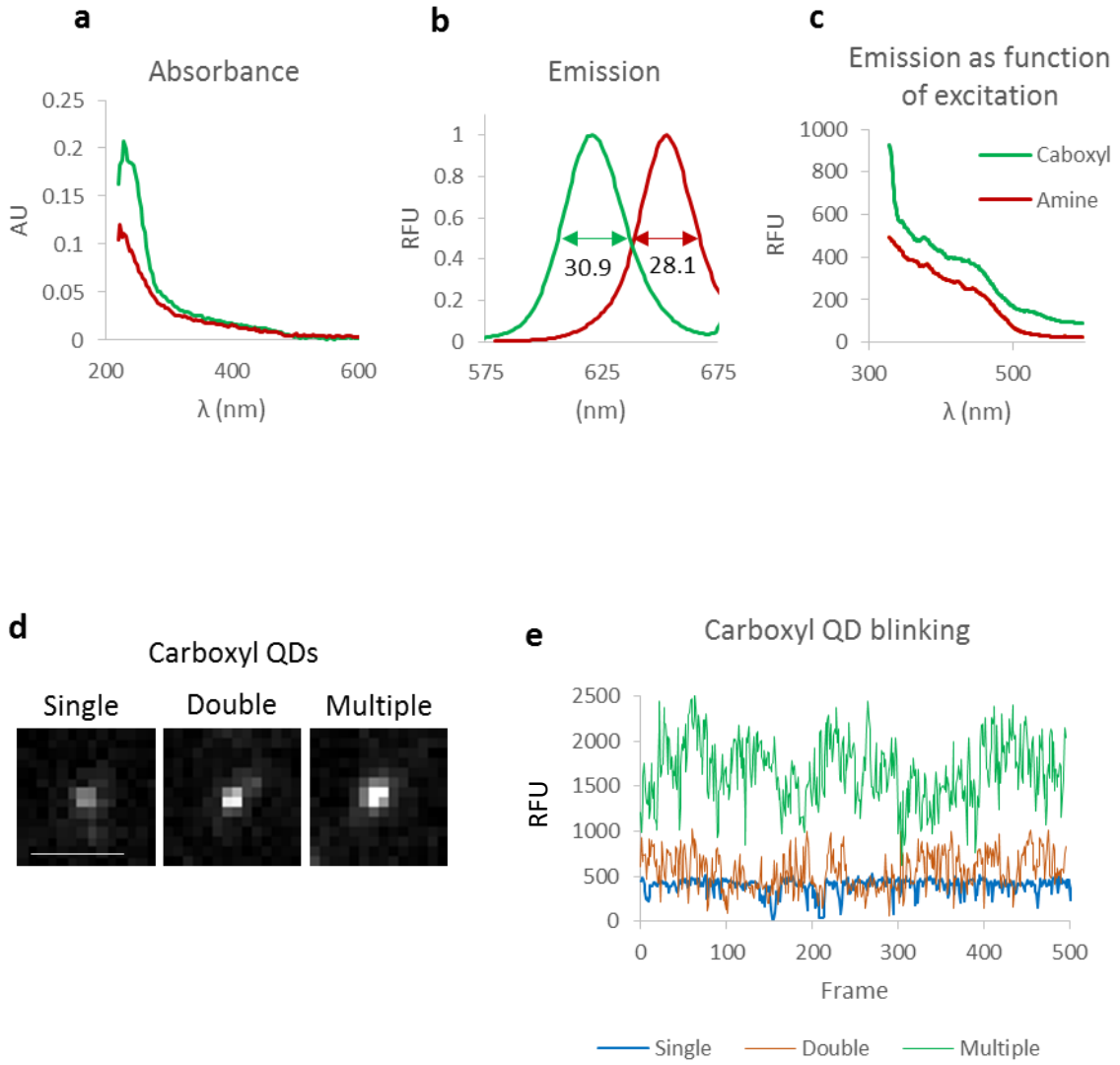

Figure 3.2 Spectral properties of commercial QDs.

The absorbance and emission profiles of commercial carboxyl and amine QDs are given in a, b, and the emission intensity as a function of excitation wavelength is shown in c. Imaging of carboxyl QDs by widefield microscopy demonstrates the ability to resolve individual particles (d). Analysis of emission intensity of carboxyl QDs using a 50 ms exposure time demonstrates the characteristic blinking behaviour of these particles which can also be used to reveal information on the number of particles occupying a diffraction limited spot (e). Scale bar in b is 1 µm.

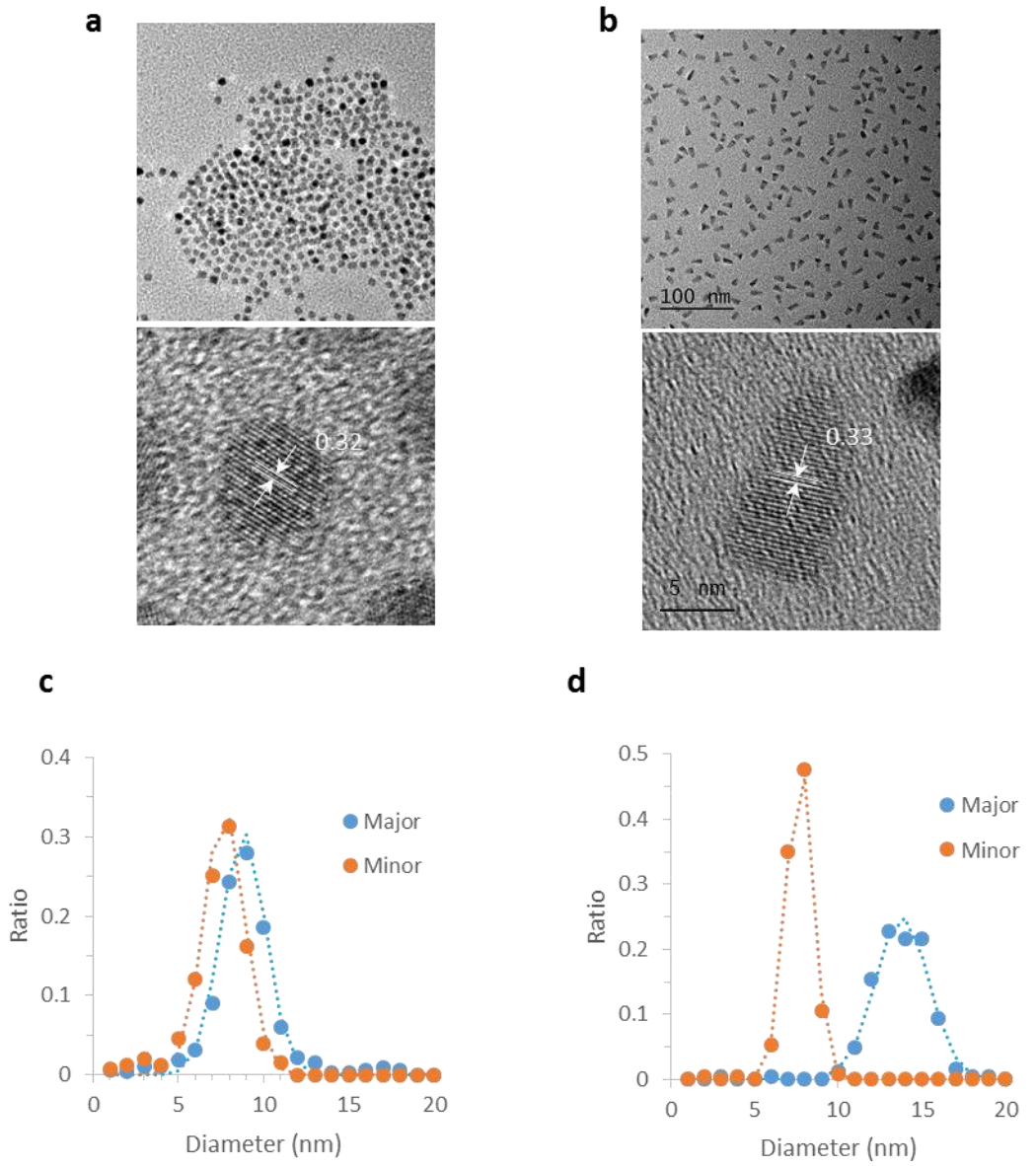

Figure 3.3 TEM analysis of carboxyl and amine QDs.

QDs were analysed by transmission electron microscopy to reveal the ultrastructure of the QD core with carboxyl QDs shown in a, c and amine QDs in b, d. The spacing of the crystal lattice is shown with white arrows. The major and minor axis of QDs were calculated using an automated routine described in Materials and Methds, and histograms of the length distributions are given for carboxyl (c), and amine (d) particles, respectively (solid markers). Particle size distributions were fit using a normal density curve, shown as dashed lines. The scale bars in b are 100 nm for the top image and 5 nm for the bottom image, these scale bars also apply for the panel of images in a.

3.2.3 TEM analysis of QDs

To analyse the ultra-structure of QDs, particles were imaged by transmission electron microscopy (TEM) using a high resolution Gatan camera (Fig.3.3). In this experiment 10 nM QDs in PBS were dried on a copper grid before mounting and imaging. The core of carboxyl QDs appeared almost spherical with a slight resemblance to a faceted hexagon whereas amine QDs resembled a bullet shape (Fig.3.3a, b). Previous studies have shown that QD anisotropy can be readily manipulated by changing crystal growth kinetics during manufacture (Peng et al., 2000). However it was not possible to resolve the polymer shell which did not show contrast using this method. Analysis of the crystal lattice revealed a similar spacing of atomic layers of 0.32 ± 0.05 and 0.33 ± 0.02 nm for carboxyl and amine QDs, respectively. The dimensions of QDs were quantified using an automated routine which consisted of isolating individual QDs using a thresholding step before measuring the length of major and minor QD axis, as described in materials and methods. Carboxyl (n = 550) and amine (n = 247) QDs were analysed and the length distributions of the major and minor axis are plotted in Fig.3.3c, d). These distributions were fit with a Gaussian distribution to calculate the dimension length and standard deviation. Carboxyl QDs were found to have dimensions of 8.8 ± 1.3 and 7.7 ± 1.2 nm consistent with a faceted hexagon shape (Peng et al., 2000). The unusual morphology of amine QDs was reflected in major and minor axis lengths of 13.8 ± 1.6 and 7.7 ± 0.8 nm. The larger surface area of amine QDs with respect to carboxyl QDs of 73.4 ± 11.18 to 46.9 ± 17.64 nm^2 suggested that amine QDs have a greater volume consistent with the relationship of increasing QD size resulting in a red-shifted emission profile.

3.2.4 EDX analysis of QDs

Carboxyl QDs were also analysed using energy dispersive X-ray spectroscopy (EDX) which is a technique that provides information on the elemental constitution of a material. EDX relies on the principle that individual elements have unique atomic structures which give rise to a unique set of peaks in an X-ray emission spectrum (Gilfrich, 1994). This technique was applied to the same sample prepared for TEM analysis consisting of 10 nM QDs dried on a copper grid. Analysis of a cluster of carboxyl QDs identified four major components as reflecting the CdSe/ZnS structure of these nanoparticles (Fig.3.4a, c). The standard deviation of each element was also provided in Fig.3.4b indicating a reasonable level of confidence for each element. The weight ratios however were somewhat surprising and suggested that the proportion of selenium and zinc was considerably lower than that of cadmium and sulphur (Fig.3.4c). For amine QDs the absence of large nanoparticle clusters made it difficult to achieve high elemental counts using EDX which was reflected in a higher standard deviation of the weight percentage measurements relative to carboxyl QDs (Fig.3.4b, d). Nevertheless amine QDs appeared to be comprised of a relatively high proportion of CdSe and lower Zn/S when compared with carboxyl QDs perhaps reflecting their larger core volume (Fig.3.4c, d).

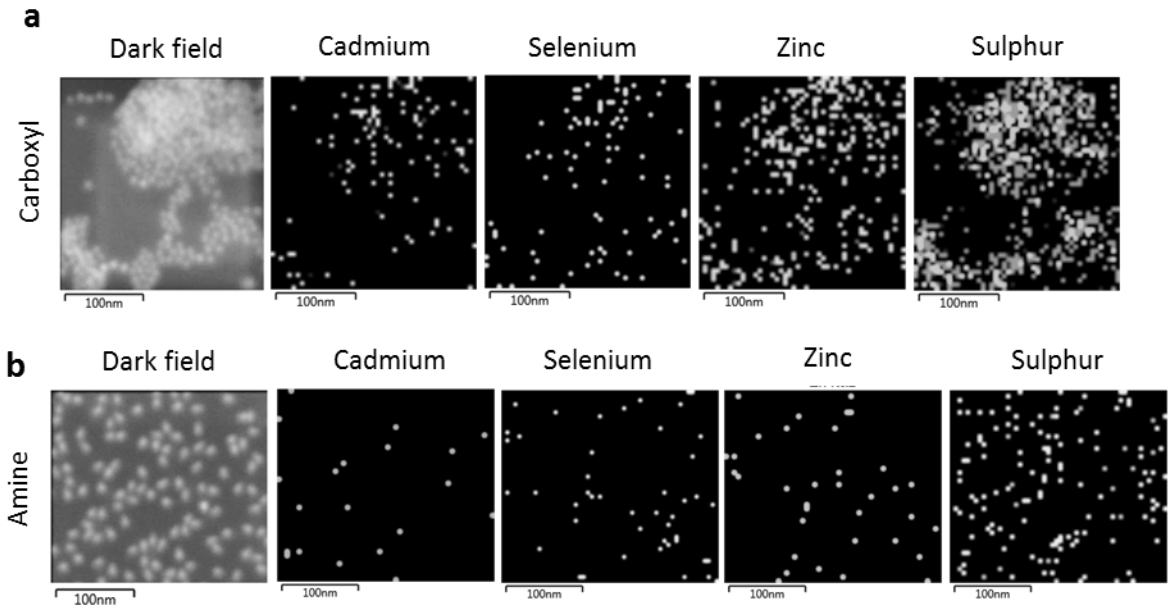

c

Element	Wt%	Wt% Sigma
N	0.00	0.00
S	38.79	3.99
Zn	7.09	1.37
Se	3.35	1.04
Cd	50.77	4.91

d

Element	Wt%	Wt% Sigma
N	0.00	0.00
S	19.19	6.19
Zn	0.21	3.23
Se	12.47	4.85
Cd	68.14	9.4

Figure 3.4 Elemental analysis of QDs by EDX.

QDs were first imaged by dark field TEM and then analysed by energy dispersive X-ray spectroscopy (EDX) to reveal information on their chemical composition, with elemental counts displayed in a, b. Owing to the clustering of carboxyl QDs higher elemental counts were obtained (a) with a reasonable level of confidence ascribed to the weight percentage for each element (c). However, this was not the case with amine QDs which demonstrated relatively poor counting statistics (b, d). Wt% = weight percentage, Wt% Sigma = standard deviation of the percentage measurement.

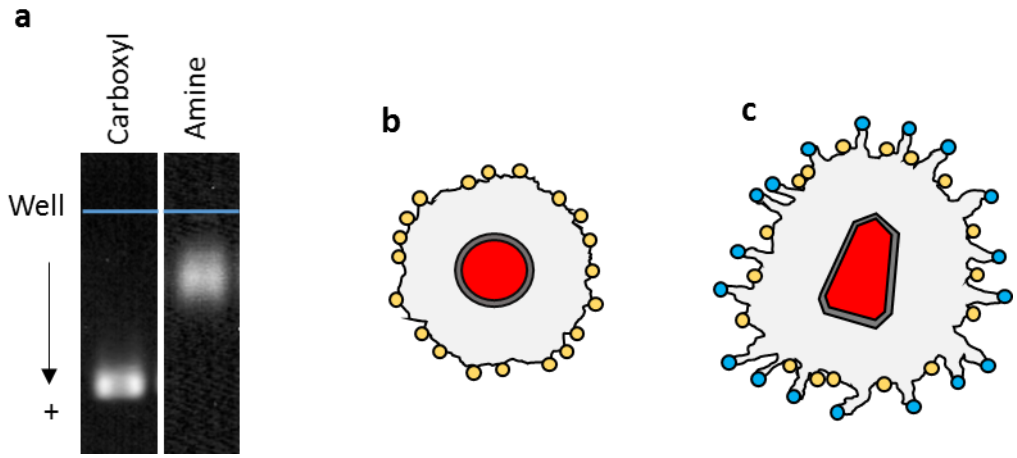

Figure 3.5 Analysis of QDs by gel electrophoresis.

QDs were run on agarose gels for 30 or 60 min for carboxyl or amine QDs, respectively (a). A schematic of the polymer shell surrounding these QDs (core shown in red) is postulated in b, c. For carboxyl QDs the surface is likely to consist of mostly carboxyl reactive groups (yellow circles), whereas amine QDs are thought to display and additional PEG linker to provide amine groups at the surface (blue circles). The electronegative character of amine QDs (a) suggests that these QD may also harbour anionic groups within the polymer structure indicated by yellow circles in c.

3.2.5 Electrophoretic analysis of QDs

A frequently used technique to analyse nanoparticle preparations is agarose gel electrophoresis which separates components in an electric field according to the hydrodynamic size and net charge of the particle (Surugau and Urban, 2009). Running of 25 nM carboxyl and amine QDs in a 0.8 % agarose gel at pH 8 demonstrated that both nanoparticles migrate towards the positive electrode and maintain an overall anionic character (Fig.3.5a). Carboxyl QDs migrated considerably quicker that amine QDs and were run for only 30 mins at 6 volts cm^{-1} whereas amine QDs required 60 mins at 10 volts cm^{-1}. The migration speed was thought to reflect the different surface functionalities of the two QDs in addition to the size. According to the manufacturer amine QDs possess additional poly ethylene glycol (PEG) linker with a distal amine group that is conjugated to the QD surface during synthesis (Fig.3.5b, c). The overall anionic character of the amine QDs may therefore be explained in terms of the incomplete crosslinking reaction during amine linker attachment, or perhaps the presence of additional electronegative groups within the polymer.

3.2.6 Analysis of QD protein corona

Following this brief assessment of the physical parameters of QDs, the interaction of these particles with biological media was also investigated. As discussed previously, when introduced into biological fluids such as serum, protein components may absorb to the particle surface in a process termed corona formation which is thought to greatly influence the identity of the particle (Fig.3.1) (Casals et al., 2010; Monopoli et al., 2012; Walczyk et al., 2010). So far few studies have investigated the protein corona of QDs (Prapainop and Wentworth, 2011; Treuel et al., 2014), and little is known regarding corona formation for the commercial QDs utilized within this study.

Here, corona formation was investigated using carboxyl QDs. QDs at 50 nM were added into in foetal bovine serum (FBS) ranging in concentration from 1% to a concentration of 99.375 % (abbreviated as 99 %) for 2 or 24 h before analysis by gel electrophoresis (Fig.3.6a, b). The highest concentration corresponded to the maximal achievable concentration using the QD stock provided by the manufacturer whereas the lowest concentration was considered to represent a low serum concentration with respect to standard tissue culture practises. QD gel migration was diminished with increasing FBS concentration indicating protein adsorption to the particle surface and an alteration to the size and/or charge of the particle. At 1 % FBS the QDs did not migrate as a tight band which may reflect a limiting protein concentration which gave rise to a heterogeneous distribution of protein components across the population of particles. At 99 % FBS QD migration within the gel was greatly reduced although it was unclear if aggregation was prevalent. By fluorescence microscopy or TEM large scale aggregation was not observed in FBS although a small increase in QD clustering was evident when compared to the control (Fig.3.6c – d).

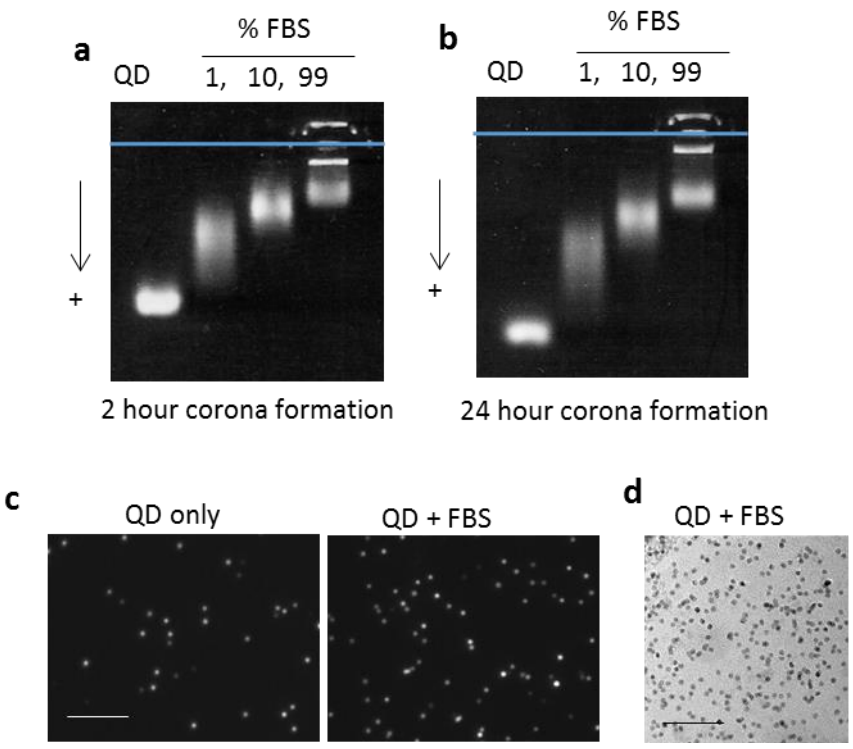

Figure 3.6 Formation of the protein corona surrounding carboxyl QDs.

Carboxyl QDs form a protein corona after 2 or 24 h incubation using varying concentrations of serum (a, b). Following corona formation few large scale aggregates are visible by widefield (c) and TEM (d). Scale bars are 20 µm (c) or 100 nm (d).

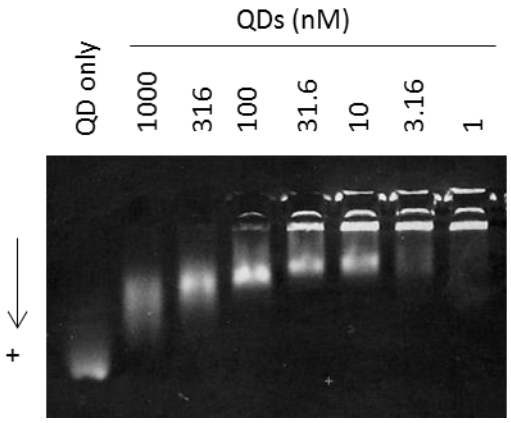

Figure 3.7 The influence of carboxyl QD concentration on corona formation.

A dilution series of QDs was introduced into 99 % FBS to induce corona formation. Higher serum to QD ratios resulted in decreased QD migration, whereas at low serum to QD ratios, coverage of QDs appears to be minimal. The same quantity of QDs was loaded into each well.

Although corona formation may not be complete after 2 hours due to the potential dynamic exchange of components over time, further changes were not detected by electrophoresis (Fig.3.6a, b) (Casals et al., 2010). The observation that 10 % FBS was insufficient to replicate the migration pattern of 99 % FBS even after 24 h was surprising considering the huge excess of protein components relative to only 50 nM QDs and suggests that corona formation may have been limited by the concentration of certain serum factors.

The effect of QD concentration on corona formation was also investigated by performing a serial dilution of QDs against 87.5 % serum over a range of three orders of magnitude (Fig.3.7). QDs were prepared over a concentration range of 8 to 8000 nM in PBS before being added straight into 87.5 % FBS to bring the final concentration of QDs to between 1 to 1000 nM final concentration. An equivalent volume of QDs (15 fmol) was then analysed by gel electrophoresis which demonstrated that decreasing QD concentration resulted in the formation of a progressively more 'mature' corona with reduced QD gel migration. At very low concentrations of 1 nM QDs, complexes were unable to migrate into the gel which may have been a result of either large size or charge neutrality, although aggregation could not be ruled out (Fig.3.7). Surprisingly, even at concentrations below 10 nM QDs, differences could still be observed in the migration of these samples suggesting that the corona had yet to reach completion (Fig.3.7). The total protein concentration of FBS used here has been reported to be 35 mg/mL (Son et al., 2001), although total serum concentrations in humans falls in the range if 60 – 100 mg/mL and 50 % total blood volume suggesting that the highest FBS concentration used here may be similar to in vivo concentrations (Gornall et al., 1949; Okutucu et al., 2007; Rauch et al., 2011).

3.2.7 Corona effects on QD cell binding

In light of these data it was pertinent to investigate the influence of serum on the binding of QDs to live cells. Initially the influence of standard tissue culture conditions on the uptake of QDs was investigated in live HeLa cells. A serial dilution of carboxyl QDs from 0.1 to 100 nM was added to cells for 30 mins in the presence or absence of 10 % FBS before fixing and imaging (Fig.3.8a). The mean fluorescence intensity of 50 cells was then quantified for each condition which demonstrated a substantial inhibitory effect of serum on the binding of QDs to cells. Very little binding was observed at 0.1 nM QDs even in the serum free condition although at higher QD concentrations of 10 nM and above, a 9.6 fold lower binding was observed in the presence of serum which may occurred due to reduced adsorption of QDs to cellular surfaces (Fig.3.8a).

In an attempt to examine the influence of different serum coronas on QD binding, QDs at a final concentration of 1 nM were prepared by mixing in FBS from 0.1 to 99 % to produce QDs with varying corona compositions (Fig.3.8b - d). These QDs were then added to live cells at 1 nM for 30 mins so that all cells received the same measure of QDs but variable levels of FBS. Imaging was performed on

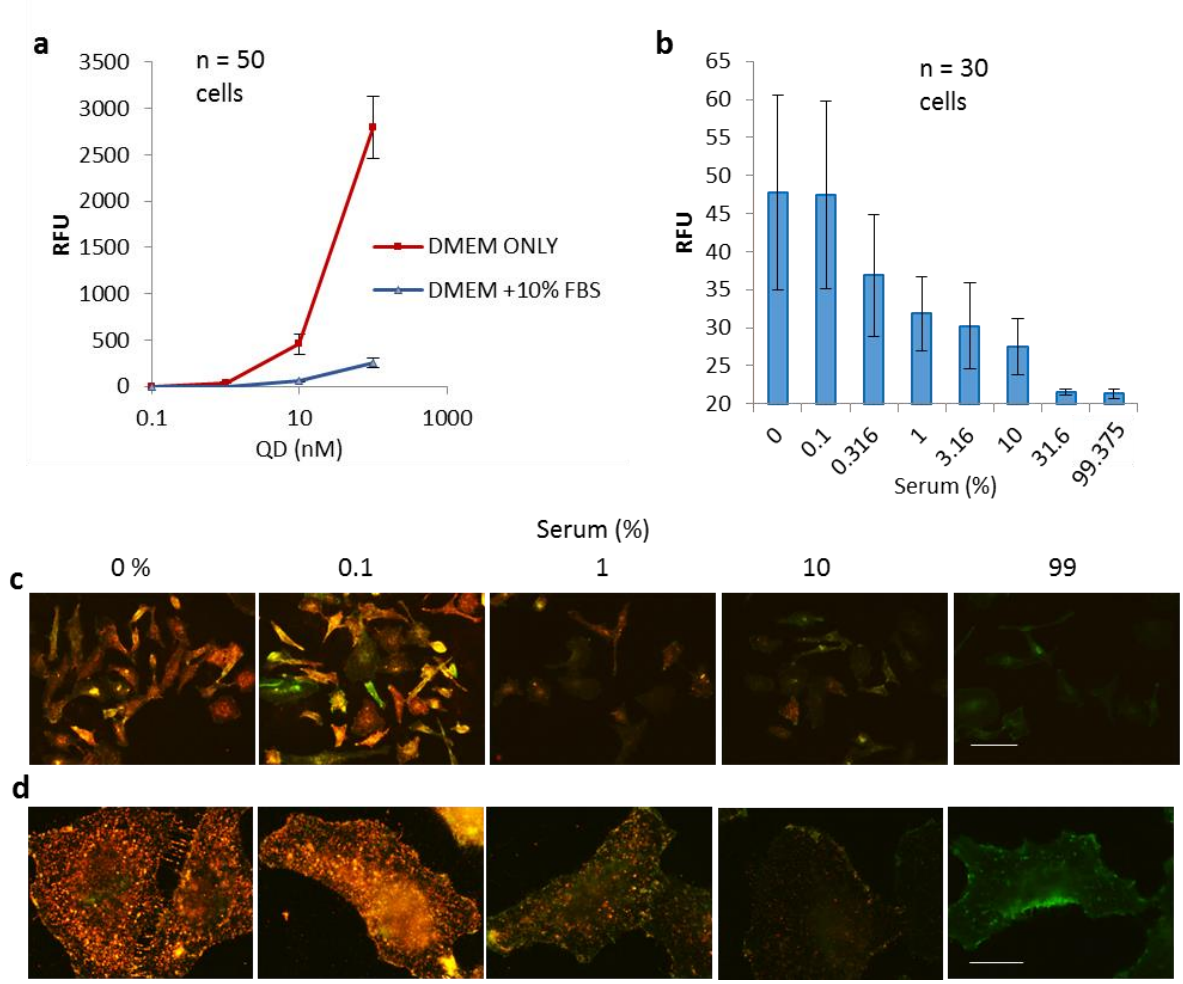

Figure 3.8 The influence of FBS on uptake of bare carboxyl QDs.

A range of carboxyl QD concentrations were investigated for cell binding in serum free media or media supplemented with 10% FBS (a). Cells were fixed and analysed by fluorescence microscopy, and quantified using ImageJ (n = 50 cells). In a similar experiment, the QD concentration was fixed at 1nM and the concentration of FBS was varied (b). Cells were fixed and stained with the cell surface marker ConA (green channel) and QD binding was quantified by fluorescence microscopy (n = 30 cells). For the highest serum concentrations QD binding was undetectable (b-d), although no background subtraction was performed in (b). Two magnifications of the same sample are shown in (c, d) to highlight the range of cell binding behaviour. Scale bars are 20 µm (c) and 100 µm (d).

fixed cells that had been counterstained with the cell surface marker concanavalin A and cell binding was then quantified as the mean fluorescence intensity over 30 cells (Fig.3.8b) (Chang et al., 2007). The degree of cell labelling was inversely associated with total serum concentration (Fig.3.8b). At 31.6 – 99 % serum, QD binding was negligible with only small fluorescence profiles whereas 0.1 % serum had no detectable influence on binding (Fig.3.8b). These data would suggest that serum components must achieve a minimum coverage of the nanoparticle surface to influence uptake which appeared to occur between 0.1-0.316 % FBS. However, at higher concentrations it was unclear if binding was influenced primarily as a result of a more mature corona or possibly through a further inhibitory effect on cell binding due to the presence of excessive free serum components. Extrapolating from these results, for a given nanoparticle to be effective a minimum nanoparticle concentration may need to be achieved in vivo relating to the expected surface coverage by corona components where lower particle concentrations would result in a complete masking of the nanoparticle surface.

The basic assessment of QDs undertaken here demonstrate their utility as model nanoparticles owing to their exceptional spectral properties and their stability in biological media. In conclusion, these data emphasise the complexity of understanding interactions between nano assemblies and the thousands of components found in biological fluids.

3.3 Discussion

A huge diversity of nanoparticles are currently under investigation for drug delivery purposes, diagnostics and theranostics (Schütz et al., 2013). Semi conducting nanocrystals or QDs are attractive candidates for applications involving an imaging component owing to their bright and stable fluorescence, and are interesting candidates for in vivo studies due to their large stokes shift and exciton decay properties (Walling et al., 2009). QDs also represent a versatile model system which can be utilized for in-depth biological studies through real-time monitoring of uptake, distribution and fate of the particle (Walling et al., 2009). Owing to the similarity of QDs to other metallic nanoparticle systems such as gold or magnetic, QDs may potentially also be swapped with those cores to facilitate optimization of certain carrier properties (Probst et al., 2013).

Commercial QDs composed of a CdSe/ZnS core encased within a proprietary polymer shell were initially analysed for their physical and chemical properties and demonstrated bright and stable emission profiles which were easily resolvable at the single particle level by widefield microscopy, even with a low integration time (Fig.3.2). Investigation of the ultrastructure of QDs by TEM revealed a very different morphology between the two particles which were either largely spherical in the case of carboxyl QDs or ‘bullet’ shaped in the case of amine QDs (Fig.3.3). Interestingly previous studies

suggest that particle morphology can have distinct effects on the interaction of nanoparticles with cellular surfaces and individual protein components which may be a concern when comparing these particles in various applications (Albanese et al., 2012). The clustering of carboxyl QDs in TEM images also permitted imaging by EDX microscopy which reported on the elemental constituents of these particles (Fig.3.4). However amine QDs were too dispersed to obtain reasonable confidence levels for weight percentage characterization although their elemental makeup as CdSe/ZnS particles was confirmed with low confidence (Fig.3.4).

Analysis of QDs by gel electrophoresis (Fig.3.5) revealed considerable differences between the particles relating to their hydrodynamic radius and overall charge. As expected carboxyl QDs displayed a strong electronegative character and migrated rapidly under gel electrophoresis whereas amine QDs migrated more slowly towards the positive electrode even under a stronger electric field (Fig.3.5). The observation that both particles maintained an overall anionic character was surprising and suggested that amine QDs had a mixture of surface groups despite their advertised amine surface functionality. The manufacturer indicated that these QDs are derivatized with amino-PEG chains suggesting that the overall anionic character may be a consequence of an incomplete crosslinking reaction during synthesis, and that the anionic character may stem from unconjugated carboxyl groups in particular, although this was not determined experimentally.

The lack of detail provided by manufacturers regarding the structure of the QD polymer coating is a hindrance to development of these nanoparticles for a wider range of applications. QDs may of course be synthesised from scratch although at the expense of time and resources. Moreover, for many applications the interactions which occur between the nanoparticle surface and biological fluids such as serum may be largely determined by the structure and chemistry of functional groups at the particle surface. Such interaction are now recognized to have a major impact on the performance of a nanoparticle and further underlies the need to characterize the polymer coat surrounding QDs (Karakoti et al., 2015).

When introduced into biological environments nanoparticles dynamically adsorb components to form the protein corona which is thought to be composed of high affinity binders which contact the particle surface with weaker binders layering on top (Monopoli et al., 2012). The process of corona formation is poorly understood even for well-studied nanoparticles such as gold and silica although is thought to greatly influence the properties of the nanoparticle and may largely determine the surface which is presented to the cell (Walczyk et al., 2010). Corona formation may depend on a number of features such as the physical and chemical properties of surface ligands, size, curvature and texture of the nanoparticle, in additionally to eccentricities of a patient's serum which may vary between individuals

(Monopoli et al., 2012). Clearly, there is a need for better understanding of the factors which govern corona formation which will probably need to be addressed for each individual nanoparticle design.

In this study, the dynamic aspects of the nanoparticle corona surrounding carboxyl QDs were investigated. By gel electrophoresis changes in corona formation could not be detected after a prolonged incubation (Fig.3.6b, c). Although an equilibrium may not have been reached the net charge and size of the corona, as assessed by gel electrophoresis did not change greatly after 2 hours. Interestingly, corona formation appeared to be strongly influenced by the concentration of serum and a 'complete' corona was not observed even when a huge excesses of serum was present (Fig.3.7). The serum protein concentration was thought to be in the range of 30 – 50 mg/mL, and the QD molecular weight was reported to be 650 kDa by the manufacturer. Thus the concentration range of QDs investigated here from 1 to 1000 nM QDs accounted for only 650 ng/mL – ug/mL by mass illustrating the scale of serum excess at low particle concentrations. This may be interpreted in terms of corona formation being reliant on lowly abundant proteins which has been reported for other nanoparticle designs (Arvizo et al., 2012; Monopoli et al., 2012).

In cell binding studies, the strong inhibitory effect of corona formation on cell binding was demonstrated by incubating in 10 % FBS in agreement with literature reports (Fig.3.8a) (Lesniak et al., 2012; Salvati et al., 2013; Walczyk et al., 2010). In a separate experiment QD concentration was fixed with respect to FBS which demonstrated that low concentrations of serum resulted in only a minimal coverage of the carboxyl QD surface and did not affect cell labelling, whereas for higher serum concentrations binding was undetectable with fluorescence signals similar to auto fluorescence (Fig.3.8a). This suggested that cell binding activity was inversely related to corona coverage although an unknown inhibitory effect on cell binding by the presence of serum could not be ruled out.

Nevertheless, the highest serum concentrations used here were thought to be similar to those found in human blood (Rauch et al., 2011; Son et al., 2001). Extrapolating these finding to an in vivo setting would suggest that for a nanoparticle therapeutic to be effective, the relative concentration or dose of the particle would need to be considered in terms of the associated corona which will form on the particle surface. At very high drug concentrations, the corona would have a minimal influence due to low coverage of the nanoparticle surface, whereas low drug concentrations may be ineffective simply due to shielding by the corona. In practise isolating the influence of the corona from the influence of free serum on nanoparticle uptake remains challenging. An obvious approach is to attempt purifying QDs with varying corona compositions from excess serum before uptake analysis which may allow a more direct assessment of the influence of different corona compositions on cell binding. A caveat to this approach is that purification may lead to loss of weakly associated components and preferential

retention of the hard corona. The cytotoxic impact of corona formation due to the sequestration of lowly abundant proteins from active roles in the bloodstream or other compartments is also a potential concern. Recent studies by Tenzer et al., suggest that corona formation can affect haemolysis, thrombocyte activation and cell death at early exposure times, further underlining the need to understand corona formation (Tenzer et al., 2011).

Despite the complexities involved, understanding interactions at the bionanointerface is crucial for nanoparticle therapeutic design and may also provide opportunities for drug delivery, by targeting the corona as a delivery platform in itself (Mahon et al., 2012). For example, the absorption of highly charged peptides or proteins to QDs, or interactions with hydrophobic moeties may mirror aspects of corona formation. As such is may be possible to utilize corona formation to stabilize peptide or protein binding at the nanoparticle surface. Additionally, the polymer coating surrounding QDs may act as a substrate for hydrophobic peptide or small molecule binding where corona formation may act as protective enclosing.

To explore these ideas further, three model cargo types were selected in an attempt to integrate corona formation with drug delivery. These cargos included the hydrophobic drug curcumin (Results Chapter 4), short model peptides containing a CPP domain (Results Chapter 5), and a model protein - enhanced green fluorescent protein appended to R8 (GFPR8, Results chapter 5).

4 Quantifying the dissociation of nanoparticle drug complexes in fetal bovine serum

4.1 Introduction

There is a great deal of interest in utilizing DDS for improving the therapeutic profiles of small molecular weight drugs which are either in clinical use or have failed during drug development. Nanoparticles may be attractive on several levels and may be used as a distribution system for improving the pharmacodynamics of a particular drug or effecting targeting of tissues in a specific manner. Exploiting non-viral nanoparticles for small molecule delivery has been extensively explored and a number of liposomal preparations have already made it into the clinic, with a particular focus on the treatment of cancers (Jain and Stylianopoulos, 2010; Wang et al., 2012).

4.1.1 Curcumin

A large variety of small molecule drugs are now under investigation for use in nanoparticle systems with the aim of overcome limitations relating to the biodistribution, bioavailability or tissue targeting of the native compound (Doane and Burda, 2013). One such drug currently under investigation is curcumin, an orange-yellow phenolic antioxidant which is found naturally in a variety of plant species and has been used in its crude form as a spice or herbal remedy for millennia (Sharma et al., 2005; Wang et al., 1997; Yallapu et al., 2014; Zhou et al., 2011). This bis-α, β-unsaturated β-diketone has been found to demonstrate therapeutic activity in a wide range of ailments and conditions such as cancer, Alzheimer's, diabetes, rheumatoid arthritis, liver injury, cataract formation, wound healing and fibrosis (Aggarwal and Harikumar, 2009; Ravindran et al., 2009; Sharma et al., 2005; Zhou et al., 2011).

Despite these promising characteristics the therapeutic potential of curcumin in vivo is severely limited by its very low bioavailability. Oral administration of a single dose of 2 g curcumin in healthy human volunteers elicited a serum concentration of only 0.006 ± 0.005 μg/mL after 1 h (Shoba et al., 1998). The poor bioavailability of curcumin is thought to stem from properties such as low water solubility which has been reported to be 0.6 μg/mL (Wang et al., 1997), poor stability in aqueous environments and rapid metabolic processing in the gut and liver (Sharma et al., 2005).

4.1.2 Curcumin loaded nanoparticles

Various nanoparticle approaches have been investigated to overcome these limitations including the use of poly (lactic-co-glycolic acid) (Yallapu et al., 2013), cellulose (Yallapu et al., 2012), magnetic (Yallapu et al., 2013, 2011) and alginate-chitosan-pluronic nanoparticles (Das et al., 2010). Magnetic nanoparticles loaded with curcumin were tested in a pancreatic cancer mouse model and were found

to reduce the rate of tumour growth and increase the survival rate (Yallapu et al., 2013). The bioavailability and distribution of curcumin was also higher when complexed with these magnetic nanoparticles demonstrating the potential for nanoparticle formulations to enhance curcumin parameters.

However, an often underappreciated aspect of nanoparticle drug design is the behaviour of the particle following contact with biological fluids whose components interact with the particle in complex and poorly understood ways. As discussed extensively in Chapter 1, the introduction of a nanoparticle into biological fluid such as serum results in protein components rapidly adsorbing to the particle surface to form a layer known as the protein corona (Casals et al., 2010; Monopoli et al., 2012; Walczyk et al., 2010). The structure, stability, composition and coverage of this layer is now regarded as being critical in determining the biological identity and fate of a particle although our understanding of this process is still in its infancy (Walkey et al., 2014; Walkey and Chan, 2012).

To reiterate, the formation of the corona is established rapidly under physiological conditions by complex and poorly characterized pathways which are determined by the specific architecture and chemistry of the nanoparticle surface and the abundance of corresponding serum factors (Monopoli et al., 2012, 2011). The formation of a corona has been implicated in modulating early pathophysiological effects including haemolysis and thrombocyte activation (Tenzer et al., 2013), in addition to inhibiting the uptake of particles by obstructing or occluding ligand binding sites at the particle surface (Salvati et al., 2013; Tenzer et al., 2013). Release of encapsulated drugs from within a nanoparticle was also recently reported to be inhibited by corona formation which was thought to be due a shielding effect by the corona layer (Behzadi et al., 2014).

The influence of serum proteins may also present further challenges associated with nanoparticle small molecule drug delivery. The binding of small molecule drugs to serum proteins is a well-documented phenomenon (Gao and Skolnick, 2013; Vuignier et al., 2010; Zhou et al., 2015), and early studies on liposomes have demonstrated that serum proteins were able to rapidly induce the leakage of a clacein cargo molecule (Allen and Cleland, 1980). However, for smaller nanoparticles little attention has been given to investigating the influence of serum proteins on small molecule drug loading. Indeed, this metric may be critical in evaluating the performance of these formulations.

Here, we investigate the loading of the model small molecule drug curcumin, to carboxyl QD nanoparticles and characterize their association as a function of serum concentration. We find that when exposed to serum, curcumin:QD complexes rapidly dissociate with curcumin being redistributed into the serum fraction. Furthermore, the level of dissociation was proportional to the serum

concentration. These data suggest that for in vivo applications nanoparticle drug dissociation behaviour may need to be addressed in ordered to maximise the efficiency of the nanoparticle system.

4.2 Results

4.2.1 Absorbance of curcumin and QDs

In this study the potential of carboxyl QDs to act as carriers for the small molecular weight compound curcumin was investigated. Curcumin exhibits promising anti-cancer properties although its poor bioavailability, relative insolubility in aqueous environments and rapid clearance have so far limited its use in the clinic (Sharma et al., 2005; Zhou et al., 2011). As discussed in Results chapter 1 carboxyl QDs used within this study were CdSe/ZnS core/shell nanoparticles (Fig.4.1c) which demonstrate a characteristic broad absorbance profile (Fig.4.1d) and were determined to possess a core diameter of roughly 8.3 nm by TEM (Fig.3.3c). Here the hydrodynamic diameter of these particles was investigated using dynamic light scattering. QDs at 100 nM were complexed with 100 µM curcumin in PBS for 30 mins before being diluted in PBS to 15 nM / µM and analysed using a Zetasizer Nano ZS (Malvern). The hydrodynamic diameter was determined as 33.72 ± 0.61 nm (polydispersity index 0.18 ± 0.04) and their zeta potential was calculated as -22.74 ± 2.22 mV (Table 4.1). The hydrodynamic diameter was considerably larger than that of the core suggesting that the anionic polymer coat extends from the QD surface for 12 nm in PBS which may potentially provide a relatively large polymer volume for drug loading.

The polymer layer surrounding metallic nanoparticles has previously been shown to support non-covalent incorporation of small molecule drugs which is thought to be permitted by hydrophobic pockets within the polymer matrix which act as sites for drug sequestration (Kim et al., 2009; Yallapu et al., 2013). Extending on this finding we investigated the possibility that QDs could act as a substrate for adsorption of curcumin within biological media.

4.2.2 Preparation of curcumin QDs

Complexes were prepared by mixing 100 nM QDs in PBS (pH 7.4) with a serial dilution of curcumin from 500 to 3.9 µM for 15 mins (Fig.4.2a, b). For samples containing serum (Foetal Bovine Serum, FBS), QDs and FBS were mixed for 15 mins prior to addition of curcumin. As a final step in preparation, all samples were centrifuged at low speed (5000 g) to remove insoluble aggregates and leave a clear supernatant. QDs were insensitive to this treatment and were retained in the supernatant fraction (Supplementary Fig.4.1). Supernatant fractions were then collected and analysed by UV/vis spectroscopy taking the area under the curve (AUC) between 325 – 600 nm to quantify the level of curcumin solubilized within the buffer system (Fig.4.2a, b).

Control tubes containing curcumin in PBS demonstrated the low solubility of curcumin in aqueous media with very low levels detected in the supernatant (Fig.4.2a, b). Reference spectra generated

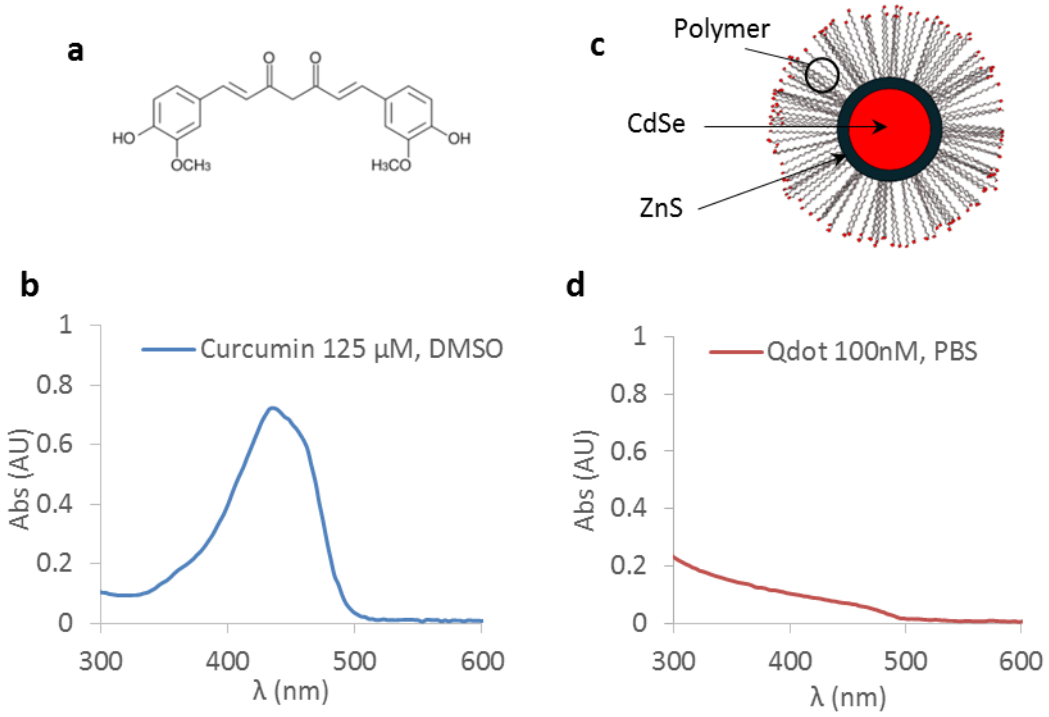

Figure 4.1 Absorbance properties of curcumin and QDs.

The conjugated double bond system of curcumin (a) gives rise to a defined absorption peak centred around 430 nm in DMSO (b). Carboxyl QDs shown in a schematic in c, display a broad absorbance shoulder in PBS (d).

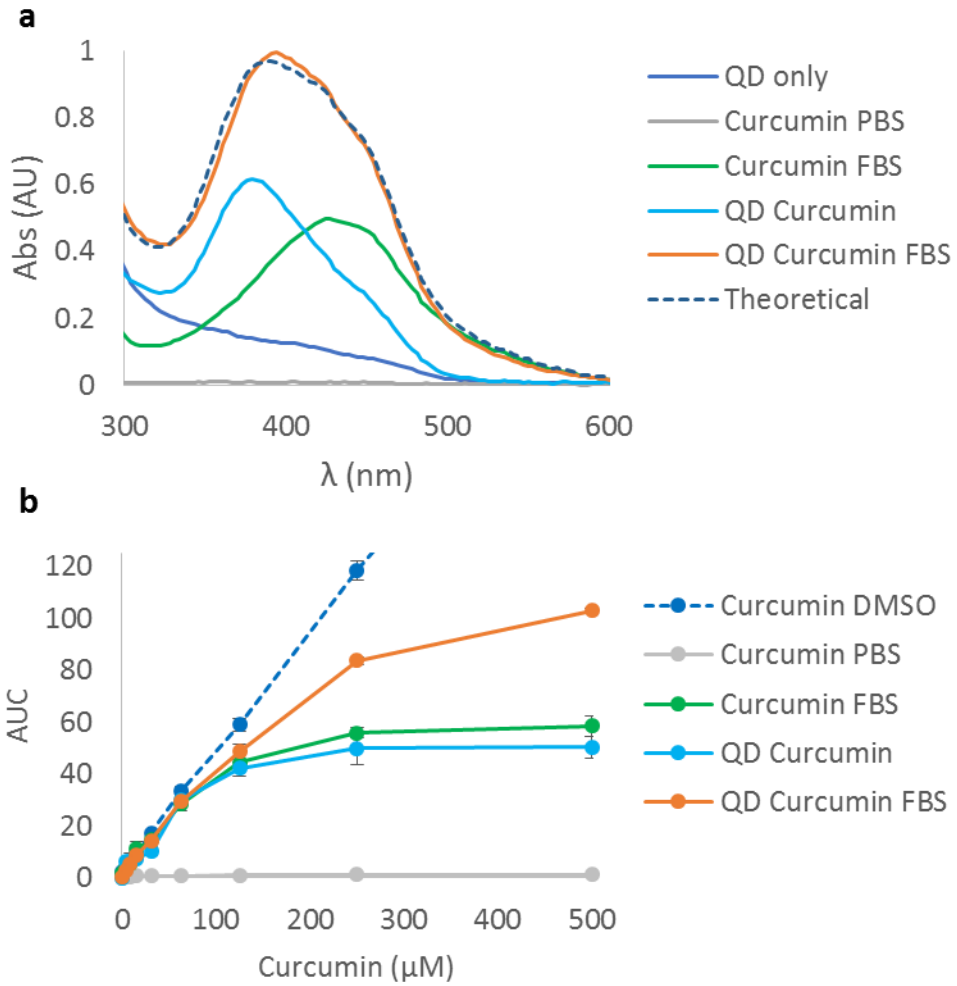

Figure 4.2 Curcumin forms complexes with QDs and FBS, alone or in combination.

The typical absorbance spectra of complexes prepared from 100 nM QDs and 500 µM curcumin are provided in a. The dashed line in a represents the expected profile from adding curcumin FBS and QD curcumin. Binding was quantified in b by taking the maximum absorbance of the curcumin peak following a background subtraction. n = 3.

	Z-Average (nm)	Polydispersity Index	Zeta Potential (mV)
QD	33.72 ± 0.61	0.18 ± 0.04	-22.74 ± 2.22
QD + Curcumin	34.77 ± 0.47	0.21 ± 0.02	-22.70 ± 0.44

Table 4.1 Hydrodynamic diameter zeta potential of curcumin QDs.

QDs or QD:curcumin complexes were analysed by dynamic light scattering and laser Doppler Micro-electrophoresis to characterize the molecular size, polydispersity, and zeta potential.

using 500 µM curcumin are provided in Fig.4.2a. Interestingly, both QDs and FBS individually appeared capable of solubilizing a large volume of curcumin (Fig.4.2a, b). At the highest drug concentration the level of curcumin retained in the supernatant fraction was calculated using a standard curve (Fig.4.2b, Supplementary Fig.4.2) and equated to roughly 122 µM for curcumin:FBS, and taking the QD absorbance as background, 106 µM for curcumin:QDs. Previous studies indicate that curcumin can form complexes with human serum albumin (HSA) with a dissociation constant of 20 µM suggesting the high level of curcumin retained in the FBS fraction was due to protein binding (Pulla Reddy et al., 1999). Here, the combination of serum and QDs had an additive effect on the level of curcumin detected in the supernatant which equated to roughly 225 µM at the highest drug concentration (Fig.4.2a, b). The additive nature is illustrated in Fig.4.2a by summing the respective absorbance spectra of curcumin:QD and curcumin:FBS (Labelled as 'Theoretical' in Fig.4.2a) which closely matched the profile of curcumin:QDs in FBS.

For curcumin:QD complexes in PBS, curcumin displayed a strong hypsochromic shift in absorbance relative to its profile in non-polar dimethylsulfoxide or serum (DMSO, Fig.4.1b, Fig.4.2a) with the peak shifting from 430 to 385 nm. A blue shift in solvatochromism corresponds to an increase in the dipole moment between the ground and excited states of a chromophore, consistent with the idea that bound curcumin was exposed to an increasingly semi-polar environment within the QD polymer with increasing drug concentration (Patra and Barakat, 2011). Drug entrapment efficiency was 72 % at 125 µM total curcumin, with a loading capacity of 61 % corresponding to almost 1100 curcumin molecules per QD. Following drug loading the particle diameter and zeta potential (Table 4.1) of curcumin:QD complexes did not change significantly, further suggesting that the drug may be sequestered within the QD polymer coating.

4.2.3 Stability of curcumin:QD complexes

To assess the stability of complexes, samples were prepared as above and periodically analysed by UV/vis spectroscopy up to 48 h following preparation (Fig.4.3a - c). QD controls in PBS or 10% FBS, and curcumin in DMSO, were both stable for the duration with little loss in absorbance over the course of the experiment (Supplementary Fig.4.3). Additionally, curcumin in FBS or curcumin complexed with QDs also demonstrated a relatively small degree of loss over the duration (Fig.4.3a, b). However, for curcumin:QD:FBS complexes a larger degree of loss was found which appeared more pronounced at lower curcumin concentrations, with an average loss of 37.5 % ± 14.7 across the whole concentration range. The reasons for this behaviour were unclear although may reflect an increased exposure of curcumin to the aqueous phase possibly as a result of transfer between these compartments or dissociation of the drug from QD complexes.

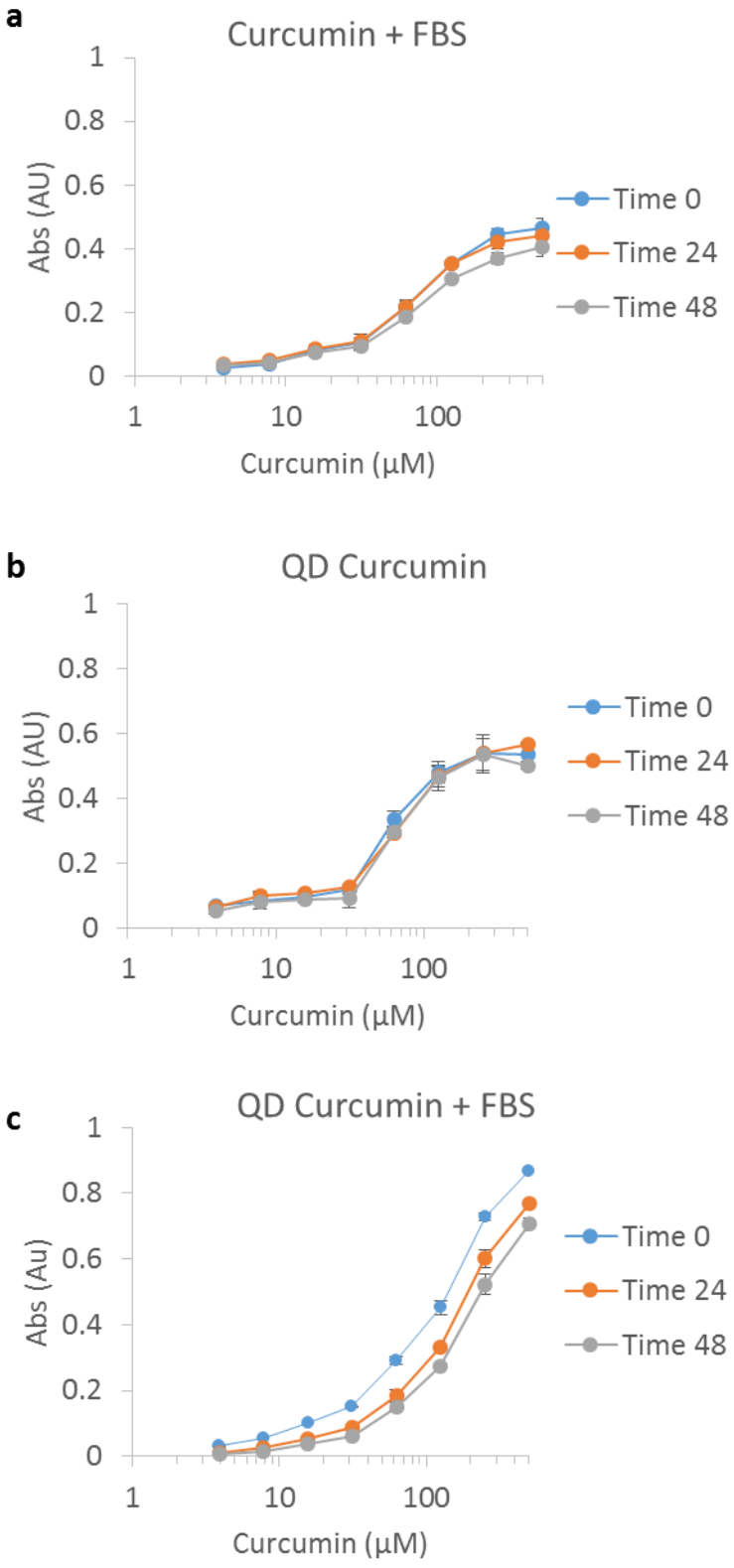

Figure 4.3 Stability of QD curcumin complexes.

The stability of curcumin when complexed with FBS (a), QDs (b), or QDs and FBS (c) was assessed by periodically quantifying the maximum absorbance of the curcumin peak up to 48 h after preparation.

4.2.4 Dissociation of curcumin:QDs in FBS

To investigate the binding behaviour of curcumin with respect to QDs and FBS, curcumin:QD complexes were prepared by mixing 200 nM QDs and 1 mM curcumin in PBS for 30 mins. Samples were then centrifuged at 5000 g and the supernatant was collected before addition of an equal volume of FBS to bring the concentration of serum to between 1.56 to 50 %. Samples were then incubated for a further 15 mins at room temperature before further analysis. Reference spectra of FBS alone are provided in Supplementary Fig.4.6. Interestingly, following addition of complexes into serum the blue chromatic shift in the peak of curcumin observed in Fig.4.2a was reversed with increasing serum concentrations, with the absorption peak now shifting to longer wavelengths (Fig.4.4a). This red-shift was suggestive of a redistribution of curcumin to a more polar environment consistent with binding to the FBS compartment (Fig.4.2a). This colour change however was rapid and essentially complete within < 20 s (Supplementary Fig.4.4). This was demonstrated by loading of samples onto the spectrophotometer immediately after mixing QD complexes with serum, with the shift in absorbance occurring before the first measurement could be taken (Supplementary Fig.4.4). This rapid colour change was presumably due to curcumin redistribution due to short-range simple diffusion.

To quantify this behaviour curcumin:QD complexes were prepared as above before separating by centrifugation at 20,000 g. Supernatant fractions of 15 µL were collected and analysed by UV/Vis spectroscopy to quantify the volume of QDs remaining. This procedure was found to remove > 96 % of QDs and retain > 99 % of serum proteins in the supernatant by measuring the area under the absorbance curve of centrifuged samples from 325 – 600 nm and comparing to QD and curcumin only standards (Supplementary Fig.4.5a, b, Supplementary Fig.4.6a - d). The level of curcumin within the supernatant was quantified by taking the integrated absorbance between 325 and 600 nm (Fig.4.4c) which again demonstrated that increasing serum addition leads to dissociation of curcumin:QD complexes and retention of the drug in the serum compartment.

In a control experiment, curcumin alone in FBS showed a variable sensitivity to centrifugation at 20,000 g, with lower serum concentrations showing a greater level of curcumin loss into the sediment fraction during centrifugation (Supplementary Fig.4.7a - d). In this experiment curcumin at 50 µM was mixed with FBS from 1.56 to 50 % with PBS as the buffer for 15 mins. Tubes were subjected to high speed centrifugation and the supernatant fraction was collected and analysed as above. Accounting for this behaviour, the dissociation of curcumin:QD complexes was calculated by taking the relative integrated absorbance from 325 – 600 nm above the FBS only baseline (Fig.4.4d). Interestingly this revealed a saturation curve with a half rate of 12.38 % FBS (95 % CI 5.86 - 19.90, R^2 = 0.990, B_{max} = 1.04) (Fig.4.4d). Taken together these data demonstrate that curcumin:QD complexes undergo

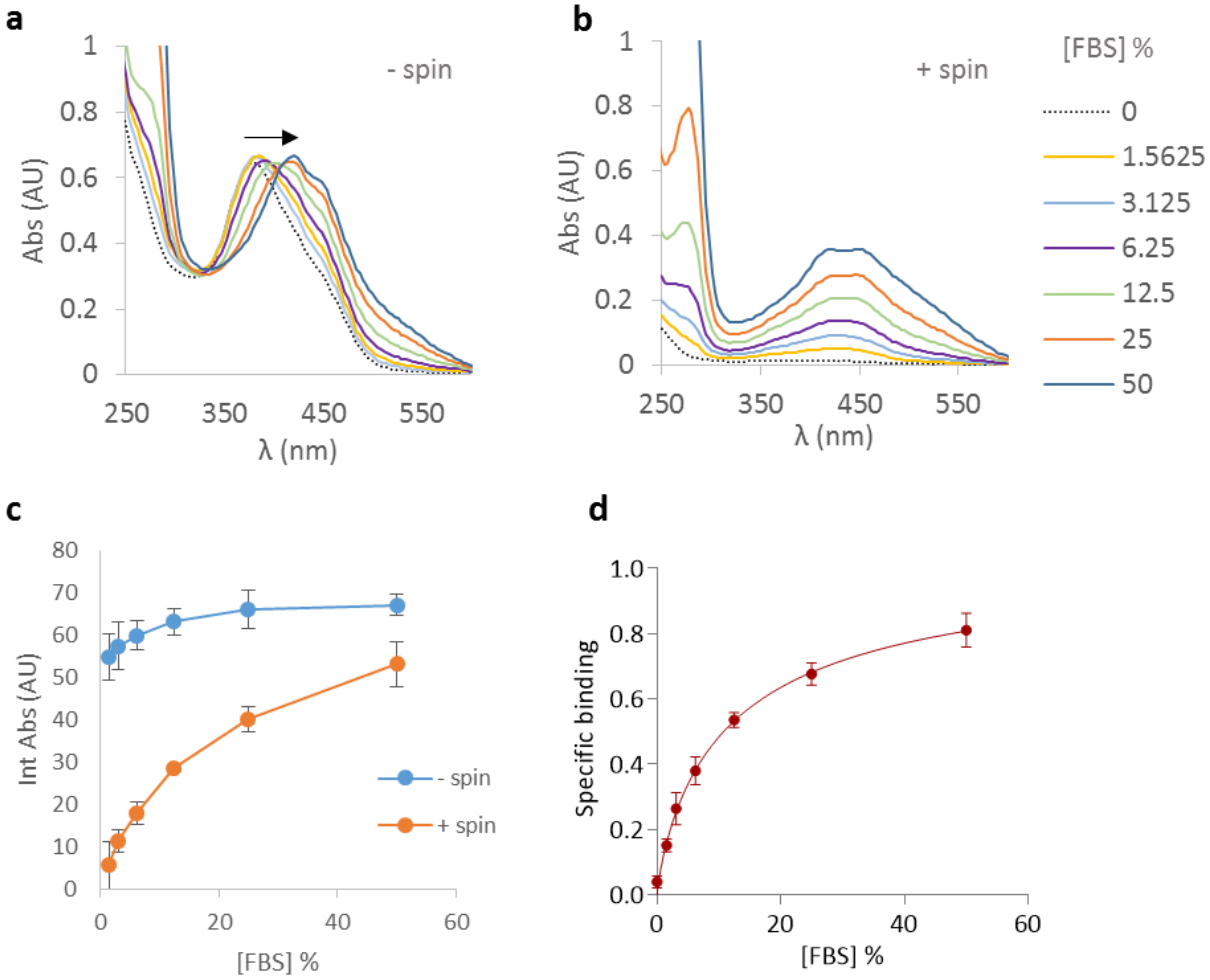

Figure 4.4 Quantification of curcumin:QD binding saturation as a function of FBS.

Addition of FBS to curcumin:QD resulted in a bathochromatic (red) shift in the curcumin absorbance peak (a). In a separate experiment, centrifugation of curcumin:QD complexes in the presence of FBS resulted in the retention of curcumin within the supernatant fraction as assessed by absorbance spectroscopy (b). The volume of curcumin retained in the supernatant fraction could be quantified by taking the integrated absorbance (c). The dissociation of curcumin from QDs was determined by quantifying the volume of curcumin remaining following centrifugation (d) n = 3.

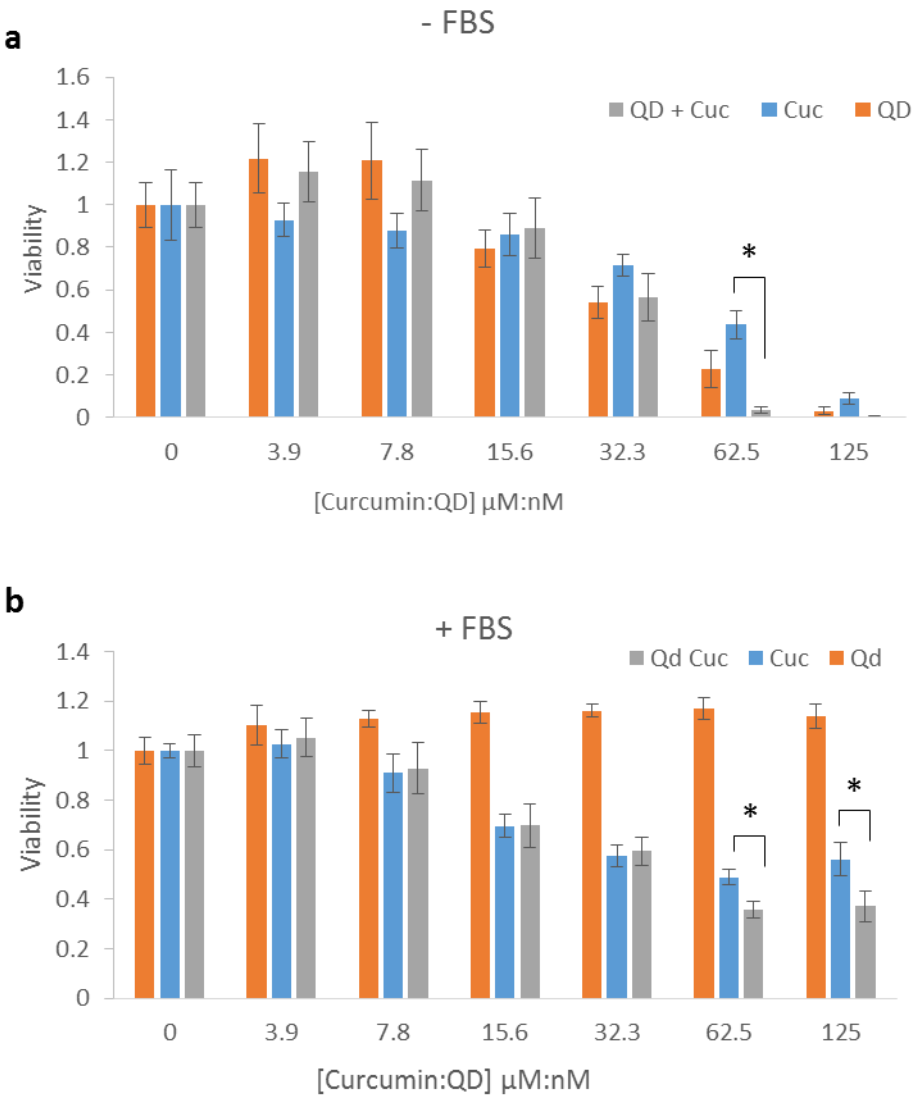

Figure 4.5 Cell viability performance of curcumin:QD complexes.

Curcumin:QD complexes were assessed in a cell viability assay using HeLa cells for 24 h in both the absence (a) and presence (b) of 10 % FBS. The reduction in viability for curcumin:QD complexes reached significance for both conditions at 62.5 µM/nm (curcumin/QD) when compared to the drug alone. * $p < 0.05$. n = 3.

dissociation due to competitive binding with serum proteins which occurs across physiologically relevant serum concentrations for in vitro and in vivo applications.

4.2.5 Effect of FBS on curcumin:QDs in a cell viability assay

To investigate the effectiveness of curcumin:QD complexes for drug delivery a cell viability assay was performed using HeLa cells over 24 h time course (Fig.4.5a, b). QD and curcumin complexes were prepared in 1:1000 ratios with QDs ranging from 1 to 316 nM and curcumin ranging from 1 to 316 µM. As with other experiments, samples were incubated for 15 mins before addition to cells. For samples containing serum, QDs and FBS were first mixed together for 15 mins prior to the addition of curcumin. In the serum free condition curcumin alone demonstrated an IC_{50} value of around 62.5 µM, with only 10 % viability remaining at the highest concentration (Fig.4.5a). However, free QDs also demonstrated substantial cytotoxicity in the absence of serum which even surpassed the effects observed with curcumin alone. QD toxicity has been previously documented in the literature and was thought to occur as a result of leaching of Cd^{2+} ions and generation of reactive oxygen species (Soenen et al., 2012). Incubation of cells with curcumin:QD complexes resulted in decreased viability over the QD control at concentrations above 31.25 µM with essentially 0 % viability ($p < 0.05$).

In the presence of serum, curcumin alone again demonstrated a cytotoxicity profile with viability falling to around 50 % at 62.5 µM. For QDs alone however, a complete reversal of the cytotoxicity profile was observed when compared to the serum free condition which may be explained in terms of sequestration of Cd^{2+} ions by serum factors (Chen et al., 2014). At 62.5 µM/nM and above curcumin:QD complexes demonstrated a significant effect on viability over the curcumin control with viability falling to around 36 %. Despite a substantial dissociation of the delivery complex under tissue culture conditions of 10 % FBS, these complexes achieved a marginal effect over the drug alone at least at higher concentrations. The observation that QDs alone demonstrated no effect on viability in the presence of serum suggests that the increased response of curcumin:QD complexes may have been achieved through increased delivery of curcumin. However a synergistic effect between QDs and curcumin may also have been likely as low concentrations of free Cd^{2+} ions may have provided an additional stress on the system.

In this study we sought to quantify the loading behaviour of curcumin and QDs as a function of serum concentration, and investigate the role of serum in determining the performance of the nanoparticle system. The conclusion that these non-covalent complexes are sensitive to rapid dissociation in serum is a potential drawback for the use of these particles in non-covalent drug systems. These findings may be relevant for other nanoparticle carriers which rely on a similar mechanism for drug loading and release. Nevertheless, despite a large dissociation of the delivery complex, a therapeutic effect was

still observed suggesting complex dissociation need not be an impasse for nanoparticle mediated drug delivery.

4.3 Discussion

There is great hope in utilizing nanoparticle carriers to enhance the pharmaceutic capacity of small molecular weight drugs through either tissue targeting or circumventing issues effecting the biodistribution, stability, and clearance of the native compound. The most straight-forward approach to assembling a drug nanoparticle complex is to exploit non-covalent interactions with the aim of sequestering the drug, often in hydrophobic domains within the nanoparticle, where breakdown of the particle, or timely dissociation of the drug results in delivery of the compound at a site of interest. A corollary of this approach is that the stability of non-covalent complexes in biological environments must be carefully considered to avoid premature dissociation of the drug which would abrogate the use of the nanoparticle vector.

In this study QD nanoparticles were investigated as carriers for the anticancer drug curcumin. By itself, curcumin is almost completely insoluble in aqueous environments and has been the subject of a number of studies using nanoparticles aimed at improving the biological effect of the drug (Das et al., 2010; Yallapu et al., 2014, 2013, 2012). Here we found that in the absence of serum, QDs proved to be capable carriers of the drug with entrapment efficiencies and loading capacities within ranges which might be useful for therapeutics with the maximum number of curcumin molecules per QD of around 1100 (Fig.4.2a Abraham et al., 2005). Drug loading appeared to result from sequestration of curcumin into the polymer matrix surrounding particles due to very little change in the hydrodynamic radius of particles following drug loading. The relative hydrophobicity of this environment however was unclear due to the chromatic shift in the peak of curcumin following QD loading which suggested the drug was exposed to a more polar environment relative to nonpolar DMSO. Taken together these metrics would generally identify QDs as promising candidates for curcumin drug delivery. Other nanoparticle systems may achieve superior loading capacities such as liposomes which have been reported to sequester 48,000 doxorubicin molecules for a 100 nm particle (Abraham et al., 2005), although these systems are also considerably larger than the nanoparticles used here in addition to being highly optimised.

Investigation of QD complexes in the presence of serum revealed an unexpected dissociation of the drug with increasing serum concentration (Fig.4.4). Using UV/vis spectroscopy the drug nanoparticle complex appeared to rapidly dissociate over short timescales of under 1 minute with the drug appearing to partition into the serum compartment. The shift in absorbance of curcumin to longer

wavelengths suggested that the drug redistributed to a more hydrophobic environment which presumably occurred as a result of simple diffusion. The routine serum concentration of 10 % for tissue culture applications accounted for almost 50 % drug dissociation from QD complexes. More alarmingly, in vivo environments where serum concentrations can approach 50 % would see a higher level of dissociation and may render the nanoparticle as essentially a bystander.

In retrospect, it is unsurprising that nanoparticle drug loading might be antagonised by the abundance of over 3700 protein factors found in serum which routinely show a propensity to bind small molecule compounds such as curcumin (Muthusamy et al., 2005; Vuignier et al., 2010). Dissociation of a nanoparticle drug complex could be expected to be governed by a variety of factors such as the affinity and kinetics of nanoparticle-drug interactions and the accessibility of the drug substrate to competitive binders. The main driver may simply be the large excess of serum protein binding sites in comparison to the nanoparticle polymer providing a steep gradient for drug repartitioning. In simple terms the binding of a drug to a nanoparticle carrier versus serum components can be viewed as a reversible equilibrium which is established according to the rates of association and dissociation of the drug with these two entities. In this study, these data underline the importance of quantifying nanoparticle drug formulations in terms of their half maximal dissociation in the presence of cell culture serum, and the rate at which this equilibrium is established.

Analysis of the performance of QD drug complexes in a cell viability assay demonstrated that the QD carrier could still impart a therapeutic effect in the presence of serum, at least at higher drug concentrations (Fig.4.5). The absence of toxicity in the presence of QDs alone suggested that the reduction in viability may have been due to enhanced delivery of curcumin, which would suggest that although complex dissociation may be prevalent, the use of the nanoparticle may still be worthwhile. Nevertheless, the high degree of toxicity of the nanoparticle vector in the serum free condition made data interpretation difficult and a synergy between the drug and vector in the presence of serum could not be ruled out. For some applications such as cancer treatment this may be desirable although a targeting mechanism may be needed to avoid off target effects in healthy tissues.

In this study we have demonstrated that small polymer coated nanoparticles may be readily loaded with a hydrophobic drug cargo although complex formation is contradicted in the presence of cell culture serum. Although other reported nanoparticle formulations may outperform these carriers in terms of their loading stability in serum, this study emphasises the importance of quantifying nanoparticle drug loading and release in the presence of biological fluids.

5 QDs as drug carriers for CPP-peptide and CPP-protein cargoes

5.1 Introduction

There is huge potential for delivering therapeutics that have macromolecular components such as peptides and proteins all the way to siRNAs, entire genes, nanoparticles and combinations thereof. These cargos may be designed to affect expression of genes, alter protein expression, interfere with protein-protein interactions, or in the case of nanoparticles impart a novel modality pertaining to imaging, sustained release of compounds or elicitation of a toxic response. However, a major hurdle to delivering therapeutic macromolecules to a specific cellular location are the lipid bilayers which comprise the plasma membrane at the cell surface or endolysosomal membranes which are exposed following endocytosis (Varkouhi et al., 2011).

Many cell types have been shown to internalize nanoparticles through active processes, although selectively targeting a specific cell type and gaining entry to the cytosol has proven immensely challenging (Akinc and Battaglia, 2013; Varkouhi et al., 2011). In solid tumours, the enhanced permeability and retention effect (EPR) offers a convenient means of concentrating macromolecules within the tumour interstitial space due to the leaky nature of tumour vasculature (Maeda, 2001). Other tissues may also display affinity for certain nanoparticle types with the liver, kidneys and lungs frequently cited as sites of 'non-specific' accumulation which may be linked to the metabolic or immune functions of these tissues and the characteristics of the nanoparticle in question (Dobrovolskaia and McNeil, 2007; He et al., 2010; Vonarbourg et al., 2006). Directing nanoparticles to other sites in general requires further targeting mechanisms such as presentation of antibodies, or adhesion peptides such as cyclic RGD or interleukin 13 (Gao et al., 2013; Guo et al., 2014; Wu et al., 2015).

5.1.1 CPPs as delivery vectors

Common to the vast majority of macromolecular vectors is that they are essentially membrane impermeable and require a further mechanism to overcome the lipid bilayer to gain access to the wealth of targets in the cell interior. A class of short sequences known as cell penetrating peptides (CPPs) have been extensively explored as potential delivery agents for biopharmaceuticals such as peptides, proteins, nucleic acids and entire nanoparticles (Bechara and Sagan, 2013; Martín et al., 2013). Cargo molecules may be attached to CPPs via different mechanisms such as extension of the N or C termini, chemical conjugation via a reactive side-chain, or non-covalent binding through electrostatic or Van der Waals interaction. For highly charged cationic CPPs such as Tat and R8 there is clear evidence that these peptides bind serum proteins which effects their stability and cell uptake

capacity (Youngblood et al., 2007). By the same principle CPPs can also be utilized to bind isolated protein components and deliver them into cells (Carter et al., 2013). This has significant potential for biopharmaceutical application and has expanded into in vivo studies involving the use of the CPP penetratin as a delivery vector for insulin (Khafagy et al., 2010).

CPPs were first discovered in the late eighties when it was demonstrated that the Trans-Activator of Transcription (Tat) protein from Human Immunodeficiency Virus (HIV) was able to promote viral gene expression, overturning the acknowledged understanding that the plasma membrane is impermeable to hydrophilic molecules (Frankel and Pabo, 1988; Green and Loewenstein, 1988). This discovery along with the isolation of the Antennapedia homeodomain transcription factor from Drosophila which also displayed cell entry properties, led to extensive structure/function studies and the isolation of the first minimal sequences responsible for driving protein entry which corresponded to the CPPs Tat and penetratin from HIV and Drosophila, respectively (Derossi et al., 1994; Green et al., 1989; Joliot et al., 1991; Vivès et al., 1997). So far a wealth of CPPs have been isolated or rationally designed, yet a general definition governing the characteristics of the class has been difficult to pin down owing to the huge variation in sequences now available (Gautam et al., 2012).

5.1.2 Mechanisms of CPP entry

In general CPPs are usually shorter than 30 residues and can facilitate cell entry in the absence of a cognate receptor, and via energy-dependent and/or independent mechanisms (Bechara and Sagan, 2013). Many CPPs have an amphipathic character although some such as R8 are entirely cationic. The mechanisms by which isolated CPPs gain entry to the cytosol has received much attention and is the subject of considerable controversy in the field. This stems in a large part from the difficulty in studying CPP uptake at the peptide level with a number of studies reporting perturbations when labelling CPPs with fluorophores which can alter the conformation, flexibility and hydrophobicity of the peptide (Bertrand et al., 2009; Puckett and Barton, 2009; Szeto et al., 2005).

Nevertheless, there has been a widespread recognition that the cationic charge (“Magic Arginine”) and/or hydrophobicity (“Tryptophan Power”) of CPPs play a crucial role in cell entry (Fig.5.1a, b) (Bechara and Sagan, 2013). Since the plasma membrane constitutes an array of negative charge, cationic residues offer a simple means of electrostatic binding to polysaccharides, lipids and protein components with the guanadinuim group found on arginine forming bidentate hydrogen bonds with carboxyl, phosphate and sulphate groups (Fig.5.1a) (Bechara and Sagan, 2013). Charge screening following binding is thus thought to form a polar ion complex which has some freedom to diffuse within the polar environment of the membrane (Nakase et al., 2008; Rothbard et al., 2004). By the same reasoning addition of hydrophobic residues such as tryptophan to a CPP has been shown to facilitate membrane insertion, although overly hydrophobic peptides can lead to less efficient

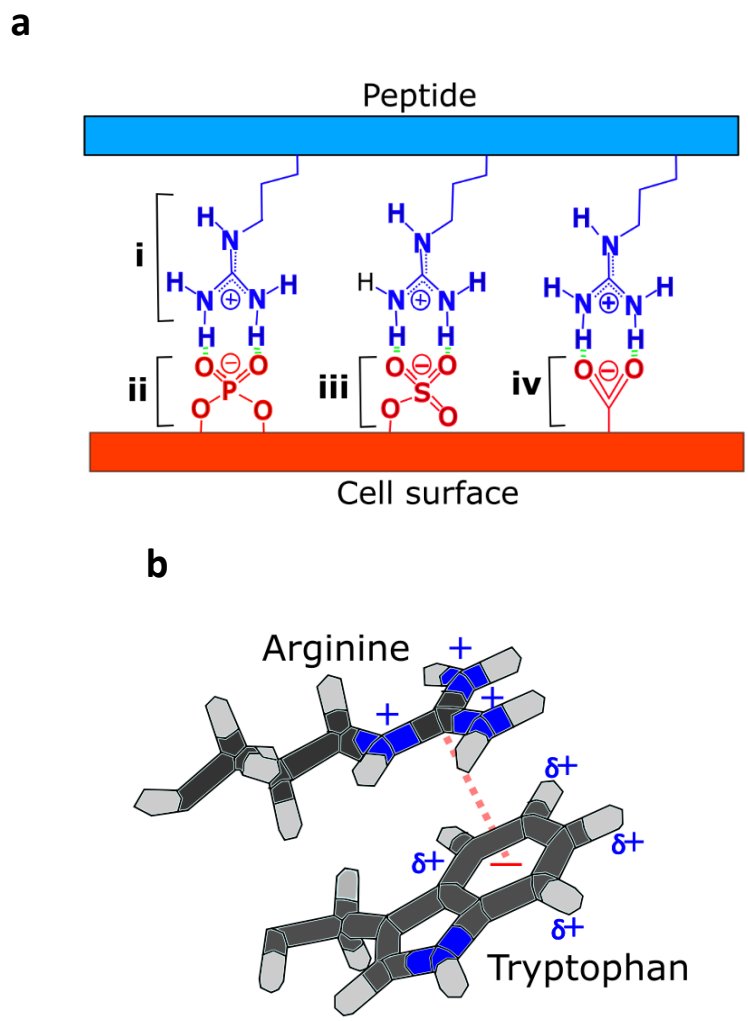

Figure 5.1 Interaction of cationic cell penetrating peptides with cellular surfaces.

CPPs are often rich in cationic residues such as arginine which has a basic guanadinium group (a, i) and can forms electrostatic interactions with anionic groups at the cell surface such as phosphate (a, ii), sulphate (a, iii) and carboxylate groups (a, iv). The guanadinuim group of arginine may also form π – cation bonds with tryptophan residues (b). This is possible as the face of the aromatic ring of tryptophan shows a slight negative charged due to the position of the electron cloud permitting an electrostatic interaction with arginine (b).

internalization as the peptide remains associated with the membrane (Magzoub et al., 2003; Walrant et al., 2012). Recent studies have extended the role of tryptophan residues in CPP uptake through the finding that tryptophan residues may bind with glycosoaminoglycan sulphate groups though pi-anion interactions (Bechara and Sagan, 2013; Demeshko et al., 2004; Ito et al., 2001). Indeed, it is well known that arginine and tryptophan can interact with one another through pi-cation bonds (Fig.5.1b), which may lead to complex formation and clustering of glycosoaminoglycans (Bechara et al., 2013; Bechara and Sagan, 2013).

The entry mechanism for CPPs has been difficult to elucidate in large part due to the wide range of parameters which affect CPP uptake relating to the physical-chemical properties of the cargo, the characteristics of the linker between the peptide and cargo, cell type differences and incubation conditions used (Jones and Sayers, 2012; Watkins et al., 2011). Furthermore CPPs may enter by multiple routes and down regulation of one entry pathway may lead to up-regulation of another. For small cargoes, typically fluorphores with molecular weight < 1 KDa, direct translocation though the plasma membrane has been reported with cargo reaching the cytoplasm and nucleus (Hirose et al., 2012; Jones and Sayers, 2012). However for much larger cargos such as nanoparticles there is a general expectation that translocation occurs across the endosomal bilayer following endocytosis (Jones and Sayers, 2012).

5.1.3 The use of CPPs in nanoparticle delivery

CPPs have also been shown to deliver a range of nanoparticles into cells ranging from polymer assemblies to small metallic particles such as QDs (Cho et al., 2008; Doane and Burda, 2013). Conjugation of CPPs to QDs has been demonstrated by both non-covalent association and covalent chemical attachment, although delivery through to the cytosol has only been reported with limited success. Perhaps the most straightforward approach of cargo attachment is to exploit non-covalent interactions which may occur between specific domains on the cargo and nanoparticle surface. As discussed in previous chapters, some of the major driving forces for adsorption of proteins and peptides to nanoparticle surfaces include electrostatic interactions and hydrophobicity (Mahon et al., 2012; Monopoli et al., 2012; Tkachenko et al., 2003). Moreover the surface of nanoparticles which are encased within an anionic polymer may mimic certain characteristics of cell membranes and act as a substrate for CPP binding.

Several studies have reported complexation of anionic QDs and CPPs though non-covalent electrostatic interaction (B. R. Liu et al., 2011, 2013; Liu et al., 2010; Xu et al., 2010; Yukawa et al., 2010). Nona-arginine QD complexes prepared via this mechanism were internalized by lung epithelia

A549 cells localizing to actin and lysosomes but not mitochondria, ER or nuclear compartments (B. R. Liu et al., 2013). The cysteine and histidine rich R9 peptide (C-5H-R9-5H-C) was designed with the aim of promoting membrane association through modifying the net hydrophobicity of the peptide (B. R. Liu et al., 2013). The peptide was found to enhance QD uptake at high particle concentrations (100 nM QDs complexed with 6 μM peptide) over R9 alone or a FFLIP modified R9 variant, although the major route of entry appeared to be a direct translocation of the complex through the plasma membrane due to the accumulation of material within cells at 4 °C (Liu et al., 2013, 2011).

Others have focused on delivering non-covalent CPP-nanoparticle complexes into adipocyte derived stem cells (ADSCs) or mesenchymal stem cells (MSCs), with the subsequent introduction of these cells into mouse models permitting the long term visualization and tracking of stem cell fate (Ranjbarvaziri et al., 2011; Yukawa et al., 2012, 2010). Carboxyl QD and R8 conjugates prepared by non-covalent complexation efficiently labelled ADSCs after 1 h incubation although cytotoxicity was observed above QD concentrations of 16 nM (Yukawa et al., 2010). At early time points QDs were distributed in a dispersed pattern throughout the cytoplasm, although complexes were not observed in the nucleus and clustering was observed after 8 hours. Prolonged incubation of these stem cells with 0.4 nM QD conjugates for 2 weeks did not appear to disrupt subsequent differentiation into osteocyte or adipose cell lineages. However, the stability and colloidality of conjugates prepared in this manner, and the effects of corona formation on these parameters have not been reported in the literature.

A number of studies have exploited the specific binding of biotinylated CPPs to streptavidin functionalised QDs or vice versa (Chen et al., 2008; Medintz et al., 2008; Ruan et al., 2007; Xu et al., 2010). Although CPP QD complexes prepared in this manner appeared to be readily taken up by cells, these particles appeared to be sequestered mainly within the endolysosomal compartment and did not show evidence of reaching the cytoplasm possibly due to their large size (Medintz et al., 2008; Ruan et al., 2007).

A variation of non-covalent attachment has also been explored for CPPs bearing a Histidine (His) tag which bind QDs though interactions between the His motif and zinc atoms of core-shell type QDs (Delehanty et al., 2010, 2006). However, conjugation of QDs with a His_6 - R9 peptide resulted in considerable entrapment in the endolysosomal compartment of HEK293T/17 or COS-1 cells, and significant dose dependent cytotoxicity was observed after 24h exposure (Delehanty et al., 2010).

For some applications attaching CPPs covalently to a macromolecule or nanoparticle of interest is considered desirable due to the high stability of covalent bonds and control in the display of the CPP ligand on the particle surface (Cleal et al., 2013; Hermanson, 2008). However, additional mechanism

are then required to release of the cargo, and evaluating the performance of such mechanisms in live cells can be challenging.

Several groups have reported covalent chemical crosslinking of CPPs and QDs (Choi et al., 2011; Kuo et al., 2011; Wei et al., 2009). Covalently conjugated Tat QDs were reported to enter the nuclear compartment in NIH/3T3 cells at concentrations of only 0.08 nM where 25 % of conjugates tracked at the single particle level suggested a "trapped", or non-diffusive environment (Kuo et al., 2011). In another study multifunctional QDs were prepared by attaching both Tat peptide and an anti-GFP antibody before uptake in HEK293 cells. Conjugates were reported to colocalize to the GFP-tagged cytoplasmic terminus of the ET_AR receptor located at the plasma membrane, and colocalization was maintained following addition of an ET_AR agonist that induced internalisation of the receptor to a perinuclear region (Choi et al., 2011).

The influence of polymer shell on CPP mediated QD uptake is rarely considered but contributes to the overall charge of the particle, its buffering properties, size and texture. Tat-functionalized QDs prepared with three different surface coatings including cysteine-terminated Tat alone, silane, and polyacrylate derivatives produced particles of varying surface charges and sizes of 6, 10, and 25nm, respectively (Wei et al., 2009). Silica and polyacrylate coatings additionally mediated a proton sponge effect due to the multiple primary and secondary amines within these polymers. The smallest QDs were efficiently internalized and localised to a perinuclear region but exhibited reduced colloidal stability and considerable toxicity. Increasing the size and charge characteristics though the different coatings increased QD cell labelling, although localization was indicative of entrapment in the endolysosomal system. Toxicity aspects of QD in different cell lines was recently highlighted (Soenen et al., 2012) and it remains to be seen whether addition of CPPs to these entities further exacerbates these effects.

Nevertheless, these reports suggest that there is great scope for exploring the uses of CPPs as delivery vectors for nanoparticles and associated cargoes. In particular, non-covalent CPP attachment to nanoparticle surfaces may share many characteristics with protein corona formation and may potentially be utilized for cargo delivery and release. In this work CPP-peptide and CPP-protein constructs are investigated for co-delivery with QDs into cultured cells through non-covalent complexation as a binding regimen.

Peptide	Sequence	Net charge (pH 7)	Hydroph-obicity (pH 6.8)	pI
$F(SG)_4R8$	Ac-FSGSGSGSGRRRRRRRRGC-NH_2	7.91	0.74	13.53
$G(SG)_4R8$	Ac-GSGSGSGSGRRRRRRRRGC-NH_2	7.91	-4.37	13.53
$F(SG)_4Pen$	Ac-FSGSGSGSGRQIKIWFQNRRMKWKKGC-NH_2	6.91	18.3	12.83
$G(SG)_4Pen$	Ac-GSGSGSGSGRQIKIWFQNRRMKWKKGC-NH_2	6.91	14.7	12.83
$F(SG)_4TP10$	Ac-FSGSGSGSGAGYLLGKINLKALAALAKKILGC-NH_2	3.91	33.09	10.66
$G(SG)_4TP10$	Ac-GSGSGSGSGAGYLLGKINLKALAALAKKILGC-NH_2	3.91	30.06	10.66
cRGD	cyclo (RGDfK)	-	-	-
Nrf2	LQLDEETGEFLPIQYGRKKRRQRRRLQ-NH_2	5.00	11.41	11.77
AcR8	Ac-RRRRRRRRGC-NH_2	8.00	-6.3	13.25
D-NuBCP-9-r8	Ac-fsrslhsllG-Ahx-rrrrrrrr-NH_2	-	-	-

Table 5.1 A list of the peptides used within this study.

Ahx denotes aminohexanoic acids, lowercase denotes D amino acids and Ac corresponds to an acetyl terminal group

5.2 Results

5.2.1 Interaction of carboxyl QDs and CPPs

Interaction of CPPs with anionic QDs has been previously documented and is thought to reflect electrostatic interactions between anionic groups on the nanoparticle surface, typically carboxyl groups as found in many commercial QD preparations, and basic arginine's or lysine's on the CPP (B. R. Liu et al., 2011, 2013; Liu et al., 2010; Yukawa et al., 2012, 2010). The specific display of a non-covalently bound CPP on the surface of a QD is expected to be critical in determining the interaction of the peptide with the cell membrane, and there is considerable scope for engineering a peptide which favourably interacts with both the nanoparticle and the cell surface.

To assess non-covalent attachment of CPPs to QDs, a panel of peptides were purchased which had varying CPP, linker and model cargo sequences (Table 5.1). Recent reports have demonstrated that a single amino acid substitution at the N-terminus of an octaarginine-peptide from an alanine to a phenylalanine had a dramatic effect on the ability of the peptide to interact with cells despite a spacing of 9 amino acids between the substitution and CPP motif (Watkins et al., 2011). It was therefore of interest to investigate the effects of a single amino acid substitution distal to the CPP sequence using the well characterized CPPs R8, TP10 and Penetratin, using the membrane impermeable sequence $(SG)_4$ as a spacer. The $(SG)_4$ motif has been previously used as a bridging sequence in protein research (Watkins et al., 2009), and was here extended to give two variants with N-terminal glycine or phenylalanine residues.

5.2.1.1 Aggregation of carboxyl QDs and CPPs

Initially QDs with a carboxyl surface coating were analysed for their binding with a panel of CPPs as several reports have exploited this interaction to form non-covalent complexes (Liu et al., 2010; Yukawa et al., 2012, 2010). QDs at 25 nM were complexed with peptide at room temperature for 30 mins over a concentration range of 0.79 to 250 µM at half-log intervals (Fig.5.2a). Analysis of conjugates by gel electrophoresis indicated that the CPP domain induced the widespread aggregation of QDs at higher peptide concentrations which resulted in the entrapment of fluorescent aggregates within the well (Fig.5.2a). The critical concentration for inducing aggregation varied slightly between the peptides with 2.5 µM for $G(SG)_4R8$ to 7.9 µM for $G(SG)_4R8$ Pen and $G(SG)_4R8$ TP10. As a control, the neutral peptide cyclicRGD (cRGD) was also included which demonstrated no interaction with carboxyl QDs and a uniform migration pattern with varying peptide concentration (Fig.5.2a).

The aggregation behaviour was further confirmed by viewing the interaction of carboxyl QDs and AcR8 in real time by widefield microscopy (Fig. 5.2.1b). Here, 1 nM QDs were utilized in ordered to resolve individual QDs and the peptide was added in a large excess at a concentration of 10 µM. Initially QDs

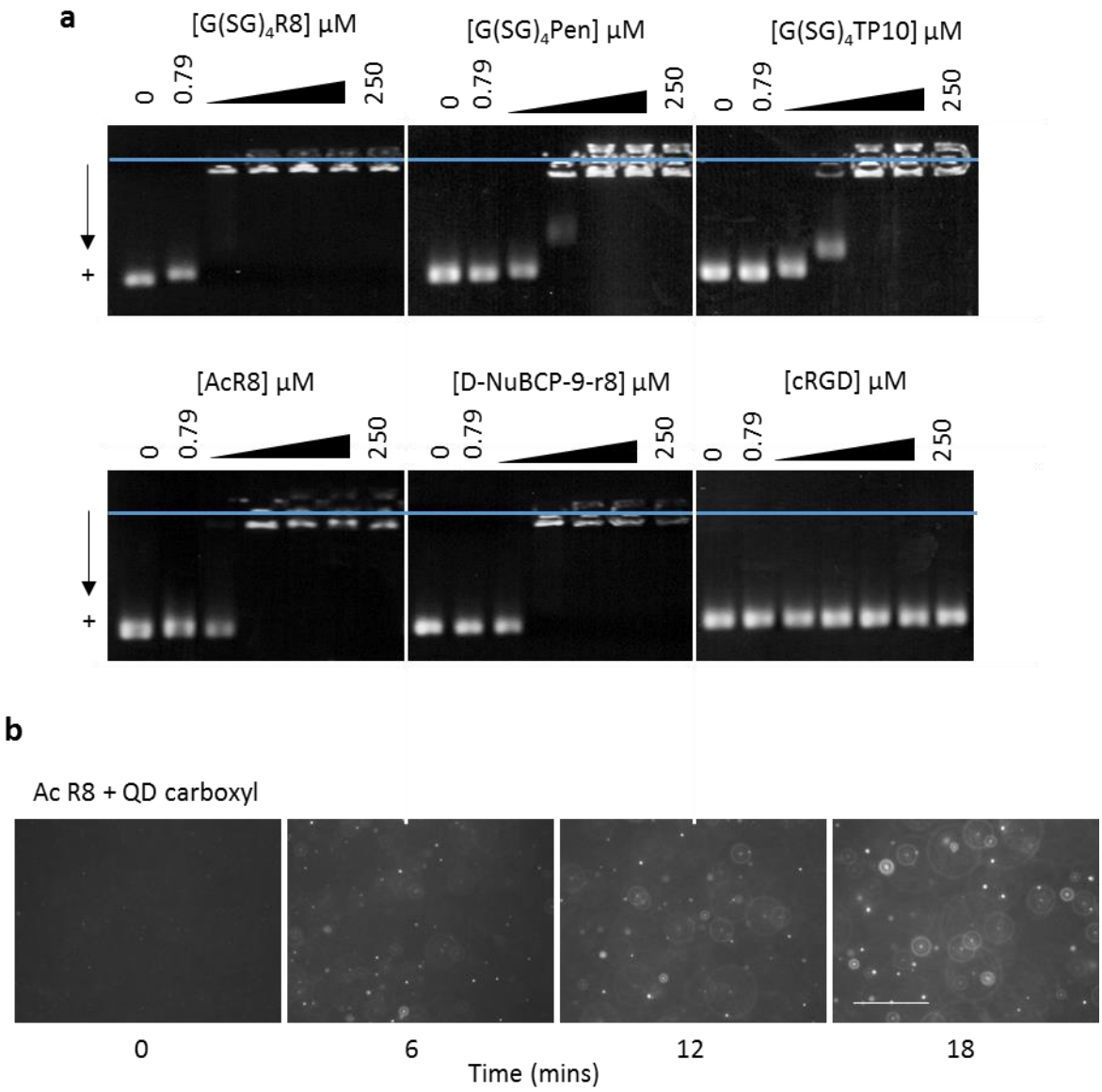

Figure 5.2 Non-covalent binding of CPPs to carboxyl QDs.

A panel of CPPs were mixed with 25 nM QDs and analysed by gel electrophoresis with the blue line indicating the position of loading wells (a). Accumulation of material within wells was taken as evidence of aggregate formation. QDs and Ac-R8 were then visualised by fluorescence microscopy to analyse the aggregation process over time (b). Scale bar is 10 µm.

appeared well dispersed and colloidal at time 0, although by 6 mins aggregates were clearly visible as brighter point-like structures which then grew further over time to form micron-sized aggregates by 18 mins (Fig. 5.2.1b), demonstrating that carboxyl QD and CPP aggregation was rapid under these conditions. The aggregation was presumably driven by inter-particle interactions which occurred as a result of the high cationic charge of the CPP forming electrostatic interactions with electronegative carboxyl groups on nearby QDs. The widespread aggregation of these QDs using a range of cationic CPPs further suggested that electrostatic interactions may be the key driver. Furthermore peptides with a lower net charge at neutral pH including $G(SG)_4$Pen and $G(SG)_4$TP10 showed the highest critical concentration for aggregation suggesting that net charge may be the key driver for aggregation rather than hydrophobicity.

5.2.1.2 Investigation of co-solvents to reverse aggregation

Aggregation of particles is an important consideration which can alter a range of critical parameters such as solubility, uptake and binding mechanism, and fate of conjugates in vitro and in vivo. To investigate if this aggregation behaviour could be inhibited or stabilized by altering buffer conditions, Carboyxl QDs at 25 nM were tested using a variety of co-solvents which were added into the initial PBS buffer at pH 7.4 (Fig. 5.3a). In the absence of CPPs the response of QDs to the co-solvent was variable with some co-solvents being well tolerated such as 2M Urea or 30 % Glycerol although all others produced an altered gel migration pattern with streaking frequently observed. For 30 % methanol, QD intensity was also greatly diminished.

Nevertheless, this panel was further tested alongside AcR8 at a concentration of 3 µM which represented the approximate critical concentration for aggregation so additive or inhibitory effects could be observed following addition of co-solvent (Fig.5.3b). QDs and CPPs were prepared separately in the altered buffer before adding together for 30 mins and analysis by gel electrophoresis. In the control lane QDs migrated as a tight band whereas the positive control consisting of QDs and AcR8 in PBS alone demonstrated a streaking pattern consistent with the formation of a heterogeneous population of aggregates, although the majority of material remained within the well. Surprisingly co-solvents including NaCl, guanadine HCl, citrate and acetate appeared to have a negative effect on aggregation with a greater proportion of QDs remaining trapped within the well, whereas urea had no discernible effect and methanol was incompatible with QD fluorescence. Only sodium dodecyl sulfate (SDS), ethylene glycol and glycerol has a positive influence on aggregation, although only SDS inhibited aggregation completely with no material observable within the well.

5.2.1.3 Carboxyl QD and CPP aggregation in the presence of serum

Surfactants such as SDS are generally considered incompatible or highly undesirable for live cell applications whereas ethylene glycol and glycerol could be expected to influence the viscosity of the

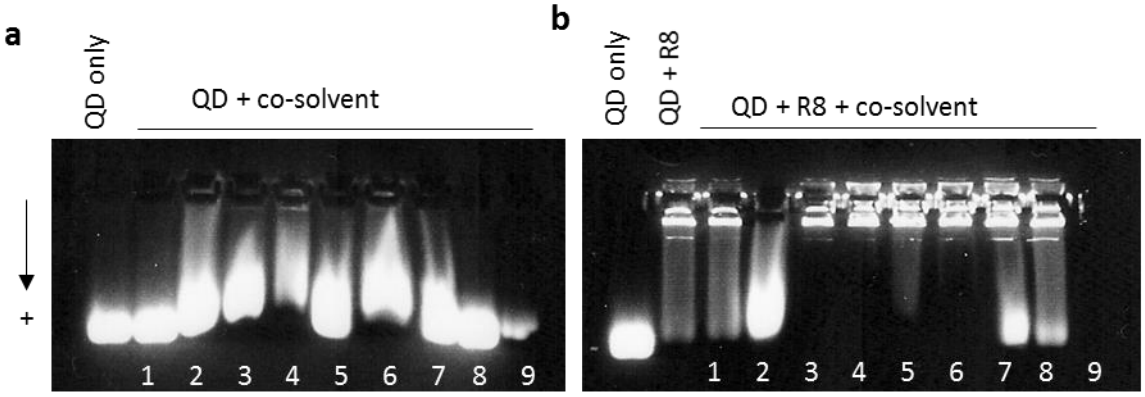

Figure 5.3 Searching for a co-solvent to promote dissolution of carboxyl QD aggregates.

The CPP Ac-R8 leads to carboxyl QD aggregate formation. At a threshold CPP concentration, QDs display a streaking pattern in the gel, demonstrated in (b, QD + R8). A small panel of co-solvents were tested for their ability to modify aggregate formation including - [1. Urea], [2. SDS], [3. NaCl], [4. Guanadine HCL], [5. Citrate], [6. Acetate], [7. Ethylene glycol], [8. Glycerol], [9. Methanol]. The response of QDs alone to co-solvent is displayed in (a) as a control, and (b) shows the effect of co-solvent exposure in the presence of the CPP. Prevention of aggregation leads to the appearance of a defined band during migration, whereas enhanced aggregate formation leads to accumulation of QDs within the wells.

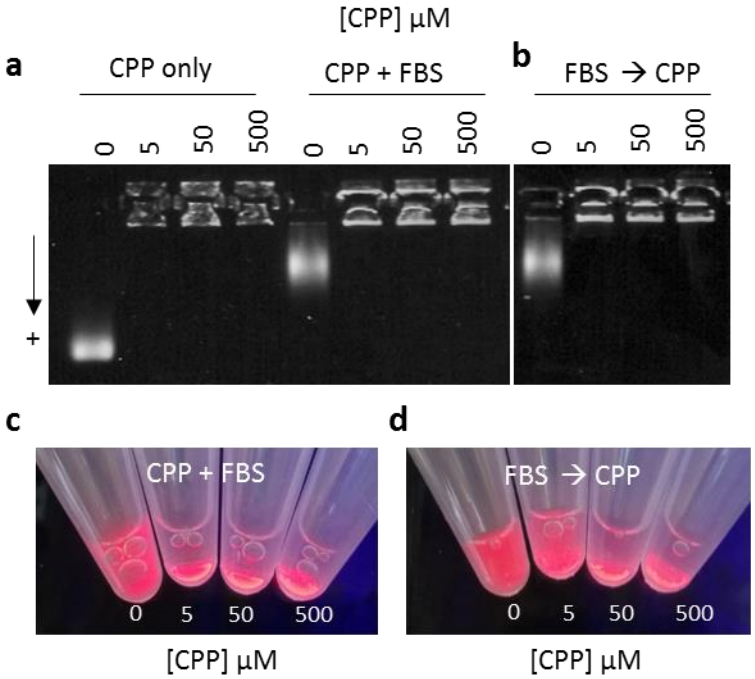

Figure 5.4 CPP induced carboxyl QD aggregation in the presence of serum.

Carboxyl QDs at 50nM were exposed to Ac-R8 only, or Ac-R8 and 10% FBS concomitantly, using between 0 and 500 µM Ac-R8 (a). Alternatively QDs were pre-treated with FBS before addition of Ac-R8 (b). For both FBS treatment conditions imaging of QD tubes revealed aggregate formation by the accumulation of insoluble material at the bottom of tubes (c, d).

media which may also have undesirable consequences. Therefore a further experiment was carried out to investigate if the presence of serum components could modify the aggregation behaviour of carboxyl QDs and CPPs. QDs at 50 nM and AcR8 from 5 to 500 µM were added concomitantly into PBS alone or PBS containing 10 % fetal bovine serum (FBS) and incubated for 30 mins (Fig.5.4a, b). Analysis of complexes by gel electrophoresis indicated that aggregation was not prevented under these conditions with material failing to migrate from the well (Fig.5.4a). In control lanes QD corona formation was evident by the reduced migration of the QD band indicating corona formation did not modify aggregation. Imaging of tubes prior to gel electrophoresis confirmed that QDs were aggregated with insoluble aggregates present at the bottom of tubes (Fig.5.4b).

To investigate if an established protein corona could prevent aggregation, QDs were first pre-treated with 10 % FBS for 30 mins before a further addition of AcR8. Surprisingly, QD aggregation was still observed under all CPP conditions by gel electrophoresis (Fig.5.4a) or by imaging of tubes (Fig.5.4c). The concentration of QDs and FBS used here may have only resulted in a partial coverage of the particle surface by corona components, inviting inter-particle interactions by surface bound QDs. Alternatively the corona may maintain an overall anionic character allowing the CPP to bind to the surface of corona components to establish inter-particle interactions. Finally, the CPP may also have promoted a reorganization of the corona to an extent to permit aggregation.

Together these data suggested that carboxyl QDs and cationic CPPs are unsuitable for non-covalent applications where aggregation is considered undesirable. As detailed in Chapter 3 (Fig.3.5a), amine QDs also displayed an anionic character despite an amine surface functionality suggesting these QDs may also bind cationic CPPs. To investigate this possibility we further explored utilizing non-covalent binding of CPPs as a paradigm for delivering anionic QDs using the panel of phenylalanine/glycine modified peptides (Table 5.1).

5.2.2 Interaction of amine QDs and CPPs

To assess binding, CPPs ranging in concetration from 0.79 to 250 µM were complexed with 25 nM amine QDs (aQDs) and analysed by agarose gel electrophoresis. Interestingly, the entire panel of CPPs formed complexes with the aQDs demonstrated by a reversal of aQD migration towards the negative electrode (Fig.5.5a). The migration pattern of CPP and aQD complexes is summarised in Fig.5.5b which is presented as the maximum migration of CPP:aQD complexes towards the positive electrode relative to aQDs alone. The anionic nature of amine QDs evidenced by their migration towards the positive electrode was presumably the principle driver for CPP complex formation occurring via

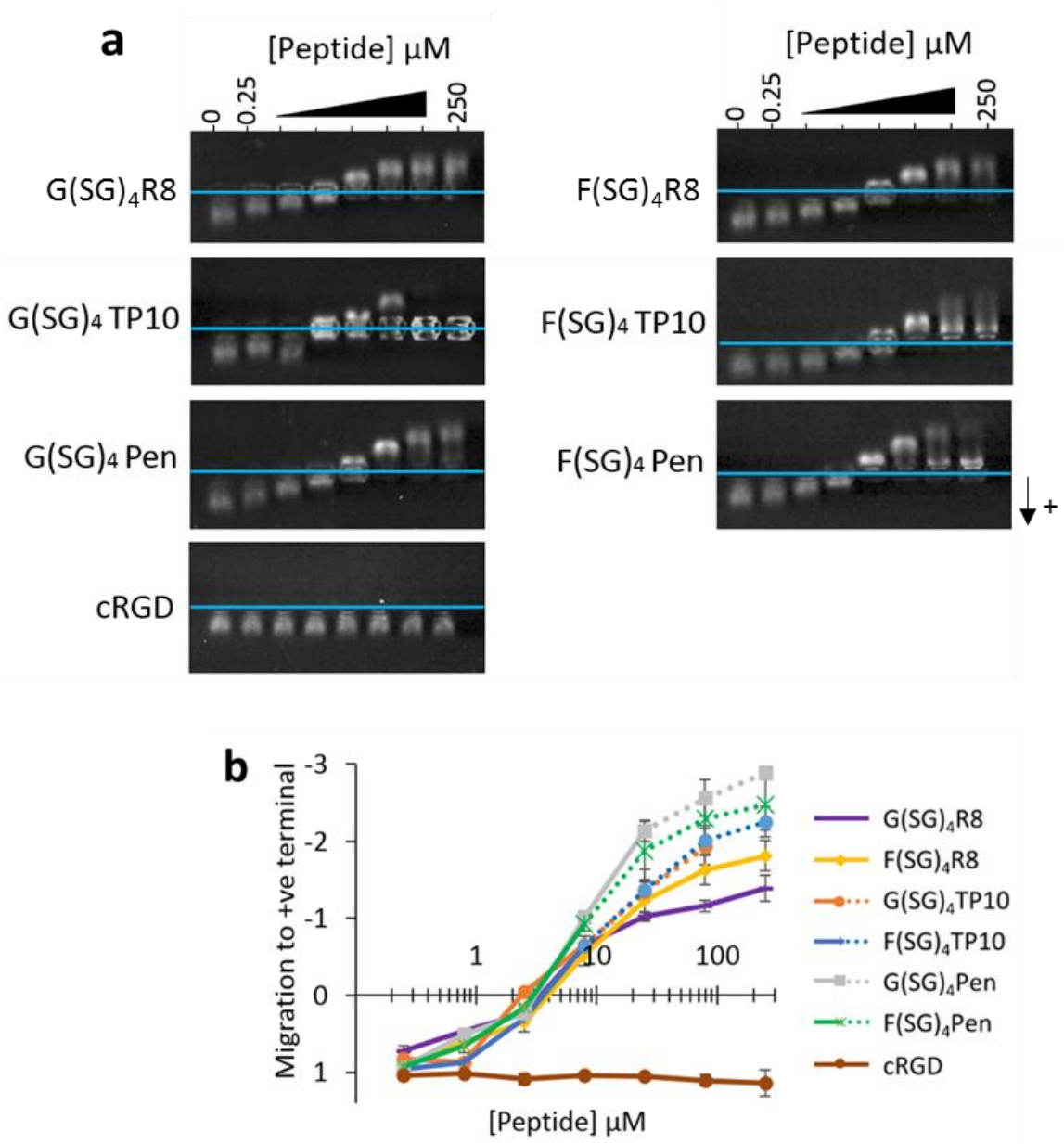

Figure 5.5 CPP-Qdot complex formation and Qdot uptake in cells.

Gly and Phe R8 CPPs and peptides described in Table 5.1 (a), were assessed for aQD binding by electrophoresis. Blue lines indicate the position of loading wells (a). Maximum migratory distance of aQD bands from the well centre towards the positive electrode was plotted for each peptide and normalised to the aQD only band (b). Dotted lines in b indicate well positions in which signs of aQD aggregation were observed due to the retention of material within the well.

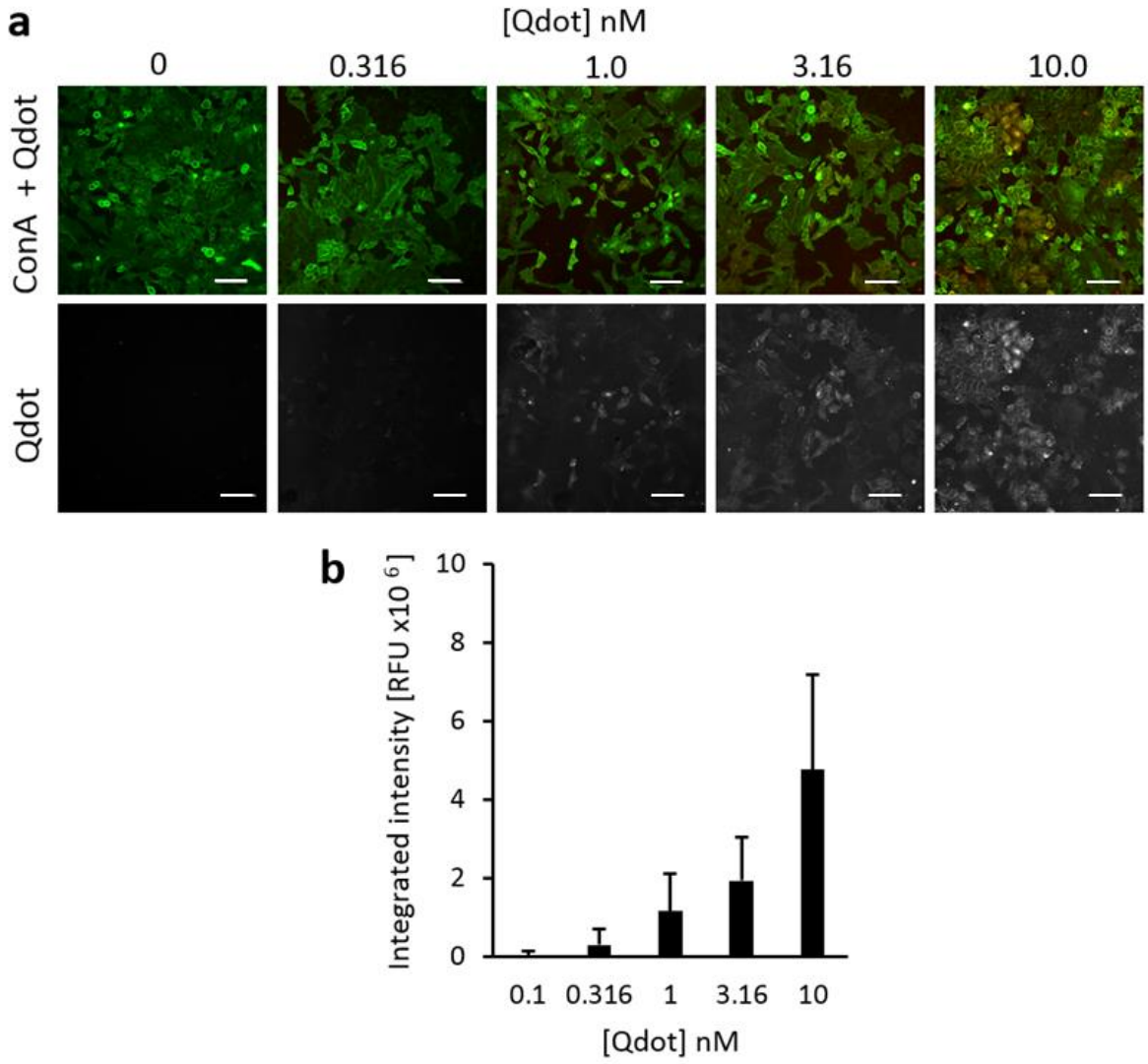

Figure 5.6 Uptake of bare amine QDs in HeLa cells.

Amine QDs (red channel) up to a concentration of 10 nM were assayed in live HeLa cells for 1 hr (a). The cell surface stain ConA-FITC (green channel) was used as a cell mask to quantify QD binding by measuring the mean integrated intensity per cell (RFU) in the QD channel (b). Scale bar = 100 µm

electrostatic binding. Moreover, the small peptide cyclicRGD with a low net charge showed no evidence of binding, and binding occurred irrespective of CPP peptide hydrophobicity (Table 5.1) supporting electrostatic binding as the common driver.

At higher CPP concentrations aQD complexes progressively acquired a positive net charge, although for some peptides, particle aggregation was apparent due to the streaking of bands or the entrapment of material within the loading-well (Fig.5.5a). Aggregation was most clearly observed in $G(SG)_4TP10$ treated aQDs which resulted in the formation of large aggregates which failed to migrate into the gel. $F(SG)_4TP10$ and Pen based peptides demonstrated streaking during migration implying the formation of heterogeneous aggregates at higher peptide concentrations. As discussed above, particle aggregation is a critical parameter when preparing drug delivery complexes due to the potential wide-ranging effects resulting from this process (Dakwar et al., 2014; Van Lehn and Alexander-Katz, 2013). Clear aggregation of aQDs when using $G(SG)_4TP10$ could result from a particular orientation of the peptide at the aQD surface which acts to destabilise the repulsive force between adjacent particles and promote agglomeration through either ionic of van der Waals modes (Van Lehn and Alexander-Katz, 2013).

5.2.2.1 Cell binding of amine QD CPP complexes

For R8 based peptides, aggregation was not evident by gel electrophoresis (Fig.5.5a) allowing for further cell-based analysis with these entities. aQDs by themselves demonstrated appreciable levels of binding to HeLa cells following a 1 h exposure in serum free media (Fig.5.6a, b). Counterstaining with the lectin ConA to label the plasma membrane at the end of the experiment suggested the majority of material was localised to this structure. Cellular labelling demonstrated a dose-dependent increase in integrated fluorescence intensity with increasing aQD concentration and there was considerable heterogeneity within the sample in terms of aQD binding (Fig.5.6b).

In the presence of a fixed concentration of 1 µM $G(SG)_4R8$ or $F(SG)_4R8$, cellular binding of aQDs was increased at low and high nanoparticle concentrations of 0.316 or 3.16 nM (Fig.5.7a). In control cells the majority of aQDs appear to localise evenly to the plasma membrane and only a small fraction appear to be internalised in punctate vesicles (Fig.5.7a). Complexation of aQDs with Gly or Phe R8 greatly increased aQDs cell binding, with enhanced labelling of both plasma membrane and internal vesicular compartments.

Binding was quantified by taking the mean integrated fluorescence intensity and demonstrated that both $G(SG)_4R8$ and $F(SG)_4R8$ peptides enhance cellular binding considerably (Fig.5.7c) with binding increased by roughly 4.8 fold and 9.5 fold respectively, over aQDs alone for Gly and Phe variants,

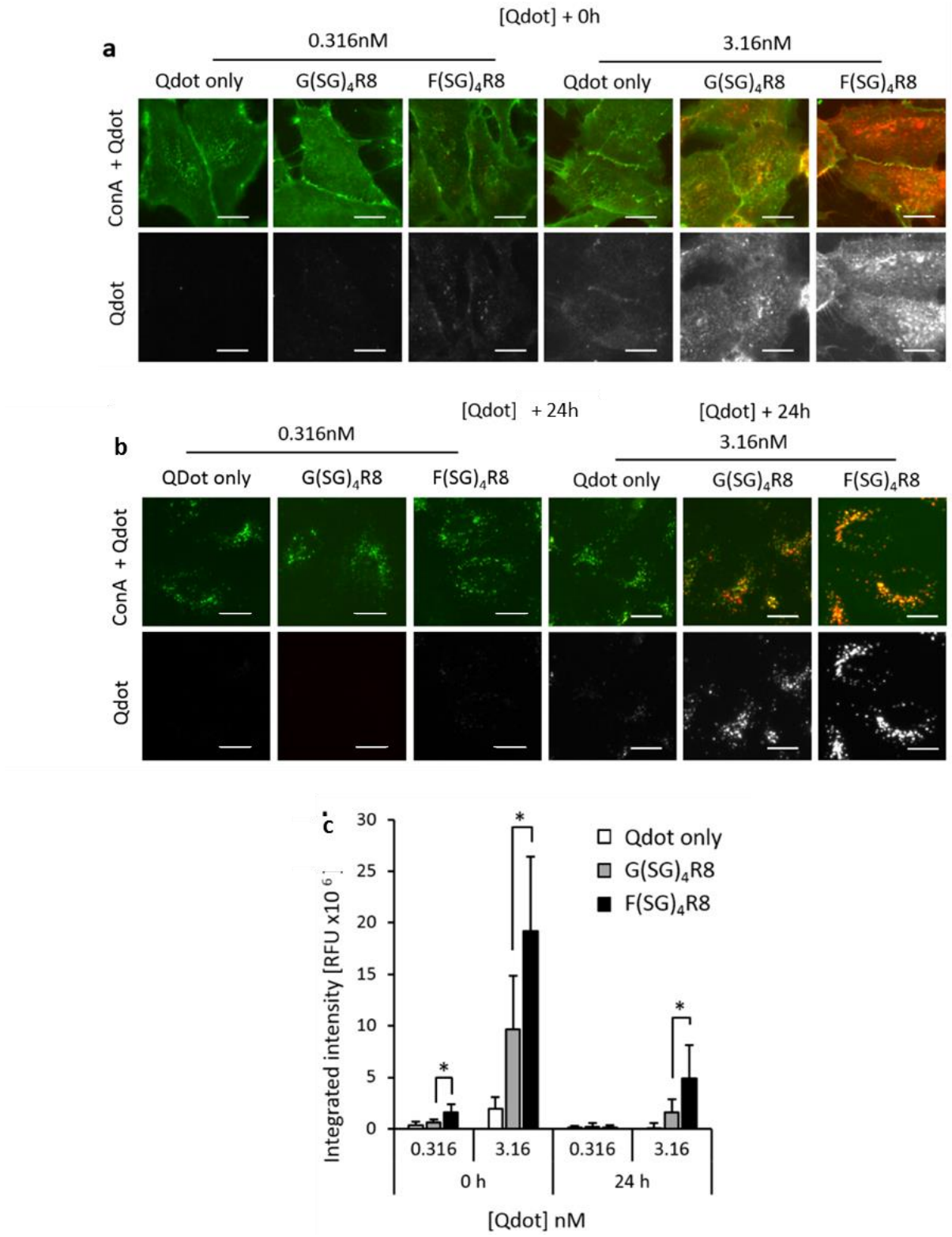

Figure 5.7 Phe R8 enhances Qdot cell uptake over Gly R8 and aQDs alone.

aQDs (red channel) at 0.316 or 3.16 nM (a) were assayed in live HeLa cells for 1 h following complexation with a fixed concentration of 1 µM $G(SG)_4R8$ or $F(SG)_4R8$. ConA-FITC (green channel) was used to label the cell surface allowing aQD binding to be quantified in (b) by measuring the mean integrated intensity per cell (RFU) in the aQD channel. After initial loading of aQD and ConA, cells were reanalysed after a 24 h chase where aQDs redistributed to a perinuclear compartment (c). Statistical significance of $p < 0.05$ is donated by *. Scale bar= 20 µm.

respectively. Here the Phe modified R8 demonstrated a significant increase in the cell binding activity when compared to the Gly-modified variant. The reasons for this could reflect a direct interaction of the phenylalanine residue with cellular surfaces, or a felicitous display of the peptide at the aQD surface which enhanced cell association via the R8 motif. For penetratin and TP10 aQDs, aggregation was clearly evident making data interpretation problematic (Fig.5.8a, b). Interestingly the aggregates were only visible on the cell surfaces rather than on the tissue culture plastic suggesting a potential role for the CPP in enhancing binding.

5.2.2.2 Cell binding of complexes over an extended time frame

In light of such a large degree of cargo binding to the plasma membrane we sought to investigate how the constant cycling of plasma membrane components over an extended time frame might affect the internalisation of this membrane associated aQD fraction. To address this question aQDs complexes were pulsed onto HeLa cells for 1 h followed by a brief counterstain with ConA and a further 24 h recovery (Fig.5.7b). Quantification of the integrated intensity per cell revealed that the majority of aQDs at the lower concentration of 0.316 nM were lost during the incubation, with fluorescent profiles only slightly above autofluorescence (Fig.5.7b, c). At 3.16 nM aQDs, control cells also showed little fluorescence, whereas G- and F-$(SG)_4$R8 aQDs complexes exhibited binding profiles which paralleled those recorded after 0 h recovery, although with markedly reduced intensities. By measuring the mean integrated intensity per cell a direct comparison between the two time points was possible, revealing that the aQD fluorescence remaining after 24 h for 3.16 nM G- and F-$(SG)_4$R8 aQD complexes stood at 17% and 26%, respectively (Fig.5.7c). Again, a significantly larger aQD profile was retained in F-$(SG)_4$R8 treated cells when compared to cells incubated with G-$(SG)_4$R8.

In control cells the majority of ConA was internalised into a perinuclear compartment after 24 h, with aQDs alone showing a reasonable degree of colocalisation with this probe (Pearson's colocalisation value 0.54 ± 0.17, Fig.5.7b). aQDs complexed with Gly or Phe R8 however both showed a striking colocalisation with ConA positive compartments that was more pronounced in the case of Phe-R8 reflecting the increased aQD cell labelling using this peptide (Pearson's value 0.71 ± 0.16 and 0.79 ± 0.12 for G- and F-$(SG)_4$R8 respectively, Fig.5.7c). F$(SG)_4$R8 complexed aQD appeared to colocalise almost exclusively with ConA. This lectin has recently received attention due its reported antitumor effects in a variety of cell lines including ML-1_{4a} hepatoma (Chang et al., 2007; Lei and Chang, 2009) and MCF-7 breast carcinoma (Shi et al., 2014) lines. In ML-1_{4a} cells, ConA was trafficked to mitochondria and lysosomes following a 3 h incubation triggering LC3-II conversion and cell death (Chang et al., 2007). The staining we observed here is consistent with localisation of aQDs

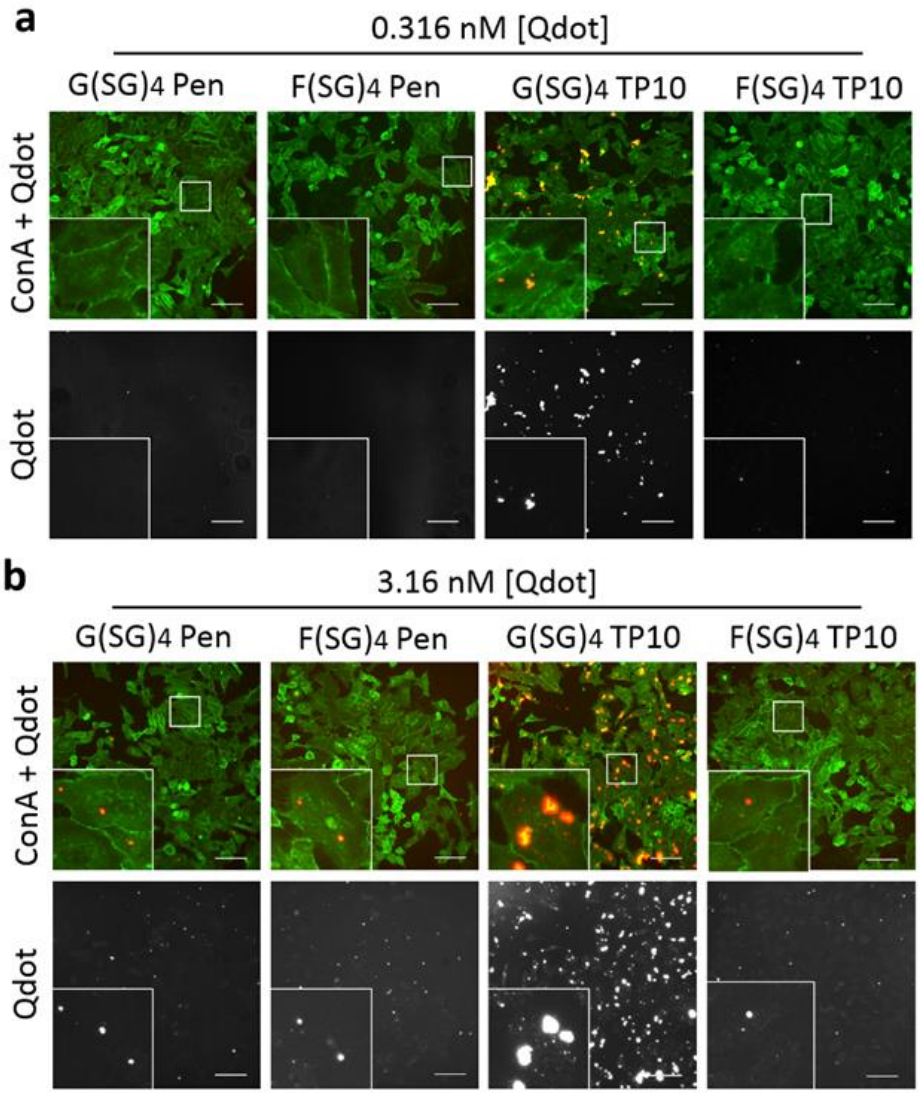

Figure 5.8 Cell binding of Gly and Phe modified TP10 and Penetratin aQD complexes.

aQDs (red channel) were complexed with 1 µM Gly or Phe modified TP10 or Penetratin peptides and analysed for binding in live HeLa cells for 1 hr. aQD concentration was fixed at 0.316 nM (a) or 3.16 nM (b). Cells were counterstained with the lectin ConA-FITC (green channel) to label the cell surface. Scale bar = 100 µm.

and ConA to endolysosomal compartments, indicating Gly and Phe R8 peptides selectively target aQD to these organelles. Moreover cell internalisation during this 24 h period may result primarily as a consequence of plasma membrane turnover opening the possibility of a controlled cell uptake mechanism of nanoparticle-CPP cargo entry.

The distribution of material in Fig.5.7b also bears a strong resemblance to staining by the commercially available QD cell label known as Qtracker (Life Technologies) (Lagerholm et al., 2004). Qtracker is a labelling kit designed for long-term cell tracking over many generations, and utilises a custom peptide to deliver material to the endolysosomal compartment. We suggest that using non-covalent binding of R8 peptides to amine aQDs may be a viable alternative for cell tracking experiments, and opens the possibility of extending this method to other nanoparticles of interest.

5.2.3 Non-covalent binding of a model therapeutic peptide to anionic QDs

The non-covalent binding of CPPs and QDs was further investigated as a potential mechanism to deliver a therapeutic macromolecular cargo. Recently, an Nrf2 peptide (Fig.5.9a) (Lo et al., 2006) derived from the nuclear factor (erythroid-derived)-like 2 transcription factor was investigated as a regulator of inflammatory pathways and was delivered in vitro by the CPP domain TAT (Steel et al., 2012). Nrf2 plays a central role in governing intracellular anti-inflammatory responses and has roles in activation of cellular antioxidants including heme-oxygenase 1 (HO-1) (Alam et al., 1999; Kobayashi and Yamamoto, 2005), drug efflux pumps (Hayashi et al., 2003), detoxification enzymes (Itoh et al., 1997), and cytoprotective genes (Chen and Kunsch, 2004). Under normal conditions Nrf2 is bound by the cytosolic Kelch-like ECH-associated protein 1 (Keap1) which induces ubiquitination and proteasome degradation to maintain a low basal level (Itoh et al., 1999). In response to stimuli such as oxidative stress, Nrf2 translocates to the nucleus to target antioxidant response elements and activation of target genes (Itoh et al., 1995). The 14mer Nrf2 peptide which was appended to Tat as described by Steel et al., was designed with the aim of disrupting the Keap1 interaction to promote activation of endogenous Nrf2 (Steel et al., 2012). In this manner Tat-Nrf2 was reported to induce activation of HO-1 in a concentration dependent manner and suggested this peptide may provide an ideal model system to investigate delivery of a model therapeutic peptide by anionic QDs (Steel et al., 2012).

Investigation of Tat-Nrf2 binding with 25 nM aQDs however revealed that these entities did not form a stable interaction (Fig.5.9b). This was somewhat surprising considering the highly cationic nature of Tat and the anionic nature of aQDs which readily formed complexes with other cationic CPPs (Fig.5.5a, b). This may have been a consequence of the peptide possessing a secondary structure (Fig.5.9a) which inhibited access of the CPP domain to anionic surfaces within the aQD polymer.

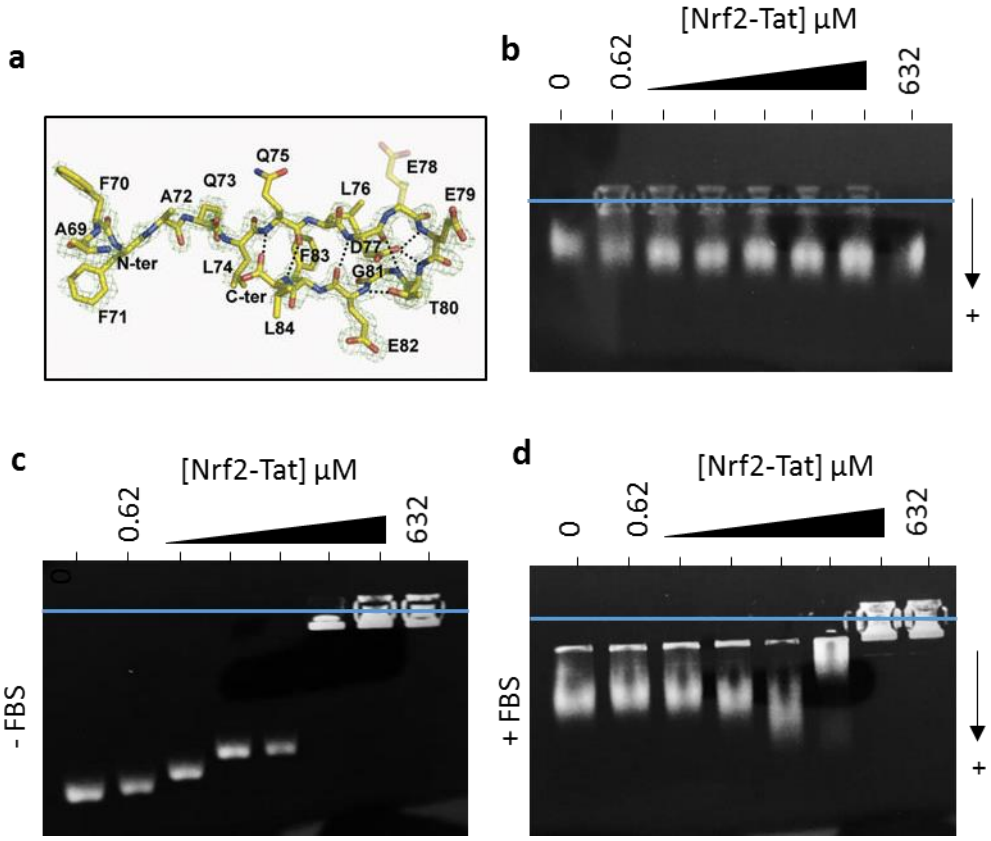

Figure 5.9 Interaction of Nrf2-Tat with amine QD and carboxyl QDs.

The small degree of secondary structure of the Nrf2 motif (a) which was thought to contribute to the lack of interaction of this peptide with aQDs during gel electrophoresis (b). However, Nrf2-Tat demonstrated a clear interaction with carboxyl QDs which was maintained to some degree following addition of 10 % FBS (c, d).

In this model, anionic groups in the aQD polymer lie interior relative to amine surface groups which may be inaccessible for electrostatic interaction with structured cationic CPP peptides. This model also suggests that the steric bulk of the peptide may also serve to hinder interparticle interactions and prevent QD aggregation which was the case when using carboxyl QDs and CPPs (Fig.5.2a).

To investigate this possibility, Tat-Nrf2 from 0.62 to 632 µM (half-log dilution) was added to carboxyl QDs at 25 nM for 30 mins before analysis by gel electrophoresis (Fig.5.9c). The peptide formed a clear binding saturation curve with carboxyl QDs which plateaued at around 20 µM before a critical concentration was reached with high peptide concentrations resulting in aggregation of QDs and entrapment of material within the well. The critical concentration however was roughly an order of magnitude higher than for CPP-peptides without a defined secondary structure (Fig.5.2a) and suggested that the secondary structure of the Nrf2 domain could inhibit particle aggregation up to a point by preventing inter-particle interactions.

To investigate the interaction of the peptide and carboxyl QDs in the presence of serum, complexes were added into 10 % FBS for 30 mins before running by gel electrophoresis (Fig.5.9d). Interestingly, the binding curve remained to an extent although with several distinguishing features. Increasing the peptide concentration now resulted in an increase in QD migration and a plateau was not reached. This suggested that the interaction between peptide and QD remained in spite of corona formation with 20 µM peptide showing the most resistance to dissociation or highest binding. Corona formation also had a small effect on reducing aggregation at 63.2 µM Tat-Nrf2 with QD migration into the gel matrix visible, although the reason for this was unclear (Fig.5.9d).

However, this peptide was not investigated further as a model cargo sequence as collaborators of ours were unable to repeat the delivery assay presented in the original paper involving HO-1 expression as a result of treatment with Tat-Nrf2. As a consequence, Tat-Nrf2 was deemed unsuitable for use as a model therapeutic peptide. Nevertheless, these data further suggest that CPP-peptides may be non-covalently assembled with nanoparticles and these entities may show resistance to corona formation. Additionally, carboxyl QD aggregation as a result of CPP addition maybe also be prevented by appending a cargo of suitable bulk to the CPP domain to inhibit inter-particle interactions.

5.2.4 Targeting the nanoparticle corona with GFPR8

As highlighted in previous chapters, the nanoparticle corona is a dynamic layer of protein components which forms rapidly at the nanoparticle surface. This corona may also undergo remodelling when exposed to new protein factors (Chapter 3, Fig.3.7) as additional factors bind to the particle surface

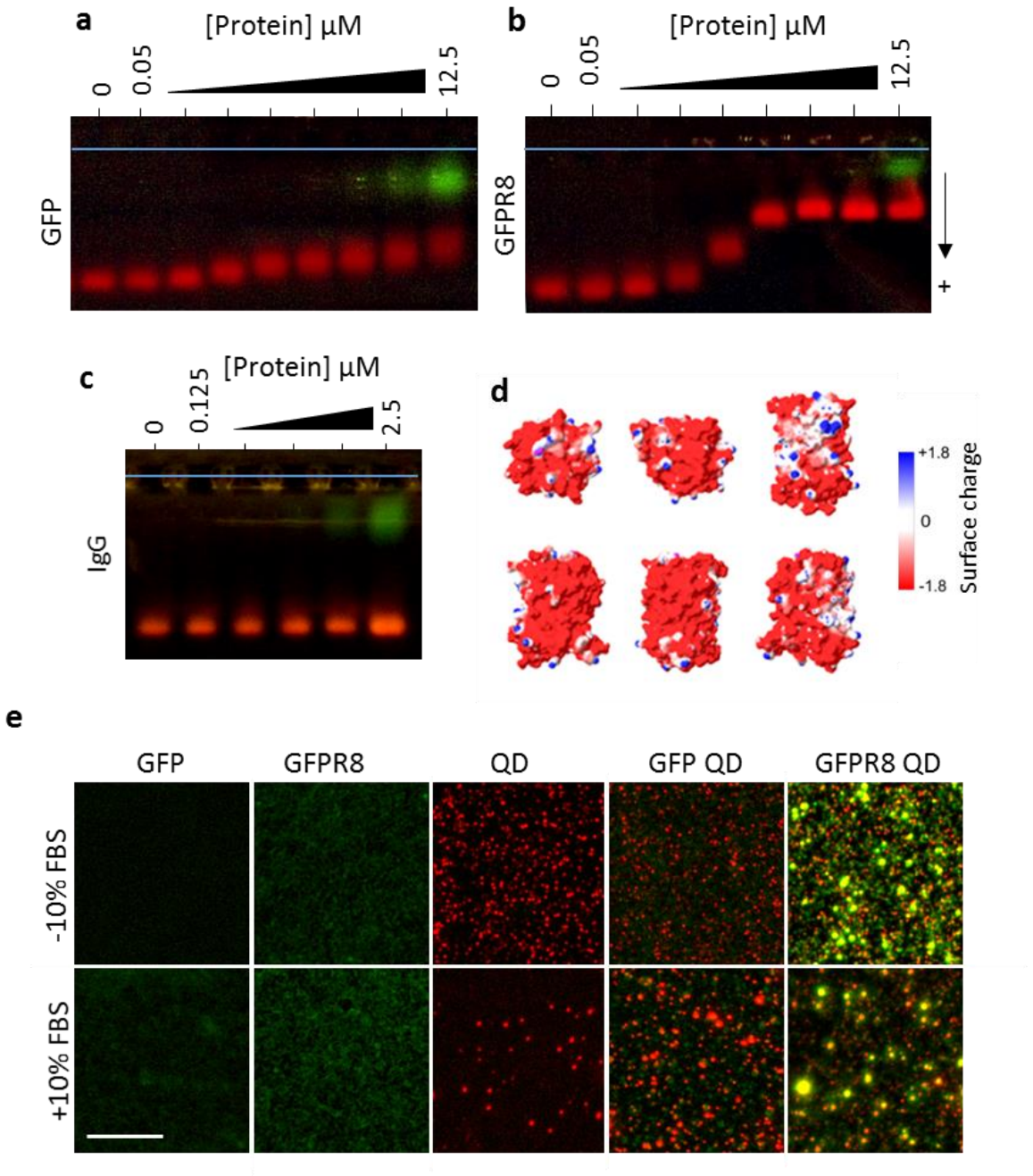

Figure 5.10 Targeting GFP to the carboxyl QD surface using a CPP sequence.

Carboxyl QDs were complexed with GFP (a), Alexa-488 IgG (c), or GFPR8 before analysis by gel electrophoresis. The GFPR8 ligand displayed a clear binding curve with carboxyl QDs (c) although the GFP control also slowed migration of QDs in a concentration dependent manner (a). The largely anionic nature of the GFP protein alone (d, calculated with SWISS PDB Viewer) suggested that the cationic CPP may drive association with QDs through an electrostatic mechanism. To investigate the potential interaction of GFP alone and QDs binding was also assess by visualizing complexes drop cast onto a glass surface in the presence or absence of 10 % FBS. Scale bar is 8 µm.

or weaker binders are replaced with higher affinity binders. Introduction of a corona modified particle into a new environment may also lead to dissociation of certain factors over time owing to a possible concentration gradient. The corona has thus been identified as a potential platform for delivery of protein therapeutics (Mahon et al., 2012), where a non-covalently bound cargo protein residing in the protein corona may be released following cell uptake or transport into the interstitial space due to competitive binding with additional protein factors. So far few reports have investigated this method of cargo binding and release and the interaction of CPPs with anionic QDs may provide a convenient model system to test this hypothesis. Indeed following from results presented in this chapter, CPPs present themselves as potential cargo adhesion motifs for targeting peptides or proteins of interest to the nanoparticle surface, potentially allowing the construct to be maintained within the corona following exposure to serum.

To investigate this strategy, enhanced green fluorescent protein (GFP) was chosen as a model cargo protein due to its relatively small size and fluorescent properties, and was appended via its C-terminus to the CPP R8 with no additional linker. As a further note, the protein also contained a His-6 motif at the N-terminus (please see Materials and methods for protein sequence). To assess binding with QDs, GFPR8 from 0.05 to 12.5 µM in quarter-log increments was added to aQDs (Supplementary Fig.5.1) or carboxyl QDs for 30 mins before analysis by agarose gel electrophoresis (Fig.5.10a, b). The GFPR8 construct exhibited no binding pattern with aQDs by gel electrophoresis (Supplementary Fig.5.1). This was presumably a result of the bulk of the GFP cargo which inhibited CPP binding to anionic surfaces within the QD polymer.

For carboxyl QDs without an additional amine-PEG linker the GFPR8 construct exhibited a clear binding saturation curve, with a saturation point around 2.5 µM GFPR8 (Fig.5.10b). Additionally, there was no signs of material entrapment within wells indicating the steric bulk of the protein was sufficient to prevent inter-particle interactions and large scale agglomeration. The appearance of a green GFPR8 band was also evident at higher protein concentrations which emerged following saturation of QD binding (Fig.5.10b). As controls, alexa-488 labelled IgG and GFP alone were also assessed with IgG displaying no interaction with carboxyl QDs, although GFP alone produced a slight slowing of QD migration in a concentration dependent manner (Fig.5.10a, c). However, the migration pattern was not indicative of a binding saturation curve and was markedly different from GFPR8 (Fig.5.10a). Analysis of the surface charge of the GFP cargo revealed only small domains of cationic charge on the surface with the majority of the protein surface maintaining an anionic character a neutral pH (Fig.5.10d). This surface was calculated with SWISS PDB Viewer (Guex and Peitsch, 1997). Nevertheless, weak interactions between GFP and carboxyl QDs may have been sufficient to produce

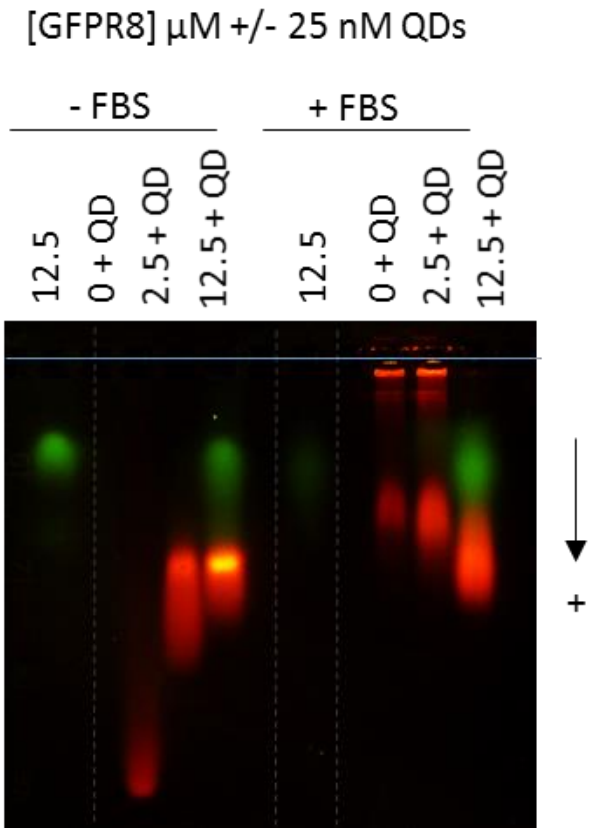

Figure 5.11 Influence of corona formation on GFPR8 binding to carboxyl QDs.

Carboxyl QDs at 25nM were complexed with either 2.5 or 12.5 µM GFPR8 (100 or 500 equivalents) before addition of FBS to 10 % v/v and analysis by dual colour gel electrophoresis.

a slight slowing of QDs during migration, although this interaction may be insufficiently stable to withstand the electric tension during electrophoresis. The absence of cationic domains on GFP alone also suggested that GFPR8 binding was driven by the highly cationic R8 sequence which stabilised the GFP cargo at the QD surface (Fig.5.10b).

Imaging of complexes adhered to a glass surface also further supported a specific binding of GFPR8 to carboxyl QDs (Fig.5.10e). For GFP QDs there was no obvious signs of colocalization in the presence or absence of 10 % FBS with a Pearson's correlation coefficient calculated at 0.29 ± 0.08 or 0.13 ± 0.11, respectively. The GFPR8 cargo however demonstrated a striking colocalization pattern with Pearson's scores of 0.77 ± 0.07 and 0.75 ± 0.14 for the serum free and serum containing conditions, respectively. For the serum positive condition, there were however a larger proportion of QD clusters, although large scale aggregation was not evident (Fig.5.10e).

To investigate the fluorescence stability of complexes, GFPR8 carboxyl QDs were prepared by mixing 25 nM QDs with 2.5 µM GFPR8 and analysed in the presence or absence of 10 % FBS (Supplementary Fig.5.2). Analysis of the red and green emission intensity revealed no noticeable loss in fluorescence for any component over an hour long incubation demonstrating the emission stability of these components in the presence of serum or following complexation with QDs.

5.2.4.1 Electrophoretic analysis of GFPR8 QD complexes

To assess the binding of GFPR8 to carboxyl QDs in the presence of FBS, QDs at 25 nM were complexed with GFPR8 before addition of FBS to a final concentration of 10 %. Complexes were then analysed by gel electrophoresis and the running time was increased to 90 mins to achieve a better separation of components (Fig.5.11). In the absence of serum GFPR8 showed evidence of QD binding due to an increase in intensity of QD bands, although at the lower concentration of 2.5 µM GFPR8, complexes appeared unstable and a streaking pattern was observed in the gel presumably as a consequence of complex dissociation. In the presence of FBS, higher concentrations of GFPR8 increased the migration of QD bands although it was difficult to identify a clear GFPR8 band which tended to produce a smear in the gel (Fig.5.11). Nevertheless these data suggested that the GFPR8 cargo could be maintained within the corona to a certain extent even during competition for binding with FBS.

5.2.4.2 Binding saturation of GFPR8 and QDs

Due to the low resolution and semi-quantitative nature of electrophoresis an assay was devised which exploited the sensitivity of QDs to centrifugation at 20,000 g for 30 mins which removed > 95 % of QDs from the supernatant fraction (Supplementary Fig.5.3). In this experiment, QDs and GFPR8 were prepared separately in PBS before combining to give a final concentration of 25 nM QDs and 1.25 to 6.25 µM GFPR8. Complexes were then centrifuged at 20,000 g and a 25 µL supernatant fraction was analysed using a fluorescence plate reader. This allowed the unbound GFPR8 fraction to be quantified

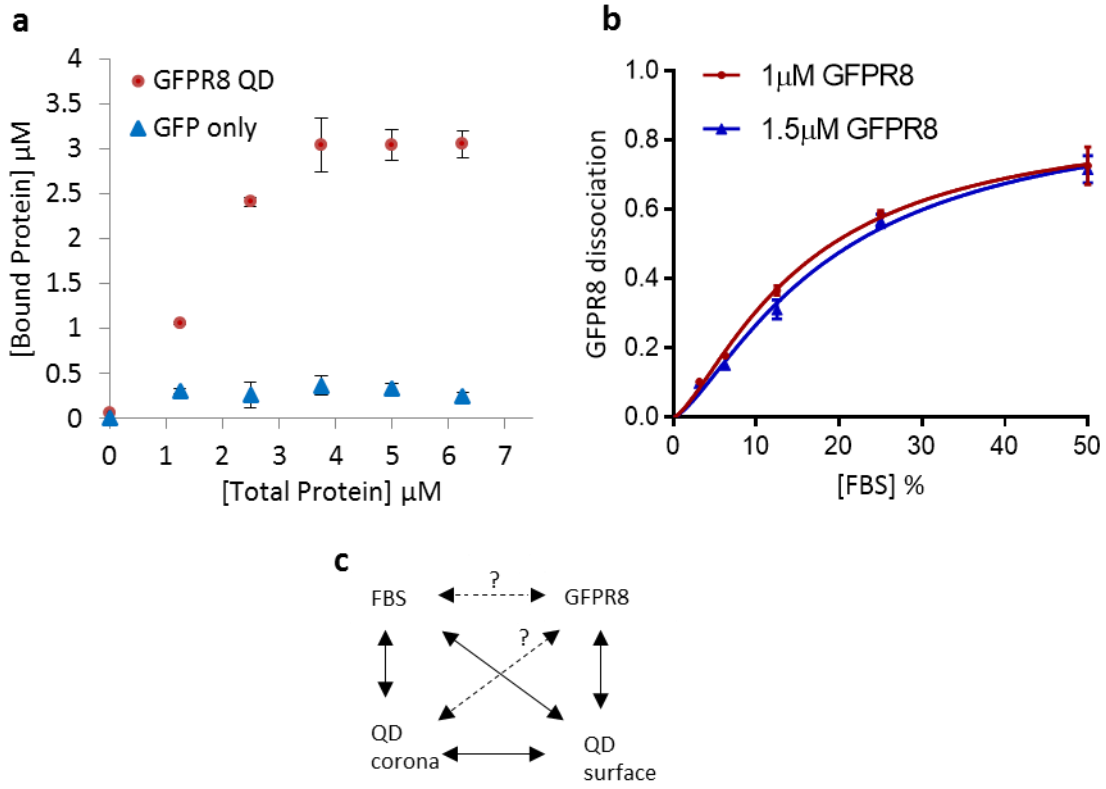

Figure 5.12 Quantification of GFPR8 binding to QDs and stability of conjugates in FBS.

QDs were complexed with GFP alone or GFPR8 before centrifugation to remove bound material. The free protein component was then quantified by fluorescence spectroscopy allowing the bound protein fraction to be determined in a. The stability of GFPR8 QD complexes in serum was analysed in (b) by quantifying the free protein fraction following addition of serum. In c, a schematic is provided illustrating the interactions which occur between the QD, FBS, corona and GFPR8 components. The dashed lines indicate further interactions which remain to be investigated.

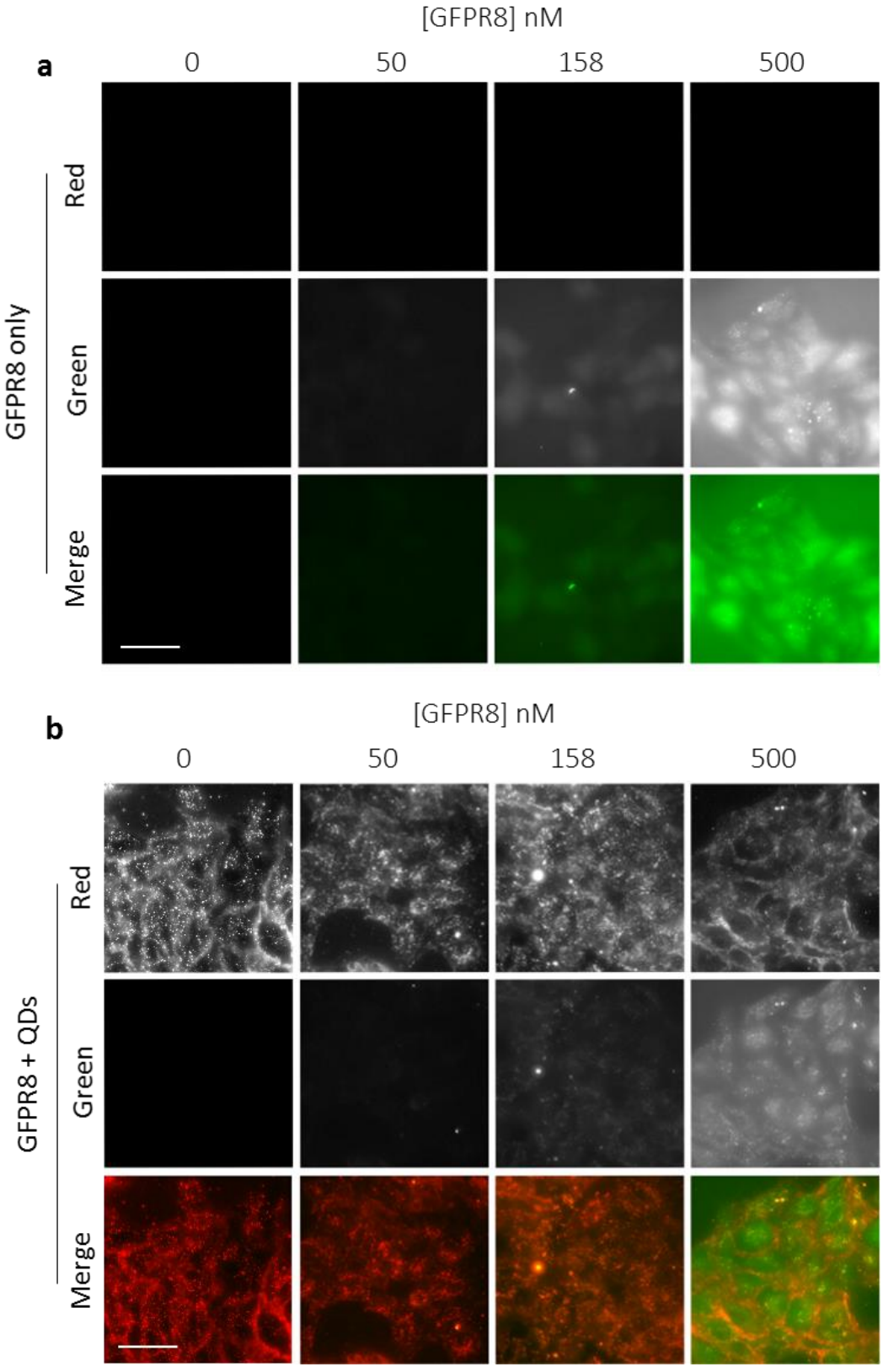

Figure 5.13 Uptake of GFPR8 QDs in live cells.

HeLa cells were treated with GFPR8 (a) or GFPR8 QD complexes (b) for 1 hour in serum free media before washing and imaging live by widefield microscopy. Images are presented as maximum intensity projections. Scale bar is 100 µm.

by measuring the emission at 525 nm in the supernatant fraction (Fig.5.12a). GFP and GFPR8 standards are provided in Supplementary Fig.5.4, along with raw data for centrifugation experiments. Analysis of GFPR8 or GFP binding with 25 nM carboxyl QDs using this assay demonstrated that only GFPR8 displayed an ability to bind these QDs (Fig.5.12a). The saturation point for GFPR8 binding occurred around 3.75 µM total protein which equated to around 3 µM of bound protein or 120 GFPR8 molecules per QD.

5.2.4.3 GFPR8 and QD binding stability in the presence of serum

To investigate the stability of GFPR8 binding in the presence of FBS, QDs were complexed with GFPR8 before adding into FBS for 30 mins to give final concentrations of 10 nM QDs with 1 or 1.5 µM GFPR8 and 0 to 50 % FBS. Components were mixed in volumetric ratios of 1:1:2 for QDs, GFPR8 and FBS respectively. QDs and GFPR8 were first mixed together for 30 mins before addition of FBS for a further 30 mins at room temperature. Following centrifugation, the fluorescence of the supernatant fraction in the green channel was quantified to assess the dissociation of GFPR8 as a function of serum concentration (Fig.5.12c). In the absence of serum dissociation was around 10 % in agreement with the binding saturation experiment (Fig.5.12a, b). However, increasing serum concentration lead to a large increase in the volume of GFPR8 detected in the supernatant and levels of dissociation exceeded 70 % at the highest serum concentration. This result was surprisingly similar to a previous experiment involving the dissociation of curcumin from carboxyl QD complexes as a function of FBS (Chapter 4, Fig.4.4d). Again, excess serum appeared to antagonise the binding of non-covalent GFPR8 QD complexes which presumably occurred as a result of a competitive interaction between the QD surface, QD corona, free FBS components and GFPR8 (Fig.5.12c).

5.2.4.4 Cell binding of GFPR8 QDs

Complexes were then assessed for cell binding activity, firstly in the absence of serum. QD GFPR8 complexes were prepared using between 50 and 500 nM GFPR8 with a fixed concentration of 5 nM QDs. Complexes were applied to HeLa cells for 1 h before washing and imaging live by widefield microscopy with all images acquired as maximum intensity projections (Fig.5.13). QDs complexed with 500 nM GFP, or GFP alone, did not demonstrate any cargo binding, with fluorescence profile in the green channel similar to autofluorescence (Supplementary Fig.5.5). GFPR8 alone however displayed a large increase in binding between 50 and 500 nM. At the higher concentration a large quantity of material appeared to localize to cellular and glass surfaces, although clear punctate vesicles were also visible in cells suggesting uptake by endocytosis (Fig.5.13a). QD GFPR8 complexes at the highest cargo concentration did not achieve the same degree of cargo labelling with intensity profiles in the green channel noticeably lower (Fig.5.13b). However a large degree of colocalization

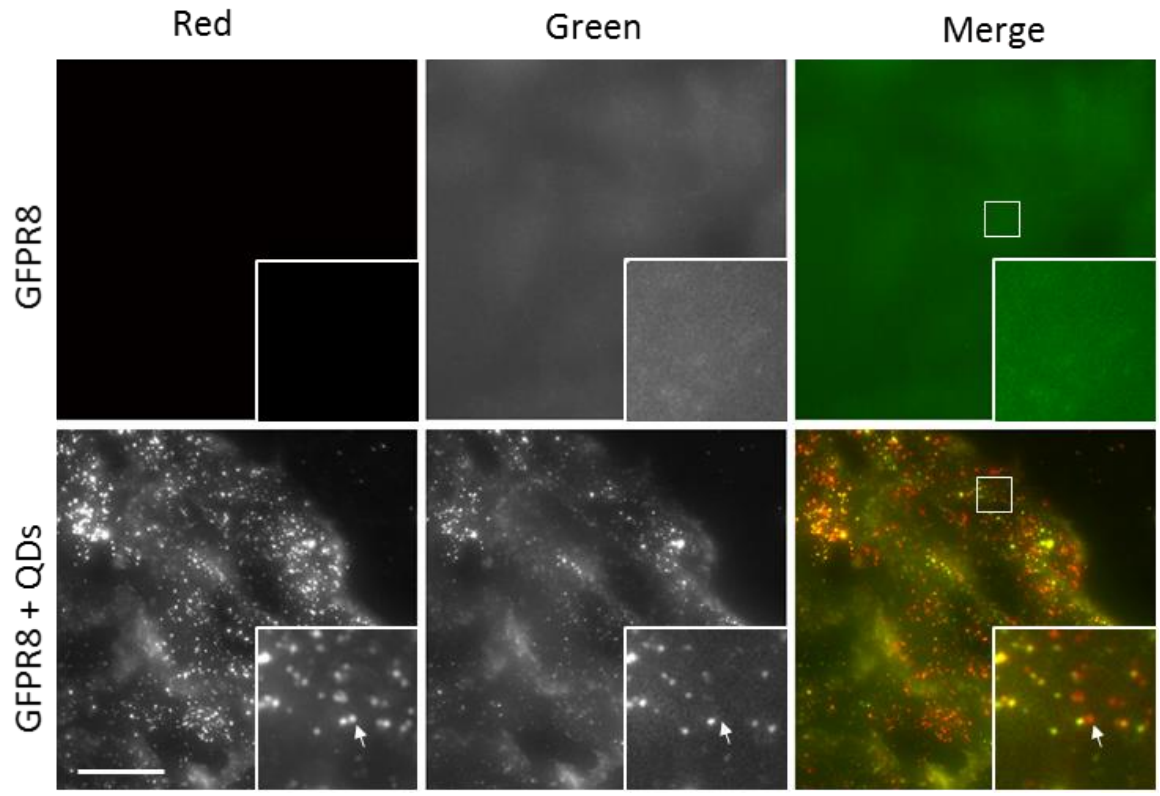

Figure 5.14 Uptake of GFPR8 QD complexes at low protein concentrations.

Cells were treated with GFPR8 alone or GFPR8 QD complexes comprising of 50 nM GFPR8 and 5 nM QDs for 1 hour before imaging by widefield. Treatment was performed under serum free conditions and images are presented as maximum intensity projections. Scale bar 40 µm.

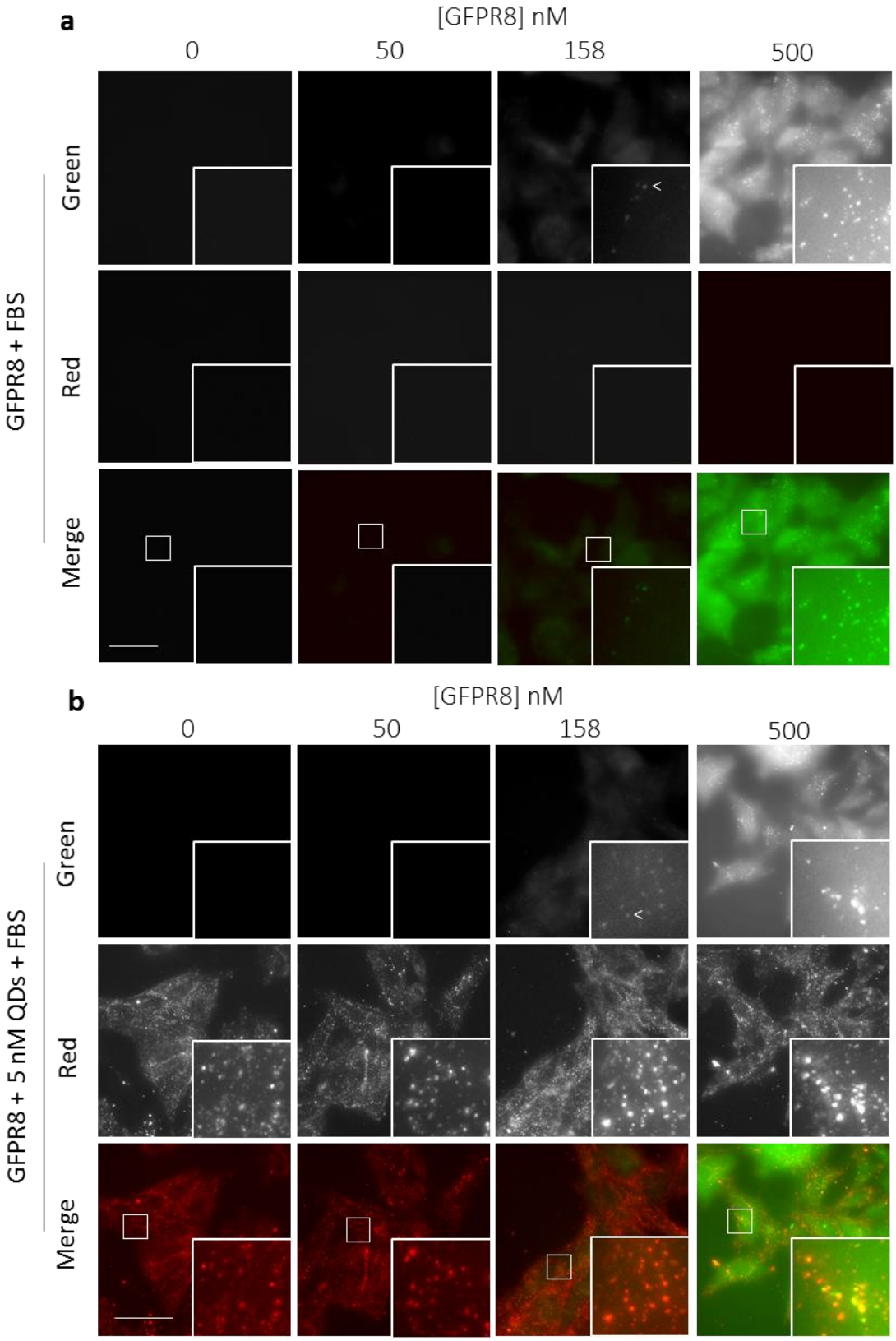

Figure 5.15 Uptake of GFPR8 QDs in the presence of serum.

HeLa cells were treated with GFPR8 alone (a) or GFPR8 QD complexes for 1 h in media containing 10 % FBS before imaging by widefield. Images are presented as maximum intensity projections. Scale bar is 100 µm.

was observed between punctate green and red structures within cells which suggested that complexes had been internalized.

Interestingly, analysing images from the lowest cargo concentration of 50 nM GFPR8 using a different intensity scale revealed a very different picture (Fig.5.14). At this concentration, the GFPR8 control did not exhibit a clear uptake profile with no punctate vesicles visible and material appearing to be localized at the plasma membrane (Fig.5.14). For GFPR8 QD complexes however, a large volume of material was visible in punctate vesicles which appeared to be localized both at the plasma membrane and within punctate vesicles. Moreover, the vast majority of punctate GFPR8 structures demonstrated a striking colocalization with QDs suggesting that the nanoparticle vector was remaining associated with GFPR8 and was facilitating cell binding and uptake at this low concentration. The lack of GFPR8 only uptake at this low concentration was unexpected and suggested that the GFPR8 QD complexes may demonstrate different cell binding kinetics compared to GFPR8 alone, and binding may be driven to some extent by the interaction of the QD with cells. A further observation was that a number of QD structures also displayed no colocalization with the green channel (Fig.5.14, white arrow) which would suggest that the cargo had been released from these structures.

Complexes were then analysed for uptake in the presence of 10 % FBS using the same experimental conditions. Again GFP alone or GFP QD complexes did not show any cargo uptake activity with low fluorescence profiles in the green channel (Supplementary Fig.5.6). For GFPR8 only and GFPR8 - QD complexes, intensity profiles in the green channel were similar at the highest cargo concentration of 500 nM, and dropped sharply with decreasing protein concentration to the extent that GFPR8 fluorescence was similar to background at the lowest concentration of 50 nM (Fig.5.15a, b). At the highest cargo concentration a large degree of colocalization was again observed between green and red punctate structures for GFPR8 QDs, although the number of green structures appeared similar between the conditions. For both conditions a large degree of GFPR8 labelling of the plasma membrane and glass surfaces was also evident suggesting that dissociation of GFPR8 from the QD may have been prominent. At the intermediate concentration of 158 nM GFPR8, the large degree of colocalization between QDs and GFPR8 was maintained with the number of green punctate structures in the QD GFPR8 condition now outweighing the GFPR8 control (Fig.5.15a, b, an example is given by a single white arrow). Crosstalk between the channels was ruled out as examples of QD or GFPR8 structures could be visualized independently in the same image. However, the level of internalization vs plasma membrane binding was difficult to compare between these conditions and more work is needed to quantify the cargo uptake characteristics under these conditions.

5.3 Discussion

There is much interest in utilizing CPPs as vectors for delivering a huge variety of macromolecular cargoes to the interior of cells that would otherwise be membrane impermeable and fail to impart a therapeutic effect (Jones and Sayers, 2012). The mechanisms of cell entry and the pathways utilized for individual CPPs remain poorly characterised with differences among CPPs and when different cargos are appended to the CPP (Jones and Sayers, 2012). Despite these complexities the cationic or amphiphilic character of these peptides has been identified to play a key role by promoting an initial association with cellular membranes and sugar groups at the cell surface though electrostatic or hydrophobic interactions. Entry into the cytosol is thought to occur, at least for large cargos, across the endosomal bilayer in a process termed endocytic escape although for smaller cargos there is evidence that the plasma membrane is the point of entry (Jones and Sayers, 2012). The remarkable ability of these short sequences to enhance the delivery of even large cargos such as nanoparticles has raised their profile to the forefront of nano-therapeutics (Farkhani et al., 2014). The superior spectral properties of QDs uniquely position these particles as probes for interrogating the uptake mechanism of CPP functionalised nanoparticles and their associated cargos.

Chemically crosslinking CPPs and QDs is desirable for applications requiring conjugate stability although further mechanisms are then required to release cargo components which greatly increases the complexity of fabricating the system. Various studies have demonstrated chemical crosslinking of

CPPs and QDs although with varying degrees of success reported in terms of functional delivery into cells (Choi et al., 2011; Medintz et al., 2008; Ruan et al., 2007; Wei et al., 2009). A simpler methodology is to exploit non-covalent interactions to form drug delivery complexes which may undergo dissociation at a site of interest to release the cargo. Initial tests using CPPs and QDs revealed clear non-covalent interaction between these components which inspired an approach here to exploit the non-covalent binding of CPPs and anionic QDs for peptide and protein cargo delivery purposes. Indeed, this approach bears many similarities with the process of corona formation (Chapter 3), involving the adsorption of protein components to the nanoparticle surface. Non-covalent binding of CPPs and QDs has been demonstrated previously although targeting of additional cargo components to the QD surface has not be investigated (B. R. Liu et al., 2013; Liu et al., 2010).

To investigate this paradigm, a panel of model CPP cargos were investigated for their binding with carboxyl and amine QDs (Table 5.1, Fig.5.2, 5.5). However carboxyl functionalised QDs proved unsuitable for further use due to the rapid formation of insoluble aggregates when challenged with a panel of CPPs (Fig.5.2a). Aggregation probably resulted from inter-particle interactions between surface bound CPPs although disrupting this process with a small panel of co-solvents was met with

limited success suggesting the process may be robust under a range of conditions (Fig.5.3). Indeed, even QDs which possessed a nanoparticle corona appeared equally susceptible to aggregation in the presence of Ac-R8 indicating that the CPP could still interact with these QDs in spite of corona formation (Fig.5.4). In a future study it would be interesting to assess the stability of QDs with a more 'mature' corona achieved by exposure of QDs to a greater excess of serum components prior to CPP addition. For the CPP Ac-R8, the reagents used here were very similar to those reported in previous studies involving in vivo cell-tracking of transplanted adipocyte derived stem cells which had been labelled with carboxyl QD-CPP complexes, suggesting that complexes in this study may have been composed largely of aggregated material (Yukawa et al., 2012, 2010). Particle aggregation is an important consideration which can alter a range of critical parameters such as solubility, uptake, binding, toxicity and fate of conjugates in vitro and in vivo, although no data was presented detailing this issue.

Here, the observation that aQDs did not undergo aggregation during exposure to R8 based CPPs opened the possibility of assessing these complexes in cell uptake studies (Fig.5.5). Complex formation was again thought to be driven through an electrostatic mechanism due to the highly cationic nature of R8 and the overall anionic nature of aQDs (Table 5.1, Fig.5.5). Binding was also observed using a wider panel of CPPs although for many amphiphilic CPPs signs of aggregation were observed during gel electrophoresis by streaking of QD bands or accumulation of material within wells (Fig.5.5). CPPs with a number of apolar residues may interact with QDs via hydrophobic interactions with the polymer coat which may lead to a different display of the peptide at the nanoparticle surface. There is considerable scope for engineering a peptide which binds to nanoparticle polymer surfaces in a defined way in the context of variable cargo types.

Analysis of aQDs in uptake studies revealed a striking increase in cell binding when complexed with R8 based CPPs with the majority of material localizing to the plasma membrane at early time points (Fig.5.7a). Interestingly a significant difference in binding was observed when a single amino acid at the distal end the linker sequence was changed from a glycine to a phenylalanine (Fig.5.7a, c). This difference was also largely maintained following a 24 hour chase, with the Phe peptide driving a larger proportion of material into the endolysosomal compartment (Fig.5.7b, c). The entry mechanism of these complexes was not investigated although may be a result of plasma membrane cycling over an extended time frame. Additionally, the cellular fate of the CPP peptide was also not investigated although dissociation of these non-covalent complexes could be expected within the cell, especially against a backdrop of competitive binding with intracellular proteins or membranes components within the endomembrane system. However, addressing these questions is challenging with current

approaches and there is a need to develop methods which can quantify the intracellular processing or trafficking of nanoparticles in real time on a single particle level.

Previous reports have also reported cargo effects when assessing delivery of a pro apoptotic peptide D-NuBCP-9-r8, with the terminal Phe residue acting in synergy with the CPP to promote uptake (Watkins et al., 2011). This work further builds on these results to underline the importance of specific residues which can be located several amino acids from the CPP sequence to promote cargo uptake. The fact this effect was also observed with nanoparticles was surprising considering the huge difference in size of a QD when compared to an individual peptide.

Non-covalent complexation of CPPs and QDs was also investigated using the therapeutically relevant peptide Nrf2-Tat which was previously reported to illicit an anti-inflammatory response by disrupting endogenous Keap1/Nrf2 binding (Steel et al., 2012)(Fig.5.9). In this case the peptide demonstrated binding only with carboxyl QDs which was thought to be a result of the small degree of secondary structure associated with the cargo sequence which may have provided a steric hindrance to binding with anionic surfaces on aQDs. Additionally, Nrf2-Tat binding to carboxyl QDs was only stable to aggregation at lower peptide concentrations suggesting the small cargo motif provided only a small degree of resistance to aggregation. Analysis of these complexes following corona formation also suggested binding of QD and peptide was maintained to some degree despite the presence of competitive binders opening the possibility to utilize QDs or perhaps other small metallic nanoparticles as delivery agents for CPP cargo peptides. However, the Nrf2-Tat peptide was not investigated further as collaborators of ours were unable to repeat key delivery experiments from the original paper (Steel et al., 2012).

The observation that Nrf2-Tat prevented carboxyl QD aggregation to a small degree led to the idea of utilizing a larger cargo appended to the CPP domain to inhibit inter particle interactions. The model cargo enhanced green fluorescent protein was thus appended to the CPP R8 (GFPR8) and assessed for binding with QDs (Fig.5.10, Supplementary Fig.5.1). The protein demonstrated a clear binding profile with carboxyl QDs with no signs of large scale aggregation by gel electrophoresis or fluorescence microscopy indicating the bulk of the protein was sufficient to prevent agglomeration (Fig.5.10). A possible non-specific interaction of the GFP alone control with carboxyl QDs was also apparent by gel electrophoresis although this was not borne out by fluorescence microscopy. As a possible explanation, an excess of anionic GFP molecules in loading wells may have disrupted QD migration during entry into the gel matrix to produce a concentration depended shift in migration.

Analysis of GFPR8 QD complexes by fluorescence microscopy or gel electrophoresis suggested that the association was maintained to a certain degree in 10 % serum (Fig.5.10e, 5.11). Investigation of

the binding properties using a sensitive fluorescence assay indicated that bare carboxyl QDs have a capacity of around 120 GFPR8 molecules per particle. Taking the average footprint of GFPR8 to be roughly 15 nm^2 (rounded up to the nearest 5 nm^2 (Phillips, 1997)) and the hydrodynamic radius of carboxyl QDs as roughly 15 nm, (Chapter 3, Table 3.1) the maximum theoretical capacity would be expected to be around 190 GFPR8 molecules per QD indicating a degree of spacing of GFPR8 at the QD surface. Interestingly, analysis of the stability of these complexes as a function of serum concentration revealed a result highly reminiscent of curcumin binding to carboxyl QDs in Chapter 4 (Fig.4.4d). Here, increasing FBS concentration again antagonized binding of the GFPR8 cargo in a concentration dependent manner to an extent that the majority of cargo was dissociated at 50 % FBS. A longer incubation time may also lead to a greater release of material from the QD assembly, although this remains to be tested. The serum concentration of 10 % which is popular in standard tissue culture practise may also have a protein concentration which is somewhat lower when compared to in vivo compartments suggesting dissociation as a result of serum competition may be a major issue for non-covalent drug delivery systems.

Analysis of GFPR8 complexes in cell binding experiments in the presence or absence of serum revealed some interesting observations (Fig.5.13, 5.14, 5.15). In the absence of serum, binding of GFPR8 when complexed with QDs appeared to lag behind GFPR8 alone at the highest protein concentration of 500 nM due to the higher overall intensity profile of the control (Fig.5.13a, b). However, quenching of GFPR8 fluorescence by the QD could not be ruled out as components were ostensibly in close spatial proximity with large overlaps in the QD absorbance (Chapter 3, Fig.3.2a) and GFPR8 emission profiles. Nevertheless, at the lowest protein concentration of 50 nM GFPR8, internalization of the GFPR8 control was virtually undetectable which was in stark contrast to GFPR8 QD complexes which were detectable on cellular surfaces and intracellularly (Fig.5.14). Additionally, a high degree of colocalization was also apparent between these components although in certain instances QDs appeared entirely absent of the GFPR8 cargo. This may be taken as evidence of cargo release although more work will be needed to confirm this suspicion and to identify the fate of the GFPR8 cargo.

In the presence of serum the picture was less clear with little difference in green intensity profiles between GFPR8 and GFPR8-QDs at the highest protein concentration, and no detectable GFPR8 signal at the lowest concentration of 50 nM for either condition (Fig.5.15a, b). At the lowest protein concentration the level of dissociation of GFPR8 and QDs may have rendered the GFPR8 signal undetectable as a low number of GFPR8 molecules per QD may be insufficiently bright to be distinguished against image noise. At the intermediate concentration of 158 nM corresponding to around 31 GFPR8 molecules per QD, the majority of punctate structures in the red channel were also positive for GFPR8, with a considerably higher number of green structures per cell when compared to

the GFPR8 only control. This result appeared to mirror the serum free condition although occurring at a GFPR8 concentration of 158 nM rather than 50 nM.

Together these data introduce the idea of exploiting the cationic charge of CPPs to assemble cargo moieties into complexes with anionic nanoparticles. Grouping of components into a nano assembly in this way may offer a way to modulate targeting of the complex, its uptake and eventual intracellular fate. The non-covalent nature of these complexes may offer a convenient release mechanism at sites of interest, particularly when exposed to a gradient of protein factors. Indeed these results further indicate that non-covalent complexes are disrupted by serum proteins in a concentration depended manner. Thus in ordered to make use of non-covalent delivery complexes in vivo, the interaction between cargo and nanoparticle must be carefully tailored to prevent premature dissociation of the particle. In conclusion, a facile and efficient mechanism of cargo attachment to anionic nanoparticles was demonstrated, although much more work is necessary to evaluate this mechanism for drug delivery purposes.

6 Automated quantification of particle trafficking through endocytic compartments

6.1 Introduction

Understanding the mechanisms of particle uptake into cells and the ability to quantify the route taken and cellular fate of the cargo is crucial in the development of nanoparticles for medical applications. However, despite considerable attention over recent years, substantial uncertainties remain over the mechanisms of nanoparticle uptake, even for very well studied particles. As highlighted in previous chapters, the problem is compounded by the highly complex and poorly understood nature of the endocytic machinery. For instance, recent studies have even questioned the prominence of many previously well-established endocytic pathways in the trafficking of cell specific cargos, suggesting the vast majority of cellular cargo traffic, as much as 95%, is mediated by the clathrin pathway alone (Bitsikas et al., 2014). DDS may be designed to gain entry in to cells by non-specific uptake or interaction with cell surface receptors in an attempt to target a specific pathway. Indeed, considering the variety of nanoparticles under investigation for drug delivery purposes it is not surprising that the majority of endocytic pathways described in the literature have been implicated in the uptake of nanoparticle complexes (Akinc and Battaglia, 2013; Ma et al., 2013). This diversity of interactions between nanoparticles and cells is driven by variations in particle architecture such as surface characteristics (Gratton et al., 2008; He et al., 2010; Lunov et al., 2011; Yue et al., 2011), particle shape (Chithrani et al., 2006; Gratton et al., 2008) and size (Gratton et al., 2008; Rejman et al., 2004), and also cell-type specific effects (Douglas et al., 2008; Lunov et al., 2011; Yue et al., 2011).

On the other hand a common finding for many nanoparticles irrespective of shape, size and surface charge, is that trafficking routinely results in routing along degradative pathways to the lysosome (Rejman et al., 2004; Yue et al., 2011). For many nanoparticle carriers a key goal is to circumvent delivery to the lysosome by crossing into the cytosol in a process termed endocytic escape (Douglas et al., 2008; Martens et al., 2014). However, to make matters worse recent reports have demonstrated that cytoplasmicaly injected nanoparticles can be processed by the autophagy pathway to result in lysosomal capture, indicating a possible further barrier for nanoparticles therapeutics (Remaut et al., 2014). In order to facilitate the development of particles which reliably follow trafficking routes to defined cellular compartments it is crucial to develop methodologies which allow for the precise quantification of nanoparticle trafficking through endocytic compartments. To date many studies aim to identify the point of entry and the final destination of the particle although a much deeper understanding of the cellular itinerary will be needed for nanoparticles to reach their potential as drug delivery agents. Previous chapters have highlighted that non-covalent nanoparticle complexes may be

susceptible to dissociation during progression through different biological environments, and so understanding of this trafficking through these environments on the cellular level will be critical. Additionally, to study rare events such as particle translocation between cellular compartments, or to capture endocytic escape in real time, dynamic information is also required.

So far fluorescence colocalization microscopy has been widely employed to investigate trafficking pathways via labelling of organelles and particles with fluorescent probes. Using a general approach, interaction events between two labelled components may be inferred by the observation of colocalization which typically occurs over spatial distances on the order of ~ 200 nm for diffraction-limited data (Lachmanovich et al., 2003). Many studies also rely on the use of endocytic inhibitors to determine the route of particle entry although questions can arise over the non-specific nature of these compounds and possible off-target effects (Dutta and Donaldson, 2012). Indeed, QD uptake has been previously investigated using a panel of endocytic inhibitors where QDs with a carboxylic acid surface coating were reported to gain entry via the G-protein-coupled receptor associated pathway and the low density lipoprotein receptor/scavenger receptor pathway (Zhang and Monteiro-Riviere, 2009). A large number of studies also utilize fixed samples which have the potential to give rise to fixation artefacts that can, for example, alter the spatial distribution of carriers (Richardson et al., 2008).

6.1.1 Colocalization methods and particle tracking

A variety of methods have been developed to give a quantitative measure of colocalization which can be broadly divided into pixel based and object-based methods (Bolte and Cordelières, 2006). Pixel based methods employ statistical analysis of pixel intensities between the two channels to calculate a global correlation coefficient such as the Pearson's correlation coefficient and the Manders coefficients (Manders et al., 1993). While pixel-based methods are easy to compute their interpretation can be difficult owing to the use of relative pixel intensities in the calculation, as well as difficulty in assessing intermediate values of these coefficients. Object-based methods are more intuitive to interpret as they rely on object recognition and segmentation techniques to detect primary objects which can then be assessed for colocalization by measuring their overlap or quantitating the separation distance between objects (Koyama-Honda et al., 2005; Lachmanovich et al., 2003; Morrison et al., 2003). These methods can determine the positions of objects with a precision much greater than that of the microscope which can help reduce spurious colocalization detection (Thompson et al., 2002). To gain dynamic information colocalization analysis can also be conducted frame by frame to measure colocalization temporally (Costes et al., 2004; Villalta et al., 2011).

On the other hand global measures of colocalization suffer from a number of drawbacks. In particular object colocalization may also occur by chance as a result of multiple labelled probes occupying the

focal volume. This problem becomes acute at higher object densities making quantification of colocalization problematic. Conversely rare events also become difficult to spot due to the noise associated with randomly colocalized objects. Recent methods have been developed to address these problems which analyse the spatial distribution of objects relative to one another (Lund et al., 2014; Shivanandan et al., 2013). A significant interaction between two components can then be defined via a spatial correlation that deviates from randomness (Shivanandan et al., 2013). However, global measures do not report on the history of individual events at the single particle level, and gaining further information on object interaction requires additional methods. A more powerful methodology to investigate particle trafficking is to follow individual particles in real time as they undergo cellular processing and observe interactions which occur with cellular components of interest. Much more information can potentially be garnered from this approach as individual events may be scrutinized allowing for fusion and splitting events between components to be studied (Deschout et al., 2013; Dupont et al., 2013; Vercauteren et al., 2011a), as well as rare interaction events to be isolated (Sandin et al., 2012).

6.1.2 Challenges associated with single particle tracking

Quantifying particle trafficking using two dimensional microscopy approaches presents several challenges. Substantial spatial displacement of the particle in question can result from cellular interactions such as directed transport along microtubules which can approach 5 µm/sec (Schmoranzer, 2003), as well as diffusive motion of the parent vesicle or the particle within a larger compartment (Hall and Hoshino, 2010; Klann et al., 2012). As a result of this movement and the limited axial resolution of high numerical aperture (NA) objectives which are often used in SPT, particles are frequently lost from the focal volume. An obvious solution to this problem is to employ 3D microscopy techniques, although this comes with the cost of requiring additional time to image and process the third dimension (S.-L. Liu et al., 2013; Ruthardt et al., 2011). Alternatively, lower magnification or lower NA objectives enable a greater depth of focus although with the trade-offs of reduced sensitivity and lower image resolution which are often non sequiturs for SPT (Ruthardt et al., 2011). As such, utilizing high NA objectives in a 2D format provides a good balance between rapid image-acquisition, ease of image processing, diffraction limited spatial resolution, although with the drawback of obtaining partial particle trajectories.

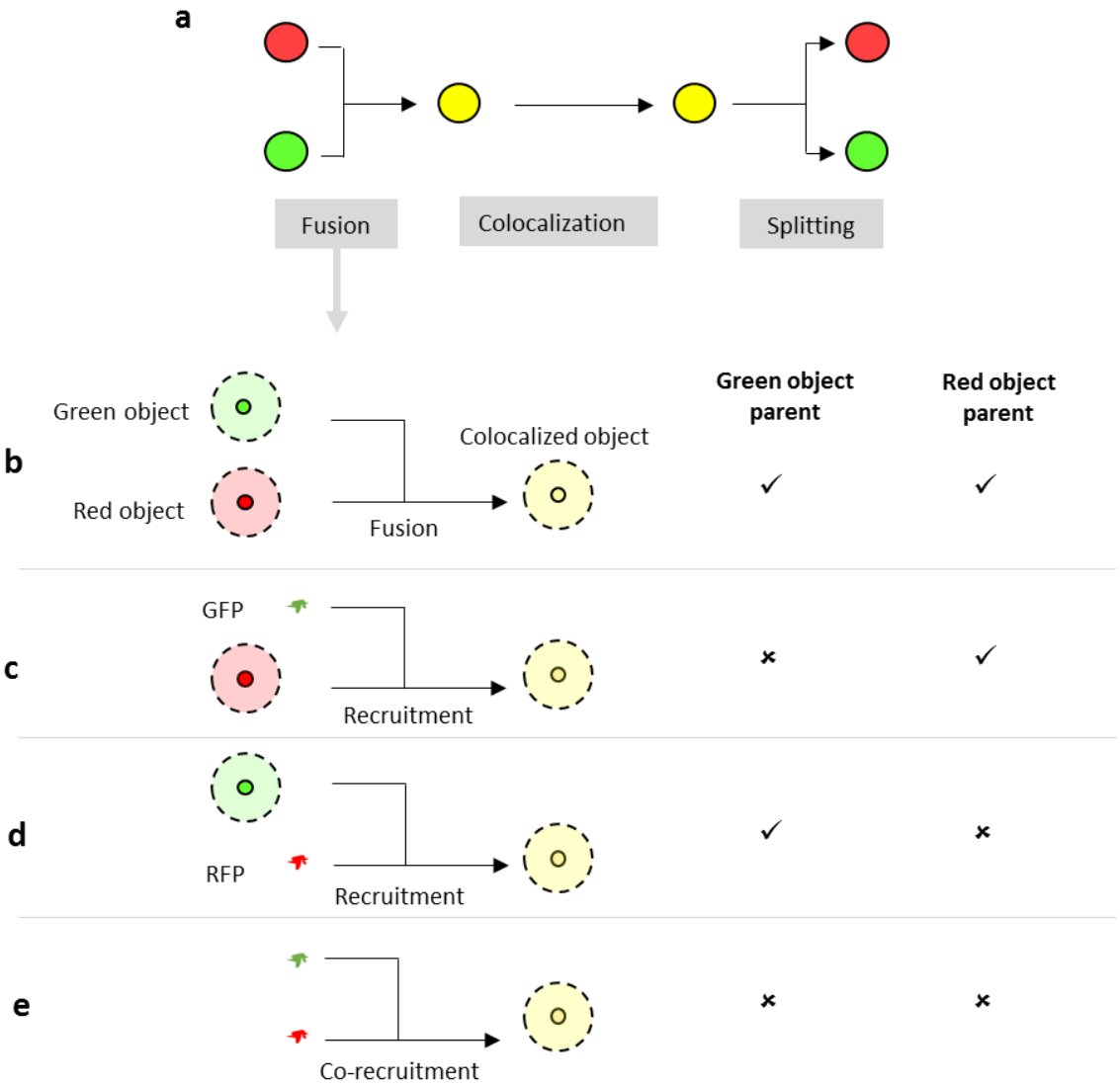

Figure 6.1 Tracking of object parentage to characterize interaction event mode.

The interaction of two probes may be split into three phases termed the fusion, colocalization and splitting phases (a). Labelling cellular compartments of interest using protein tags such as GFP or RFP is generally achieved by a concentration of the probe at the compartment of interest which increases the intensity profile of the labelled compartment above background. This model of labelling can be exploited to reveal information on the mode of interaction events (b - e). For example, identification of genuine colocalization between a red and green component could occur in one of four ways depending on the type of 'fusion' event. A red and green vesicle undergoing a classic fusion process would both be visible in the preceding frame resulting in both objects possessing a prior history (b). An alternative 'fusion' event may also occur from recruitment of a green component to a red vesicle which would result in only the red object possessing a prior history as commonly used fluorescent tags are not generally bright enough to be detected alone (c). Likewise, the opposite occurs from recruitment of a red component to a green vesicle (d). Finally, recruitment of both components simultaneously to the same location would result in neither object possessing a prior history (e). Tracking of object parentage in this way may therefore reveal clues as to the type of cellular fusion event taking place.

This issue is also further compounded by the imperfection of tracking algorithms which tend to further fragment trajectories due to failures in the linking step of the algorithm (Chenouard et al., 2014). This can lead to a single particle being sampled many times during a time course. Consequentially the interaction of a particle and a labelled compartment of interest may be categorized into three phases defined here as the fusion, colocalization and splitting phases (Fig.6.1a). In the colocalization phase particles are found to be exclusively colocalized (i.e. from the first frame of the track at track-index = 0, to the last frame) whereas fusion and splitting phases constitute a gain or loss of colocalization in the track (Fig.6.1a).

6.1.3 Recent methodologies leveraging SPT

A number of methods have been proposed which leverage single particle tracking (SPT) in this way to retain spatial information associated with object based methods and enable the study of individual particle histories during negotiation of the endocytic system in time-lapse experiments. Previous approaches have utilized spatial and temporal information to determine true colocalization, where the centroid positions of two objects are required to appear closer than a threshold distance for multiple consecutive frames, although these methods have currently focused on obtaining more accurate measures of colocalization and have not been applied to search for fusion and splitting events (Dunne et al., 2009; Koyama-Honda et al., 2005; Varela et al., 2014). Alternatively the Trajectory Image Correlation (TrIC) method was recently described which identifies interaction events by performing image cross correlation between the two channels in trajectories of interest (Dupont et al., 2013). In this approach a small window centred on the particle is analysed for correlation in both channels although a drawback with this approach is that nearby objects in the opposing channel also give rise to a correlation signal and so random colocalization events will still be regarded as true events.

An improved approach has been described which assesses correlation between the displacement vectors of particles and labelled cellular components (Deschout et al., 2013; Vercauteren et al., 2011a). Correlated motion can be a good indicator of genuine interaction and here trajectories of particles and cellular components are compared pairwise to generate a correlation score between tracks. This has the advantage of requiring a time dependency as particle and object correlated motion tends to threshold (Deschout et al., 2013). However a drawback with this method is the requirement to track both sets of objects which may not be straightforward using the same tracking algorithm. Additionally, correlating object motion alone may not be sufficient to distinguish events between irregular shaped cellular structures such as tubules, or objects which show only weakly correlated movement, such as movement of a particle in the plane of a membrane. Finally, this method may also be expensive computationally due to the need to track both components as well as potentially

requiring a large number of trajectory comparison calculations to isolate those with high correlation scores.

Taken together these methods demonstrate that SPT approaches can provide additional information from colocalization studies, and in particular allow for the quantification of fusion and splitting events which are visualized as a gain or loss of colocalization in particle tracks (Deschout et al., 2013; Dupont et al., 2013; Vercauteren et al., 2011a). Building on these methods SPT potentially allows for more elaborate means of event characterization. A relatively unexplored idea is to characterize colocalization events according to the individual histories of the interacting components. For example, a fusion event between two probes of interest may be expected to occur between objects that are both visible in the frames preceding the event (Fig.6.1b). In this case both objects would possess a 'parent' object in the preceding frame. This behaviour is commonly visualized when tracking viral particles during endocytosis and trafficking through labelled endocytic compartments for example (Liu et al., 2012; van der Schaar et al., 2008). Alternatively, genuine colocalization may also occur as a result of recruitment of labelled cellular factor to the resident compartment of the red or green particle (Fig.6.1c, d). As individual cellular components tagged with fluorescent proteins such as GFP are not easily visualized alone, concentration of the factor due to recruitment will be visualized as the emergence of a green or red object in Fig.6.1c and d, respectively. This has been classically illustrated during Rab conversion as a mechanism of progression from early to late endosomes (Poteryaev et al., 2010; Rink et al., 2005). During this type of gain-of-colocalization, only one component will possess a 'parent'. Finally both red and green probes may also be simultaneously recruited to a site with neither object possessing a prior history (Fig.6.1e). Thus by following the parentage of objects undergoing interaction events it may be possible to distinguish a signature which would inform on the type of interaction at this juncture. This framework can also be applied to investigate splitting events in a similar manner with the splitting object giving rise to a 'child' object in the adjacent frame. Together, this simple method may allow for a further characterization of cargo transport through a labelled compartment.

In this work, object-based methods are explored with the aim of quantifying interaction events between particles and labelled cellular components. This work builds on previous studies which encode spatial and temporal information to identify interaction events in particle tracks, whilst also introducing a novel filter algorithm for event detection. So far few studies have explored integrating multiple event detection methods where there may be potential to reduce the false error rate of detection. The combination of multiple filters is thus explored as a means to improve event recognition. Finally, the concept of characterizing colocalization events with respect to parentage is also investigated with synthetic and live cell data.

6.2 Results

6.2.1 Investigation of published methods to isolate interaction events in particle tracks

In order to develop a means of quantifying fusion and splitting events using SPT data, a variety of methods proposed in the literature were first investigated. In the TrIC method particle tracks are analysed using image cross correlation over a small window centred on the particle, although others have aired concerns over the utility of this methods for capturing events in crowded images (Deschout et al., 2013; Dupont et al., 2013). To assess this method here a particle simulation software was developed (as described in materials and methods) which allowed for a straight forward investigation of the method using an objective dataset. Synthetic data were generated which consisted of a 2D plane of randomly diffusing particles with 84 red and 16 green particles over 30 frames (Fig.6.2a – c). The image was also seeded with three colocalized red and green particles (white arrows indicated in Fig.6.2a) that underwent splitting events at random times during the sequence and occurred in frames 5, 14 and 22. Particle tracks were then generated using the MOSAIC algorithm as described in materials and methods (Sbalzarini and Koumoutsakos, 2005).

Using the TrIC method, cross correlation of red and green channels in a region of interest surrounding the red particle produced a strong signal due to a nearby green particle and a very low signal when correlated with the green image background (Fig.6.3a). However, in the case of the relatively high object density of the synthetic image sequence, a very high level of variability was observed in the cross correlation signal when plotted for all tracks (Fig.6.3b). This was a direct result of many nearby green particles entering the region of interest used for cross correlation calculation which made it extremely challenging to isolate the two splitting events using this method alone (Fig. 6.2.2b). The densities of particles used in this simulation were not regarded as especially high and a similar density can be readily achieved in live cell particle tracking experiments using even low nanomolar concentrations of QDs suggesting that the TrIC method may only be useful for applications involving very low particle densities.

An alternative method to quantify interaction events involves the analysis of pixel intensities in a trajectory of interest (Rink et al., 2005). The fitting procedures included as part of many tracking algorithms enable the location of particle centres to be determined with sub pixel accuracy (Fig.6.4a – b), enabling a straight forward analysis of the fluorescence intensity at the particle centre in both channels. Intensity fluctuations in the opposing channel may then be indicative of the occurrence of interaction events (Rink et al., 2005). An example of this approach is given in Fig.6.4c, where a single particle is tracked as it undergoes a splitting event from a green object. Owing to the relatively high

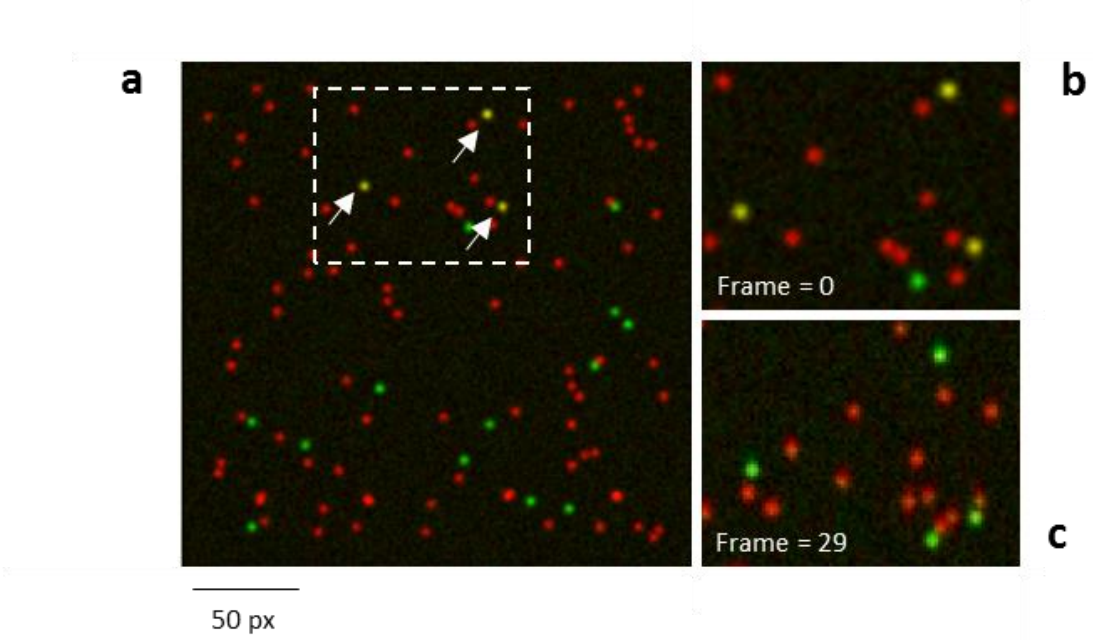

Figure 6.2 Simulation of red and green particle splitting events.

A small simulation involving multiple red and green particles over 30 frames was run to generate basic splitting events between three colocalized red and green particles (a – c, white arrows). The three particle were colocalized at frame=0 (b) and underwent splitting events at random times so that all three colocalized particles were separated by frame=29.

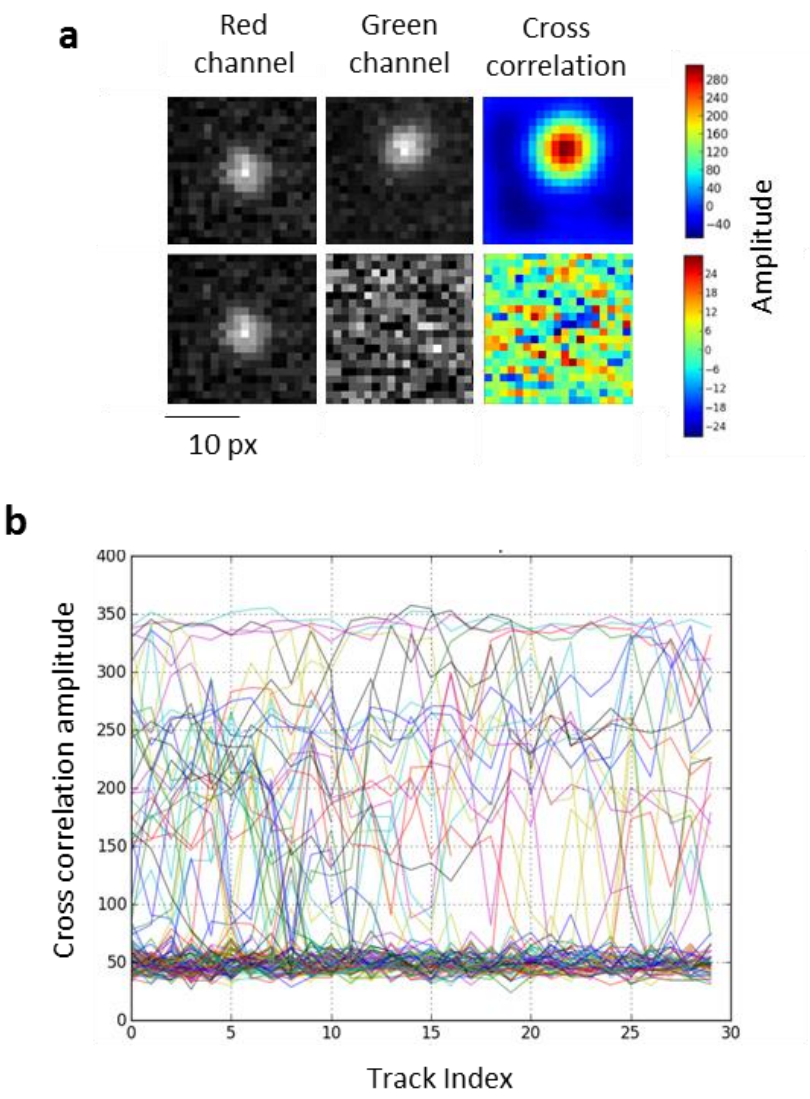

Figure 6.3 Assessment of the TrIC method for isolating basic splitting events.

Applying the TrIC method to simulated data, cross-correlation of two nearby red and green particles produced a large cross correlation signal, whereas an isolated particles generated a very low signal (a). This method was then applied to simulated data in an attempt to isolate three trajectories containing basic splitting events (b). The cross correlation signal for all tracks was plotted in b to illustrate the complexity of isolating the three events using this method alone.

signal to noise ratio in this image the separation event can be clearly visualized as a sharp drop in intensity in the green channel (Fig.6.4c).

However, when applied to the simulated time-lapse discussed above, interaction events become more difficult to isolate (Fig.6.4d). This was a result of false positive interactions due to particles crossing over one another which produced peaks in the green intensity of particle tracks (Fig.6.4d). The relatively high SNR of the simulated data analysed here, and the uniformity of the background is not always common during particle tracking applications in live cells. As an example, a HeLa cell was transfected with Rab21-GFP, a small GTPase that localizes to the early endocytic pathway (Simpson et al., 2004). Small GTPases have critical roles in orchestrating membrane trafficking during endocytosis with Rab21 here serving as a model for investigating these protein factors (Rink et al., 2005; Sandin et al., 2012; Simpson et al., 2004). This cell was then stained with transferrin Alexa 568 for 5 mins, before tracking of Rab21 was performed. Transferrin is glycoprotein with crucial roles in iron transport and cellular iron uptake (Gkouvatsos et al., 2012). The intensity profiles of red and green channels at the particle centre were then plotted as intensity distributions in Supplementary Fig.6.1 to illustrate the variable nature of pixel intensities centred over the particle. The complexity of intensity profiles renders the automated quantification of interaction events extremely challenging due to such a wide range of foreground and background intensities, and suggests that a binarization of the data may be worthwhile to isolate track events.

A further method proposes to identify colocalization events based on the spatial proximity of objects over an extended time frame (Dunne et al., 2009; Koyama-Honda et al., 2005; Lachmanovich et al., 2003; Varela et al., 2014). This approach first identifies the discrete position of particles and objects followed by isolation of objects which fall within spatial and temporal parameters defined by the user. Applying this method to the simulated time lapse in discussion, particle locations were determined during particle tracking using the MOSAIC software (Sbalzarini and Koumoutsakos, 2005), whereas object locations were found using a Gaussian fitting procedure as described in materials and methods (Fig.6.5a). The threshold distance for colocalization was then arbitrarily defined as a distance closer than 0.6 pixels (px) and the temporal requirement for colocalization detection was set at 3 frames. Splitting events were then identified when colocalization was lost for a further 3 frames. Using these parameters it was possible to correctly identify the three colocalized particles with no false positives which suggested this approach may be suitable for further development for use in live cell time lapse experiments (Fig.6.5b). As a comparison the cross correlation amplitude calculated using the TrIC method was also plotted which did not produce any clear signal on particle splitting (Fig.6.5b). This appeared to result from the separated objects remaining in relatively close proximity to one another

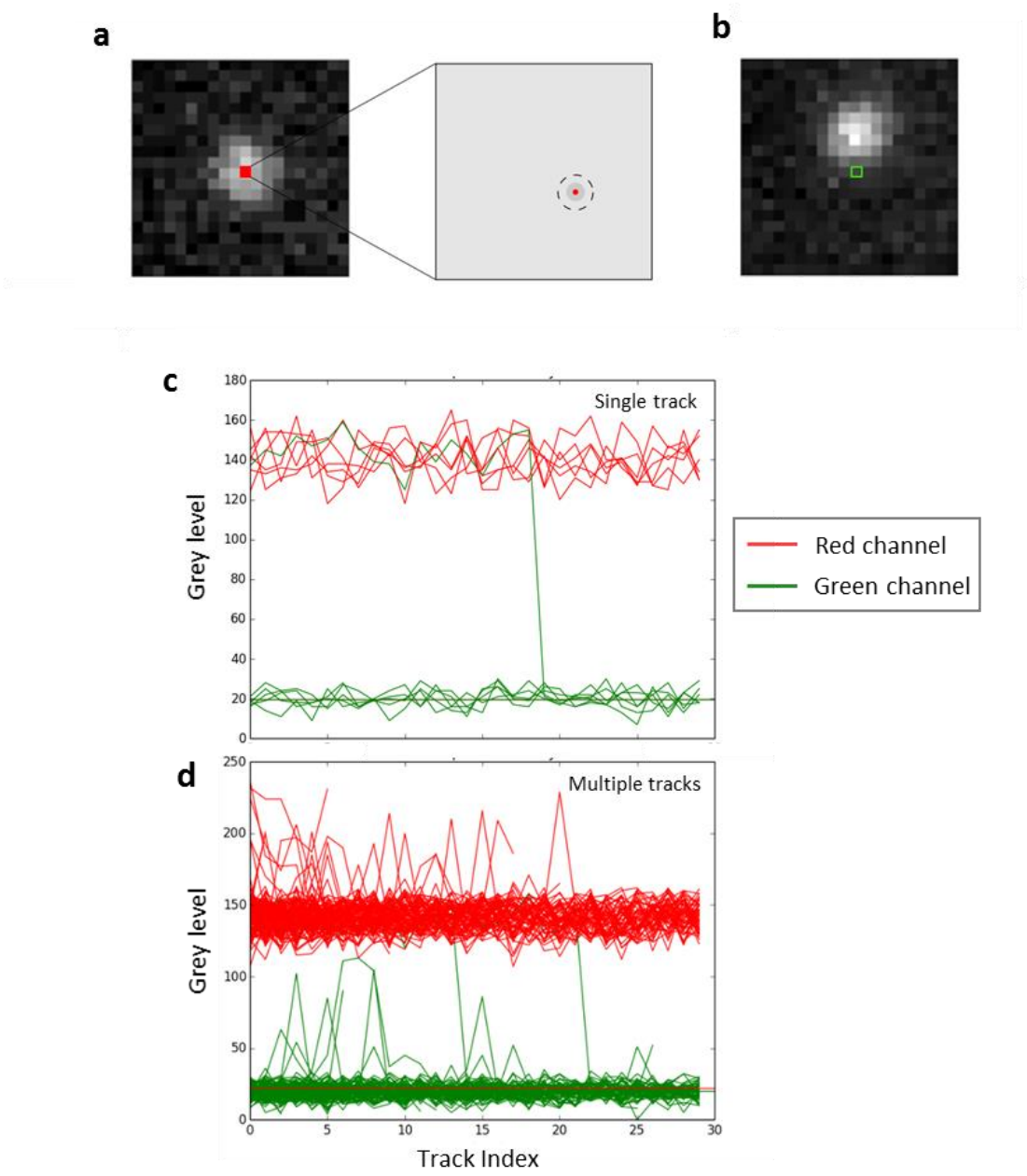

Figure 6.4 Utilizing pixel intensities to isolate basic splitting events.

Many tracking algorithms apply fitting procedures to determine the centroid of particles with sub-pixel precision (a). This allows for characterizing the pixel intensity in the opposing channel to isolate splitting events in particle trajectories (b). Applying this technique to an isolated track containing a single split event (c) makes the event relatively easy to identify. However, random crossing of red and green particles also gives rise to an intensity signal which is demonstrated by plotting of 84 trajectories in d. The three split events in this dataset are now more difficult to identify against the background of random colocalization (d).

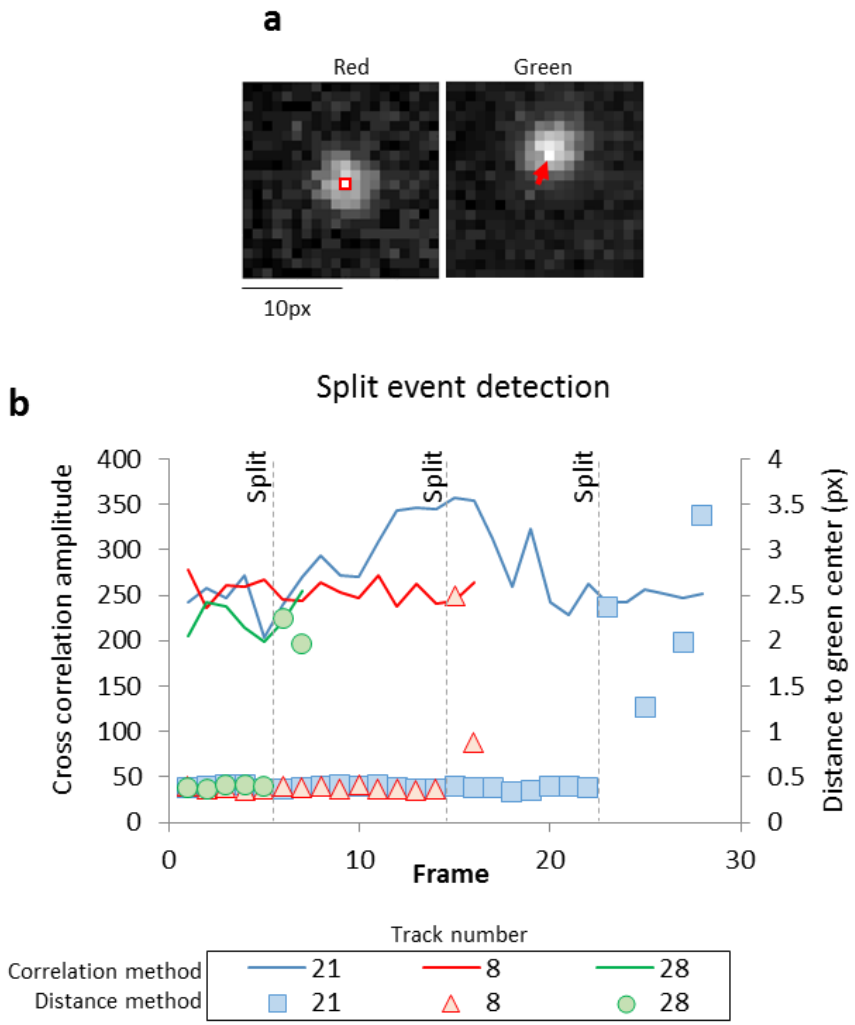

Figure 6.5 Utilizing object proximity over a temporal window as a means to isolate basic splitting events.

For each particle trajectory the distance to nearby green objects was determined using a Gaussian fitting procedure on a small window centred on the particle (a). Particles could then be characterized as fused if the distance to an object was < 0.6 px for at least 3 frames and splitting events were characterized when the distance to a nearby object was > 0.6 px for 3 frames or more. Applying this approach to simulated data, all three tracks containing split events could be easily identified with no errors (b, scatter plot). However, applying the TrIC method to these trajectories, it was not possible to discern the split events as the cross correlation amplitude did not show a large change (b, line plot).

following splitting and the interference of additional nearby particles.

6.2.2 Object recognition procedures

Automated object recognition is a large area of research with widespread applications pertaining to computer vision and artificial intelligence (Andreopoulos and Tsotsos, 2013). For the cell biologist a frequent problem is to perform image thresholding to transform an image into a binary object scene (Sankur, 2004). In live cells labelled cellular objects are commonly set against a highly variable background caused by non-discrete localization of reporter molecules in addition to autofluorescence which makes basic fixed value thresholding unsuitable to isolate individual objects. As an example, a HeLa cell stained with Rab7a-GFP and transferrin-Alexa568 and was subjected to value based thresholding which failed to isolate green objects with any integrity (Fig.6.6c). The morphology of compartments of the endomembrane system can also be highly variable taking the form of vesicles, tubules or membraneous stacks (Murk et al., 2003). Techniques which identify point-like structures such as Gaussian fitting procedures are therefore also unsuitable for use in a general method applicable to the study of a variety of cellular compartments.

A technique known as adaptive Gaussian thresholding (AGT) was therefore investigated as a means of identify primary objects which generates a binary image based on local image features (van der Walt et al., 2014; Wellner, 1993). The main difference with AGT compared to fixed value methods is that a different threshold is calculated for each pixel in the image providing more robustness against uneven image backgrounds. The method works by comparing each pixel with the average of nearby pixels. If the current pixel value is less than *t* percent of the average then it is recorded as black otherwise it is set to white. Here *t* is referred to as the mean offset and is set by the user along with the block size used for averaging. As an additional step the threshold value is determined after applying a Gaussian window to the block when calculating the weighted sum of neighbourhood values. The Gaussian filter with a sigma value defined by the user acts to improve object definition in noisy images during the thresholding step (Oberholzer et al., 1996). Due to the relative simplicity of the method, the binary image can be generated in a single pass, making AGT a fast technique to implement.

Applying AGT to the example image in Fig.6.6a – c, the technique effectively deals with the uneven background to generate a robust representation of primary objects in the green channel. In addition, the technique is not discriminatory against object shape and isolates irregular shaped objects as well as larger and smaller objects (Fig.6.6d). Determining the colocalization state of a particle now

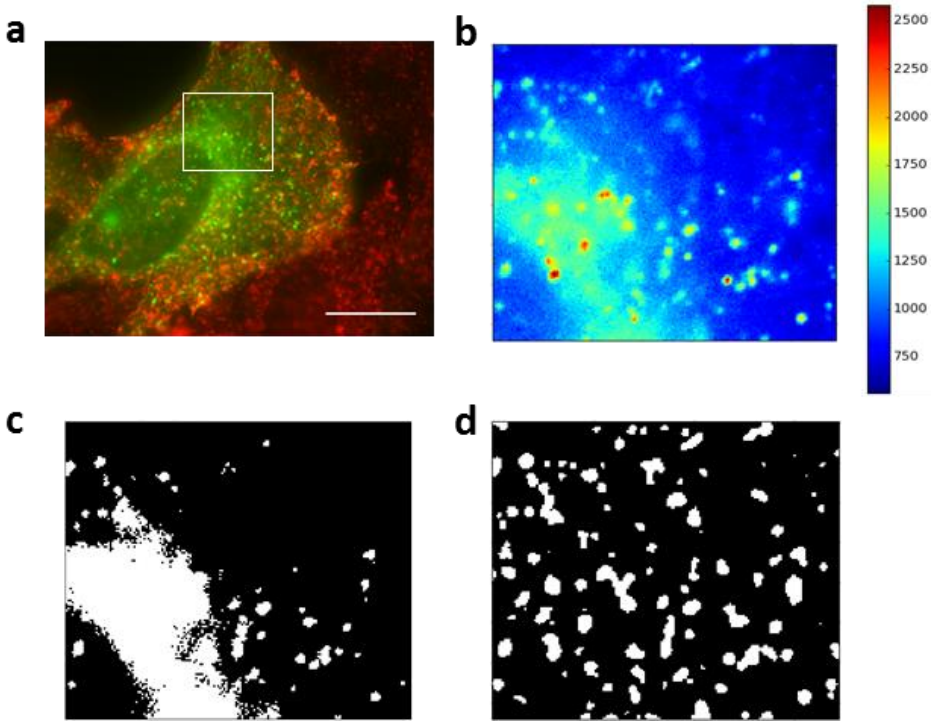

Figure 6.6 Isolation of primary objects using adaptive Gaussian thresholding.

To isolate cellular objects of interest, the green channel of a representative live-cell image (a, b) was subjected to value based (c) and adaptive Gaussian thresholding techniques (d). Owing to the uneven image background (b), value based thresholding proved unsuitable for isolating green objects (c). However, the adaptive threshold provided a more robust detection of cellular objects (d). Scale bar is 15 µm.

becomes trivial and can be defined when the particle centre falls within the bounds of a binary object. The ability to binarize the colocalization state of a particle using AGT paves the way for further techniques to discriminate genuine interaction events from random object colocalization.

6.2.3 Temporal filter implementation

From a brief review of previously described methods to isolate colocalization events in SPT experiments, the best performing method for a simple simulated data sequence relied on spatial proximity over a temporal window to characterize colocalization events (Fig.6.5). The idea of requiring a temporal constraint has been raised by various studies to isolate colocalization events (Dunne et al., 2009; Koyama-Honda et al., 2005; Lachmanovich et al., 2003; Varela et al., 2014), although differences arise in determining the spatial constraint, and no studies have utilized this method to isolate the fuse and split stages of interaction events.

As discussed, the spatial constraint of the filter is determined using AGT and a particle is considered colocalized if its centre falls within the bounds of a binary object. Utilizing this method over an absolute distance to the centroid of an object has the advantage of being insensitive to object size or morphology and so may be applicable to the study of a wider range of cellular compartments. Additionally, utilizing a threshold image as a spatial map is also generally faster computationally when compared to methods which calculate object centroids. The main disadvantage lies in the accuracy of object boundary detection which is determined by the image resolution and level of noise. Further methods in the literature have been described which provide sub pixel object boundaries although these were not further investigated due to the additional computational running cost associated with these methods (Oakley and Shann, 1991; Ruusuvuori et al., 2010).

Focusing on the temporal aspect of the filter, a free particle which undergoes a fusion event with a cellular object may be considered as fused after the particle remains colocalized with the object for a fixed length of time. Likewise, separation of the particle from the object for a further time period distinguishes a splitting event. This gives rise to the concept of a ‘fuse-length’ and a ‘split-length’ which are defined in frames and constitute the temporal threshold for characterizing these events (Fig.6.7). These user defined parameters may take on different values to enable a varying level of sensitivity to be allocated for each event type.

An efficient implementation of this algorithm was devised as follows.

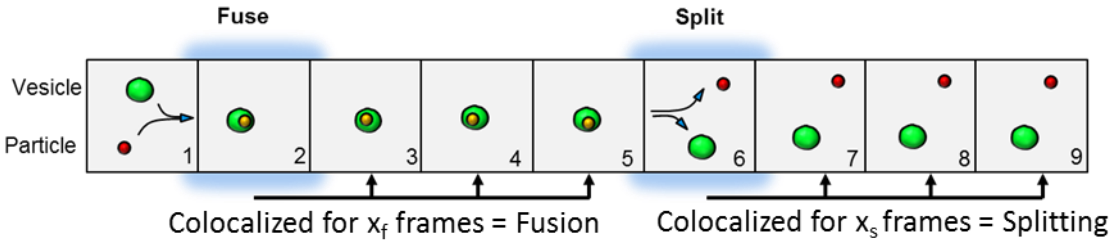

Figure 6.7 Overview of the temporal filter for isolation of fusion and splitting events.

Fusion events are characterized when a red particle and green object remain colocalized for a defined number of frames given by the fuse length x_f. Likewise once an object and particle are characterized as fused, a split event is identified when loss of colocalization occurs for a further number of frames defined by the split length, x_s.

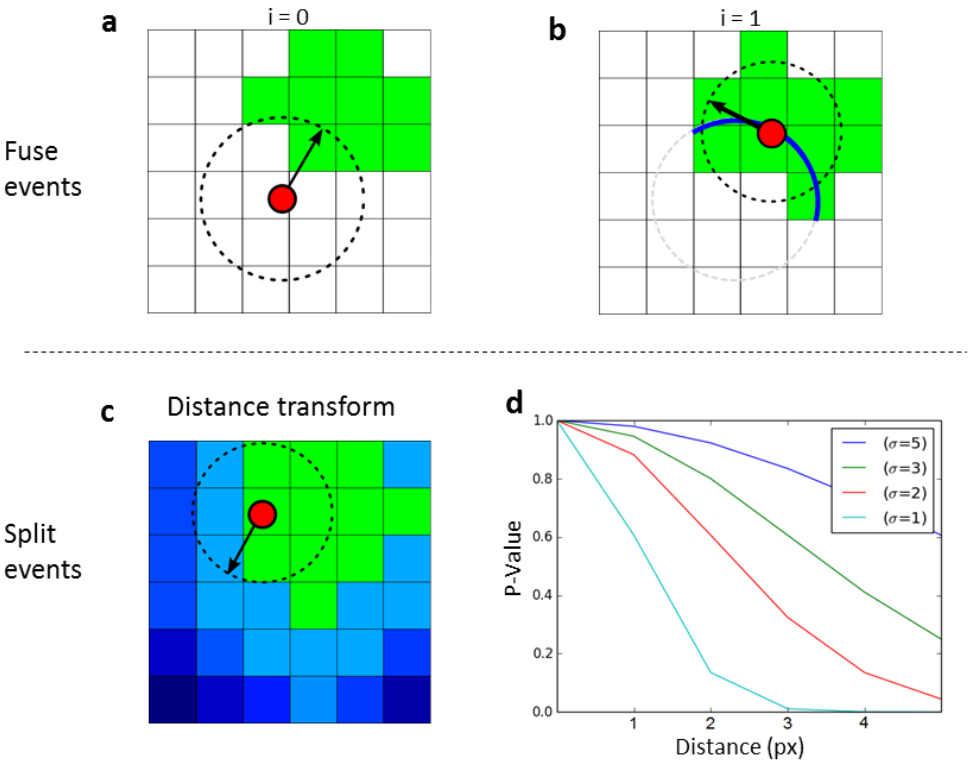

Figure 6.8 Overview of the spatial filter for fusion and splitting event detection.

To identify fusion events, the direction of particle displacement is considered to be entirely random which allows the list of potential positions that the particle could occupy in the following frame to be traced using a circle with radius equivalent to the particle displacement (a). The probability of the particle colocalizing with a green object can then be found as the relative length of the arc which intersects binary object pixels in the following frame, illustrated with a blue arc in (b). This process is repeated for each particle step to generate a cumulative probability of fusion (b). Splitting events are identified by analysing the relative distance of a particle to a green object (c, d). The distance of a particle to a green object is determined by a distance transform of the binary object image (c). The likelihood for the distance parameter to take on the observed value is then modelled using a normal probability density function with a user defined standard deviation (d). Repeating this process allows a cumulative probability of splitting to be calculated.

1. Particle centres are first localized to pixel coordinates using the fitting procedures available in most particle tracking software.
2. Cellular objects are then found using the adaptive Gaussian thresholding technique as discussed above to generate a binary representation of objects which allows for stretches in trajectories which fall within the bounds of objects to be defined as colocalized. Array lookup's in this manner are generally fast for in-memory operations.
3. Each track may then be divided into 'blocks' of colocalization and processed with the presumption that at the first frame in the track, at trajectory index = 0, particles are not fused with cellular objects.
4. Processing of a track begins by a search for blocks of colocalization which allows for skipping of non-colocalized blocks and tracks saving processing time. Once a colocalization block is found the length of the block is tested against the fuse-length parameter defined by the user. If the block length meets the threshold then a fusion event is defined occurring in the initial frame of the block (Fig.6.7).
5. Having established object fusion the search for a splitting event now begins in a similar manner. The search continues until a non-colocalized block is found with a length exceeding the split-length provided by the user (Fig.6.7).
6. The program flow returns to point 4.

Once colocalization states have been determined through identification of particle and object locations the problem of identifying interaction events becomes purely time-dependent. For this reason this method is referred to as a temporal filter, and for illustration an overview of the algorithm is depicted in Fig.6.7.

To test the performance of the algorithm, simulated data was generated which aimed to model conditions that are frequently found within a cellular context in SPT experiments. Employing particle simulations also allowed for a straightforward investigation into the false positive and event detection rates of this algorithm. These rates are critical in determining the utility of the algorithm although can be challenging to estimate objectively in live cells. Simulations employed here primarily allowed for precise control over parameters such as object sizes, velocity of components, number of fusion and splitting events, complete particle histories and the ability to adjust signal to noise ratios.

As such, a particle simulation was employed to initially investigate the false positive rate of detection as a function of binary object size. For a detailed description of the particle simulation software which was developed as part of this work, please refer to materials and methods. Each particle simulation consisted of a 250 x 250 pixel (px) window with 100 red particles and 200 green objects, and was run

for 100 frames. Each red particle underwent random movement with a maximum velocity of 5 px per frame (px/f). Green objects were added to the scene to model endosomes and were also assigned a maximum displacement velocity of 5 px. Separate simulations were run to generate object scenes with relative object radii of 2 to 5 px per object. Ten sequences were generated for each condition and the SNR ratio was set to 20 to simulate a high quality dataset. The probability of interaction between a particle and an endosome was set to zero ensuring no genuine interactions between components which allowed for an estimation of the false event detection rate. Complete particle trajectories were also recorded during the simulation which removed uncertainty associated with utilizing particle tracking algorithms and allowed an objective analysis of temporal filter performance. For an in depth description of the simulation software please refer to material and methods.

The simulated time-lapse and both sets of trajectories were then analysed using the temporal filter with the fuse length and split length arbitrarily set to 3 frames (Fig.6.9b, c). As no genuine interaction events occurred during the time-lapse all identified events could be characterized as false positives. As a control, tracks were not processed using a filtering technique. Instead, for the control condition, all changes in colocalization status were regarded as true events, which was equivalent to setting the fuse length and split length to zero (Fig.6.9b, labelled as 'None', for no filter). Taking this condition as baseline allowed for the rate of false positive event detection to be quantified in Fig.6.9c. Analysis of the dataset using the temporal filter revealed that the algorithm performed best at the lowest object size with a low level of spurious event detection for either event types. This stemmed from the low probability associated with two randomly moving small objects to remain colocalized for at least 3 frames. However, increasing the object size lead to a large increase in the false positive rate with objects of relative radius of 5 px giving a false rate of around 8 % for fuse and split events (Fig.6.9b). This could be expected given the increased chance of remaining coincident for 3 frames with a larger object size. This observation may also be reiterated for objects and particles with lower displacement velocities which would tend to pass over one another more slowly.

Estimation of the false negative rate is more challenging as the total number of identified events is comprised of true events mixed together with false positives. In ordered to estimate the event detection rate an identical simulation was run with the probability of fusion and splitting adjusted to 0.2. In this context, red particles which underwent random colocalization with a green object now gained a 20 % chance of fusing with that green object, where the red particle is confined within the bounds of the green object for a minimum of three 3 frames. After this arbitrary period of 3 frames, red particles then gained a 20 % chance every frame of ending the interaction and undergoing a

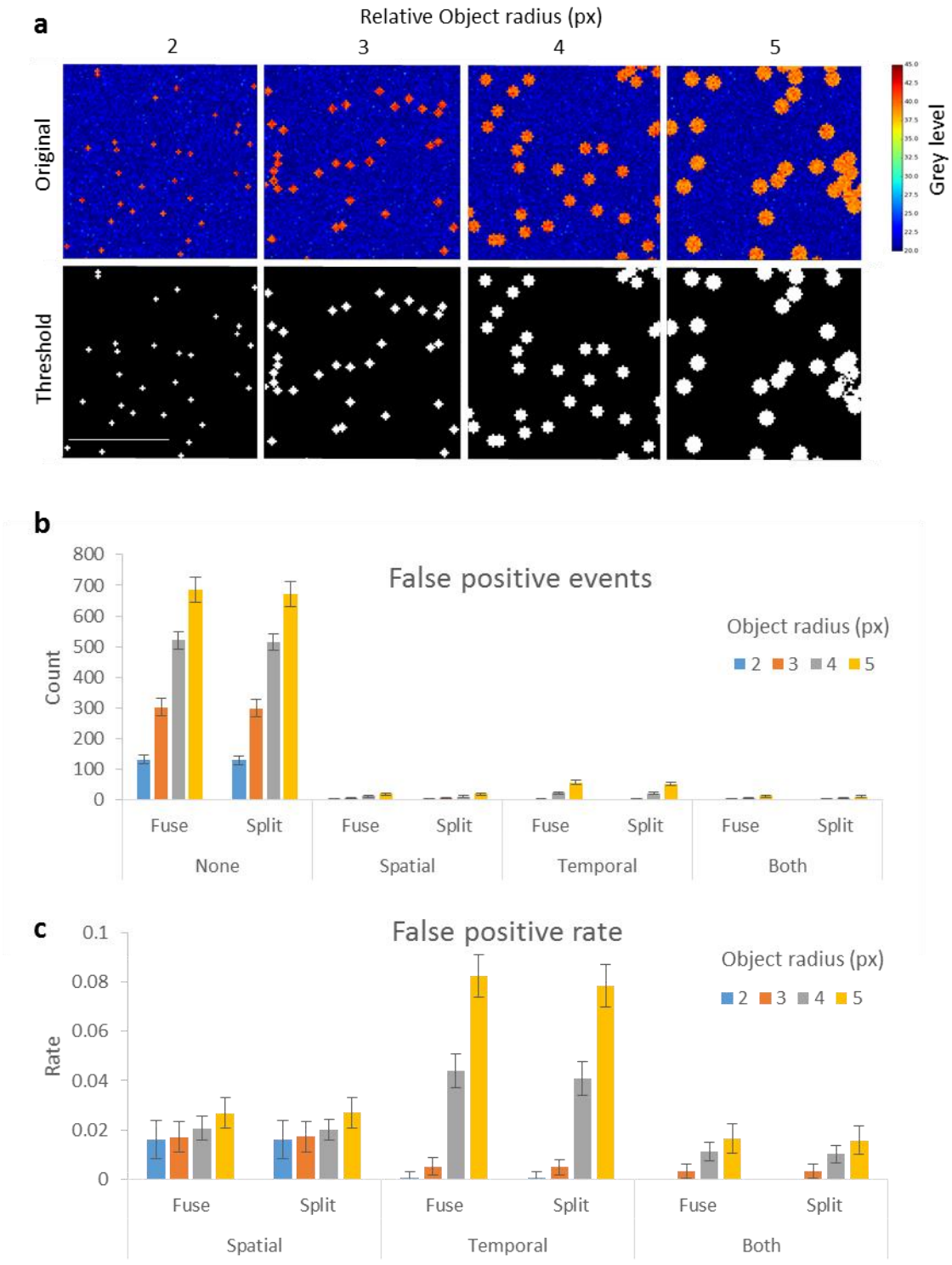

Figure 6.9 Quantifying filter performance in a false positive simulation.

A simulation was run consisting of randomly moving green objects of variable sizes from relative radius of 2 to 5 px, in addition to point like particles for 100 frames (a). A zero probability of fusion was attributed to all particles in ordered to test the false positive event detection rate of the filters alone or in combination (b, c). In the absence of a filter listed as None in b, every change in colocalization status was regarded as an event. Taking the None value as baseline allowed for a rate of false positive event detection to be calculated (c). Scale bar is 50 px.

splitting event. The number of interaction events was then quantified using the temporal filter using the same parameters defined above and compared to the actual number of events determined during the simulation (Fig.6.10a, b). Here, the number of events identified using the temporal filter provided a good reflection of the actual number of events for all object sizes despite the variable level of false positive detection which suggested the accuracy of the method is degraded with object size.

Taken together, these data indicate that although the filter performs well when object sizes are minimal, the high false positive rate with larger objects diminishes the quality of analysis. This is principally due to the simplistic nature of the filter which had no power to encode information such as particle velocity or object size in discriminating interaction events. As such further methods for event detection were explored which exploit dynamic information to discern interaction events.

6.2.4 Spatial filter development

A variety of techniques have been proposed to hunt for interaction events in particle trajectories as discussed above although no methods have been developed which utilize dynamic information form a single channel to identify interaction events (Deschout et al., 2013; Dunne et al., 2009; Dupont et al., 2013; Koyama-Honda et al., 2005; Lachmanovich et al., 2003; Rink et al., 2005; Varela et al., 2014; Vercauteren et al., 2011a). The method proposed by Deschout et al., utilizes particle tracking of both channels to correlate object movement which encodes spatial and temporal information although with the added complexity of requiring both sets of objects to be tracked and analysed (Deschout et al., 2013). Here a method is proposed which attempts to utilize spatial information to define a measure of object interaction with particle trajectories taken from a single channel which may allow for a simplification of analysis. Additionally this may also allow the analysis to be combined with the output from the temporal filter discussed above which may permit a further suppression of the false positive detection rate.

The initial assumption of the algorithm is that the direction of particle displacement is purely random, as is the case of simple Brownian motion. To illustrate, consider a particle moving from track index i = 0 to i = 1. If the direction of the particle in this step is considered arbitrary then the particle has an equal chance of moving with the observed displacement in all directions, and the list of potential locations of the particle at i = 1 could be traced with a circle centred on the coordinates of the particle at i = 0 (Fig.6.8a, b). The probability of the particle moving with the observed displacement and direction to land at its new pixel location in i = 1 can now be reduced to a geometric problem defined

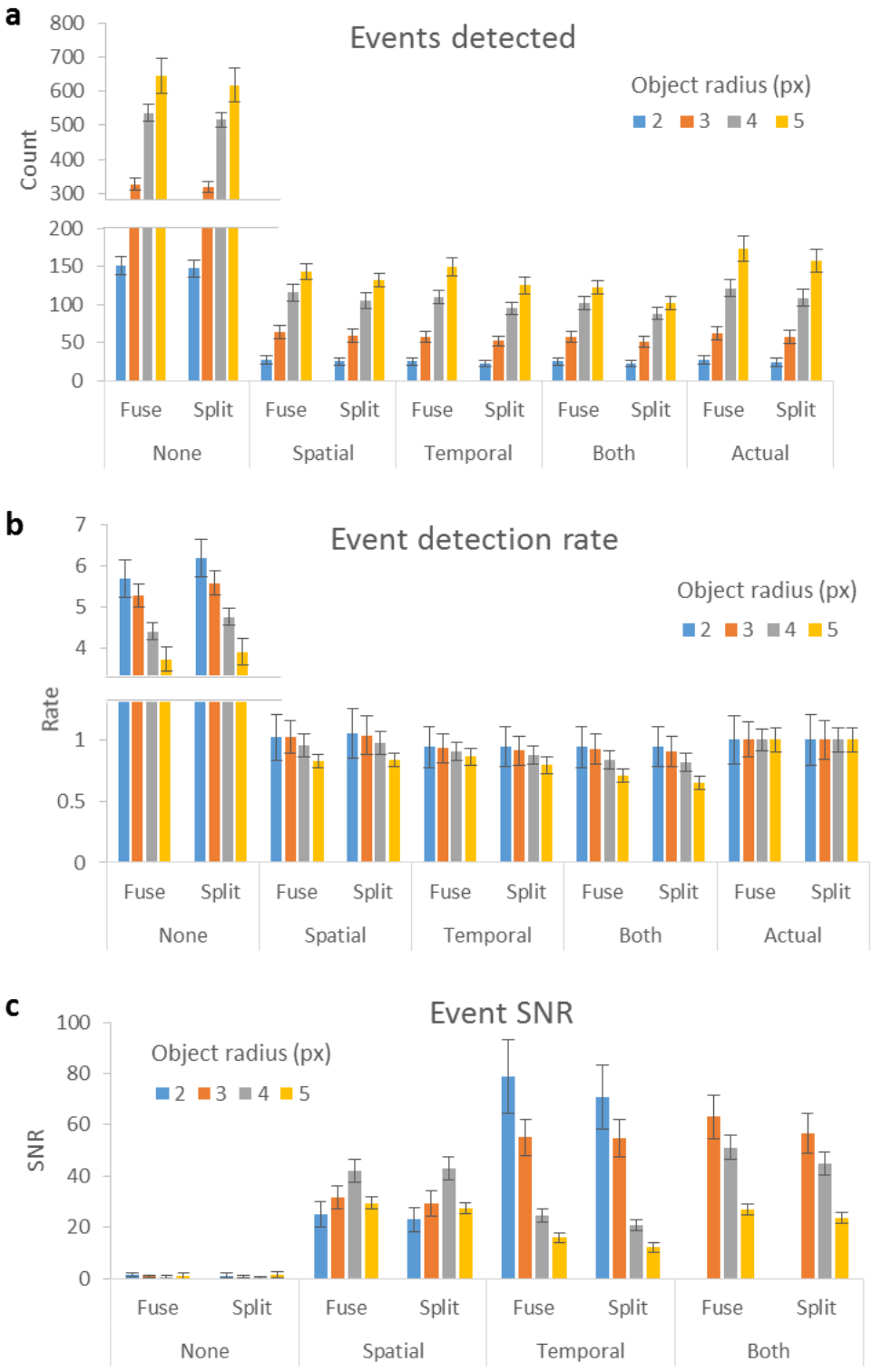

Figure 6.10 Quantification of the event detection rate of filters in a particle simulation.

A simulation was run consisting of randomly moving red particles and green objects of variable radii for 100 frames (a - c). Particles had a 20 % chance of undergoing fusion and splitting events. The total number of events was characterized using different filter arrangements given in a, and the rate of event detection relative to the actual number of events was calculated in b. Calculating the false positive rate and the rate of event detection also allowed an estimation of the SNR of the various filters (c).

as the length of the arc which falls within the destination pixel divided by the circumference of the circle (Fig.6.8a, b).

Adding an additional channel to the analysis which contains a binary representation of objects, it now becomes possible to define a model for observing fusion events in particle trajectories. Continuing with the example, the probability of landing within the bounds of an object in the opposing channel can now be determined by finding the relative length of the arc which coincides with this binary object (Fig.6.8b). Repeating this process for every displacement in the trajectory generates a probability of the particle landing within a binary object at every frame. A fusion event can then be defined when the cumulative probability, termed the fusion p-value, falls below a threshold set by the user. For example a fusion p-value of 0.02 implies random movement would account for the observed localization in 2 % of trials in the context of this model.

Once a particle has been characterized as fused with a cellular object, the direction of particle displacement now becomes irrelevant as it will be confined to the bounds of the cellular object as long as the interaction remains. Therefore an alternative method was employed to isolate splitting events which relied simply on the distance of the particle from the bounds of an object (Fig.6.8c, d).

Observing a particle which has been classified as fused external to a binary object is a good indication of splitting if the distance involve is large, although a split event may be less certain if the particle lies in very close proximity to the object which may be a result of imprecise object boundary detection. Therefore the distance of a particle to the bounds of a cellular object may be used to model the likelihood of splitting via the use of a probability density function (PDF). Here, the PDF is a function which describes the relative likelihood for the distance variable to take on an observed value in the absence of a split event (Fig.6.8d).

For practicality, the PDF of a truncated normal distribution $\frac{1}{\sqrt{2\pi}\sigma}e^{-\frac{(x-\mu)^2}{2\sigma^2}}$ was chosen to model the probability of splitting as a function of distance to a binary object, with mean μ = 0 and variance σ^2 chosen by the user. The distribution is truncated at zero so that the distance variable is restricted to only positive values (Fig.6.8d), with the variance describing the broadness of the distribution. The range of the density function is the interval $\left(0, \frac{1}{\sqrt{2\pi}\sigma}\right]$ with the maximum y -value $\frac{1}{\sqrt{2\pi}\sigma}$ set to 1 which provides an intuitive representation of distance with chance of splitting. The variance of the distribution in this model can be roughly interpreted as the confidence ascribed to object boundary detection. For example, robust object detection would be better modelled by a low σ^2 so that pixel locations even nearby an object would be ascribed a low probability of occurring by chance. Likewise, high levels of image noise might lead to a lower confidence in object detection and one might choose

a higher σ^2 value so that a particle mistakenly determined external to the bounds of an object may be ascribed a higher probability of occurring by chance.

The probability of splitting for each step in a trajectory may now be calculated according to this model and a split event can be characterized in the same way as during fusion, occurring when the cumulative probability falls below a user defined threshold, termed the split p-value. Due to the procedure relying primarily on the spatial relationship between particles and objects this method is referred to as spatial filtering.

An implementation of this algorithm is discussed below:

1. The same initial processing steps described above for temporal filtering are applied as detailed in points 1 – 3, which has the added benefit of only being performed once when both filters are used.
2. Focusing on fusion events, the method requires that the probability of fusion is determined for each particle step. This is achieved by finding the relative length of the displacement arc which overlaps a binary objects. However this is not a trivial problem primarily because particle positions and displacements are known with sub pixel accuracy and multiple objects may overlap the displacement arc at one time. The general concept is to generate a list of potential positions along the displacement arc which a particle may inhabit in the following frame. The problem is then solved by 'walking around' the perimeter positions and tallying the number which fall within a binary object pixel. Sampling along this perimeter is achieved in a linear fashion and the density of sampling is calculated according to density * circumference, where density is a user parameter set to 10 by default.
3. Fusion events are characterized when the cumulative probability of fusion falls below the fusion p-value threshold defined by the user. Once fusion has been established the search for a split event then begins.
4. The distance to the nearest binary object of a particle is determined by performing a distance transform of the binary object image.
5. The probability of splitting is determined by the use of a normal PDF, where the distance variable is formulated in terms of the relative likelihood of occurring by chance alone.
6. Splitting events can then be determined when the cumulative probability falls below the split p-value.
7. The program flow is then returned to point 2.

To assess the performance of the spatial filter, the simulated data discussed above for analysis of the temporal filter was reanalysed for a direct comparison between the two filters. Spatial filter parameters were chosen arbitrarily with the fuse p-value = 0.05, split p-value = 0.05 and variance = 1. Analysis of the data revealed a very different performance relationship with respect to object size when compared with the temporal filter (Fig.6.9b, c). The spatial filter made more mistakes compared to the temporal filter with a smaller object size, although the false positive rate still remained under 2 % for fusion and splitting events at relative object radius = 2 px. This result can be explained due to the higher significance attributed to colocalization of a particle with a small object which is a general feature of the algorithm. Additionally, the maximum velocity of particles and green objects in the simulation was set at a relatively high rate of 5 px which would also would tend to predispose the spatial filter to attribute significance to colocalization events.

Interestingly for larger objects with relative radii of 4 or greater, the spatial filter outperformed the temporal method in terms of the number of false positive events detected, with the error rate staying below 3 % for radius = 5 px. The observation of a relatively constant error rate with respect to object size can be explained in terms of the algorithm attributing relatively lower significance to particles colocalized with larger objects as for each particle step there was a higher chance of remaining colocalized between frames.

To investigate the rate of event detection, simulated data used to assess the temporal filter was reanalysed using spatial filter parameters kept constant as above (Fig.6.10). Here the spatial filter performance differed only slightly to that of the temporal filter, with a slightly higher rate of detection for all object sizes. This was surprising considering that the two filters demonstrated differing abilities to discriminate false positive events across different object sizes (Fig.6.10), and suggested that the number of genuine events detected relative to the noise from false positive event detection was different for each filter.

To investigate this possibility, the SNR of each filter was calculated according to the formula SNR = μ_s / σ_{bg} where μ_s is the relative signal strength (above the background of false positives) and σ_{bg} is the standard deviation of the background, which in this case was the standard deviation of the false positive rate (Fig.6.10). Analysis of filters separately revealed that spatial filtering maintained a high signal to noise ratio of > 25 for all object sizes, whereas temporal filtering displayed a strong inverse relationship between SNR and increasing object size with the SNR dropping to around 14 for the largest object size. This occurred primarily as a result of the higher incidence of false positive events using this filter. Again, data analysed in the absence of a filter was taken as a control which exhibited

a negligible SNR further highlighting the need to employ filtering techniques to enrich event detection (Fig.6.10c).

These data revealed that the two filters have different strengths when discriminating false positive events with the temporal filter performing better with smaller objects and the spatial filter faring better with larger objects. This suggested that combining these filters may have a complementary effect on reducing the false positive rate which may allow for an improvement of the SNR of event detection.

6.2.5 Spatial-temporal filtering for improved event detection

As discussed previously a variety of methods have been proposed to isolate events in particle trajectories although combining different methods in order to improve the rate of event detection relative to the false positive rate of detection has so far not been explored. Suppression of the false positive rate is critical for the study of rare events in ordered to isolate a weak signal from the noise of erroneous event detection. At the same-time the rate of event detection must remain high in ordered to maximise the SNR.

A straight forward approach to combining filters is to pass the results of each filter through an 'AND gate' which implies that both filters have to agree for an event to be classified. Additionally this has the added benefit of being straightforward to implement in software. Additionally, as both filters rely on the same initial steps, these can be carried out only once (see steps 1-3 for spatial and temporal filters above) to avoid computational load.

In order to test the combination of filters, referred to here as the spatial-temporal filter setup (STF), the particle simulation data discussed above were analysed to characterize the rates of event detection and false positive event detection (Fig.6.9, 6.10). The same parameters were utilized for each of the filters discussed above with the fuse/split length of the temporal filter set to 3 and the fuse/split p-value and variance set to 0.05 and 1, respectively. Analysis of the false positive dataset revealed that the error rate was further reduced using the STF across all object sizes when compared to either filter alone, indicating that the individual filters tended to identify a different subset of false positive events (Fig.6.9b, c). The overall false positive rate for the STF remained below 2 % with 0 events detected for the smallest object size.

Analysis of the STF detection rate indicated a slightly lower rate when compared to either filter alone which was as expected given that events are drawn from only a subset from each filter (Fig.6.10a, b). The relatively low false positive rate and high levels of event detection using the STF was also

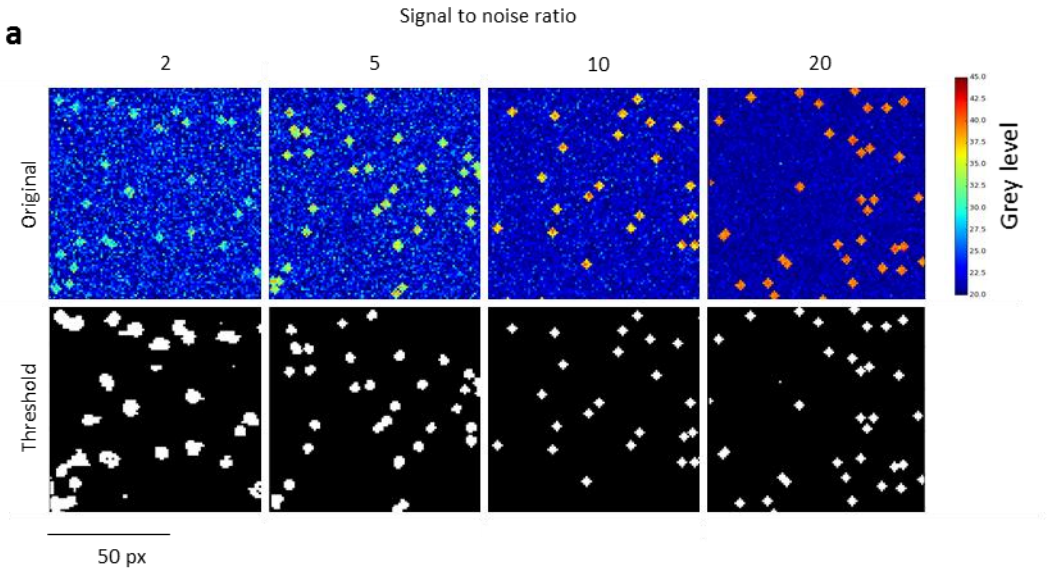

b

Signal to noise ratio

Detection Parameters	2	5	10	20
Initial Gaussian σ	2	1	0	0
Block size	30	30	30	30
Offset	0.99	1	6	6
σ	5	5	5	5

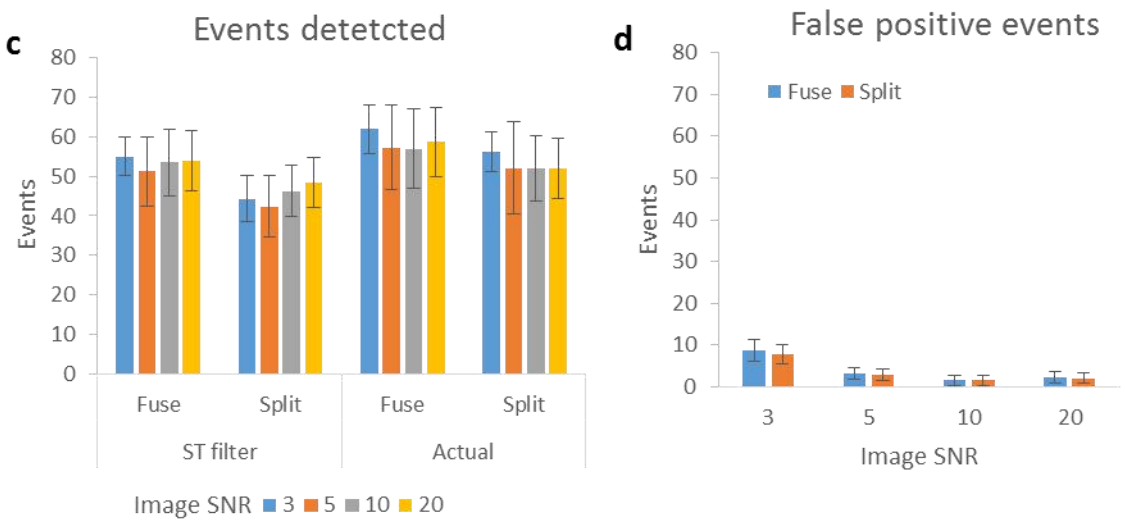

Figure 6.11 Spatial-Temporal filter event detection under different SNR offsets.

Particle simulations were run to generate movies with SNRs between 3 and 20 and relative object radii = 3 px allowing an estimation of the event detection rate and the false positive rate (a). The top panel of images (original) in a are auto scaled. Object thresholding (a) required an optimisation of detection parameters due to the variable SNR (b). Fusion and splitting events were then determined using the spatial-temporal filter (c, d), and compared with the actual number of events determined during simulation (c).

reflected in a high SNR of event detection (Fig.6.10c). The SNR at relative object radii = 2 px however could not be calculated as no false positive events were detected using the STF under these conditions. In fact, only the spatial filter at radii = 5 px offered a marginal improvement over the STF indicating that for the majority of object sizes the STF is superior to either filter alone in its power of event detection.

6.2.6 STF event detection as a function of image noise

Image noise is a frequent problem in live cell time lapse experiments which can be a barrier to effective image analysis. To test the robustness of the STF technique to variable image noise a further simulation was run with object sizes fixed at a relative radius = 3 px and a probability of fusion/splitting set at 0.2 (n = 10 simulations per condition). The noise level was then adjusted by adding Poisson noise to both channels to give SNRs between 3 and 20 (Fig.6.11a). Before analysis using the STF, an optimisation of the detection parameters used for object thresholding was required in ordered to identify primary objects (Fig.6.11a, b). At the lowest SNR of 3, object recognition was somewhat corrupted with a general overestimation of object size, and a relatively uneven determination of object bounds. This appeared to result from the initial Gaussian processing step with $\sigma = 2$ (Fig.6.11b), although this step was necessary to provide any object recognition in this low SNR image set. At SNR of 5 and above recognition showed a good level of robustness with SNR 10 or higher essentially being faultless (Fig.6.11a).

To assess the performance of the STF, particle tracks and primary objects were analysed using the same parameters outlined above with fuse/split length = 3, fuse/split p-value = 0.05 and variance = 1. Surprisingly, analysis of the event detection rate revealed that the number of events identified did not deviate substantially with respect to SNR with mean values all falling within one standard deviation and a close approximation to the actual number of events which occurred during simulation (Fig.6.11c). To investigate the level of false positive events under these conditions, identical sets of simulations were run but with the fuse/split probability set to 0. Analysis using the STF indicated a low level of false positives for SNRs of 5 to 20, although at the lowest image SNR an increase was observed which appeared to stem directly from the issues surrounding the object recognition step (Fig.6.11d). Nevertheless, even at very low image SNRs the STF filter proved capable of returning a low false positive rate whilst maintaining a high level of event detection demonstrating the robustness of adaptive thresholding and the STF method to discriminate events in noisy images.

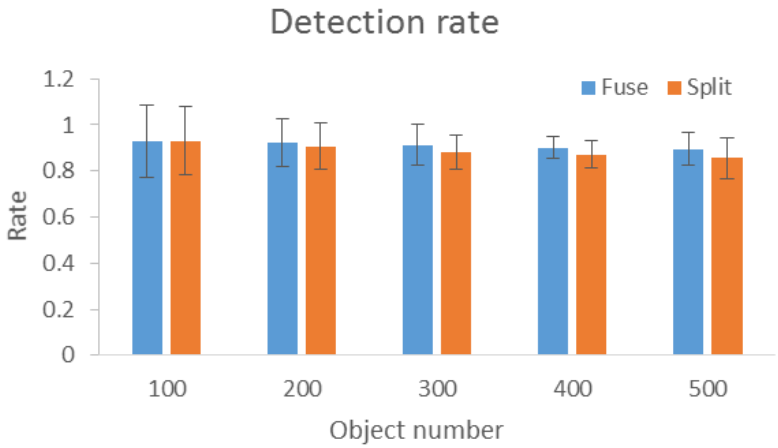

Figure 6.12 Event detection rate as a function of binary object density.

Particle simulations were run to assess filter event detection rate as a function of object density. Object densities between 100 and 500 per frame were generated and analysed using the spatial temporal filter.

6.2.7 STF detection rate as a function of object density

In live cell movies object density can vary greatly depending on the number and distribution of labelled compartments which may have unforeseen consequences on the performance of the STF. To test the STF detection rate with respect to object number, a simulation was run with object numbers ranging from 100 to 500 green objects per frame (radius = 3 px). The detection rate of the STF was then assessed (Fig.6.12) by comparing the number of events identified using the STF to the actual incidence of events during simulation (Supplementary Fig.6.2). Here analysis revealed that the detection rate was not greatly influenced by object density with the detection rate for fuse/split events around 0.91± 0.02 / 0.89 ±0.03 (SD), demonstrating that the STF method may also be applicable to the study of dense object scenes.

6.2.8 Object parentage tracking to characterize event modes

As discussed previously, the occurrence or loss of colocalization between a red and green object can arise through different modes depending on whether each object was visible in the adjacent frame. For example, recruitment of a green probe to a red labelled vesicle would be expected to result in the emergence of colocalization, where the green object would not have a parent object in the preceding frame. Distinguishing whether each object has a 'parent' or 'child' in the adjacent frame may therefore be a simple way to further classify fusion and splitting events, and may have some power to distinguish a true fusion process from instances of factor recruitment. The STF method relies on particle tracking algorithms to generate trajectories which can then be analysed alongside binary objects found by image thresholding. Thus particle trajectories for only one of the channels are determined during SPT requiring a further step to obtain object histories in the opposing channel.

A straightforward tracking method was employed which relied on determining the overlap of binary objects from one frame to the next which provided a simple means of testing if a particular binary object possessed a parent or child object in adjacent frames (Fig.6.13a). In the case of a fusion event identified using the STF, the binary object is queried for a parent in the frame previous to the occurrence of the event (i = -1 in Fig.6.13a), whereas a split event is tested for a child object by searching the in the subsequent frame (i = 1 in Fig.6.13a).

Employing such a simple method for object parent-child tracking has potentially a number of drawbacks. In particular the method has no power to distinguish one binary object from another and so errors may arise from interference due to nearby objects. Additionally, the sampling rate or frame rate here with respect to object velocity is crucial in ordered to ensure that every object maintains an

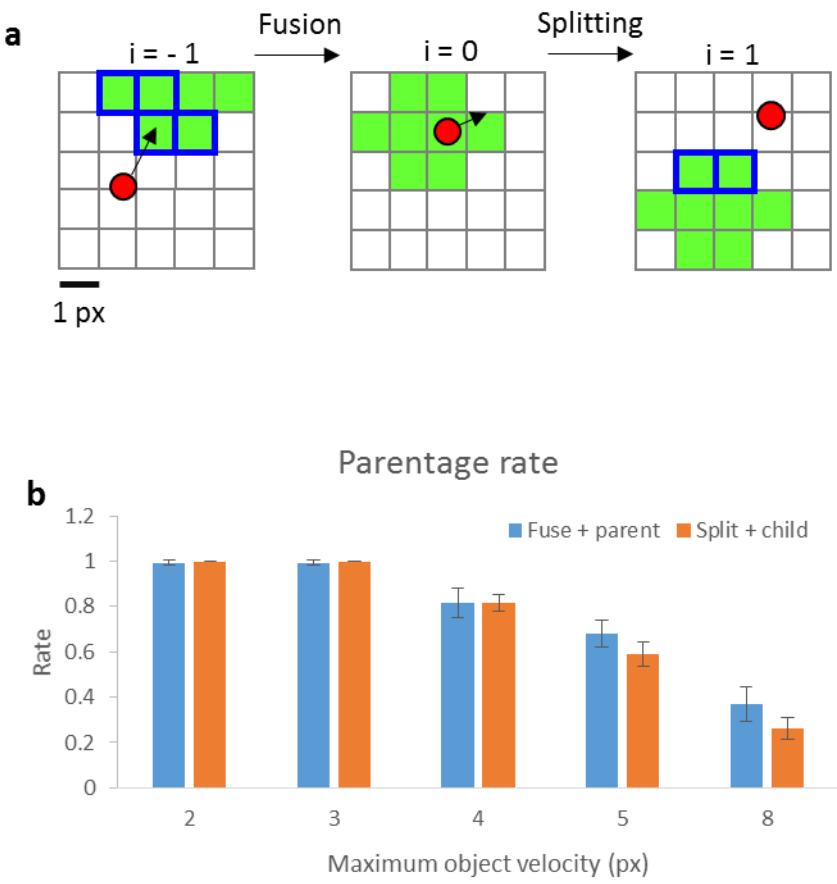

Figure 6.13 Assessment of object parent tracking as a function of object velocity.

Tracking of object parentage using an overlap method requires at least one pixel from the object to remain visible in consecutive frames (a). A green binary object at frame index i = 0 is considered to possess a parent if an overlapping green pixel is also found at i = -1, highlighted here in blue. Likewise the green object gives rise to a child object if an overlapping pixel is found at i = 1 (a). The performance of this method with respect to object velocity was tested using a simulation (b). As no objects disappear in the simulation all events are expected to possess parent/child objects. Total fusion and splitting events were then quantified using the STF and the relative number of events with parent objects was calculated.

overlap between frames. However, the advantage of this method is a low computational cost which was achieved through an efficient algorithm implementation as follows:

1. Firstly, only objects which undergo a colocalization or loss of colocalization event with a particle are analysed for parent/child partners in the adjacent frame which greatly reduces the number of objects to assess.
2. The list of green (in this example) pixel positions which comprise the colocalized object are then determined using a form of flood-fill algorithm which essentially 'walks' through pixels surrounding the particle to create a set of pixel coordinates.
3. Each pixel in the set is then checked against the previous frame to the fusion event (frame index i – 1), or the subsequent frame for a splitting event (i + 1).
4. If any tested pixel value is equivalent to 1 then the object is determined to possess a parent/child and the search ends.

To perform a basic test of this method a simulation was run with relative object radius = 3 px and a fusion/splitting probability of 0.2. To investigate how object velocity affected the rate of object parent/child detection the maximum object velocity was varied between 2 and 8 px/frame before analysis using the STF and parentage method described here. As none of the objects in the simulation disappeared, all events were expected to possess a parent or child object (Fig.6.13b). At maximum object velocities which were equal to or lower than the relative object radius, the method performed well with essentially all fusion/split events correctly identified as possessing parent/child objects (Fig.6.13b, Supplementary Fig.6.3). However increasing the velocity further lead to a decrease in the number of parent/child objects identified which was expected given that increasing the maximum object velocity per frame essentially leads to a higher proportion of objects which move with a displacement greater than the object radius resulting in a failure of the method.

Although this simulation is simplistic in nature and fails to reproduce much of the complexity found in live cells, these data suggest that under certain conditions with an adequate sampling rate this method of characterising the parentage of fusion split events may provide further insights into the mode of interaction. However, a concern is that the low SNR found in live cells may introduce a further source of error using this approach, although further detailed studies in live cells will be needed to address this question.

6.2.9 Application of the STF method to a live cell time-lapse

Though simulations allow for a straightforward assessment of various performance metrics associated with the STF method, trajectories from live cells provides much additional complexity which is difficult

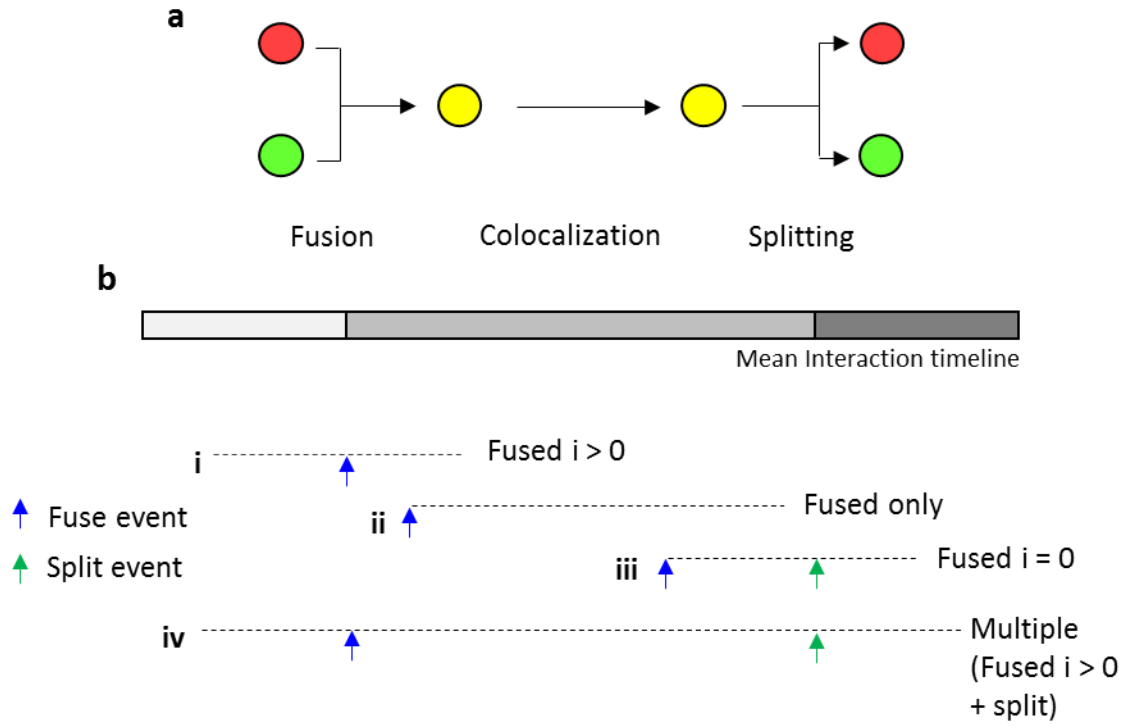

Figure 6.14 Characterizing interaction events in partial trajectories.

The entire lifetime of an interaction between a red and green object may be broken into three general phases termed the fusion, colocalization and splitting phases (a). However, in live-cells the entire interaction is rarely sampled leading to many shorter 'reads' of the mean interaction (b). A track sampling the fusion phase would comprise of a particle which undergoes a fusion event at track index > 0, where an isolated particle merges with an object (b i). In the colocalization phase, the two components remain coincident for the entire trajectory, although a fusion event must still be defined at track index = 0 to characterize the interaction (b ii). A track which captures only the splitting phase would be characterized as fused at track index = 0, with a split event occurring later in the track (b iii). Finally, multiple interactions may occur with a trajectory, in this example a fusion event at index > 0 and a split event both occur (b iv).

to reproduce in a simulation. For example, particles in a cell undergo active transport processes as well as diffusive motion and particles can be lost out of focus as a result of movement in the axial plane. Additionally, the morphology, distribution and dynamics of membranous compartments are often variable with objects regularly set against an uneven image background. A further issue concerns the acquisition of accurate particle trajectories which can often can often be challenging in live cells.

As discussed above, a common problem associated with many tracking algorithms is the occasional failure in the linking stage of the algorithm which leads to fragmentation of trajectories. Classifying interaction events in partial trajectories with the STF presents its own challenges depicted in Fig.6.14. For example, a particle undergoing a fusion event would be expected to occur at a track index > 0 as a non-colocalized particle and object merge. However, a trajectory which samples only the colocalization stage of interaction would still be characterized as fused by the STF but the event would be determined to occur at track index = 0, in the first frame of the trajectory. The STF simply identifies the binary state within a trajectory, switching between the 'fused' and 'split' condition. An important distinction in the STF method then is the track index at which an event is identified. Characterizing fusion events according to track index identifies a true fusion event which occurs at index > 0, from the initial condition of a particle at the start of the track at index = 0 (Fig.6.14b).

To investigate the use of the STF method in live cells, uptake of transferrin-Alexa 568 into Rab21-GFP vesicles was used as a model system to test the utility of the method. Previous studies indicate that Rab21 localizes to early endosomes and colocalizes with the transferrin receptor at an early stage in the endocytic pathway (Simpson et al., 2004). Here, a total of six HeLa cells were analysed with treatment consisting of a 5 min incubation with transferrin at 37^{o}C which was expected to confine the probe to early endosomes before washing and imaging for 2 mins (Fig.6.15a) (Simpson et al., 2004). Imaging resulted in the generation of 159 MB files with 118 frames. Particle tracking was performed on the Rab21 vesicular compartment using the MOSAIC software as described in materials and methods, which generated 963 ± 111 trajectories which exceeded 10 frames in length. The transferrin channel was then subjected to thresholding before analysis of the dataset using the STF to assess the level of interaction of Rab21 with respect to the transferrin compartment (Fig.6.15b, 6.16).

The STF method identified a large number of event types with an example of a splitting event given in Fig.6.15b. The analysis was performed a number of times using three sets of parameters from a relatively low stringency of fuse/split length = 3, fuse/split p-value = 0.05 (3 / 0.05), to a higher stringency with parameters of 5 / 0.002 for the length / p-values respectively, with the variance being fixed at $\sigma^2 = 1$ throughout. The reason for performing the analysis using different parameters was to

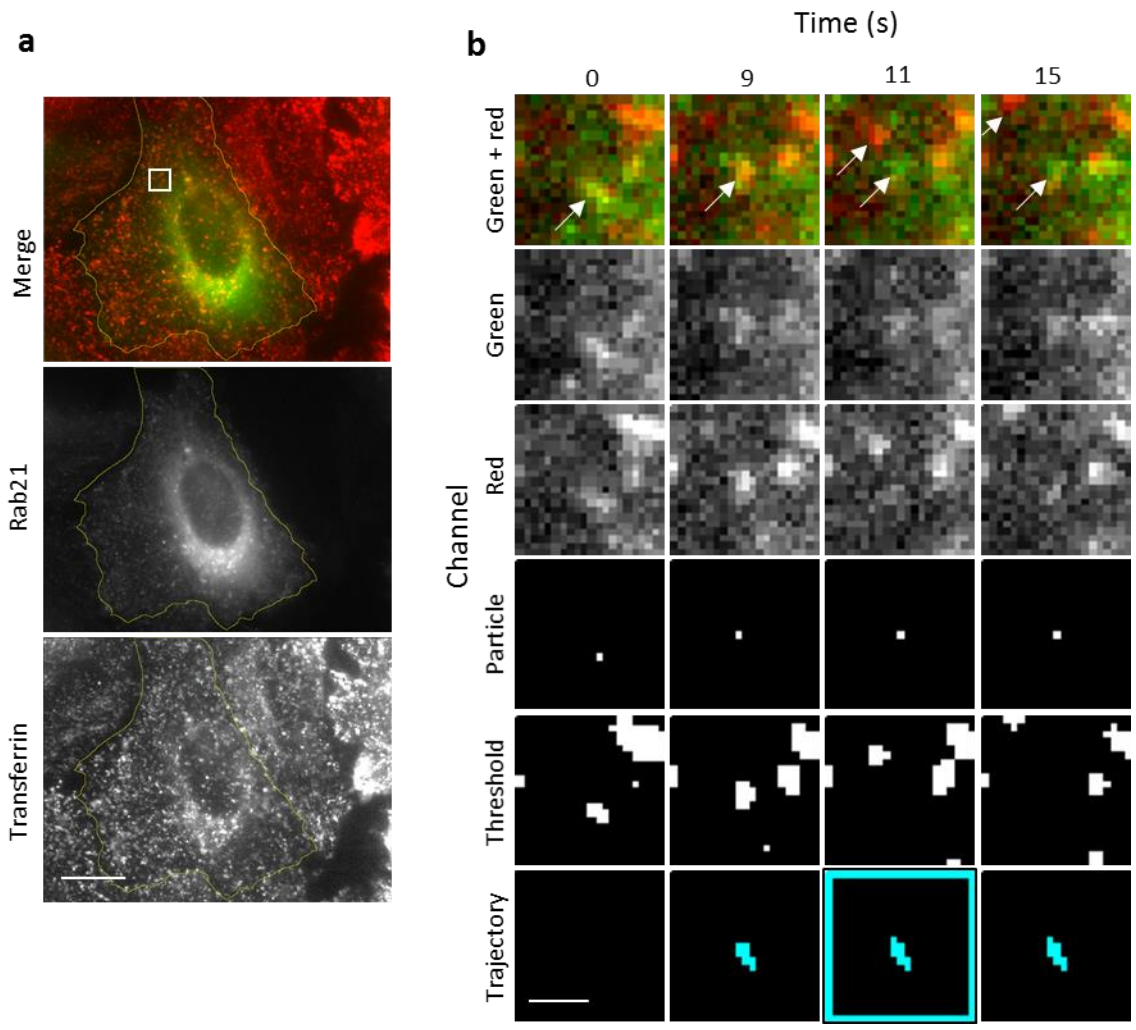

Figure 6.15 Application of spatial-temporal filtering in live cells.

Live HeLa cells transfected with rab 21-GFP were treated with transferrin-Alexa568 and imaged for 2 mins (a). The channels were then split with green rab 21 particles trajectories determined using particle tracking software. The remaining analysis was handled by the STF analysis software which first identifies primary objects through thresholding of the red channel before analysing objects and trajectories using the STF method. An example event identified using the STF is provided in b, showing a splitting event between a green rab 21 object and a red transferrin vesicle. The individual channels utilized during analysis are also provided illustrating the localization of the particle, and the thresholding step of the red channel to identify binary objects (b). Scale bars are 10 and 1 µm.

investigate the level of parameter bias associated with the method, with the concern being that the number of events identified may be heavily influenced by the choice of parameters.

However, parameter choice did not appear to have a large effect on the numbers of events identified, with the majority of mean values falling within a single standard deviation for each of the parameter inputs (Fig.6.16a). Only the numbers of split events/tracks identified showed a marked change with parameter choice which can be explained in terms of the total track length as the limiting factor for event identification. Put simply, a split event within a shorter track with length 11 frames for instance, may be less likely to be identified using more stringent parameters with fuse and split length of 5 frames. Overall, the relative consistency of event numbers suggested that the STF method was reasonably robust to parameter bias and that the events identified may be more likely to reflect a biological process within the cell rather than a particular set of input parameters.

Analysis revealed that around 67 % ± 3.4 (standard error of the mean for the different input parameter conditions) of Rab21 tracks exhibited an interaction with transferrin containing vesicles. Previous reports calculated that around 60 % of transferrin vesicles displayed colocalization with Rab21 after 4 mins uptake, although no data was given regarding the converse, or the number of Rab21 vesicles which showed colocalization with transferrin (Simpson et al., 2004).

6.2.10 Analysis of cellular trafficking dynamics

Interestingly, the analysis here suggested a highly dynamic relationship between the two components. Only 37.5 % ± 0.3 of Rab21 particles remained colocalized for the duration of the trajectory with around 26 % ± 2.6 of tracks undergoing a fusion event at index > 0 and 9 % ± 2.9 exhibiting a split event. Moreover the number of tracks with multiple events, defined as a track with a minimum of one fuse event at index > 0 in addition to a split event, was around 6.6 % ± 2.3 suggesting that the majority of split events originated from a dynamic population of Rab21 particles which underwent transient interactions with transferrin vesicles. The larger proportion of fusion events (index > 0) relative to split events tentatively suggested a net trafficking of transferrin to the Rab21 compartment. Additionally, the majority of fusion (i > 0) and splitting events also possessed a parent/child object suggesting that transferrin was transported to existing Rab21 structures. Subjectively, it was difficult to assess the net trafficking of material by eye due to the extremely large numbers of structures involved and the highly dynamic nature of the movie. However, the assessment that most events possessed a partner/child object did appear to be born out, although this result would need to be confirmed using additional methods. Indeed, a much more thorough analysis of the data will be needed to validate the findings of this investigation, preferably by employing an impartial observer to validate individual events by eye which would also allow for a characterization of the false positive rate of this method in live cells.

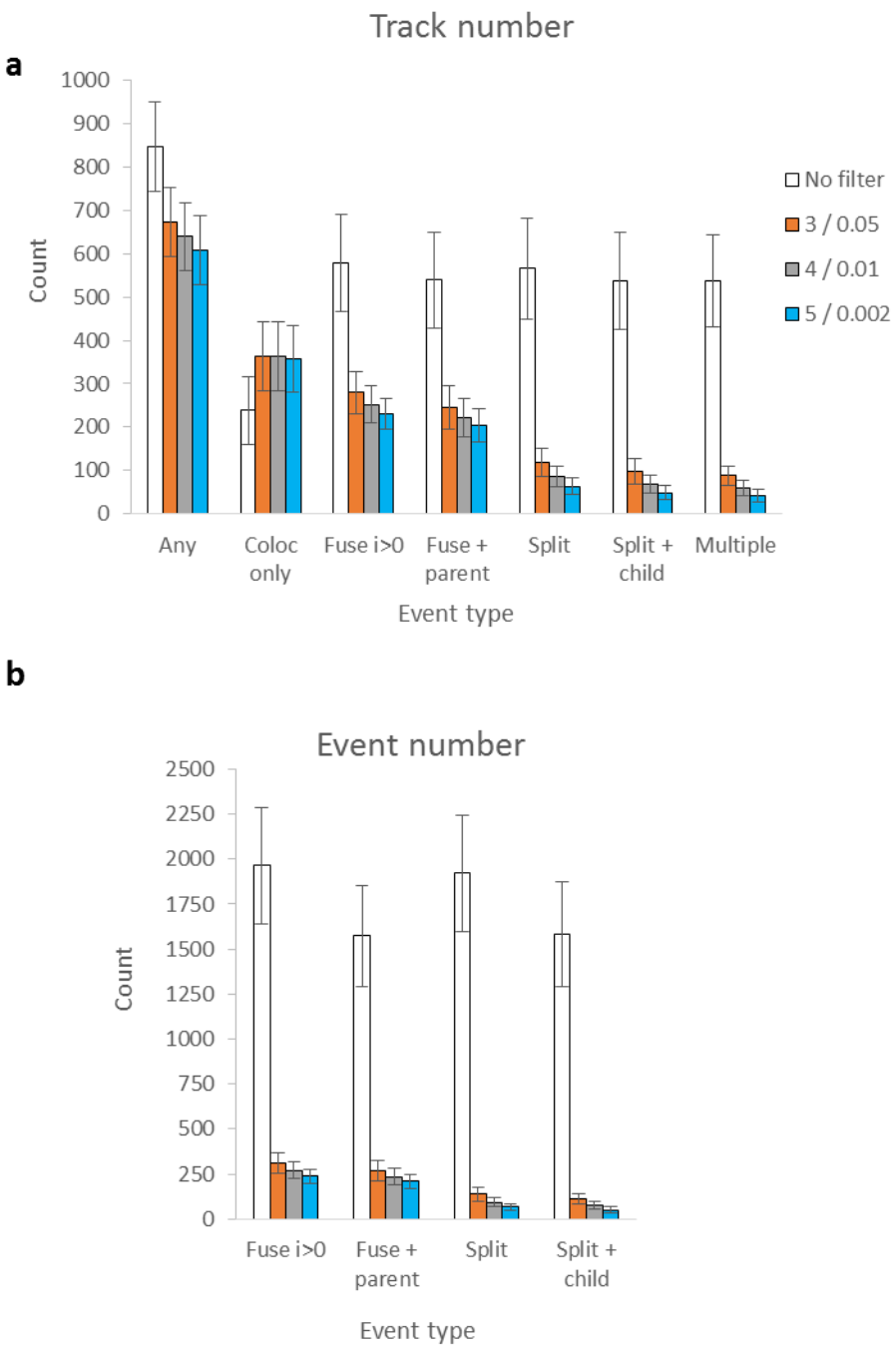

Figure 6.16 Quantification of rab 21 - transferrin dynamics by spatial-temporal filtering.

Tracking of rab 21 particles generated an average of 963 ±111 trajectories which exceeded 10 frames in length. Trajectories were then analysed using the STF with parameters of varying stringency (a – b). The fuse/split length was varied from 5 to 3 frames, and the fuse/split p-value from 0.002 to 0.05 with variance = 1. As a control, data wan analysed in the absence of filtering where every change in colocalization status was regarded as a genuine event. The number of tracks displaying an event were then quantified in a and the total number of events are given in b. Error bars represent the standard deviation.

The method discussed in this chapeter was written into a basic software package named 'Quacker' (Supplementary Methods 2). Benchmarking of Quacker revealed that acquisition of particle trajectories was the most time consuming step taking around 5 mins for the six cells. The remaining analysis consisting of the thresholding step combined with the STF analysis took around 45 s on a dual core Intel i3 4130 3.4 GHz processor although quad or octa-core systems provide substantial speedups due to the multiprocessing implementation of the method.

In conclusion, a novel method was developed for the automated identification of cellular interaction events at the single particle level in dual colour movies. Using particle simulations the method performed well with a low false positive rate which enabled a high level of event-signal to noise ratio to be achieved over a wide range of conditions. Application of a parentage/child object tracking method also enabled a simple means to classify interaction events with the aim of determining a mode of interaction. Investigation of the technique in a live cell model generated a tentative analysis which appeared to reflect certain characteristics of the interaction of two cellular compartments, although a more detailed analysis will be needed to corroborate these findings.

6.3 Discussion

Single particle tracking promises to address many problems in cell biology particularly in the understanding of dynamic processes such as the uptake of nanoformulations into cells. Quantifying cargo trafficking through the endomembrane system over time would be an especially valuable tool for drug development purposes although may be equally applicable for the study of cellular events. In ordered to isolate and study such processes methods are needed to separate genuine interactions in particle trajectories from random colocalization events which frequently occur in live movies due to the limited lateral and axial resolutions of many microscopes. In this report, a novel method was developed to analyses particle trajectories taken from dual colour movies with the specific aim of identifying and quantifying the stage at which a nanoparticle enters or exits a cellular compartment. The method was developed with a focus on nanoparticle trafficking, although in the brief example provided to demonstrate the method, transferrin and Rab21 interaction was analysed demonstrating the utility of the method for potentially studying a wider range of endogenous processes. However, due to the time constraints associated with this project, only a basic assessment of the method was performed.

Development of the method was based heavily on an initial evaluation of previous methods which analyse dual colour trajectories(Deschout et al., 2013; Rink et al., 2005; Vercauteren et al., 2011a). However many methods focus specifically on achieving more accurate measures of colocalization and

are not specifically focused towards studying the entire interaction process between two components (Koyama-Honda et al., 2005; Vercauteren et al., 2011a; Villalta et al., 2011). It was therefore necessary to define a straightforward model of cellular interactions which could serve as the basis for developing methods to pinpoint events.

The model simplified the overall interaction of two components to three stages, or the fusion, colocalization and splitting stages. The fusion stage establishes a particle and cellular object as 'fused', and would be expected to occur as a result of two nearby objects merging together to substantiate the interaction, whereas the splitting stage occurs by physical separation of the entities following a period of prolonged colocalization. This model was further elaborated in an attempt to account for factor recruitment, a potentially widespread cellular mechanism where individual reporter molecules are trafficked to a site of interest to establish colocalization (Rink et al., 2005). Recruitment in this way would not normally entail the observation of coloured components merging together as many single emitters, particularly fluorescent protein tags, are not normally bright enough to be visualized alone. Therefore factor recruitment would be expected in most cases to result in the emergence of colocalization with the recruited factor rising above the threshold for detection to constitute an object which appears coincident with the opposing label (Fig.6.1). The reverse case is applicable during the splitting stage of interaction where cellular processes such as sorting, degradation or trafficking may lead to the loss or disappearance of only one of the colocalized objects.

A major omission from this model is intra-compartment interactions which occur between objects in the same compartment. These types of interactions are also commonplace with the endosomal network being described structurally as a funnel, with the cell periphery containing many small early endosomes which progressively fuse homotypically and migrate towards the cell centre (Foret et al., 2012). The methodology developed here is from the outset not concerned with homotypic interactions and may therefore be best described as a system which identifies interactions at the interface of cellular compartments where the gain or loss of components identifies a particular stage in the endocytic pathway.

Here, the initial review of current methods used to identify events in particle tracks indicated that a temporal based method was the most performant for correctly identifying three splitting events in a simple simulated dataset (Fig.6.2, 6.6). The initial method identified fusion events by simply relying on the observation of colocalization which exceeded a temporal threshold. Here the method was expanded to allow temporal fuse and split lengths measured in frames to be defined by the user to permit a differing level of sensitivity to be set for each event type when determining the binary state of particle (Fig.6.7). The spatial constraint used for identification of colocalization was also modified,

and was determined through an adaptive thresholding technique with the option of additional Gaussian filtering for use in noisy time lapses (Fig.6.6).

Initial tests of the temporal filtering method using particle simulations indicated a good level of performance in terms of the low false positive rate and high event detection rate for small object sizes, although larger objects predictably degraded the performance of the method with an increase in the false positive rate (Fig.6.9, 6.10). This was expected due to the increased probability of a particle and object remaining colocalized with larger object sizes, and one would expect a similar problem with objects which move more slowly relative to one another.

The maintenance of colocalization for an extended timeframe is generally a good indicator of a genuine interaction although false positives can predominate with extremes of large or slow moving objects. The temporal threshold for event identification determined in seconds rather than frames can of course be increased in an attempt to improve detection, although it may not be possible to remove all false positives without at some point introducing a selection bias towards slower cellular processes (or indeed ones involving larger objects) at the expense of more rapid interactions. Additionally, achieving a suitable number of lengthier trajectories in live cells can be challenging particularly when imaging in 2D, and a further bias can be introduced as slower moving objects tend to dominate in longer particle trajectories. In fact a key challenge with single particle trajectory analysis is understanding a biological processes in terms of trajectory length and frequency distributions as many shorter trajectories are typically generated using tracking algorithms relative to longer tracks, and understanding how these distributions relate to a biological processes can be challenging. Ideally then, as many trajectories as possible should be retained for analysis in order to reflect the biological process in question.

To circumvent issues with the temporal filter, a novel method was devised termed the spatial filter which encoded spatial and dynamic information to obtain a probability score for interaction events (Fig.6.8). The filter identified fusion and splitting events by alternate means with fusion events requiring the particle velocity and local object density to be determined whereas the likelihood of splitting was modelled by the distance to the nearest object. For fusion event classification the filter was designed with the aim of penalising both slower moving particles and crossing of particles and larger objects which tended to be a major source of error when using the temporal filter. For a very slow particle crossing a cellular object, the majority of displacements would result in 100 % chance of remaining colocalized with the object and so a likelihood of fusion would only approach threshold after the particle undergoes multiple approaches with the object edge (Fig.6.8). This may reflect a logical means to test for fusion although noise in the bounds of object detection may also interfere

with this process. On the contrary, this filter was also expected to attribute more significance to interactions between faster moving particles and smaller objects due to the probability of a chance colocalization determined to be lower using this filter. Analysis using particle simulations largely confirmed these expectations with a relatively higher false positive rate with smaller objects and a lower rate for larger objects relative to the temporal filter (Fig.6.9). The false positive rate of the spatial filter remained surprisingly consistent across different object sizes which was an initial goal of the method, although the false positive rate as a function of object velocity remains to be investigated.

Splitting events using the spatial filter were determined by simply modelling the distance of a particle from the nearest binary object to a probability density function. The distance variable was calculated using a distance transform function which calculated the Euclidean distance for individual pixels. This aspect of the algorithm is thus not a sub-pixel technique which may present an issue for rapid frame rate applications. A clear future improvement to the technique would be to calculate the Euclidean distance to the particle centre and not the pixel centre in which the particle is localized which would be more accurate for smaller displacements.

The design of both filter sets ensured that they could be combined in a straightforward manner, where an interaction event is only classified when both filters agree. Combination of both filters using the STF setup was therefore investigated as a means of improving the analysis when compared to either filter alone. Analysis of the simulated dataset indeed appeared to confirm the superiority of the STF with a low false positive rate whilst maintaining a high level of detection under variable conditions of object size and density, and image noise (Fig.6.9 – 6.12). Future work might seek a more elaborate statistical framework to combine the filters rather than relying on a simple 'AND' gate, although the method provides a simple framework for the inclusion of additional filters.

Finally, simulated data was also used in a basic assessment of the object parentage tracking method which aimed to distinguish if parent or child objects where observable in frames surrounding an interaction event (Fig.6.13). An obvious concern with this method is that a higher relative velocity of objects would lead to a breakdown of the method which was demonstrated using a simulation with increasing object velocities (Fig.6.13). Nevertheless, at lower relative velocity, the technique performed well with simulated data, although image noise and the accuracy of object detection could also be expected to interfere with the accuracy of this method.

A brief analysis of the STF and parentage tracking method was investigated in a live cell model which involved the uptake of transferrin into Rab21 positive cellular structures. Uptake consisted of a brief 5 min pulse to confine transferrin to the early endosomal network before analysis with the STF using a variety of input parameters (Fig.6.15) (Simpson et al., 2004). Only a basic analysis was conducted

looking at the numbers of tracks which contained a particular event type, or the total numbers of events (Fig.6.16). The choice of input parameters did not have appear to have a large effect on the number of events or tracks identified for most event types suggesting a reasonably low level of parameter bias with the method (Fig.6.16). However for splitting events which occur most frequently in the distal portion of a trajectory, more stringent parameters did appear to result in a drop in the number of events identified which may be explained in terms of the track length as a limiting factor in event detection. For instance, the minimum track length was set at 10 frames in the experiment which would make identifying a splitting event in a track with length 11 frames somewhat unlikely with paramaters of 5/5 frames for the fuse and split lengths respectively.

The analysis did appear to echo certain characteristics of the time-lapse, and in particular the majority of fusion and splitting events which showed evidence of parentage was reflected in the results of the STF (Fig.6.16). However, the complexity of live-cell images is far beyond what can be achieved using simulated data, and so the relative rates of detection and the false positive rate will need to be determined using a more careful analysis. Nevertheless an advantage of this technique over manual methods is the objective nature of the technique in addition to its high-throughput. Extrapolating from the benchmark figure, this method could analyse on the order of 500 cells per hour which is considerably faster than a typical observer.

A further concern with the method is that live cell data may also be influenced by differences in the localization method used for each of the channels. As detailed above Rab21 structures were identified using a fitting procedure during particle tracking whereas transferrin was identified using an adaptive thresholding technique. The fact that different techniques were used for each component may lead to inconsistencies when dealing with poorly focused or low intensity components, as objects in one channel may be detected with one technique whereas detection of objects in the other channel may fail. Confocal of deconvolution techniques may help to reduce certain facets of this issue although would be unlikely to abrogate the problem completely.

An additional limitation of both spatial and temporal filter methods is that trajectories are broken into ‘chunks’ of colocalized or non-colocalized stretches for processing through each filter. This is a computationally efficient method which both filters employ, although can lead to complications especially in noisy images. For example, a particle which is colocalized for a significant stretch of time but for a single frame loses colocalization due to noise in object boundary detection, would be processed as three distinct chunks using the filters. If each colocalization phase does not meet the threshold then the event could be missed, or the event could be incorrectly determined to occur in the second block of colocalization.

A further approach for inclusion in a future iteration of the method would be to investigate the use of a statistical model to estimate if a given stretch of colocalization is significant, rather than relying simply on the direct output of the adaptive threshold technique. Binary colocalization state could for example be modelled by a Poisson distribution that expresses the probability of a given number of observations occurring in a fixed interval of time, and could supplement the STF method in noisy images. A final drawback with both filters is the difficulty in determining the optimal set of input parameters. Each filter may be described as a heuristic technique which employ a practical methodology to determine interaction events. Heuristic techniques are often describes as a rule of thumb approach requiring an intuitive judgment to apply a set of rules to satisfactorily model the problem in hand (Farreny and Prade, 1986). The parameter choice of spatial and temporal filters is thus left to the discretion of the user, although it may be possible to implement a machine learning approach to objectively optimise parameters for a given dataset.

In conclusion, a novel technique was developed to hunt for interaction events in dual colour trajectories. The simplicity of the method allowed for a fast implementation and preliminary data indicate a good level of performance in terms of the numbers of events identifies and the false positive rate of detection. Analysis in live cells suggested the technique was capable of capturing relevant interaction events indicating that further studies are warranted to investigate the technique more thoroughly in a model system.

7 Discussion

Over the last 15 years there has been an explosion of interest for using nanoparticles in biomedical applications ranging from imaging to diagnostics and therapeutics. A huge diversity of nanoparticles are currently under investigation with novel assemblies continually being invented. There is great hope that nanoparticles will help realize long standing goals in drug delivery relating to targeting of macromolecules to the interior of cells, such as peptides, proteins or nuclei acid constructs, in addition to enhancing the therapeutic index of small molecule drugs which are already in use, or failed during development. By grouping multiple functionalities into one entity the functions of the cargo may be separated from mechanisms focused on receptor interactions or release. The physical dimensions of these assemblies can also permit large cargoes such as individual genes, or large numbers of individual factors to be assembled or sequestered. Thus for each nanoparticle successfully reaching its target, potentially hundreds of active molecules may be released. Several enduring challenges remain relating to a poor understanding of the basic science concerning endocytic uptake and processing, in addition to our limited skill in fabricating at the nanoscale (Drbohlavova et al., 2013; Wohlfart et al., 2012).

A great deal of inspiration has been drawn from studying viruses which are marvels of nature with respect to gene delivery. Viruses come ready equipped with mechanisms to evade the host immune system, target cell surface receptors, facilitate endocytic escape and release the nuclei acid cargo which is then followed by intracellular processing and integration into the host genome. However, whilst viral particles can exhibit high transfection efficiencies, several drawbacks have limited their approval for clinical use. In particular the tropism of viral vectors sometimes do not meet clinical standard with further concerns over potential immunogenic responses (Thomas et al., 2003; Waehler et al., 2007). Nevertheless, a major success for the field came in 2012 with the approval of Glybera (Alipogene tiparvovec) by the European Commission, an adeno-associated virus serotype 1 (AAV1) vector for the treatment of lipoprotein lipase deficiency (LPLD) (Hastie and Samulski, 2015). In other conditions these vectors have demonstrated some miraculous preclinical results and the dozens of clinical trials now underway suggest these entities may see wider adoption for gene therapy in the near future (Hastie and Samulski, 2015; Wang and Gao, 2014). However, the high cost of these treatments remains a further concern with Glybera set to be the most expensive medicine in the world at around $1.4 million for treatment (Ylä-Herttuala, 2015).

To circumvent difficulties associated with viral particles, an attractive idea has been to design nanoparticle vectors composed of biocompatible materials with the aim of achieving virus-like drug delivery characteristics whilst minimising immune recognition or other off target effects, in addition

to being amenable to manufacturing scale up. Furthermore, a much wider range of materials and compositions are available with non-viral vectors, and novel properties associated with nanoscale materials can be utilized for imaging applications (e.g. QDs, magnetic particles, nanodiamonds, gold nanoparticles), or photodynamic therapy (e.g. gold nanoparticles), for example. In this study QDs were utilized as model nanoparticles for investigating the loading of small and macromolecule cargoes and their uptake in cells. The exceptional spectral properties of QDs with their bright emission profiles and broad absorbance peak (Fig.3.2) make these nanoparticles excellent tools for quantifying interactions at the nano scale through spectroscopic methods or microscopy. The ability to resolve these particles on a single particle level means uptake and trafficking studies can be conducted with individual particles as they interact with cellular factors although so far few methods have been developed which can quantify these datasets.

An initial goal of this investigation was to characterise commercially available QDs before further application. Two different types of QDs were purchased and their composition as CdSe/ZnS particles was confirmed by EDX microscopy (Fig.3.4). As described by the manufacturer these QDs displayed a 625 or 655 nm emission (Fig.3.2) and a carboxyl or amine surface functionality, respectively. Interestingly, ultrastructural analysis by TEM revealed a very different core morphology between these particles with carboxyl QDs appearing largely spherical whereas amine QDs resembled a bullet shape (Fig.3.3). The larger surface area of amine QDs was consistent with the relationship of QD size giving rise to a longer wavelength emission. However, it was not possible to resolve the polymer coat which surrounds these particle in electron micrographs presumably due to the low density of this layer. Running of these QDs by gel electrophoresis indicated that both particles displayed on overall anionic character despite the advertised surface functionalities (Fig.3.5). For amine QDs this was thought to be a result of an abundance of anionic groups within the polymer structure although the exact nature of these groups was unclear and could have consisted of carboxyl groups which were left unconjugated during manufacture or perhaps sulfoxide groups, or a mixture.

The proprietary nature of this polymer is a drawback of using these commercial nanoparticles and it would be useful on several levels to determine the composition of this polymer further. However, the three dimensional structure of this polymer and the precise surface exposed for biological interaction is also crucial for understanding the interactions of these nanoparticles. Unfortunately there are few methods available which can investigate structure on such a fine scale, and polymers can display dynamic behaviour which may be sensitive to environmental conditions and may not be amenable to techniques such as crystallography. The heterogeneity and polydispersity of nanoparticles at the molecular scale also presents a problem and properties of nanoparticles are usually characterized as an ensemble average over the entire population. One technique which may shed light on the

molecular structure of nanoparticle surfaces is molecular dynamics computer simulations although a detailed knowledge of the constituent parts is needed in ordered to construct a simulation. Recent studies suggest that microsecond molecular dynamics simulations are already being used for studying large nanoparticle assemblies such as viruses (Freddolino et al., 2006; Larsson et al., 2012). For instance, a recent study investigated how the capsid of satellite tobacco necrosis virus undergoes dissolution as a result of calcium binding (Larsson et al., 2012). This simulation involved the motions of 1.2 million particles over microsecond timescales indicating that investigation of nanoparticle interactions is feasible with modern supercomputers (Larsson et al., 2012). Characterizing the structure of the QD polymer coat would also be useful for interpreting how biological systems interact with the particle, in addition to how small molecule drugs such as curcumin (Chapter 4) or macromolecular components such as CPPs or GFPR8 (Chapter 5) can form complexes with these particles.

7.1.1 QD protein corona

An area of growing importance in nanoparticle vector design is understanding the interactions which occur on direct contact of a nanoparticle with biological fluid which results in the binding of biological components to form the protein corona (Walczyk et al., 2010). Several studied have demonstrated the significance of this process for non-viral nanoparticle systems, with the potential to accelerate the clearance of the nanoparticle or mask a nanoparticle associated ligand intended for receptor mediated targeting (Gunawan et al., 2014; Salvati et al., 2013; Tenzer et al., 2013). Corona formation is driven by the physicochemical characteristics of nanoparticle surfaces which give rise to a protein corona 'fingerprint' with a range of possible downstream effects (Walkey et al., 2014). Although initial investigations have focused on the negative impacts of corona formation there is a growing interest to exploit this process for nanoparticle therapeutics (Walkey et al., 2014). For example, adsorption of certain proteins may render the nanoparticle bioavailable by initiating recognition by receptors to achieve cell-specific targeting. This has already been demonstrated with nanoparticle antigen delivery to lymph node dendritic cells which was facilitated by corona mediated targeting (Reddy et al., 2007). Alternatively, specific corona compositions may trigger cell signalling pathways or initiate an immune response and the ability of nanoparticles to modulate pathological processes such as fibrillogenesis is also under investigation (Ilinskaya and Dobrovolskaia, 2013). Another interesting use of corona formation was reported by Arvizo et al., who analysed the protein corona of gold nanoparticles which formed following exposure to malignant ovarian lysates. This approach allowed the identification of a novel cancer marker, hepatoma-derived growth factor (HDGF), which was enriched in the nanoparticle protein corona in the disease condition (Arvizo et al., 2012). Thus there may be many ways in which corona formation may be exploited to enhance the properties of nanoparticles and a broader goal of

this work was to investigate if corona formation could be utilized for cargo loading and release purposes.

The QD nanoparticles utilized here were found to rapidly form a protein corona when exposed to FBS (Fig.3.6). Interestingly the extent of corona formation was highly sensitive to the relative concentrations of QDs and FBS, and the corona appeared to continually evolve during addition of FBS (Fig.3.7). Even low QD concentrations of 3.16 - 1 nM in 99 % FBS appeared to display differences in their corona properties during gel electrophoresis suggesting corona formation may be limited by the concentration of certain FBS components (Fig.3.7). This observation may be in agreement with other reports which indicate that lowly abundant proteins are often constituents of the nanoparticle corona (Monopoli et al., 2012, 2011). The extent of corona formation on QDs was unclear and may involve multiple protein layers, although one would expect that at some point a surface would be generated which would not lead to further protein binding. However, in this study a 'complete' corona was not observed underlining the difficulties in characterizing this dynamic process. It was unclear if corona evolution was a consequence of increased binding at the surface, or if exchange of components was prominent. The greatly reduced cell binding of corona modified QDs was also in line with other reports and was thought to reflect the screening of the anionic QD surface which reduced binding to the cell surface through electrostatic means (Fig.3.8)(Gunawan et al., 2014; Walczyk et al., 2010).

7.1.2 QDs as carriers for curcumin

In light of these results QDs were assessed for binding of the small molecule cancer drug curcumin. There has been much interest in utilizing nanoparticle preparations for enhancing the delivery of this compound owing to its very low bioavailability in vivo which is a consequence of its poor water solubility and rapid clearance (Marchiani et al., 2013). Recent research using magnetic and polymer based nanoparticles have demonstrated that curcumin can bind to hydrophobic domains within the polymer region of nanoparticles (Yallapu et al., 2011, 2010). Magnetic curcumin nanoparticles from these studies were shown to reduce tumour growth in a mouse model and extended survival demonstrating the potential of nanoparticles for enhancing curcumin efficacy (Yallapu et al., 2011).

In this study QDs were also found to be capable carriers for curcumin in serum free conditions with a large volume of the drug being solubilized by these nanoparticles (Fig.4.2). The drug appeared to be sequestered within the QD polymer due to little difference in the hydrodynamic size of particles following drug loading. The maximum capacity for curcumin loading was calculated at an impressive 1100 drug molecules per QD which equates to roughly 62 % of the weight of a pristine particle. This binding was presumably mediated by the relative hydrophobicity of the polymer environment which appeared capable of achieving a high local concentration of curcumin. However, a very different picture emerged when drug loading was investigated in the presence of FBS. By itself, FBS was also

found to solubilize a relatively large volume of curcumin which was thought to occur as a result of protein binding (Pulla Reddy et al., 1999). Analysis of the solvatochromism of curcumin suggested that the polarity of this environment was markedly different compared to the QD polymer, with the FBS constituting a more hydrophobic environment relative to the QD polymer (Fig.4.2). For QDs the curcumin peak blue-shifted with increasing curcumin concentration suggesting a more polar local relative to FBS which may have been less energetically favourable for the apolar curcumin cargo. Experiments indicated that QDs and FBS had an additive effect on the maximum amount of curcumin solubilized in the buffer system although the relative affinity of the drug for each of these components was unclear (Fig.4.2). This lead to an investigation of the partitioning behaviour of this compound when varying the concentration of serum up to 50 % FBS.

This dissociation of curcumin from the QD polymer into the FBS fraction was assessed by two means which exploited the unique spectral properties of these components (Fig.4.4). Following the introduction of QD and curcumin complexes into FBS the shift in the absorbance peak was reversed which was suggestive of curcumin redistributing to the more hydrophobic FBS compartment (Fig.4.4a). To quantify this behaviour QDs were subject to separation by high speed centrifugation which removed the majority of QDs from the supernatant fraction. The remaining curcumin in the supernatant was quantified to assess the level of curcumin redistribution from QD complexes which revealed a clear dissociation curve as a function of FBS concentration with a half-rate of approximately 12.4 % FBS (Fig.4.4d). This kinetics of this process also appeared to be rapid, with the colour change due to the shift in the absorbance peak of curcumin taking on the order of a few seconds to reach completion. Dissociation presumably occurred as a result of short-range simple diffusion of curcumin from the QD polymer to establish an equilibrium. It was unclear how corona formation influenced this processes as previous studies using iron oxide and polymeric nanocapsules report that corona formation had a shielding effect on these particles and inhibited drug release in a buffer system (Behzadi et al., 2014). Methodological differences may account for this discrepancy as the study by Behzadi et al., utilized corona modified nanoparticles that had been separated from excess serum proteins prior to analyses in drug release studies. In this study drug dissociation was monitored during exposure to complete serum indicating that this study characterizes a different phenomenon which may have relevance for in vivo applications.

Investigation of these complexes in a cell viability assay indicated that the nanoparticle vector had a small but significant effect on decreasing viability at higher drug concentrations in the serum positive condition of 10 % FBS (Fig.4.5). However, the high toxicity of QDs alone in serum free conditions complicated data interpretation and there may have been a cooperative effect on viability between QDs and curcumin in the presence of FBS (Fig.4.5). From these studies it was also surprising to find

that the high toxicity of QDs in serum free conditions was abrogated in the presence of 10 % FBS. It would be interesting to determine if these QDs are also compatible with viability over longer timescales.

The concentration of FBS used here was expected to result in an almost 50 % dissociation of curcumin:QD complexes making it difficult to determine the effects of QD delivery from the free drug. Higher serum concentrations would be expected to result in greater complex dissociation and presumably a lower effect from the nanoparticle. Thus dissociativity is a concern for utilizing these complexes in vivo where serum protein concentrations are generally higher than the 10 % investigated here. A large number of studies utilize non-covalent loading of small molecule drugs into nanoparticle complexes although few reports have reported rapid dissociation in the presence of serum. Other nanoparticles such as liposomes or polymeric nanospheres may be tuned to provide a stable drug release profile (Abraham et al., 2005; Allen and Cullis, 2013; Barratt et al., 2001). The QDs assessed here could be described as displaying a rapid burst of drug release following introduction into serum to establish an equilibrium suggesting the release kinetics of these nanoparticles may potentially be tuned by modifying the polymer coat. Additionally it would be interesting to explore the use of a targeting mechanism which may enhance drug delivery by these nanoparticles. The findings from this chapter may be relevant for other polymer based nanoparticle formulations which rely on non-covalent drug loading, and highlights the need to pay careful attention to possible serum effects in nanoparticle studies.

7.1.3 Binding of CPPs and QDs

The binding of adsorption of protein factors to particle surfaces during corona formation may bare many similarities with the binding of CPPs to anionic nanoparticles. A number of studies have demonstrated interaction of cationic CPPs with QDs which is thought to occur by electrostatic means (B. R. Liu et al., 2013, 2011). In this study a panel of CPPs consisting of isolated CPPs or CPPs bearing a cargo sequence, were investigated for binding with amine and carboxyl QDs. For carboxyl QDs, the introduction of CPPs resulted in large scale agglomeration of nanoparticles and the formation of large scale aggregates presumably as a result of interparticle interactions mediated by the CPP (Fig.5.2). This aggregation behaviour was surprising considering that QDs from this manufacturer baring the same surface functionality have been used with cationic CPPs in cell labelling experiments in vivo, although aggregation was not reported in these studies (Yukawa et al., 2012, 2010). Aggregation status is an important property which effects the in vivo behaviour of nanoparticle complexes although often goes unreported in nanoparticle studies. The aggregation observed here also appeared to be robust under a range of buffer conditions and even occurred with particles which already possessed a protein corona (Fig.5.3, 5.4). However, the coverage of the nanoparticle surface by corona

proteins was unclear owing to the relatively low serum concentration of 10 % FBS and it would be interesting to observe the aggregation behaviour of QDs and CPPs using a greater excess of serum proteins. Thus these studies demonstrated the robust nature of CPP binding to anionic QDs although the aggregation of these carboxyl modified particles was undesirable for cell studies.

The observation that amine QDs also displayed an overall anionic charge lead to the idea of using these particles for CPP binding. Remarkably, all CPPs from an initial panel of peptides demonstrated a clear binding profile with these QDs by gel electrophoresis with a greatly reduced occurrence of aggregates compared to QDs with carboxyl functionality (Fig.5.5). However at high CPP concentrations aggregation was evident for some peptides which may have reflected a differing binding mechanism and display of the peptide at the QD surface. Nevertheless, for R8 based peptides no aggregation was detected permitting their further use in cell binding studies. The absence of aggregation was attributed to differences in the polymer coat of these QDs which are advertised as possessing an additional PEG-amine linker appended to the surface. This additional modification may have caused a steric effect to prevent interparticle interactions and the CPP may have bound to anionic groups within the polymer structure (Fig.3.5 Results chapter 3). The different shape of amine QDs may have also played a role although this was not investigated.

Analysis of R8 modified amine QDs in cell binding studies revealed a large increase in cell labelling in the presence of the CPP (Fig.5.7). Interestingly, a significant difference was found in the ability of R8 to enhance QD cell binding when a single amino acid substitution in the peptide linker region was changed from Gly to Phe (Fig.5.7). This finding was in agreement with earlier studies which indicate that both cargo and CPP domains may have co-operative effects on cell membrane binding (Watkins et al., 2011). However, with other CPP variants which comprised of the CPPs TP10 and Penetratin, QDs appeared aggregated when added to cells and did not appear to be endocytosed (Fig.5.8). For R8 peptides in this study, complexes appeared to mostly localize to the cell surface at early time points although following a 24 h chase appeared to be internalized into the endolysosomal compartment (Fig.5.7). The route of internalization was not investigated although the high degree of plasma membrane labelling and only a small level of internalization after 1 h suggested a non-specific entry mechanism may have predominated. Quantifying the volume of QDs associated with cells by measuring the fluorescence intensity revealed that roughly 15 – 25 % of the nanoparticle signal remained following the 24 h chase. The reasons for this are speculative although may have reflected recycling of QD material out of the cell following internalization, or that much of the cell surface associated QD fraction was not internalized and underwent dissociation from the cell membrane. Alternatively, QD fluorescence may have been reduced by trafficking to the low pH environment of endolysosomes. It was unclear if any QDs had reached the cytosol during the time course, and the fate

of the CPP peptide was also undetermined. It is plausible that these complexes may have dissociated whilst inside the cell as a result of competitive binding with cellular factors residing in the endomembrane system. Future studies investigating the trafficking of these components or complexes over time may address some of these questions.

7.1.4 Utilizing CPP QD binding for cargo transport

The non-covalent binding of CPPs and QDs was also investigated using a therapeutically relevant peptide known as Nrf2 which was appended to the CPP Tat (Fig.5.9). A study by Steel et al., reported that this peptide enters cells to disrupt the endogenous Nrf2/Keap1 interaction and promote HO-1 transcription in a concentration dependent manner. Thus an initial goal was to utilize this delivery assay to investigate the use of QDs as a vector for Nrf2-Tat. Unfortunately, collaborators of ours were unable to repeat this crucial experiment and so the investigation of this peptide was restricted to characterizing its binding with QDs (Fig.5.9). Interestingly, this peptide did not demonstrate any appreciable binding with amine QDs during gel electrophoresis which was in contrast to earlier experiments using a panel of CPPs discussed above. This was thought to be a result of a small degree of secondary structure in the Nrf domain which may have provided a steric hinderence to binding, although differences in the orientation and structure of the CPP may also have had an effect. Interestingly, analysis of Nrf2-Tat and carboxyl QDs using this binding assay revealed a very different picture. Using these QDs Nrf2-Tat appeared to form a stable interaction at lower peptide concentrations before reaching a critical concentration of around 63 μM which resulted in the aggregation of QDs (Fig.5.9). This critical concentration was approximately an order of magnitude higher than for other CPPs which were appended to cargo peptides which lacked a secondary structure (Fig.5.2, 5.9). Binding of Nrf2-Tat also appeared to be maintained to some degree following introduction into 10 % FBS, suggesting that anionic nanoparticles may be utilized alongside CPP-peptides for delivery applications. It will be interesting to determine how these complexes perform in terms of their internalization efficiency and delivery capacity. Addition of targeting motifs may also be investigated as a means of achieving receptor mediated targeting of therapeutic CPP peptides.

The observation that carboxyl QDs displayed some resistance to aggregation when using Nrf2-Tat suggested that using a larger cargo motif may abrogate this issue. To investigate this possibility, the cargo protein GFP was appended to the CPP R8. This GFPR8 sequence did not demonstrate any obvious binding with amine QDs further suggesting that these QDs only accept relatively unstructured peptide sequences. However, GFPR8 demonstrated a clear binding curve when added to carboxyl QDs with no signs of large scale aggregation by gel electrophoresis (Fig.5.10). The GFP only control by itself appeared to display a non-specific interaction with carboxyl QDs during gel electrophoresis although the reasons for this were unclear as no obvious signs of binding were found when imaging QDs

adhered to a glass surface due to a lack of colocalization, or when using a biochemical assay which relied on separation of complexes from unbound material by centrifugation (Fig.5.10, 5.12). Thus this interaction may have been difficult to detect using these additional techniques or may have been artefact of gel electrophoresis.

Analysis of GFPR8 on the other hand demonstrated clear signs of binding by microscopy with a high degree of colocalization between GFPR8 and QDs (Fig.5.10). Quantifying GFPR8 binding using a centrifugation assay suggested the carboxyl QD surface had a capacity of around 120 GFPR8 molecules per QD (Fig.5.12). The binding of these components was also investigated following introduction into 10 % FBS. By microscopy, a high degree of colocalization was maintained in the presence of serum with a noticeable degree of QD clustering in this assay, although large scale agglomeration did not occur. By gel electrophoresis, GFPR8 and carboxyl QD association was also preserved to some degree following introduction into FBS due to differences in the gel migration pattern of QD bands when complexed with the protein cargo (Fig.5.10). To determine the level of dissociation in serum a centrifugation assay was utilized, allowing the level of unbound GFPR8 to be quantified following introduction into serum (Fig.5.12b). Interestingly, varying the serum concentration again had a large effect on the level of complex dissociation which mirrored the dissociation of curcumin:QDs in serum (Fig.4.4b, 5.12).

Arginine rich CPPs have previously been reported to bind serum proteins which greatly reduced their internalization capacity (Kosuge et al., 2008). Therefore QD GFPR8 complex dissociation could be expected due to competition for with serum factors for binding the CPP motif, although additional protein-protein interactions with the GFPR8 domain may potentially have had a role in disrupting these complexes. This dissociation behaviour may be undesirable for maintaining the integrity of a delivery complex although on the other hand may also provide a convenient cargo release mechanism depending on the level and rates of dissociation. These parameters could potentially be tuned by modifying the strength of the CPP-polymer interaction through directed engineering approaches.

These QD and GFPR8 complexes were also assessed in a cell binding assay in the presence or absence of 10 % FBS. The QD concentration was in this case fixed at 5 nM, and complexes were formed by addition of GFPR8 from 50 – 500 nM to assess the influence of the nanoparticle on GFPR8 cell binding. In the serum free condition, the GFPR8 only control demonstrated a higher level of cell binding at the top protein concentration when compared to QD complexes although it was unclear if QDs were quenching the GFPR8 signal (Fig.5.13). In the presence of serum, there appeared to be little difference in green fluorescence between these conditions at the highest protein concentration (Fig.5.15). However lowering the GFPR8 concentration saw a sharp drop in the number of punctate structures

within cells for the GFPR8 control. This was in contrast to QD GFPR8 samples which showed a prevalence of punctate green structures that demonstrated colocalization with the QD channel (Fig.5.13, 5.15). In serum free conditions, a high degree of colocalization was observed between QDs and GFPR8 at 50 nM, although in the serum positive condition colocalized structures were only seen at 158 nM GFPR8 and above indicating a role for corona formation and/or serum protein binding in limiting cell binding. Nevertheless the finding that QDs appeared to enhance GFPR8 labelling at lower concentrations was unexpected and demonstrated that the QD can act as a carrier for this cargo to facilitate internalization into punctate structures (Fig.5.12, 5.15). In this model, the nanoparticle complex possesses its own internalization characteristics and acting independently of the unbound protein component. The absence of green punctate structures for QD GFPR8 50 nM in the presence of serum may have been a consequence of low levels of GFPR8 being retained at the QD surface, and an almost complete dissociation of the complex. Therefore to enhance nanoparticle cargo delivery at the lowest concentration range, the stability of these complexes to dissociation may need to be enhanced. It would also be interesting to investigate the internalization behaviour of these complexes over a longer time course and characterize the respective intracellular fates of these components.

7.1.5 Objective quantification of nanoparticle trafficking and dynamics

Currently there are few methods which allow researchers to quantify nanoparticle trafficking in live cells on a single particle level. Combined with a poor understanding of the endocytic machinery, optimizing nanoparticles for intracellular delivery remains a considerable challenge. Being able to quantify instances of nanoparticle trafficking as a nanoparticle progresses from one cellular compartment into another, would allow detailed investigations into the factors which govern such processes. Additionally, visualizing nanoparticle escape on a single particle level would also be a considerable technical achievement and would enable optimization strategies to enhance cytosolic delivery of nanoparticle systems.

However, a challenge with single particle tracking relates to the limited spatial resolution of light microscopy techniques such as widefield. For instance the fluorescence emission from two probes can appear coincident when their separation is on the order of half the wavelength of the emission light (North, 2006). For applications which rely on colocalization to identify an interaction between two intracellular fluorescent labels, this gives rise to false positive identification which presents a problem during quantification. The majority of nanoparticles for intracellular applications are also considerably smaller than the visible wavelength of light and can frequently give rise to this type of event. Imaging in two dimensions tends to compound this issue further although imaging the third dimension comes at a cost of limiting the temporal acquisition rate whilst increasing the computational cost of processing the data which can be non-trivial for large datasets. Therefore to quantify single particle

tracking data by colocalization microscopy, methods have to be employed which remove false positives otherwise the final analyses may be swamped by these spurious events.

Due to the current paucity of methods available for quantifying nanoparticle trafficking in real time, in this work a novel method was investigated which relied on the use to two algorithms to identify the point at which a reporter molecule enters or escapes a labelled endocytic compartment. Both methods were focused on reducing the incidence of false positive colocalization detection. One of these algorithms has been employed previously in various contexts and relies on the observation of colocalization over an extended time frame before identifying a 'fusion' event (Dunne et al., 2009; Koyama-Honda et al., 2005; Lachmanovich et al., 2003; Varela et al., 2014). Likewise, once an object has been characterized as fused, a splitting event can be identified when colocalization is lost for a further length of time which lead to this method being referred to as the 'temporal filter'. Temporal colocalization is often a good indicator of genuine interaction, although problems can arise at extremes of object velocity. For instance, slow moving objects take longer to pass over the top of one another which can generate a false positive identification if the temporal threshold is set too low. The threshold can be increased although at the expense of increasing the time needed to identify an event which may lead to more rapid interactions being missed in the form of a false negative. Therefore whilst this method can potentially provide a useful analysis its several drawbacks led to the idea of developing a novel method that was sensitive to the dynamics of object interaction.

This algorithm relied on two different methods to identify fusion and splitting events separately. For fusion events a model was utilized which relied on the assumption that the direction of the tracked object/particle was random during each step of the trajectory. This implied that the list of potential positions the particle may occupy in the next frame could be traced using a circle with radius equivalent to the displacement and whose centre lies at the initial position of the particle (Fig.6.8a). In this way, the probability of the particle moving to a location within a labelled cellular object in the opposing channel (giving rise to colocalization) can be found as the relative length of the arc which overlaps this object of interest (Fig.6.8b). Using this procedure the probability of landing within an object is sensitive to both the velocity of the particle which is encoded as the radius of the circle, as well as the local object density. For a slow moving colocalized particle, the small displacements will be mapped to a small radius and a relatively large proportion of the displacement arc will then fall within the colocalized object. This process is then repeated iteratively for each particle step to calculate the probability that the two entities have fused. Slower moving particle will require more observations for the probability of fusion to reach threshold in comparison to a rapidly moving particle. Likewise, the same will be true for a particle moving over a larger object in comparison to a small object. The

probability of the particle remaining within the large object during each particle step will be higher relative to the small object and will require further observations to determine if fusion has occurred.

Splitting events in this method were calculated in a different manner, with the distance of the particle to the nearest object being used as a metric to determine the likelihood of splitting (Fig.6.8c, d). Observing a particle which has been characterized as 'fused' external to its parent object is a good indication of splitting although discrepancies can arise due to image noise and inaccurate object boundary detection. Therefore the further a particle is found from an object the more likely a split event has occurred. Using this principle, the distance parameter was mapped to a normal probability density function to provide a simple relationship between the distance parameter and the likelihood of splitting. As both the fusion and splitting parts of this algorithm rely on spatial information, this filter was referred to as the spatial filter.

As both the temporal and spatial filters were compatible with the same data formats and types, these filters were also easily combined in the spatial temporal filter setup, where both filters had to agree on a particular event for the event to be classified. To test the temporal and spatial filters alone or in combination, a particle simulation was constructed which allowed various image and input parameters to be assessed individually. Simulations consisted of randomly moving point like particles in the red channel, with spherical green objects in the green channel which were intended to model intracellular vesicles or endosomes. Initially a simulation was run which assessed the false positive rate of these filters when varying the green object size (Fig.6.9). This was performed by simply observing randomly moving particles and objects which did not undergo any genuine interactions, so any identified events were regarded as a false positives. In the absence of any filter method, relying on the observation of colocalization alone to characterize and event, a very large number of false positives were recorded which scaled with increasing object size (Fig.6.10b). This scaling was simply a result of an increased chance of particle crossing during the simulation. Using either filter alone or in combination saw a drastically reduced number of false positives. Taking the 'no filter' condition as a baseline the number of events were reformulated into a false positive rate which demonstrated some important differences between the filter sets (Fig.6.9c). For the temporal filter the false positive rate increased sharply with increasing object size for reasons discussed above, whilst the spatial filter maintained a relatively constant false positive rate. This was an initial goal of the method and demonstrates how the sensitivity of the spatial filter is inversely associated with object size. This effect would also be expected to occur when varying particle velocity although this remains to be investigated directly.

Achieving a low false positive rate is only worthwhile if the number of true events detected also remains at a practical level. Thus testing of the event detection rate was also performed using particle simulations. In this case, each particle gained a fixed probability of undergoing a fusion event if it encountered a green object, where the two entities would remain colocalized for a minimum of five frames before a splitting event was then allowed to occur. During simulations the actual number of events was recorded and then compared to the number generated by each of the filter sets. Interestingly, all filters performed reasonably well under these conditions in terms of reproducing the actual numbers of events (Fig.6.10a, b). However, estimating the signal to noise ratio of each filter suggested that the use of both filters in combination was the most performant (Fig.6.10c). The spatial temporal filter was also tested in the context of variable image noise (Fig.6.11). In these simulations the false positive rate increased only marginally at the lowest signal to noise ratio of 3 whereas the level of event detection remained high demonstrating that the technique also performed well across a range of noise levels (Fig.6.11).

As discussed, identifying fusion and splitting events as the gain or loss of genuine colocalization may be used to isolate particles which undergo trafficking between labelled cellular compartments. However, these events may also be categorized further depending on how the interaction is established or ended. In the example provided in Fig.6.1 a fusion event, or genuine colocalization event, may arise in one of four ways depending on which red and green components were visible in the preceding frame. These different modes may arise if individual reporter molecules are insufficiently bright to be detected above image noise. Extremely bright probes such as QDs, which are distinguishable on a single particle level, would invariably be detected prior to fusion with a green object. However, individual protein reporters such as GFP are usually poorly resolved in low concentrations and require an enrichment at a site to be visualized. A simple method was implemented in an attempt to utilize this model of object interaction to further characterise fusion and splitting event. This method relied on an object tracking technique to determine if objects of interest were visible in the preceding frame prior to a fusion event, or in the subsequent frame following a splitting event (Fig.6.13a). A parent or child object was detected by simply testing if the original object possessed an overlap in the adjacent frames. Owing to its simplicity this technique may suffer from several drawbacks and may be error prone in scenes with high object densities, although this remains to be tested directly. Additionally, if object displacement is larger than the average diameter of the object in question, the method may also fail. This expectation was largely borne out when tested with a particle simulation. Here the object velocity was varied and the rate of parent or child object detection steadily dropped from its expected value when the velocity exceeded the object

size (Fig.6.13b). Therefore a high image acquisition rate may be critical for this method to work effectively.

Taken together, particle simulations suggested that these methods were promising for application in live cells. However the cellular environment is considerably more complex and a detailed investigation into the false positive and event detection rates is needed before these methods can be employed to study biological processes with confidence. A particular concern in live cells relates to objects that are poorly focused at the limits of the axial focal plane which may give rise to inconsistencies during quantification. Future work may focus on adapting these techniques to 3D data sets which may allow complete particle trajectories to be studied. In this work only an exploratory experiment was carried out in live cells and involved the application of these methods to quantify interactions between rab21 labelled endosomes and transferrin (Fig.6.15). Interestingly, spatial temporal filtering retrieved numerous particle trajectories which contained fusion and splitting events, many of which appeared to be genuine events as depicted in Fig.6.15. However the huge volume of data generated from even a single cell means a detailed analysis of the performance of the method has yet to be undertaken. Utilizing a simpler system involving the trafficking of a handful of reporter molecules may be necessary to undertake robust performance studies. In summary, a promising framework is demonstrated which may find use in quantifying nanoparticle trafficking in live cells. Studying the trafficking of endogenous cargoes may be equally accessible, demonstrated here with transferrin uptake, although further work is required to establish the performance of the technique. With regard to this study single particle tracking combined with spatial temporal filtering may be applied to investigating the uptake of QD complexes with CPP peptide or curcumin cargoes for example, although this remains to be pursued.

Throughout this study an emphasis has been placed on the multitude of biological barriers associated with nanoparticle therapeutics. This study has focused mainly on challenges relating to nanoparticle cargo attachment and quantification of uptake in vitro. Scaling some of these concepts to in vivo studies would be a considerable undertaking. A significant and often overlooked challenge for nanoparticle therapeutics relates to their manufacturing cost (Cheng et al., 2012). This problem is compounded as complexity is added to the nanoparticle in the form of targeting motifs, endocytic escape mechanisms, contrast agents, etc. Even for biologicals which are already approved for clinical use in the form of antibodies, or peptides, their high price tag can restrict their use. For example several recent high profile cases in the UK have seen the NICE (National Institute for Clinical Excellence) refusing to approve certain drugs for use within the NHS (National Health Service) on grounds of cost including Avastin (bevacizumab) and Kadcyla (trastuzumab) (NICE, 2015). For Avastin the dosage regime for metastatic colorectal cancer is recommended as 10 mg/kg every 2 weeks

(Genentec, Inc, 2014) which adds up to a cost of around £20,800 for a yearly course (NICE, 2010), indicating that even relatively low dosing regimens can be prohibitively expensive.

In light of these numbers the difficulties facing multifunctional nanoparticles become clear and a level of cost-effectiveness must be attained in ordered to achieve widespread use. To labour the point, consider the curcumin – carboxyl QD nanoparticles investigated within this study (Chapter 4). To achieve a blood concentration of 100 nM, which was the concentration utilized here in a cell viability assay (Fig.4.5), a patient would need to be dosed with roughly 5.1mg/kg of carboxyl QDs alone, assuming a body weight of 70 kg and a molecular weight of 650 kDa for QDs. At the current sale price (£250 for 250 µL at the time of writing), this would equate to around £17,200 for a single dose of this reagent alone. This is on a similar scale to Glybera, the AAV1 viral treatment for LPLD as discussed above, which equates to around £38,500 per dose for a potentially curative medicine (Ylä-Herttuala, 2015). Of course, the economies of scale can be applied to large scale drug manufacturing but these numbers highlight that in ordered for multifunctional nanoparticles to achieve their goals, their therapeutic indexes must match their expected high price tags.

In conclusion, this work investigated the use of QDs as model small nanoparticles for quantitative drug delivery applications. These polymer coated particles displayed an ability to be non-covalently loaded with small molecules in addition to peptide and protein cargoes. However a common finding was that the binding of these entities was antagonized by the presence of serum proteins which underlines the need to characterize DDS for possible serum effects. A methodology was also developed to investigate the uptake and trafficking of nanoparticle complexes although further work is needed to assess the performance of the method in live cells. Collectively this work introduces a number of novel concepts relating to cargo binding and quantification methodologies and paves the way for further studies to build upon these ideas.

8 Acknowledgments

I would like to thank all my supervisors Professor Arwyn Jones, Professor Poala Borri, Professor Wolfgang Langbein and expressly Dr Pete Watson whose provision of encouragement and freedom to experiment made this project possible. I would additionally like to thank Professor Arwyn Jones and members of his lab Lin He and Ed Sayers for our joint collaboration on scientific manuscripts. I would like to thanks my funding bodies which included the Cardiff University Presidents Research Scholarship and an EPSRC Cross-Disciplinary Interfaces Program. And finally, a huge thank you to my friends, and family Nia and Madoc.

References

Abraham, S.A., Waterhouse, D.N., Mayer, L.D., Cullis, P.R., Madden, T.D., Bally, M.B., 2005. The liposomal formulation of doxorubicin. Methods Enzymol. 391, 71–97. doi:10.1016/S0076-6879(05)91004-5

Aderem, A., Underhill, D.M., 1999. Mechanisms of phagocytosis in macrophages. Annu. Rev. Immunol. 17, 593–623. doi:10.1146/annurev.immunol.17.1.593

Aggarwal, B.B., Harikumar, K.B., 2009. Potential therapeutic effects of curcumin, the anti-inflammatory agent, against neurodegenerative, cardiovascular, pulmonary, metabolic, autoimmune and neoplastic diseases. Int. J. Biochem. Cell Biol. 41, 40–59. doi:10.1016/j.biocel.2008.06.010

Aghi, M., Martuza, R.L., 2005. Oncolytic viral therapies - the clinical experience. Oncogene 24, 7802–7816. doi:10.1038/sj.onc.1209037

Akinc, A., Battaglia, G., 2013. Exploiting endocytosis for nanomedicines. Cold Spring Harb. Perspect. Biol. 5, a016980. doi:10.1101/cshperspect.a016980

Alam, J., Stewart, D., Touchard, C., Boinapally, S., Choi, A.M., Cook, J.L., 1999. Nrf2, a Cap'n'Collar transcription factor, regulates induction of the heme oxygenase-1 gene. J. Biol. Chem. 274, 26071–26078.

Albanese, A., Tang, P.S., Chan, W.C.W., 2012. The effect of nanoparticle size, shape, and surface chemistry on biological systems. Annu. Rev. Biomed. Eng. 14, 1–16. doi:10.1146/annurev-bioeng-071811-150124

Alexis, F., Pridgen, E., Molnar, L.K., Farokhzad, O.C., 2008. Factors Affecting the Clearance and Biodistribution of Polymeric Nanoparticles. Mol. Pharm. 5, 505–515. doi:10.1021/mp800051m

Allen, T.M., Cleland, L.G., 1980. Serum-induced leakage of liposome contents. Biochim. Biophys. Acta 597, 418–426.

Allen, T.M., Cullis, P.R., 2013. Liposomal drug delivery systems: From concept to clinical applications. Adv. Drug Deliv. Rev. 65, 36–48. doi:10.1016/j.addr.2012.09.037

Almeida, A., Souto, E., 2007. Solid lipid nanoparticles as a drug delivery system for peptides and proteins☆. Adv. Drug Deliv. Rev. 59, 478–490. doi:10.1016/j.addr.2007.04.007

Andaloussi, S. EL, Mäger, I., Breakefield, X.O., Wood, M.J.A., 2013. Extracellular vesicles: biology and emerging therapeutic opportunities. Nat. Rev. Drug Discov. 12, 347–357. doi:10.1038/nrd3978

Anderson, N.L., Anderson, N.G., 2002. The human plasma proteome: history, character, and diagnostic prospects. Mol. Cell. Proteomics MCP 1, 845–867.

Andreopoulos, A., Tsotsos, J.K., 2013. 50 Years of object recognition: Directions forward. Comput. Vis. Image Underst. 117, 827–891. doi:10.1016/j.cviu.2013.04.005

Andrews, N.W., 2005. Membrane repair and immunological danger. EMBO Rep. 6, 826–830. doi:10.1038/sj.embor.7400505

Appelqvist, H., Waster, P., Kagedal, K., Ollinger, K., 2013. The lysosome: from waste bag to potential therapeutic target. J. Mol. Cell Biol. 5, 214–226. doi:10.1093/jmcb/mjt022

Argyo, C., Weiss, V., Bräuchle, C., Bein, T., 2014. Multifunctional Mesoporous Silica Nanoparticles as a Universal Platform for Drug Delivery. Chem. Mater. 26, 435–451. doi:10.1021/cm402592t

Arnspang, E.C., Brewer, J.R., Lagerholm, B.C., 2012. Multi-color single particle tracking with quantum dots. PloS One 7, e48521. doi:10.1371/journal.pone.0048521

Arvizo, R.R., Giri, K., Moyano, D., Miranda, O.R., Madden, B., McCormick, D.J., Bhattacharya, R., Rotello, V.M., Kocher, J.-P., Mukherjee, P., 2012. Identifying New Therapeutic Targets via Modulation of Protein Corona Formation by Engineered Nanoparticles. PLoS ONE 7, e33650. doi:10.1371/journal.pone.0033650

Audi, J., Belson, M., Patel, M., Schier, J., Osterloh, J., 2005. Ricin poisoning: a comprehensive review. JAMA 294, 2342–2351. doi:10.1001/jama.294.18.2342

Bakal, C., Perrimon, N., 2010. Realizing the promise of RNAi high throughput screening. Dev. Cell 18, 506–507. doi:10.1016/j.devcel.2010.04.005

Bangham, A.D., Standish, M.M., Watkins, J.C., 1965. Diffusion of univalent ions across the lamellae of swollen phospholipids. J. Mol. Biol. 13, 238–252.

Banning, A., Tomasovic, A., Tikkanen, R., 2011. Functional aspects of membrane association of reggie/flotillin proteins. Curr. Protein Pept. Sci. 12, 725–735.

Barratt, G., Couarraze, G., Couvreur, P., Dubernet, C., Fattal, E., Gref, R., Labarre, D., Legrand, P., Ponchel, G., Vauthier, C., 2001. Polymeric Micro- and Nanoparticles as Drug Carriers, in: Dumitriu, S. (Ed.), Polymeric Biomaterials, Revised and Expanded. CRC Press.

Bastiani, M., Liu, L., Hill, M.M., Jedrychowski, M.P., Nixon, S.J., Lo, H.P., Abankwa, D., Luetterforst, R., Fernandez-Rojo, M., Breen, M.R., Gygi, S.P., Vinten, J., Walser, P.J., North, K.N., Hancock, J.F., Pilch, P.F., Parton, R.G., 2009. MURC/Cavin-4 and cavin family members form tissue-specific caveolar complexes. J. Cell Biol. 185, 1259–1273. doi:10.1083/jcb.200903053

Baumann, C.A., Ribon, V., Kanzaki, M., Thurmond, D.C., Mora, S., Shigematsu, S., Bickel, P.E., Pessin, J.E., Saltiel, A.R., 2000. CAP defines a second signalling pathway required for insulin-stimulated glucose transport. Nature 407, 202–207. doi:10.1038/35025089

Bawendi, M.G., Steigerwald, M.L., Brus, L.E., 1990. The Quantum Mechanics of Larger Semiconductor Clusters ("Quantum Dots"). Annu. Rev. Phys. Chem. 41, 477–496. doi:10.1146/annurev.pc.41.100190.002401

Bechara, C., Pallerla, M., Zaltsman, Y., Burlina, F., Alves, I.D., Lequin, O., Sagan, S., 2013. Tryptophan within basic peptide sequences triggers glycosaminoglycan-dependent endocytosis. FASEB J. Off. Publ. Fed. Am. Soc. Exp. Biol. 27, 738–749. doi:10.1096/fj.12-216176

Bechara, C., Sagan, S., 2013. Cell-penetrating peptides: 20years later, where do we stand? FEBS Lett. 587, 1693–1702. doi:10.1016/j.febslet.2013.04.031

Behnia, R., Munro, S., 2005. Organelle identity and the signposts for membrane traffic. Nature 438, 597–604. doi:10.1038/nature04397

Behzadi, S., Serpooshan, V., Sakhtianchi, R., Müller, B., Landfester, K., Crespy, D., Mahmoudi, M., 2014. Protein corona change the drug release profile of nanocarriers: the "overlooked" factor at the nanobio interface. Colloids Surf. B Biointerfaces 123, 143–149. doi:10.1016/j.colsurfb.2014.09.009

Bertrand, J.-R., Malvy, C., Auguste, T., Tóth, G.K., Kiss-Ivánkovits, O., Illyés, E., Hollósi, M., Bottka, S., Laczkó, I., 2009. Synthesis and studies on cell-penetrating peptides. Bioconjug. Chem. 20, 1307–1314. doi:10.1021/bc900005j

Bexiga, M., Simpson, J., 2013. Human Diseases Associated with Form and Function of the Golgi Complex. Int. J. Mol. Sci. 14, 18670–18681. doi:10.3390/ijms140918670

Bitsikas, V., Corrêa, I.R., Nichols, B.J., 2014. Clathrin-independent pathways do not contribute significantly to endocytic flux. eLife 3, e03970. doi:10.7554/eLife.03970

Bolte, S., Cordelières, F.P., 2006. A guided tour into subcellular colocalization analysis in light microscopy. J. Microsc. 224, 213–232. doi:10.1111/j.1365-2818.2006.01706.x

Boucrot, E., Ferreira, A.P.A., Almeida-Souza, L., Debard, S., Vallis, Y., Howard, G., Bertot, L., Sauvonnet, N., McMahon, H.T., 2015. Endophilin marks and controls a clathrin-independent endocytic pathway. Nature 517, 460–465. doi:10.1038/nature14067

Braet, F., Wisse, E., Bomans, P., Frederik, P., Geerts, W., Koster, A., Soon, L., Ringer, S., 2007. Contribution of high-resolution correlative imaging techniques in the study of the liver sieve in three-dimensions. Microsc. Res. Tech. 70, 230–242. doi:10.1002/jemt.20408

Bruchez, M., Moronne, M., Gin, P., Weiss, S., Alivisatos, A.P., 1998. Semiconductor nanocrystals as fluorescent biological labels. Science 281, 2013–2016.

Bunschoten, A., Buckle, T., Kuil, J., Luker, G.D., Luker, K.E., Nieweg, O.E., van Leeuwen, F.W.B., 2012. Targeted non-covalent self-assembled nanoparticles based on human serum albumin. Biomaterials 33, 867–875. doi:10.1016/j.biomaterials.2011.10.005

Canton, I., Battaglia, G., 2012. Endocytosis at the nanoscale. Chem. Soc. Rev. 41, 2718–2739. doi:10.1039/c2cs15309b

Capriotti, A.L., Caracciolo, G., Caruso, G., Cavaliere, C., Pozzi, D., Samperi, R., Laganà, A., 2013. Label-free quantitative analysis for studying the interactions between nanoparticles and plasma proteins. Anal. Bioanal. Chem. 405, 635–645. doi:10.1007/s00216-011-5691-y

Carmona, S., Jorgensen, M.R., Kolli, S., Crowther, C., Salazar, F.H., Marion, P.L., Fujino, M., Natori, Y., Thanou, M., Arbuthnot, P., Miller, A.D., 2009. Controlling HBV replication in vivo by intravenous administration of triggered PEGylated siRNA-nanoparticles. Mol. Pharm. 6, 706–717. doi:10.1021/mp800157x

Carter, E., Lau, C.Y., Tosh, D., Ward, S.G., Mrsny, R.J., 2013. Cell penetrating peptides fail to induce an innate immune response in epithelial cells in vitro: implications for continued therapeutic use. Eur. J. Pharm. Biopharm. Off. J. Arbeitsgemeinschaft Für Pharm. Verfahrenstechnik EV 85, 12–19. doi:10.1016/j.ejpb.2013.03.024

Casals, E., Pfaller, T., Duschl, A., Oostingh, G.J., Puntes, V., 2010. Time Evolution of the Nanoparticle Protein Corona. ACS Nano 4, 3623–3632. doi:10.1021/nn901372t

Chang, C.-P., Yang, M.-C., Liu, H.-S., Lin, Y.-S., Lei, H.-Y., 2007. Concanavalin A induces autophagy in hepatoma cells and has a therapeutic effect in a murine in situ hepatoma model. Hepatol. Baltim. Md 45, 286–296. doi:10.1002/hep.21509

Chan, W.C.W., Maxwell, D.J., Gao, X., Bailey, R.E., Han, M., Nie, S., 2002. Luminescent quantum dots for multiplexed biological detection and imaging. Curr. Opin. Biotechnol. 13, 40–46.

Chen, B., Liu, Q., Zhang, Y., Xu, L., Fang, X., 2008. Transmembrane delivery of the cell-penetrating peptide conjugated semiconductor quantum dots. Langmuir ACS J. Surf. Colloids 24, 11866–11871. doi:10.1021/la802048s

Cheng, Z., Zaki, A. Al, Hui, J.Z., Muzykantov, V.R., Tsourkas, A., 2012. Multifunctional nanoparticles: cost versus benefit of adding targeting and imaging capabilities. Science 338, 903–910. doi:10.1126/science.1226338

Chen, M., Guo, H., Liu, Y., Zhang, Q., 2014. Structural changes of human serum albumin induced by cadmium acetate. J. Biochem. Mol. Toxicol. 28, 281–287. doi:10.1002/jbt.21564

Chenouard, N., Smal, I., de Chaumont, F., Maška, M., Sbalzarini, I.F., Gong, Y., Cardinale, J., Carthel, C., Coraluppi, S., Winter, M., Cohen, A.R., Godinez, W.J., Rohr, K., Kalaidzidis, Y., Liang, L., Duncan, J., Shen, H., Xu, Y., Magnusson, K.E.G., Jaldén, J., Blau, H.M., Paul-Gilloteaux, P., Roudot, P., Kervrann, C., Waharte, F., Tinevez, J.-Y., Shorte, S.L., Willemse, J., Celler, K., van Wezel, G.P., Dan, H.-W., Tsai, Y.-S., de Solórzano, C.O., Olivo-Marin, J.-C., Meijering, E., 2014. Objective comparison of particle tracking methods. Nat. Methods 11, 281–289. doi:10.1038/nmeth.2808

Chen, X.-L., Kunsch, C., 2004. Induction of cytoprotective genes through Nrf2/antioxidant response element pathway: a new therapeutic approach for the treatment of inflammatory diseases. Curr. Pharm. Des. 10, 879–891.

Chen, X., Shank, S., Davis, P.B., Ziady, A.G., 2011. Nucleolin-Mediated Cellular Trafficking of DNA Nanoparticle Is Lipid Raft and Microtubule Dependent and Can Be Modulated by Glucocorticoid. Mol. Ther. 19, 93–102. doi:10.1038/mt.2010.214

Chen, Z.G., 2010. Small-molecule delivery by nanoparticles for anticancer therapy. Trends Mol. Med. 16, 594–602. doi:10.1016/j.molmed.2010.08.001

Chetta, A., Zanini, A., Torre, O., Olivieri, D., 2007. Vascular remodelling and angiogenesis in asthma: morphological aspects and pharmacological modulation. Inflamm. Allergy Drug Targets 6, 41–45.

Chien, F.-C., Kuo, C.W., Chen, P., 2011. Localization imaging using blinking quantum dots. The Analyst 136, 1608–1613. doi:10.1039/c0an00859a

Chithrani, B.D., Ghazani, A.A., Chan, W.C.W., 2006. Determining the size and shape dependence of gold nanoparticle uptake into mammalian cells. Nano Lett. 6, 662–668. doi:10.1021/nl052396o

Choi, Y., Kim, K., Hong, S., Kim, H., Kwon, Y.-J., Song, R., 2011. Intracellular protein target detection by quantum dots optimized for live cell imaging. Bioconjug. Chem. 22, 1576–1586. doi:10.1021/bc200126k

Cho, K., Wang, X., Nie, S., Chen, Z., Shin, D.M., 2008. Therapeutic Nanoparticles for Drug Delivery in Cancer. Clin. Cancer Res. 14, 1310–1316. doi:10.1158/1078-0432.CCR-07-1441

Clausen, M.P., Lagerholm, B.C., 2011. The probe rules in single particle tracking. Curr. Protein Pept. Sci. 12, 699–713.

Cleal, K., He, L., Watson, P.D., Jones, A.T., 2013. Endocytosis, intracellular traffic and fate of cell penetrating peptide based conjugates and nanoparticles. Curr. Pharm. Des. 19, 2878–2894.

Collinet, C., Stöter, M., Bradshaw, C.R., Samusik, N., Rink, J.C., Kenski, D., Habermann, B., Buchholz, F., Henschel, R., Mueller, M.S., Nagel, W.E., Fava, E., Kalaidzidis, Y., Zerial, M., 2010. Systems survey of endocytosis by multiparametric image analysis. Nature 464, 243–249. doi:10.1038/nature08779

Colombo, M., Corsi, F., Foschi, D., Mazzantini, E., Mazzucchelli, S., Morasso, C., Occhipinti, E., Polito, L., Prosperi, D., Ronchi, S., Verderio, P., 2010. HER2 targeting as a two-sided strategy for breast cancer diagnosis and treatment: Outlook and recent implications in nanomedical approaches. Pharmacol. Res. Off. J. Ital. Pharmacol. Soc. 62, 150–165. doi:10.1016/j.phrs.2010.01.013

Conniot, J., Silva, J.M., Fernandes, J.G., Silva, L.C., Gaspar, R., Brocchini, S., Florindo, H.F., Barata, T.S., 2014. Cancer immunotherapy: nanodelivery approaches for immune cell targeting and tracking. Front. Chem. 2, 105. doi:10.3389/fchem.2014.00105

Costes, S.V., Daelemans, D., Cho, E.H., Dobbin, Z., Pavlakis, G., Lockett, S., 2004. Automatic and quantitative measurement of protein-protein colocalization in live cells. Biophys. J. 86, 3993–4003. doi:10.1529/biophysj.103.038422

Cremona, M.L., Matthies, H.J.G., Pau, K., Bowton, E., Speed, N., Lute, B.J., Anderson, M., Sen, N., Robertson, S.D., Vaughan, R.A., Rothman, J.E., Galli, A., Javitch, J.A., Yamamoto, A., 2011. Flotillin-1 is essential for PKC-triggered endocytosis and membrane microdomain localization of DAT. Nat. Neurosci. 14, 469–477. doi:10.1038/nn.2781

Dakwar, G.R., Zagato, E., Delanghe, J., Hobel, S., Aigner, A., Denys, H., Braeckmans, K., Ceelen, W., De Smedt, S.C., Remaut, K., 2014. Colloidal stability of nano-sized particles in the peritoneal fluid: towards optimizing drug delivery systems for intraperitoneal therapy. Acta Biomater. 10, 2965–2975. doi:10.1016/j.actbio.2014.03.012

Das, R.K., Kasoju, N., Bora, U., 2010. Encapsulation of curcumin in alginate-chitosan-pluronic composite nanoparticles for delivery to cancer cells. Nanomedicine Nanotechnol. Biol. Med. 6, 153–160. doi:10.1016/j.nano.2009.05.009

Delehanty, J.B., Bradburne, C.E., Boeneman, K., Susumu, K., Farrell, D., Mei, B.C., Blanco-Canosa, J.B., Dawson, G., Dawson, P.E., Mattoussi, H., Medintz, I.L., 2010. Delivering quantum dot-peptide bioconjugates to the cellular cytosol: escaping from the endolysosomal system. Integr. Biol. Quant. Biosci. Nano Macro 2, 265–277. doi:10.1039/c0ib00002g

Delehanty, J.B., Medintz, I.L., Pons, T., Brunel, F.M., Dawson, P.E., Mattoussi, H., 2006. Self-assembled quantum dot-peptide bioconjugates for selective intracellular delivery. Bioconjug. Chem. 17, 920–927. doi:10.1021/bc060044i

Demeshko, S., Dechert, S., Meyer, F., 2004. Anion-pi interactions in a carousel copper(II)-triazine complex. J. Am. Chem. Soc. 126, 4508–4509. doi:10.1021/ja049458h

Derossi, D., Joliot, A.H., Chassaing, G., Prochiantz, A., 1994. The third helix of the Antennapedia homeodomain translocates through biological membranes. J. Biol. Chem. 269, 10444–10450.

Deschout, H., Martens, T., Vercauteren, D., Remaut, K., Demeester, J., De Smedt, S.C., Neyts, K., Braeckmans, K., 2013. Correlation of dual colour single particle trajectories for improved

detection and analysis of interactions in living cells. Int. J. Mol. Sci. 14, 16485–16514. doi:10.3390/ijms140816485
Dharmawardhane, S., Schürmann, A., Sells, M.A., Chernoff, J., Schmid, S.L., Bokoch, G.M., 2000. Regulation of macropinocytosis by p21-activated kinase-1. Mol. Biol. Cell 11, 3341–3352.
DiCiccio, J.E., Steinberg, B.E., 2011. Lysosomal pH and analysis of the counter ion pathways that support acidification. J. Gen. Physiol. 137, 385–390. doi:10.1085/jgp.201110596
Dietrich, O., Raya, J.G., Reeder, S.B., Reiser, M.F., Schoenberg, S.O., 2007. Measurement of signal-to-noise ratios in MR images: Influence of multichannel coils, parallel imaging, and reconstruction filters. J. Magn. Reson. Imaging 26, 375–385. doi:10.1002/jmri.20969
Doane, T., Burda, C., 2013. Nanoparticle mediated non-covalent drug delivery. Adv. Drug Deliv. Rev. 65, 607–621. doi:10.1016/j.addr.2012.05.012
Doan, L.G., 2004. Ricin: mechanism of toxicity, clinical manifestations, and vaccine development. A review. J. Toxicol. Clin. Toxicol. 42, 201–208.
Dobrovolskaia, M.A., McNeil, S.E., 2007. Immunological properties of engineered nanomaterials. Nat. Nanotechnol. 2, 469–478. doi:10.1038/nnano.2007.223
Dobrovolskaia, M.A., Patri, A.K., Zheng, J., Clogston, J.D., Ayub, N., Aggarwal, P., Neun, B.W., Hall, J.B., McNeil, S.E., 2009. Interaction of colloidal gold nanoparticles with human blood: effects on particle size and analysis of plasma protein binding profiles. Nanomedicine Nanotechnol. Biol. Med. 5, 106–117. doi:10.1016/j.nano.2008.08.001
Doherty, G.J., McMahon, H.T., 2009. Mechanisms of Endocytosis. Annu. Rev. Biochem. 78, 857–902. doi:10.1146/annurev.biochem.78.081307.110540
Domenech, M., Marrero-Berrios, I., Torres-Lugo, M., Rinaldi, C., 2013. Lysosomal Membrane Permeabilization by Targeted Magnetic Nanoparticles in Alternating Magnetic Fields. ACS Nano 7, 5091–5101. doi:10.1021/nn4007048
Douglas, K.L., Piccirillo, C.A., Tabrizian, M., 2008. Cell line-dependent internalization pathways and intracellular trafficking determine transfection efficiency of nanoparticle vectors. Eur. J. Pharm. Biopharm. Off. J. Arbeitsgemeinschaft Für Pharm. Verfahrenstechnik EV 68, 676–687. doi:10.1016/j.ejpb.2007.09.002
Drbohlavova, J., Chomoucka, J., Adam, V., Ryvolova, M., Eckschlager, T., Hubalek, J., Kizek, R., 2013. Nanocarriers for anticancer drugs - new trends in nanomedicine. Curr. Drug Metab. 14, 547–564.
Dreaden, E.C., Austin, L.A., Mackey, M.A., El-Sayed, M.A., 2012. Size matters: gold nanoparticles in targeted cancer drug delivery. Ther. Deliv. 3, 457–478.
Dunne, P.D., Fernandes, R.A., McColl, J., Yoon, J.W., James, J.R., Davis, S.J., Klenerman, D., 2009. DySCo: Quantitating Associations of Membrane Proteins Using Two-Color Single-Molecule Tracking. Biophys. J. 97, L5–L7. doi:10.1016/j.bpj.2009.05.046
Dupont, A., Stirnnagel, K., Lindemann, D., Lamb, D.C., 2013. Tracking image correlation: combining single-particle tracking and image correlation. Biophys. J. 104, 2373–2382. doi:10.1016/j.bpj.2013.04.005
Dutta, D., Donaldson, J.G., 2012. Search for inhibitors of endocytosis: Intended specificity and unintended consequences. Cell. Logist. 2, 203–208. doi:10.4161/cl.23967
Eldem, T., Speiser, P., Hincal, A., 1991. Optimization of spray-dried and -congealed lipid micropellets and characterization of their surface morphology by scanning electron microscopy. Pharm. Res. 8, 47–54.
Farkhani, S.M., Valizadeh, A., Karami, H., Mohammadi, S., Sohrabi, N., Badrzadeh, F., 2014. Cell penetrating peptides: Efficient vectors for delivery of nanoparticles, nanocarriers, therapeutic and diagnostic molecules. Peptides 57, 78–94. doi:10.1016/j.peptides.2014.04.015
Farreny, H., Prade, H., 1986. Heuristics—intelligent search strategies for computer problem solving, by Judea Pearl. (Reading, Ma: Addison-Wesley, 1984). Int. J. Intell. Syst. 1, 69–70. doi:10.1002/int.4550010107

Fay, F., Scott, C.J., 2011. Antibody-targeted nanoparticles for cancer therapy. Immunotherapy 3, 381–394. doi:10.2217/imt.11.5
FDA, 2014. New Molecular Entity (NME) Drug and New Biologic Approvals. http://www.fda.gov/Drugs/DevelopmentApprovalProcess/HowDrugsareDevelopedandApproved/DrugandBiologicApprovalReports/NDAandBLAApprovalReports/ucm373420.htm.
Folkman, J., 2003. Fundamental concepts of the angiogenic process. Curr. Mol. Med. 3, 643–651.
Foret, L., Dawson, J.E., Villaseñor, R., Collinet, C., Deutsch, A., Brusch, L., Zerial, M., Kalaidzidis, Y., Jülicher, F., 2012. A general theoretical framework to infer endosomal network dynamics from quantitative image analysis. Curr. Biol. CB 22, 1381–1390. doi:10.1016/j.cub.2012.06.021
Frankel, A.D., Pabo, C.O., 1988. Cellular uptake of the tat protein from human immunodeficiency virus. Cell 55, 1189–1193.
Freddolino, P.L., Arkhipov, A.S., Larson, S.B., McPherson, A., Schulten, K., 2006. Molecular dynamics simulations of the complete satellite tobacco mosaic virus. Struct. Lond. Engl. 1993 14, 437–449. doi:10.1016/j.str.2005.11.014
Galland, C., Ghosh, Y., Steinbrück, A., Sykora, M., Hollingsworth, J.A., Klimov, V.I., Htoon, H., 2011. Two types of luminescence blinking revealed by spectroelectrochemistry of single quantum dots. Nature 479, 203–207. doi:10.1038/nature10569
Gao, H., Yang, Z., Zhang, S., Cao, S., Shen, S., Pang, Z., Jiang, X., 2013. Ligand modified nanoparticles increases cell uptake, alters endocytosis and elevates glioma distribution and internalization. Sci. Rep. 3, 2534. doi:10.1038/srep02534
Gao, M., Skolnick, J., 2013. A comprehensive survey of small-molecule binding pockets in proteins. PLoS Comput. Biol. 9, e1003302. doi:10.1371/journal.pcbi.1003302
Gao, W., Fang, R.H., Thamphiwatana, S., Luk, B.T., Li, J., Angsantikul, P., Zhang, Q., Hu, C.-M.J., Zhang, L., 2015. Modulating Antibacterial Immunity via Bacterial Membrane-Coated Nanoparticles. Nano Lett. 15, 1403–1409. doi:10.1021/nl504798g
Garcea, R.L., Gissmann, L., 2004. Virus-like particles as vaccines and vessels for the delivery of small molecules. Curr. Opin. Biotechnol. 15, 513–517. doi:10.1016/j.copbio.2004.10.002
Gasser, M., Rothen-Rutishauser, B., Krug, H.F., Gehr, P., Nelle, M., Yan, B., Wick, P., 2010. The adsorption of biomolecules to multi-walled carbon nanotubes is influenced by both pulmonary surfactant lipids and surface chemistry. J. Nanobiotechnology 8, 31. doi:10.1186/1477-3155-8-31
Gautam, A., Singh, H., Tyagi, A., Chaudhary, K., Kumar, R., Kapoor, P., Raghava, G.P.S., 2012. CPPsite: a curated database of cell penetrating peptides. Database J. Biol. Databases Curation 2012, bas015. doi:10.1093/database/bas015
Genentec, Inc, 2014. Avastin Prescribing Information. http://www.gene.com/download/pdf/avastin_prescribing.pdf.
Giannotti, M.I., Esteban, O., Oliva, M., García-Parajo, M.F., Sanz, F., 2011. pH-Responsive Polysaccharide-Based Polyelectrolyte Complexes As Nanocarriers for Lysosomal Delivery of Therapeutic Proteins. Biomacromolecules 12, 2524–2533. doi:10.1021/bm2003384
Gilfrich, J., 1994. Handbook of X-Ray Spectrometry: Methods and Techniques Edited by: Rene E. Van Grieken and Andrzej A. Markowicz Published by Marcel Dekker, Inc., New York, 1993; xiv + 704 pp., $195, ISBN 0-8247-8483-9. X-Ray Spectrom. 23, 45–46. doi:10.1002/xrs.1300230110
Gkouvatsos, K., Papanikolaou, G., Pantopoulos, K., 2012. Regulation of iron transport and the role of transferrin. Biochim. Biophys. Acta 1820, 188–202. doi:10.1016/j.bbagen.2011.10.013
Glomski, I.J., Gedde, M.M., Tsang, A.W., Swanson, J.A., Portnoy, D.A., 2002. The Listeria monocytogenes hemolysin has an acidic pH optimum to compartmentalize activity and prevent damage to infected host cells. J. Cell Biol. 156, 1029–1038. doi:10.1083/jcb.200201081
Gornall, A.G., Bardawill, C.J., David, M.M., 1949. Determination of serum proteins by means of the biuret reaction. J. Biol. Chem. 177, 751–766.

Grant, B.D., Donaldson, J.G., 2009. Pathways and mechanisms of endocytic recycling. Nat. Rev. Mol. Cell Biol. 10, 597–608. doi:10.1038/nrm2755
Gratton, S.E.A., Ropp, P.A., Pohlhaus, P.D., Luft, J.C., Madden, V.J., Napier, M.E., DeSimone, J.M., 2008. The effect of particle design on cellular internalization pathways. Proc. Natl. Acad. Sci. U. S. A. 105, 11613–11618. doi:10.1073/pnas.0801763105
Green, M., Ishino, M., Loewenstein, P.M., 1989. Mutational analysis of HIV-1 Tat minimal domain peptides: identification of trans-dominant mutants that suppress HIV-LTR-driven gene expression. Cell 58, 215–223.
Green, M., Loewenstein, P.M., 1988. Autonomous functional domains of chemically synthesized human immunodeficiency virus tat trans-activator protein. Cell 55, 1179–1188.
Guex, N., Peitsch, M.C., 1997. SWISS-MODEL and the Swiss-PdbViewer: an environment for comparative protein modeling. Electrophoresis 18, 2714–2723. doi:10.1002/elps.1150181505
Guillot, F.L., Audus, K.L., Raub, T.J., 1990. Fluid-phase endocytosis by primary cultures of bovine brain microvessel endothelial cell monolayers. Microvasc. Res. 39, 1–14.
Gunawan, C., Lim, M., Marquis, C.P., Amal, R., 2014. Nanoparticle–protein corona complexes govern the biological fates and functions of nanoparticles. J. Mater. Chem. B 2, 2060. doi:10.1039/c3tb21526a
Guo, X., Szoka, F.C., 2001. Steric stabilization of fusogenic liposomes by a low-pH sensitive PEG--diortho ester--lipid conjugate. Bioconjug. Chem. 12, 291–300.
Guo, Z., He, B., Jin, H., Zhang, H., Dai, W., Zhang, L., Zhang, H., Wang, X., Wang, J., Zhang, X., Zhang, Q., 2014. Targeting efficiency of RGD-modified nanocarriers with different ligand intervals in response to integrin αvβ3 clustering. Biomaterials 35, 6106–6117. doi:10.1016/j.biomaterials.2014.04.031
Gupta, A.K., Gupta, M., 2005. Synthesis and surface engineering of iron oxide nanoparticles for biomedical applications. Biomaterials 26, 3995–4021. doi:10.1016/j.biomaterials.2004.10.012
Gu, Z., Noss, E.H., Hsu, V.W., Brenner, M.B., 2011. Integrins traffic rapidly via circular dorsal ruffles and macropinocytosis during stimulated cell migration. J. Cell Biol. 193, 61–70. doi:10.1083/jcb.201007003
Hall, D., Hoshino, M., 2010. Effects of macromolecular crowding on intracellular diffusion from a single particle perspective. Biophys. Rev. 2, 39–53. doi:10.1007/s12551-010-0029-0
Hansen, C.G., Nichols, B.J., 2010. Exploring the caves: cavins, caveolins and caveolae. Trends Cell Biol. 20, 177–186. doi:10.1016/j.tcb.2010.01.005
Hansen, C.G., Shvets, E., Howard, G., Riento, K., Nichols, B.J., 2013. Deletion of cavin genes reveals tissue-specific mechanisms for morphogenesis of endothelial caveolae. Nat. Commun. 4, 1831. doi:10.1038/ncomms2808
Harush-Frenkel, O., Debotton, N., Benita, S., Altschuler, Y., 2007. Targeting of nanoparticles to the clathrin-mediated endocytic pathway. Biochem. Biophys. Res. Commun. 353, 26–32. doi:10.1016/j.bbrc.2006.11.135
Hastie, E., Samulski, R.J., 2015. AAV at 50: A golden anniversary of discovery, research, and gene therapy success, a personal perspective. Hum. Gene Ther. 150326045720006. doi:10.1089/hum.2015.025
Hayashi, A., Suzuki, H., Itoh, K., Yamamoto, M., Sugiyama, Y., 2003. Transcription factor Nrf2 is required for the constitutive and inducible expression of multidrug resistance-associated protein 1 in mouse embryo fibroblasts. Biochem. Biophys. Res. Commun. 310, 824–829.
He, C., Hu, Y., Yin, L., Tang, C., Yin, C., 2010. Effects of particle size and surface charge on cellular uptake and biodistribution of polymeric nanoparticles. Biomaterials 31, 3657–3666. doi:10.1016/j.biomaterials.2010.01.065
Hermanson, G.T., 2008. Chapter 5 - Heterobifunctional Crosslinkers, in: Bioconjugate Techniques (Second Edition). Academic Press, New York, pp. 276–335.

Heyes, J., Palmer, L., Bremner, K., MacLachlan, I., 2005. Cationic lipid saturation influences intracellular delivery of encapsulated nucleic acids. J. Control. Release Off. J. Control. Release Soc. 107, 276–287. doi:10.1016/j.jconrel.2005.06.014

Hillaireau, H., Couvreur, P., 2009. Nanocarriers' entry into the cell: relevance to drug delivery. Cell. Mol. Life Sci. 66, 2873–2896. doi:10.1007/s00018-009-0053-z

Hirose, H., Takeuchi, T., Osakada, H., Pujals, S., Katayama, S., Nakase, I., Kobayashi, S., Haraguchi, T., Futaki, S., 2012. Transient focal membrane deformation induced by arginine-rich peptides leads to their direct penetration into cells. Mol. Ther. J. Am. Soc. Gene Ther. 20, 984–993. doi:10.1038/mt.2011.313

Höfling, F., Franosch, T., 2013. Anomalous transport in the crowded world of biological cells. Rep. Prog. Phys. Phys. Soc. G. B. 76, 046602. doi:10.1088/0034-4885/76/4/046602

Howes, M.T., Kirkham, M., Riches, J., Cortese, K., Walser, P.J., Simpson, F., Hill, M.M., Jones, A., Lundmark, R., Lindsay, M.R., Hernandez-Deviez, D.J., Hadzic, G., McCluskey, A., Bashir, R., Liu, L., Pilch, P., McMahon, H., Robinson, P.J., Hancock, J.F., Mayor, S., Parton, R.G., 2010. Clathrin-independent carriers form a high capacity endocytic sorting system at the leading edge of migrating cells. J. Cell Biol. 190, 675–691. doi:10.1083/jcb.201002119

Huang, C., Neoh, K.G., Kang, E.-T., Shuter, B., 2011. Surface modified superparamagnetic iron oxide nanoparticles (SPIONs) for high efficiency folate-receptor targeting with low uptake by macrophages. J. Mater. Chem. 21, 16094. doi:10.1039/c1jm11270h

Huang, F., Watson, E., Dempsey, C., Suh, J., 2013. Real-time particle tracking for studying intracellular trafficking of pharmaceutical nanocarriers. Methods Mol. Biol. Clifton NJ 991, 211–223. doi:10.1007/978-1-62703-336-7_20

Huang, J.G., Leshuk, T., Gu, F.X., 2011. Emerging nanomaterials for targeting subcellular organelles. Nano Today 6, 478–492. doi:10.1016/j.nantod.2011.08.002

Huang, Y.-W., Lee, H.-J., Tolliver, L.M., Aronstam, R.S., 2015. Delivery of Nucleic Acids and Nanomaterials by Cell-Penetrating Peptides: Opportunities and Challenges. BioMed Res. Int. 2015, 1–16. doi:10.1155/2015/834079

Huotari, J., Helenius, A., 2011. Endosome maturation: Endosome maturation. EMBO J. 30, 3481–3500. doi:10.1038/emboj.2011.286

Ilinskaya, A.N., Dobrovolskaia, M.A., 2013. Nanoparticles and the blood coagulation system. Part II: safety concerns. Nanomed. 8, 969–981. doi:10.2217/nnm.13.49

Itoh, K., Chiba, T., Takahashi, S., Ishii, T., Igarashi, K., Katoh, Y., Oyake, T., Hayashi, N., Satoh, K., Hatayama, I., Yamamoto, M., Nabeshima, Y., 1997. An Nrf2/small Maf heterodimer mediates the induction of phase II detoxifying enzyme genes through antioxidant response elements. Biochem. Biophys. Res. Commun. 236, 313–322.

Itoh, K., Igarashi, K., Hayashi, N., Nishizawa, M., Yamamoto, M., 1995. Cloning and characterization of a novel erythroid cell-derived CNC family transcription factor heterodimerizing with the small Maf family proteins. Mol. Cell. Biol. 15, 4184–4193.

Itoh, K., Wakabayashi, N., Katoh, Y., Ishii, T., Igarashi, K., Engel, J.D., Yamamoto, M., 1999. Keap1 represses nuclear activation of antioxidant responsive elements by Nrf2 through binding to the amino-terminal Neh2 domain. Genes Dev. 13, 76–86.

Ito, K., Olsen, S.L., Qiu, W., Deeley, R.G., Cole, S.P., 2001. Mutation of a single conserved tryptophan in multidrug resistance protein 1 (MRP1/ABCC1) results in loss of drug resistance and selective loss of organic anion transport. J. Biol. Chem. 276, 15616–15624. doi:10.1074/jbc.M011246200

Jain, R.K., Stylianopoulos, T., 2010. Delivering nanomedicine to solid tumors. Nat. Rev. Clin. Oncol. 7, 653–664. doi:10.1038/nrclinonc.2010.139

James, N.D., Coker, R.J., Tomlinson, D., Harris, J.R., Gompels, M., Pinching, A.J., Stewart, J.S., 1994. Liposomal doxorubicin (Doxil): an effective new treatment for Kaposi's sarcoma in AIDS. Clin. Oncol. R. Coll. Radiol. G. B. 6, 294–296.

Janeway, C.A., Medzhitov, R., 2002. Innate immune recognition. Annu. Rev. Immunol. 20, 197–216. doi:10.1146/annurev.immunol.20.083001.084359
Jaqaman, K., Loerke, D., Mettlen, M., Kuwata, H., Grinstein, S., Schmid, S.L., Danuser, G., 2008. Robust single-particle tracking in live-cell time-lapse sequences. Nat. Methods 5, 695–702. doi:10.1038/nmeth.1237
Jiang, X., Weise, S., Hafner, M., Rocker, C., Zhang, F., Parak, W.J., Nienhaus, G.U., 2010. Quantitative analysis of the protein corona on FePt nanoparticles formed by transferrin binding. J. R. Soc. Interface 7, S5–S13. doi:10.1098/rsif.2009.0272.focus
Johannes, L., Römer, W., 2010. Shiga toxins--from cell biology to biomedical applications. Nat. Rev. Microbiol. 8, 105–116. doi:10.1038/nrmicro2279
Joliot, A., Pernelle, C., Deagostini-Bazin, H., Prochiantz, A., 1991. Antennapedia homeobox peptide regulates neural morphogenesis. Proc. Natl. Acad. Sci. U. S. A. 88, 1864–1868.
Jones, A.T., Sayers, E.J., 2012. Cell entry of cell penetrating peptides: tales of tails wagging dogs. J. Control. Release Off. J. Control. Release Soc. 161, 582–591. doi:10.1016/j.jconrel.2012.04.003
Jovic, M., Sharma, M., Rahajeng, J., Caplan, S., 2010. The early endosome: a busy sorting station for proteins at the crossroads. Histol. Histopathol. 25, 99–112.
Kakimoto, S., Hamada, T., Komatsu, Y., Takagi, M., Tanabe, T., Azuma, H., Shinkai, S., Nagasaki, T., 2009. The conjugation of diphtheria toxin T domain to poly(ethylenimine) based vectors for enhanced endosomal escape during gene transfection. Biomaterials 30, 402–408. doi:10.1016/j.biomaterials.2008.09.042
Kalmanti, L., Saussele, S., Lauseker, M., Müller, M.C., Dietz, C.T., Heinrich, L., Hanfstein, B., Proetel, U., Fabarius, A., Krause, S.W., Rinaldetti, S., Dengler, J., Falge, C., Oppliger-Leibundgut, E., Burchert, A., Neubauer, A., Kanz, L., Stegelmann, F., Pfreundschuh, M., Spiekermann, K., Scheid, C., Pfirrmann, M., Hochhaus, A., Hasford, J., Hehlmann, R., 2015. Safety and efficacy of imatinib in CML over a period of 10 years: data from the randomized CML-study IV. Leukemia. doi:10.1038/leu.2015.36
Karakoti, A.S., Shukla, R., Shanker, R., Singh, S., 2015. Surface functionalization of quantum dots for biological applications. Adv. Colloid Interface Sci. 215, 28–45. doi:10.1016/j.cis.2014.11.004
Kasper, J., Hermanns, M.I., Bantz, C., Koshkina, O., Lang, T., Maskos, M., Pohl, C., Unger, R.E., Kirkpatrick, C.J., 2013. Interactions of silica nanoparticles with lung epithelial cells and the association to flotillins. Arch. Toxicol. 87, 1053–1065. doi:10.1007/s00204-012-0876-5
Khafagy, E.-S., Morishita, M., Ida, N., Nishio, R., Isowa, K., Takayama, K., 2010. Structural requirements of penetratin absorption enhancement efficiency for insulin delivery. J. Control. Release Off. J. Control. Release Soc. 143, 302–310. doi:10.1016/j.jconrel.2010.01.019
Khandare, J., Calderón, M., Dagia, N.M., Haag, R., 2012. Multifunctional dendritic polymers in nanomedicine: opportunities and challenges. Chem. Soc. Rev. 41, 2824–2848. doi:10.1039/c1cs15242d
Kim, C.K., Ghosh, P., Pagliuca, C., Zhu, Z.-J., Menichetti, S., Rotello, V.M., 2009. Entrapment of Hydrophobic Drugs in Nanoparticle Monolayers with Efficient Release into Cancer Cells. J. Am. Chem. Soc. 131, 1360–1361. doi:10.1021/ja808137c
Kirkham, M., Fujita, A., Chadda, R., Nixon, S.J., Kurzchalia, T.V., Sharma, D.K., Pagano, R.E., Hancock, J.F., Mayor, S., Parton, R.G., 2005. Ultrastructural identification of uncoated caveolin-independent early endocytic vehicles. J. Cell Biol. 168, 465–476. doi:10.1083/jcb.200407078
Klann, M., Koeppl, H., Reuss, M., 2012. Spatial Modeling of Vesicle Transport and the Cytoskeleton: The Challenge of Hitting the Right Road. PLoS ONE 7, e29645. doi:10.1371/journal.pone.0029645
Kobayashi, M., Yamamoto, M., 2005. Molecular mechanisms activating the Nrf2-Keap1 pathway of antioxidant gene regulation. Antioxid. Redox Signal. 7, 385–394. doi:10.1089/ars.2005.7.385

Koivusalo, M., Welch, C., Hayashi, H., Scott, C.C., Kim, M., Alexander, T., Touret, N., Hahn, K.M., Grinstein, S., 2010. Amiloride inhibits macropinocytosis by lowering submembranous pH and preventing Rac1 and Cdc42 signaling. J. Cell Biol. 188, 547–563. doi:10.1083/jcb.200908086
Koltover, I., 1998. An Inverted Hexagonal Phase of Cationic Liposome-DNA Complexes Related to DNA Release and Delivery. Science 281, 78–81. doi:10.1126/science.281.5373.78
Kosaka, N., Iguchi, H., Ochiya, T., 2010. Circulating microRNA in body fluid: a new potential biomarker for cancer diagnosis and prognosis. Cancer Sci. 101, 2087–2092. doi:10.1111/j.1349-7006.2010.01650.x
Kosuge, M., Takeuchi, T., Nakase, I., Jones, A.T., Futaki, S., 2008. Cellular internalization and distribution of arginine-rich peptides as a function of extracellular peptide concentration, serum, and plasma membrane associated proteoglycans. Bioconjug. Chem. 19, 656–664. doi:10.1021/bc700289w
Koyama-Honda, I., Ritchie, K., Fujiwara, T., Iino, R., Murakoshi, H., Kasai, R.S., Kusumi, A., 2005. Fluorescence imaging for monitoring the colocalization of two single molecules in living cells. Biophys. J. 88, 2126–2136. doi:10.1529/biophysj.104.048967
Krauss, T.D., Peterson, J.J., 2011. Quantum dots: A charge for blinking. Nat. Mater. 11, 14–16. doi:10.1038/nmat3206
Kullberg, M., Owens, J.L., Mann, K., 2010. Listeriolysin O enhances cytoplasmic delivery by Her-2 targeting liposomes. J. Drug Target. 18, 313–320. doi:10.3109/10611861003663549
Kuo, C.-W., Chueh, D.-Y., Singh, N., Chien, F.-C., Chen, P., 2011. Targeted nuclear delivery using peptide-coated quantum dots. Bioconjug. Chem. 22, 1073–1080. doi:10.1021/bc100527m
Lachmanovich, E., Shvartsman, D.E., Malka, Y., Botvin, C., Henis, Y.I., Weiss, A.M., 2003. Co-localization analysis of complex formation among membrane proteins by computerized fluorescence microscopy: application to immunofluorescence co-patching studies. J. Microsc. 212, 122–131.
Lagerholm, B.C., Wang, M., Ernst, L.A., Ly, D.H., Liu, H., Bruchez, M.P., Waggoner, A.S., 2004. Multicolor Coding of Cells with Cationic Peptide Coated Quantum Dots. Nano Lett. 4, 2019–2022. doi:10.1021/nl049295v
Larsson, D.S.D., Liljas, L., van der Spoel, D., 2012. Virus Capsid Dissolution Studied by Microsecond Molecular Dynamics Simulations. PLoS Comput. Biol. 8, e1002502. doi:10.1371/journal.pcbi.1002502
Lei, H.-Y., Chang, C.-P., 2009. Lectin of Concanavalin A as an anti-hepatoma therapeutic agent. J. Biomed. Sci. 16, 10. doi:10.1186/1423-0127-16-10
Lengfeld, J., Cutforth, T., Agalliu, D., 2014. The role of angiogenesis in the pathology of multiple sclerosis. Vasc. Cell 6, 23. doi:10.1186/s13221-014-0023-6
Lesniak, A., Fenaroli, F., Monopoli, M.P., Åberg, C., Dawson, K.A., Salvati, A., 2012. Effects of the presence or absence of a protein corona on silica nanoparticle uptake and impact on cells. ACS Nano 6, 5845–5857. doi:10.1021/nn300223w
Lidke, K., Rieger, B., Jovin, T., Heintzmann, R., 2005. Superresolution by localization of quantum dots using blinking statistics. Opt. Express 13, 7052–7062.
Lim, J.P., Gleeson, P.A., 2011. Macropinocytosis: an endocytic pathway for internalising large gulps. Immunol. Cell Biol. 89, 836–843. doi:10.1038/icb.2011.20
Liu, B.R., Huang, Y., Winiarz, J.G., Chiang, H.-J., Lee, H.-J., 2011. Intracellular delivery of quantum dots mediated by a histidine- and arginine-rich HR9 cell-penetrating peptide through the direct membrane translocation mechanism. Biomaterials 32, 3520–3537. doi:10.1016/j.biomaterials.2011.01.041
Liu, B.R., Li, J.-F., Lu, S.-W., Leel, H.-J., Huang, Y.-W., Shannon, K.B., Aronstam, R.S., 2010. Cellular internalization of quantum dots noncovalently conjugated with arginine-rich cell-penetrating peptides. J. Nanosci. Nanotechnol. 10, 6534–6543.
Liu, B.R., Lo, S.-Y., Liu, C.-C., Chyan, C.-L., Huang, Y.-W., Aronstam, R.S., Lee, H.-J., 2013. Endocytic Trafficking of Nanoparticles Delivered by Cell-penetrating Peptides Comprised of Nona-

arginine and a Penetration Accelerating Sequence. PLoS ONE 8, e67100. doi:10.1371/journal.pone.0067100
Liu, S.-L., Li, J., Zhang, Z.-L., Wang, Z.-G., Tian, Z.-Q., Wang, G.-P., Pang, D.-W., 2013. Fast and High-Accuracy Localization for Three-Dimensional Single-Particle Tracking. Sci. Rep. 3. doi:10.1038/srep02462
Liu, S.-L., Zhang, Z.-L., Sun, E.-Z., Peng, J., Xie, M., Tian, Z.-Q., Lin, Y., Pang, D.-W., 2011. Visualizing the endocytic and exocytic processes of wheat germ agglutinin by quantum dot-based single-particle tracking. Biomaterials 32, 7616–7624. doi:10.1016/j.biomaterials.2011.06.046
Liu, S.-L., Zhang, Z.-L., Tian, Z.-Q., Zhao, H.-S., Liu, H., Sun, E.-Z., Xiao, G.F., Zhang, W., Wang, H.-Z., Pang, D.-W., 2012. Effectively and efficiently dissecting the infection of influenza virus by quantum-dot-based single-particle tracking. ACS Nano 6, 141–150. doi:10.1021/nn2031353
Lo, S.-C., Li, X., Henzl, M.T., Beamer, L.J., Hannink, M., 2006. Structure of the Keap1:Nrf2 interface provides mechanistic insight into Nrf2 signaling. EMBO J. 25, 3605–3617. doi:10.1038/sj.emboj.7601243
Lowe, A.R., Siegel, J.J., Kalab, P., Siu, M., Weis, K., Liphardt, J.T., 2010. Selectivity mechanism of the nuclear pore complex characterized by single cargo tracking. Nature 467, 600–603. doi:10.1038/nature09285
Lund, F.W., Jensen, M.L.V., Christensen, T., Nielsen, G.K., Heegaard, C.W., Wüstner, D., 2014. SpatTrack: An Imaging Toolbox for Analysis of Vesicle Motility and Distribution in Living Cells. Traffic Cph. Den. 15, 1406–1429. doi:10.1111/tra.12228
Lundmark, R., Doherty, G.J., Howes, M.T., Cortese, K., Vallis, Y., Parton, R.G., McMahon, H.T., 2008. The GTPase-activating protein GRAF1 regulates the CLIC/GEEC endocytic pathway. Curr. Biol. CB 18, 1802–1808. doi:10.1016/j.cub.2008.10.044
Lundqvist, M., Stigler, J., Cedervall, T., Berggård, T., Flanagan, M.B., Lynch, I., Elia, G., Dawson, K., 2011. The evolution of the protein corona around nanoparticles: a test study. ACS Nano 5, 7503–7509. doi:10.1021/nn202458g
Lundqvist, M., Stigler, J., Elia, G., Lynch, I., Cedervall, T., Dawson, K.A., 2008. Nanoparticle size and surface properties determine the protein corona with possible implications for biological impacts. Proc. Natl. Acad. Sci. U. S. A. 105, 14265–14270. doi:10.1073/pnas.0805135105
Lunov, O., Syrovets, T., Loos, C., Beil, J., Delacher, M., Tron, K., Nienhaus, G.U., Musyanovych, A., Mailänder, V., Landfester, K., Simmet, T., 2011. Differential uptake of functionalized polystyrene nanoparticles by human macrophages and a monocytic cell line. ACS Nano 5, 1657–1669. doi:10.1021/nn2000756
Maeda, H., 2001. The enhanced permeability and retention (EPR) effect in tumor vasculature: the key role of tumor-selective macromolecular drug targeting. Adv. Enzyme Regul. 41, 189–207.
Magzoub, M., Eriksson, L.E.G., Gräslund, A., 2003. Comparison of the interaction, positioning, structure induction and membrane perturbation of cell-penetrating peptides and non-translocating variants with phospholipid vesicles. Biophys. Chem. 103, 271–288.
Mahon, E., Salvati, A., Baldelli Bombelli, F., Lynch, I., Dawson, K.A., 2012. Designing the nanoparticle-biomolecule interface for “targeting and therapeutic delivery.” J. Control. Release Off. J. Control. Release Soc. 161, 164–174. doi:10.1016/j.jconrel.2012.04.009
Majoros, I.J., Thomas, T.P., Mehta, C.B., Baker, J.R., 2005. Poly(amidoamine) dendrimer-based multifunctional engineered nanodevice for cancer therapy. J. Med. Chem. 48, 5892–5899. doi:10.1021/jm0401863
Manders, E.M.M., Verbeek, F.J., Aten, J.A., 1993. Measurement of co-localization of objects in dual-colour confocal images. J. Microsc. 169, 375–382. doi:10.1111/j.1365-2818.1993.tb03313.x
Ma, N., Ma, C., Li, C., Wang, T., Tang, Y., Wang, H., Moul, X., Chen, Z., Hel, N., 2013. Influence of nanoparticle shape, size, and surface functionalization on cellular uptake. J. Nanosci. Nanotechnol. 13, 6485–6498.
Marchiani, A., Rozzo, C., Fadda, A., Delogu, G., Ruzza, P., 2013. Curcumin And Curcumin-Like Molecules: From Spice To Drugs. Curr. Med. Chem.

Marfori, M., Mynott, A., Ellis, J.J., Mehdi, A.M., Saunders, N.F.W., Curmi, P.M., Forwood, J.K., Bodén, M., Kobe, B., 2011. Molecular basis for specificity of nuclear import and prediction of nuclear localization. Biochim. Biophys. Acta BBA - Mol. Cell Res. 1813, 1562–1577. doi:10.1016/j.bbamcr.2010.10.013

Martens, T.F., Remaut, K., Demeester, J., De Smedt, S.C., Braeckmans, K., 2014. Intracellular delivery of nanomaterials: How to catch endosomal escape in the act. Nano Today 9, 344–364. doi:10.1016/j.nantod.2014.04.011

Martin, A., Komada, M.R., Sane, D.C., 2003. Abnormal angiogenesis in diabetes mellitus. Med. Res. Rev. 23, 117–145. doi:10.1002/med.10024

Martín, I., Teixidó, M., Giralt, E., 2013. Intracellular fate of peptide-mediated delivered cargoes. Curr. Pharm. Des. 19, 2924–2942.

Matsumura, Y., Maeda, H., 1986. A new concept for macromolecular therapeutics in cancer chemotherapy: mechanism of tumoritropic accumulation of proteins and the antitumor agent smancs. Cancer Res. 46, 6387–6392.

Maxfield, F.R., McGraw, T.E., 2004. Endocytic recycling. Nat. Rev. Mol. Cell Biol. 5, 121–132. doi:10.1038/nrm1315

Ma, X., Wu, Y., Jin, S., Tian, Y., Zhang, X., Zhao, Y., Yu, L., Liang, X.-J., 2011. Gold Nanoparticles Induce Autophagosome Accumulation through Size-Dependent Nanoparticle Uptake and Lysosome Impairment. ACS Nano 5, 8629–8639. doi:10.1021/nn202155y

McNaughton, B.R., Cronican, J.J., Thompson, D.B., Liu, D.R., 2009. Mammalian cell penetration, siRNA transfection, and DNA transfection by supercharged proteins. Proc. Natl. Acad. Sci. U. S. A. 106, 6111–6116. doi:10.1073/pnas.0807883106

Medintz, I.L., Pons, T., Delehanty, J.B., Susumu, K., Brunel, F.M., Dawson, P.E., Mattoussi, H., 2008. Intracellular delivery of quantum dot-protein cargos mediated by cell penetrating peptides. Bioconjug. Chem. 19, 1785–1795. doi:10.1021/bc800089r

Meng, H., Yang, S., Li, Z., Xia, T., Chen, J., Ji, Z., Zhang, H., Wang, X., Lin, S., Huang, C., Zhou, Z.H., Zink, J.I., Nel, A.E., 2011. Aspect Ratio Determines the Quantity of Mesoporous Silica Nanoparticle Uptake by a Small GTPase-Dependent Macropinocytosis Mechanism. ACS Nano 5, 4434–4447. doi:10.1021/nn103344k

Mercer, J., Helenius, A., 2008. Vaccinia virus uses macropinocytosis and apoptotic mimicry to enter host cells. Science 320, 531–535. doi:10.1126/science.1155164

Michalet, X., 2005. Quantum Dots for Live Cells, in Vivo Imaging, and Diagnostics. Science 307, 538–544. doi:10.1126/science.1104274

Milani, S., Bombelli, F.B., Pitek, A.S., Dawson, K.A., Rädler, J., 2012. Reversible versus irreversible binding of transferrin to polystyrene nanoparticles: soft and hard corona. ACS Nano 6, 2532–2541. doi:10.1021/nn204951s

Miller, D.K., Griffiths, E., Lenard, J., Firestone, R.A., 1983. Cell killing by lysosomotropic detergents. J. Cell Biol. 97, 1841–1851.

Monopoli, M.P., Aberg, C., Salvati, A., Dawson, K.A., 2012. Biomolecular coronas provide the biological identity of nanosized materials. Nat. Nanotechnol. 7, 779–786. doi:10.1038/nnano.2012.207

Monopoli, M.P., Walczyk, D., Campbell, A., Elia, G., Lynch, I., Bombelli, F.B., Dawson, K.A., 2011. Physical-chemical aspects of protein corona: relevance to in vitro and in vivo biological impacts of nanoparticles. J. Am. Chem. Soc. 133, 2525–2534. doi:10.1021/ja107583h

Moreira, C., Oliveira, H., Pires, L.R., Simões, S., Barbosa, M.A., Pêgo, A.P., 2009. Improving chitosan-mediated gene transfer by the introduction of intracellular buffering moieties into the chitosan backbone. Acta Biomater. 5, 2995–3006. doi:10.1016/j.actbio.2009.04.021

Morrison, I.E.G., Karakikes, I., Barber, R.E., Fernández, N., Cherry, R.J., 2003. Detecting and quantifying colocalization of cell surface molecules by single particle fluorescence imaging. Biophys. J. 85, 4110–4121. doi:10.1016/S0006-3495(03)74823-1

Mullard, A., 2015. 2014 FDA drug approvals. Nat. Rev. Drug Discov. 14, 77–81. doi:10.1038/nrd4545

Murk, J.L.A.N., Humbel, B.M., Ziese, U., Griffith, J.M., Posthuma, G., Slot, J.W., Koster, A.J., Verkleij, A.J., Geuze, H.J., Kleijmeer, M.J., 2003. Endosomal compartmentalization in three dimensions: Implications for membrane fusion. Proc. Natl. Acad. Sci. 100, 13332–13337. doi:10.1073/pnas.2232379100

Murphy, J.R., 2011. Mechanism of Diphtheria Toxin Catalytic Domain Delivery to the Eukaryotic Cell Cytosol and the Cellular Factors that Directly Participate in the Process. Toxins 3, 294–308. doi:10.3390/toxins3030294

Muthu, M.S., Kulkarni, S.A., Raju, A., Feng, S.-S., 2012. Theranostic liposomes of TPGS coating for targeted co-delivery of docetaxel and quantum dots. Biomaterials 33, 3494–3501. doi:10.1016/j.biomaterials.2012.01.036

Muthusamy, B., Hanumanthu, G., Suresh, S., Rekha, B., Srinivas, D., Karthick, L., Vrushabendra, B.M., Sharma, S., Mishra, G., Chatterjee, P., Mangala, K.S., Shivashankar, H.N., Chandrika, K.N., Deshpande, N., Suresh, M., Kannabiran, N., Niranjan, V., Nalli, A., Prasad, T.S.K., Arun, K.S., Reddy, R., Chandran, S., Jadhav, T., Julie, D., Mahesh, M., John, S.L., Palvankar, K., Sudhir, D., Bala, P., Rashmi, N.S., Vishnupriya, G., Dhar, K., Reshma, S., Chaerkady, R., Gandhi, T.K.B., Harsha, H.C., Mohan, S.S., Deshpande, K.S., Sarker, M., Pandey, A., 2005. Plasma Proteome Database as a resource for proteomics research. Proteomics 5, 3531–3536. doi:10.1002/pmic.200401335

Nakase, I., Takeuchi, T., Tanaka, G., Futaki, S., 2008. Methodological and cellular aspects that govern the internalization mechanisms of arginine-rich cell-penetrating peptides. Adv. Drug Deliv. Rev. 60, 598–607. doi:10.1016/j.addr.2007.10.006

NICE, 2015. National Institute for Clinical Excellence (NICE). https://www.nice.org.uk/.

NICE, 2010. Bevacizumab in combination with a taxane for the first-line treatment of metastatic breast cancer. https://www.nice.org.uk/guidance/ta214.

Nonnenmacher, M., Weber, T., 2011. Adeno-associated virus 2 infection requires endocytosis through the CLIC/GEEC pathway. Cell Host Microbe 10, 563–576. doi:10.1016/j.chom.2011.10.014

North, A.J., 2006. Seeing is believing? A beginners' guide to practical pitfalls in image acquisition. J. Cell Biol. 172, 9–18. doi:10.1083/jcb.200507103

Oakley, J.P., Shann, R.T., 1991. Efficient method for finding the position of object boundaries to sub-pixel precision. Image Vis. Comput. 9, 262–272. doi:10.1016/0262-8856(91)90030-S

Oberholzer, M., Ostreicher, M., Christen, H., Brühlmann, M., 1996. Methods in quantitative image analysis. Histochem. Cell Biol. 105, 333–355.

Okutucu, B., Dınçer, A., Habib, Ö., Zıhnıoglu, F., 2007. Comparison of five methods for determination of total plasma protein concentration. J. Biochem. Biophys. Methods 70, 709–711. doi:10.1016/j.jbbm.2007.05.009

Oliphant, T.E., 2007. Python for Scientific Computing. Comput. Sci. Eng. 9, 10–20. doi:10.1109/MCSE.2007.58

Pack, D.W., Putnam, D., Langer, R., 2000. Design of imidazole-containing endosomolytic biopolymers for gene delivery. Biotechnol. Bioeng. 67, 217–223.

Parthasarathy, R., 2012. Rapid, accurate particle tracking by calculation of radial symmetry centers. Nat. Methods 9, 724–726. doi:10.1038/nmeth.2071

Parton, R.G., del Pozo, M.A., 2013. Caveolae as plasma membrane sensors, protectors and organizers. Nat. Rev. Mol. Cell Biol. 14, 98–112. doi:10.1038/nrm3512

Parton, R.G., Howes, M.T., 2010. Revisiting caveolin trafficking: the end of the caveosome. J. Cell Biol. 191, 439–441. doi:10.1083/jcb.201009093

Patra, D., Barakat, C., 2011. Synchronous fluorescence spectroscopic study of solvatochromic curcumin dye. Spectrochim. Acta. A. Mol. Biomol. Spectrosc. 79, 1034–1041. doi:10.1016/j.saa.2011.04.016

Pavlides, S., Gutierrez-Pajares, J.L., Danilo, C., Lisanti, M.P., Frank, P.G., 2012. Atherosclerosis, caveolae and caveolin-1. Adv. Exp. Med. Biol. 729, 127–144. doi:10.1007/978-1-4614-1222-9_9

Pene, F., Courtine, E., Cariou, A., Mira, J.-P., 2009. Toward theragnostics. Crit. Care Med. 37, S50–58. doi:10.1097/CCM.0b013e3181921349

Peng, null, Manna, null, Yang, null, Wickham, null, Scher, null, Kadavanich, null, Alivisatos, null, 2000. Shape control of CdSe nanocrystals. Nature 404, 59–61. doi:10.1038/35003535

Petre, C.E., Dittmer, D.P., 2007. Liposomal daunorubicin as treatment for Kaposi's sarcoma. Int. J. Nanomedicine 2, 277–288.

Petryayeva, E., Algar, W.R., Medintz, I.L., 2013. Quantum dots in bioanalysis: a review of applications across various platforms for fluorescence spectroscopy and imaging. Appl. Spectrosc. 67, 215–252. doi:10.1366/12-06948

Pfeffer, S.R., 2009. Multiple routes of protein transport from endosomes to the trans Golgi network. FEBS Lett. 583, 3811–3816. doi:10.1016/j.febslet.2009.10.075

Phillips, G.N., 1997. Structure and dynamics of green fluorescent protein. Curr. Opin. Struct. Biol. 7, 821–827.

Pierobon, P., Cappello, G., 2012. Quantum dots to tail single bio-molecules inside living cells. Adv. Drug Deliv. Rev. 64, 167–178. doi:10.1016/j.addr.2011.06.004

Pinaud, F., Clarke, S., Sittner, A., Dahan, M., 2010. Probing cellular events, one quantum dot at a time. Nat. Methods 7, 275–285. doi:10.1038/nmeth.1444

Poteryaev, D., Datta, S., Ackema, K., Zerial, M., Spang, A., 2010. Identification of the switch in early-to-late endosome transition. Cell 141, 497–508. doi:10.1016/j.cell.2010.03.011

Prapainop, K., Wentworth, P., 2011. A shotgun proteomic study of the protein corona associated with cholesterol and atheronal-B surface-modified quantum dots. Eur. J. Pharm. Biopharm. 77, 353–359. doi:10.1016/j.ejpb.2010.12.026

Probst, C.E., Zrazhevskiy, P., Bagalkot, V., Gao, X., 2013. Quantum dots as a platform for nanoparticle drug delivery vehicle design. Adv. Drug Deliv. Rev. 65, 703–718. doi:10.1016/j.addr.2012.09.036

Puckett, C.A., Barton, J.K., 2009. Fluorescein redirects a ruthenium-octaarginine conjugate to the nucleus. J. Am. Chem. Soc. 131, 8738–8739. doi:10.1021/ja9025165

Pulla Reddy, A.C., Sudharshan, E., Appu Rao, A.G., Lokesh, B.R., 1999. Interaction of curcumin with human serum albumin--a spectroscopic study. Lipids 34, 1025–1029.

Rabinovitch, M., 1995. Professional and non-professional phagocytes: an introduction. Trends Cell Biol. 5, 85–87. doi:10.1016/S0962-8924(00)88955-2

Ranjbarvaziri, S., Kiani, S., Akhlaghi, A., Vosough, A., Baharvand, H., Aghdami, N., 2011. Quantum dot labeling using positive charged peptides in human hematopoetic and mesenchymal stem cells. Biomaterials 32, 5195–5205. doi:10.1016/j.biomaterials.2011.04.004

Rappoport, J., Smith, Giroud, Wiggins, Mazzolin, Dyson, 2012. Cellular entry of nanoparticles via serum sensitive clathrin-mediated endocytosis, and plasma membrane permeabilization. Int. J. Nanomedicine 2045. doi:10.2147/IJN.S29334

Rauch, C., Feifel, E., Amann, E.-M., Spötl, H.P., Schennach, H., Pfaller, W., Gstraunthaler, G., 2011. Alternatives to the use of fetal bovine serum: human platelet lysates as a serum substitute in cell culture media. ALTEX 28, 305–316.

Ravindran, J., Prasad, S., Aggarwal, B.B., 2009. Curcumin and cancer cells: how many ways can curry kill tumor cells selectively? AAPS J. 11, 495–510. doi:10.1208/s12248-009-9128-x

Reddy, S.T., van der Vlies, A.J., Simeoni, E., Angeli, V., Randolph, G.J., O'Neil, C.P., Lee, L.K., Swartz, M.A., Hubbell, J.A., 2007. Exploiting lymphatic transport and complement activation in nanoparticle vaccines. Nat. Biotechnol. 25, 1159–1164. doi:10.1038/nbt1332

Reeves, V.L., Thomas, C.M., Smart, E.J., 2012. Lipid rafts, caveolae and GPI-linked proteins. Adv. Exp. Med. Biol. 729, 3–13. doi:10.1007/978-1-4614-1222-9_1

Reinemann, C., Strehlitz, B., 2014. Aptamer-modified nanoparticles and their use in cancer diagnostics and treatment. Swiss Med. Wkly. 144, w13908. doi:10.4414/smw.2014.13908
Rejman, J., Oberle, V., Zuhorn, I.S., Hoekstra, D., 2004. Size-dependent internalization of particles via the pathways of clathrin- and caveolae-mediated endocytosis. Biochem. J. 377, 159–169. doi:10.1042/BJ20031253
Remaut, K., Oorschot, V., Braeckmans, K., Klumperman, J., De Smedt, S.C., 2014. Lysosomal capturing of cytoplasmic injected nanoparticles by autophagy: An additional barrier to non viral gene delivery. J. Controlled Release 195, 29–36. doi:10.1016/j.jconrel.2014.08.002
Rennert, R., Wespe, C., Beck-Sickinger, A.G., Neundorf, I., 2006. Developing novel hCT derived cell-penetrating peptides with improved metabolic stability. Biochim. Biophys. Acta BBA - Biomembr. 1758, 347–354. doi:10.1016/j.bbamem.2005.10.006
Richardson, S.C.W., Wallom, K.-L., Ferguson, E.L., Deacon, S.P.E., Davies, M.W., Powell, A.J., Piper, R.C., Duncan, R., 2008. The use of fluorescence microscopy to define polymer localisation to the late endocytic compartments in cells that are targets for drug delivery. J. Control. Release Off. J. Control. Release Soc. 127, 1–11. doi:10.1016/j.jconrel.2007.12.015
Rink, J., Ghigo, E., Kalaidzidis, Y., Zerial, M., 2005. Rab Conversion as a Mechanism of Progression from Early to Late Endosomes. Cell 122, 735–749. doi:10.1016/j.cell.2005.06.043
Röcker, C., Pötzl, M., Zhang, F., Parak, W.J., Nienhaus, G.U., 2009. A quantitative fluorescence study of protein monolayer formation on colloidal nanoparticles. Nat. Nanotechnol. 4, 577–580. doi:10.1038/nnano.2009.195
Rosenthal, S.J., Chang, J.C., Kovtun, O., McBride, J.R., Tomlinson, I.D., 2011. Biocompatible quantum dots for biological applications. Chem. Biol. 18, 10–24. doi:10.1016/j.chembiol.2010.11.013
Rothbard, J.B., Jessop, T.C., Lewis, R.S., Murray, B.A., Wender, P.A., 2004. Role of membrane potential and hydrogen bonding in the mechanism of translocation of guanidinium-rich peptides into cells. J. Am. Chem. Soc. 126, 9506–9507. doi:10.1021/ja0482536
Rothberg, K.G., Heuser, J.E., Donzell, W.C., Ying, Y.S., Glenney, J.R., Anderson, R.G., 1992. Caveolin, a protein component of caveolae membrane coats. Cell 68, 673–682.
Ruan, G., Agrawal, A., Marcus, A.I., Nie, S., 2007. Imaging and tracking of tat peptide-conjugated quantum dots in living cells: new insights into nanoparticle uptake, intracellular transport, and vesicle shedding. J. Am. Chem. Soc. 129, 14759–14766. doi:10.1021/ja074936k
Ruoslahti, E., Bhatia, S.N., Sailor, M.J., 2010. Targeting of drugs and nanoparticles to tumors. J. Cell Biol. 188, 759–768. doi:10.1083/jcb.200910104
Ruthardt, N., Lamb, D.C., Bräuchle, C., 2011. Single-particle Tracking as a Quantitative Microscopy-based Approach to Unravel Cell Entry Mechanisms of Viruses and Pharmaceutical Nanoparticles. Mol. Ther. 19, 1199–1211. doi:10.1038/mt.2011.102
Ruusuvuori, P., Aijo, T., Chowdhury, S., Garmendia-Torres, C., Selinummi, J., Birbaumer, M., Dudley, A.M., Pelkmans, L., Yli-Harja, O., 2010. Evaluation of methods for detection of fluorescence labeled subcellular objects in microscope images. BMC Bioinformatics 11, 248. doi:10.1186/1471-2105-11-248
Sabharanjak, S., Sharma, P., Parton, R.G., Mayor, S., 2002. GPI-anchored proteins are delivered to recycling endosomes via a distinct cdc42-regulated, clathrin-independent pinocytic pathway. Dev. Cell 2, 411–423.
Safra, T., Muggia, F., Jeffers, S., Tsao-Wei, D.D., Groshen, S., Lyass, O., Henderson, R., Berry, G., Gabizon, A., 2000. Pegylated liposomal doxorubicin (doxil): reduced clinical cardiotoxicity in patients reaching or exceeding cumulative doses of 500 mg/m2. Ann. Oncol. Off. J. Eur. Soc. Med. Oncol. ESMO 11, 1029–1033.
Saha, K., Agasti, S.S., Kim, C., Li, X., Rotello, V.M., 2012. Gold Nanoparticles in Chemical and Biological Sensing. Chem. Rev. 112, 2739–2779. doi:10.1021/cr2001178
Sahay, G., Querbes, W., Alabi, C., Eltoukhy, A., Sarkar, S., Zurenko, C., Karagiannis, E., Love, K., Chen, D., Zoncu, R., Buganim, Y., Schroeder, A., Langer, R., Anderson, D.G., 2013. Efficiency of

siRNA delivery by lipid nanoparticles is limited by endocytic recycling. Nat. Biotechnol. 31, 653–658. doi:10.1038/nbt.2614

Sallusto, F., Cella, M., Danieli, C., Lanzavecchia, A., 1995. Dendritic cells use macropinocytosis and the mannose receptor to concentrate macromolecules in the major histocompatibility complex class II compartment: downregulation by cytokines and bacterial products. J. Exp. Med. 182, 389–400.

Salvati, A., Pitek, A.S., Monopoli, M.P., Prapainop, K., Bombelli, F.B., Hristov, D.R., Kelly, P.M., Åberg, C., Mahon, E., Dawson, K.A., 2013. Transferrin-functionalized nanoparticles lose their targeting capabilities when a biomolecule corona adsorbs on the surface. Nat. Nanotechnol. 8, 137–143. doi:10.1038/nnano.2012.237

Sandin, P., Fitzpatrick, L.W., Simpson, J.C., Dawson, K.A., 2012. High-speed imaging of Rab family small GTPases reveals rare events in nanoparticle trafficking in living cells. ACS Nano 6, 1513–1521. doi:10.1021/nn204448x

Sandvig, K., Torgersen, M.L., Engedal, N., Skotland, T., Iversen, T.-G., 2010. Protein toxins from plants and bacteria: Probes for intracellular transport and tools in medicine. FEBS Lett. 584, 2626–2634. doi:10.1016/j.febslet.2010.04.008

Sankur, B., 2004. Survey over image thresholding techniques and quantitative performance evaluation. J. Electron. Imaging 13, 146. doi:10.1117/1.1631315

Savina, A., Amigorena, S., 2007. Phagocytosis and antigen presentation in dendritic cells. Immunol. Rev. 219, 143–156. doi:10.1111/j.1600-065X.2007.00552.x

Sayers, E.J., Cleal, K., Eissa, N.G., Watson, P., Jones, A.T., 2014. Distal phenylalanine modification for enhancing cellular delivery of fluorophores, proteins and quantum dots by cell penetrating peptides. J. Control. Release Off. J. Control. Release Soc. 195, 55–62. doi:10.1016/j.jconrel.2014.07.055

Sbalzarini, I.F., Koumoutsakos, P., 2005. Feature point tracking and trajectory analysis for video imaging in cell biology. J. Struct. Biol. 151, 182–195. doi:10.1016/j.jsb.2005.06.002

Schäffler, M., Semmler-Behnke, M., Sarioglu, H., Takenaka, S., Wenk, A., Schleh, C., Hauck, S.M., Johnston, B.D., Kreyling, W.G., 2013. Serum protein identification and quantification of the corona of 5, 15 and 80 nm gold nanoparticles. Nanotechnology 24, 265103. doi:10.1088/0957-4484/24/26/265103

Schlegel, A., Largeau, C., Bigey, P., Bessodes, M., Lebozec, K., Scherman, D., Escriou, V., 2011. Anionic polymers for decreased toxicity and enhanced in vivo delivery of siRNA complexed with cationic liposomes. J. Control. Release Off. J. Control. Release Soc. 152, 393–401. doi:10.1016/j.jconrel.2011.03.031

Schmoranzer, J., 2003. Role of Microtubules in Fusion of Post-Golgi Vesicles to the Plasma Membrane. Mol. Biol. Cell 14, 1558–1569. doi:10.1091/mbc.E02-08-0500

Schneider, C.A., Rasband, W.S., Eliceiri, K.W., 2012. NIH Image to ImageJ: 25 years of image analysis. Nat. Methods 9, 671–675. doi:10.1038/nmeth.2089

Schulte, T., Paschke, K.A., Laessing, U., Lottspeich, F., Stuermer, C.A., 1997. Reggie-1 and reggie-2, two cell surface proteins expressed by retinal ganglion cells during axon regeneration. Dev. Camb. Engl. 124, 577–587.

Schütz, C.A., Juillerat-Jeanneret, L., Mueller, H., Lynch, I., Riediker, M., NanoImpactNet Consortium, 2013. Therapeutic nanoparticles in clinics and under clinical evaluation. Nanomed. 8, 449–467. doi:10.2217/nnm.13.8

Scikit-image, 2015. Scikit-image, image processing in python. http://scikit-image.org/.

Sergé, A., Bertaux, N., Rigneault, H., Marguet, D., 2008. Dynamic multiple-target tracing to probe spatiotemporal cartography of cell membranes. Nat. Methods 5, 687–694. doi:10.1038/nmeth.1233

Serra, P., Santamaria, P., 2015. Nanoparticle-based autoimmune disease therapy. Clin. Immunol. Orlando Fla. doi:10.1016/j.clim.2015.02.003

Settembre, C., Fraldi, A., Medina, D.L., Ballabio, A., 2013. Signals from the lysosome: a control centre for cellular clearance and energy metabolism. Nat. Rev. Mol. Cell Biol. 14, 283–296. doi:10.1038/nrm3565

Shan, D., Li, J., Cai, P., Prasad, P., Liu, F., Rauth, A.M., Wu, X.Y., 2015. RGD-conjugated solid lipid nanoparticles inhibit adhesion and invasion of αvβ 3 integrin-overexpressing breast cancer cells. Drug Deliv. Transl. Res. 5, 15–26. doi:10.1007/s13346-014-0210-2

Sharma, R.A., Gescher, A.J., Steward, W.P., 2005. Curcumin: the story so far. Eur. J. Cancer Oxf. Engl. 1990 41, 1955–1968. doi:10.1016/j.ejca.2005.05.009

Shatz, M., Liscovitch, M., 2008. Caveolin-1: a tumor-promoting role in human cancer. Int. J. Radiat. Biol. 84, 177–189. doi:10.1080/09553000701745293

Shivanandan, A., Radenovic, A., Sbalzarini, I.F., 2013. MosaicIA: an ImageJ/Fiji plugin for spatial pattern and interaction analysis. BMC Bioinformatics 14, 349. doi:10.1186/1471-2105-14-349

Shi, Z., Chen, J., Li, C., An, N., Wang, Z., Yang, S., Huang, K., Bao, J., 2014. Antitumor effects of concanavalin A and Sophora flavescens lectin in vitro and in vivo. Acta Pharmacol. Sin. 35, 248–256. doi:10.1038/aps.2013.151

Shoba, G., Joy, D., Joseph, T., Majeed, M., Rajendran, R., Srinivas, P.S., 1998. Influence of piperine on the pharmacokinetics of curcumin in animals and human volunteers. Planta Med. 64, 353–356. doi:10.1055/s-2006-957450

Simpson, J.C., Griffiths, G., Wessling-Resnick, M., Fransen, J.A.M., Bennett, H., Jones, A.T., 2004. A role for the small GTPase Rab21 in the early endocytic pathway. J. Cell Sci. 117, 6297–6311. doi:10.1242/jcs.01560

Sleep, D., 2014. Albumin and its application in drug delivery. Expert Opin. Drug Deliv. 1–20. doi:10.1517/17425247.2015.993313

Smith, J.J., Aitchison, J.D., 2013. Peroxisomes take shape. Nat. Rev. Mol. Cell Biol. 14, 803–817. doi:10.1038/nrm3700

Soenen, S.J., Demeester, J., De Smedt, S.C., Braeckmans, K., 2012. The cytotoxic effects of polymer-coated quantum dots and restrictions for live cell applications. Biomaterials 33, 4882–4888. doi:10.1016/j.biomaterials.2012.03.042

Sonawane, N.D., Szoka, F.C., Verkman, A.S., 2003. Chloride accumulation and swelling in endosomes enhances DNA transfer by polyamine-DNA polyplexes. J. Biol. Chem. 278, 44826–44831. doi:10.1074/jbc.M308643200

Son, K.K., Tkach, D., Rosenblatt, J., 2001. Delipidated serum abolishes the inhibitory effect of serum on in vitro liposome-mediated transfection. Biochim. Biophys. Acta BBA - Biomembr. 1511, 201–205. doi:10.1016/S0005-2736(01)00297-8

Soo Choi, H., Liu, W., Misra, P., Tanaka, E., Zimmer, J.P., Itty Ipe, B., Bawendi, M.G., Frangioni, J.V., 2007. Renal clearance of quantum dots. Nat. Biotechnol. 25, 1165–1170. doi:10.1038/nbt1340

Steel, R., Cowan, J., Payerne, E., O'Connell, M.A., Searcey, M., 2012. Anti-inflammatory Effect of a Cell-Penetrating Peptide Targeting the Nrf2/Keap1 Interaction. ACS Med. Chem. Lett. 3, 407–410. doi:10.1021/ml300041g

Steinman, R.M., Brodie, S.E., Cohn, Z.A., 1976. Membrane flow during pinocytosis. A stereologic analysis. J. Cell Biol. 68, 665–687.

Steinman, R.M., Mellman, I.S., Muller, W.A., Cohn, Z.A., 1983. Endocytosis and the recycling of plasma membrane. J. Cell Biol. 96, 1–27.

Stolnik, S., Illum, L., Davis, S.S., 1995. Long circulating microparticulate drug carriers. Adv. Drug Deliv. Rev. 16, 195–214. doi:10.1016/0169-409X(95)00025-3

Stuermer, C.A.O., 2011. Reggie/flotillin and the targeted delivery of cargo: Reggie/flotillin and the targeted delivery of cargo. J. Neurochem. 116, 708–713. doi:10.1111/j.1471-4159.2010.07007.x

Stuermer, C.A.O., Langhorst, M.F., Wiechers, M.F., Legler, D.F., Von Hanwehr, S.H., Guse, A.H., Plattner, H., 2004. PrPc capping in T cells promotes its association with the lipid raft proteins reggie-1 and reggie-2 and leads to signal transduction. FASEB J. Off. Publ. Fed. Am. Soc. Exp. Biol. 18, 1731–1733. doi:10.1096/fj.04-2150fje

Subramanian, A., Ma, H., Dahl, K.N., Zhu, J., Diamond, S.L., 2002. Adenovirus or HA-2 fusogenic peptide-assisted lipofection increases cytoplasmic levels of plasmid in nondividing endothelium with little enhancement of transgene expression. J. Gene Med. 4, 75–83.

Suresh, D., Zambre, A., Chanda, N., Hoffman, T.J., Smith, C.J., Robertson, J.D., Kannan, R., 2014. Bombesin peptide conjugated gold nanocages internalize via clathrin mediated endocytosis. Bioconjug. Chem. 25, 1565–1579. doi:10.1021/bc500295s

Surugau, N., Urban, P.L., 2009. Electrophoretic methods for separation of nanoparticles. J. Sep. Sci. 32, 1889–1906. doi:10.1002/jssc.200900071

Susumu, K., Oh, E., Delehanty, J.B., Blanco-Canosa, J.B., Johnson, B.J., Jain, V., Hervey, W.J., 4th, Algar, W.R., Boeneman, K., Dawson, P.E., Medintz, I.L., 2011. Multifunctional compact zwitterionic ligands for preparing robust biocompatible semiconductor quantum dots and gold nanoparticles. J. Am. Chem. Soc. 133, 9480–9496. doi:10.1021/ja201919s

Szeto, H.H., Schiller, P.W., Zhao, K., Luo, G., 2005. Fluorescent dyes alter intracellular targeting and function of cell-penetrating tetrapeptides. FASEB J. Off. Publ. Fed. Am. Soc. Exp. Biol. 19, 118–120. doi:10.1096/fj.04-1982fje

Tan, Y.-X., Chen, C., Wang, Y.-L., Lin, S., Wang, Y., Li, S.-B., Jin, X.-P., Gao, H.-W., Du, F.-S., Gong, F., Ji, S.-P., 2012. Truncated peptides from melittin and its analog with high lytic activity at endosomal pH enhance branched polyethylenimine-mediated gene transfection. J. Gene Med. 14, 241–250. doi:10.1002/jgm.2609

Tekle, C., van Deurs, B., Sandvig, K., Iversen, T.-G., 2008. Cellular Trafficking of Quantum Dot-Ligand Bioconjugates and Their Induction of Changes in Normal Routing of Unconjugated Ligands. Nano Lett. 8, 1858–1865. doi:10.1021/nl0803848

Tenzer, S., Docter, D., Kuharev, J., Musyanovych, A., Fetz, V., Hecht, R., Schlenk, F., Fischer, D., Kiouptsi, K., Reinhardt, C., Landfester, K., Schild, H., Maskos, M., Knauer, S.K., Stauber, R.H., 2013. Rapid formation of plasma protein corona critically affects nanoparticle pathophysiology. Nat. Nanotechnol. 8, 772–781. doi:10.1038/nnano.2013.181

Tenzer, S., Docter, D., Rosfa, S., Wlodarski, A., Kuharev, J., Rekik, A., Knauer, S.K., Bantz, C., Nawroth, T., Bier, C., Sirirattanapan, J., Mann, W., Treuel, L., Zellner, R., Maskos, M., Schild, H., Stauber, R.H., 2011. Nanoparticle size is a critical physicochemical determinant of the human blood plasma corona: a comprehensive quantitative proteomic analysis. ACS Nano 5, 7155–7167. doi:10.1021/nn201950e

Théry, C., Ostrowski, M., Segura, E., 2009. Membrane vesicles as conveyors of immune responses. Nat. Rev. Immunol. 9, 581–593. doi:10.1038/nri2567

Thomas, C.E., Ehrhardt, A., Kay, M.A., 2003. Progress and problems with the use of viral vectors for gene therapy. Nat. Rev. Genet. 4, 346–358. doi:10.1038/nrg1066

Thompson, D.B., Villaseñor, R., Dorr, B.M., Zerial, M., Liu, D.R., 2012. Cellular uptake mechanisms and endosomal trafficking of supercharged proteins. Chem. Biol. 19, 831–843. doi:10.1016/j.chembiol.2012.06.014

Thompson, R.E., Larson, D.R., Webb, W.W., 2002. Precise nanometer localization analysis for individual fluorescent probes. Biophys. J. 82, 2775–2783. doi:10.1016/S0006-3495(02)75618-X

Thorén, P.E., Persson, D., Karlsson, M., Nordén, B., 2000. The antennapedia peptide penetratin translocates across lipid bilayers - the first direct observation. FEBS Lett. 482, 265–268.

Thukral, D.K., Dumoga, S., Mishra, A.K., 2014. Solid lipid nanoparticles: promising therapeutic nanocarriers for drug delivery. Curr. Drug Deliv. 11, 771–791.

Tkachenko, A.G., Xie, H., Coleman, D., Glomm, W., Ryan, J., Anderson, M.F., Franzen, S., Feldheim, D.L., 2003. Multifunctional Gold Nanoparticle−Peptide Complexes for Nuclear Targeting. J. Am. Chem. Soc. 125, 4700–4701. doi:10.1021/ja0296935

Tokatlian, T., Segura, T., 2010. siRNA applications in nanomedicine. Wiley Interdiscip. Rev. Nanomed. Nanobiotechnol. 2, 305–315. doi:10.1002/wnan.81

Tomczak, N., Liu, R., Vancso, J.G., 2013. Polymer-coated quantum dots. Nanoscale 5, 12018–12032. doi:10.1039/c3nr03949h

Treuel, L., Brandholt, S., Maffre, P., Wiegele, S., Shang, L., Nienhaus, G.U., 2014. Impact of Protein Modification on the Protein Corona on Nanoparticles and Nanoparticle–Cell Interactions. ACS Nano 8, 503–513. doi:10.1021/nn405019v

Tros de Ilarduya, C., Sun, Y., Düzgüneş, N., 2010. Gene delivery by lipoplexes and polyplexes. Eur. J. Pharm. Sci. 40, 159–170. doi:10.1016/j.ejps.2010.03.019

Urban-Klein, B., Werth, S., Abuharbeid, S., Czubayko, F., Aigner, A., 2005. RNAi-mediated gene-targeting through systemic application of polyethylenimine (PEI)-complexed siRNA in vivo. Gene Ther. 12, 461–466. doi:10.1038/sj.gt.3302425

Vachon, E., Martin, R., Plumb, J., Kwok, V., Vandivier, R.W., Glogauer, M., Kapus, A., Wang, X., Chow, C.-W., Grinstein, S., Downey, G.P., 2006. CD44 is a phagocytic receptor. Blood 107, 4149–4158. doi:10.1182/blood-2005-09-3808

van der Schaar, H.M., Rust, M.J., Chen, C., van der Ende-Metselaar, H., Wilschut, J., Zhuang, X., Smit, J.M., 2008. Dissecting the Cell Entry Pathway of Dengue Virus by Single-Particle Tracking in Living Cells. PLoS Pathog. 4, e1000244. doi:10.1371/journal.ppat.1000244

van der Walt, S., Schönberger, J.L., Nunez-Iglesias, J., Boulogne, F., Warner, J.D., Yager, N., Gouillart, E., Yu, T., scikit-image contributors, 2014. scikit-image: image processing in Python. PeerJ 2, e453. doi:10.7717/peerj.453

Van Lehn, R.C., Alexander-Katz, A., 2013. Ligand-mediated short-range attraction drives aggregation of charged monolayer-protected gold nanoparticles. Langmuir ACS J. Surf. Colloids 29, 8788–8798. doi:10.1021/la400756z

Varela, J.A., Åberg, C., Simpson, J.C., Dawson, K.A., 2014. Trajectory-Based Co-Localization Measures for Nanoparticle-Cell Interaction Studies. Small n/a–n/a. doi:10.1002/smll.201401849

Varkouhi, A.K., Scholte, M., Storm, G., Haisma, H.J., 2011. Endosomal escape pathways for delivery of biologicals. J. Controlled Release 151, 220–228. doi:10.1016/j.jconrel.2010.11.004

Vercauteren, D., Deschout, H., Remaut, K., Engbersen, J.F.J., Jones, A.T., Demeester, J., De Smedt, S.C., Braeckmans, K., 2011a. Dynamic colocalization microscopy to characterize intracellular trafficking of nanomedicines. ACS Nano 5, 7874–7884. doi:10.1021/nn2020858

Vercauteren, D., Piest, M., van der Aa, L.J., Soraj, M. Al, Jones, A.T., Engbersen, J.F.J., De Smedt, S.C., Braeckmans, K., 2011b. Flotillin-dependent endocytosis and a phagocytosis-like mechanism for cellular internalization of disulfide-based poly(amido amine)/DNA polyplexes. Biomaterials 32, 3072–3084. doi:10.1016/j.biomaterials.2010.12.045

Vercauteren, D., Vandenbroucke, R.E., Jones, A.T., Rejman, J., Demeester, J., De Smedt, S.C., Sanders, N.N., Braeckmans, K., 2010. The Use of Inhibitors to Study Endocytic Pathways of Gene Carriers: Optimization and Pitfalls. Mol. Ther. 18, 561–569. doi:10.1038/mt.2009.281

Verkaik, N.J., Dauwalder, O., Antri, K., Boubekri, I., de Vogel, C.P., Badiou, C., Bes, M., Vandenesch, F., Tazir, M., Hooijkaas, H., Verbrugh, H.A., van Belkum, A., Etienne, J., Lina, G., Ramdani-Bouguessa, N., van Wamel, W.J.B., 2010. Immunogenicity of toxins during Staphylococcus aureus infection. Clin. Infect. Dis. Off. Publ. Infect. Dis. Soc. Am. 50, 61–68. doi:10.1086/648673

Villalta, J.I., Galli, S., Iacaruso, M.F., Antico Arciuch, V.G., Poderoso, J.J., Jares-Erijman, E.A., Pietrasanta, L.I., 2011. New algorithm to determine true colocalization in combination with image restoration and time-lapse confocal microscopy to MAP kinases in mitochondria. PloS One 6, e19031. doi:10.1371/journal.pone.0019031

Vivès, E., Brodin, P., Lebleu, B., 1997. A truncated HIV-1 Tat protein basic domain rapidly translocates through the plasma membrane and accumulates in the cell nucleus. J. Biol. Chem. 272, 16010–16017.
Voigt, J., Christensen, J., Shastri, V.P., 2014. Differential uptake of nanoparticles by endothelial cells through polyelectrolytes with affinity for caveolae. Proc. Natl. Acad. Sci. 111, 2942–2947. doi:10.1073/pnas.1322356111
Vonarbourg, A., Passirani, C., Saulnier, P., Benoit, J.-P., 2006. Parameters influencing the stealthiness of colloidal drug delivery systems. Biomaterials 27, 4356–4373. doi:10.1016/j.biomaterials.2006.03.039
von Heijne, G., 2005. Signal Peptides, in: John Wiley & Sons, Ltd (Ed.), Encyclopedia of Life Sciences. John Wiley & Sons, Ltd, Chichester.
Vuignier, K., Schappler, J., Veuthey, J.-L., Carrupt, P.-A., Martel, S., 2010. Drug-protein binding: a critical review of analytical tools. Anal. Bioanal. Chem. 398, 53–66. doi:10.1007/s00216-010-3737-1
Waehler, R., Russell, S.J., Curiel, D.T., 2007. Engineering targeted viral vectors for gene therapy. Nat. Rev. Genet. 8, 573–587. doi:10.1038/nrg2141
Wagner, M.K., Li, F., Li, J., Li, X.-F., Le, X.C., 2010. Use of quantum dots in the development of assays for cancer biomarkers. Anal. Bioanal. Chem. 397, 3213–3224. doi:10.1007/s00216-010-3847-9
Walczyk, D., Bombelli, F.B., Monopoli, M.P., Lynch, I., Dawson, K.A., 2010. What the cell “sees” in bionanoscience. J. Am. Chem. Soc. 132, 5761–5768. doi:10.1021/ja910675v
Walkey, C.D., Chan, W.C.W., 2012. Understanding and controlling the interaction of nanomaterials with proteins in a physiological environment. Chem. Soc. Rev. 41, 2780–2799. doi:10.1039/c1cs15233e
Walkey, C.D., Olsen, J.B., Song, F., Liu, R., Guo, H., Olsen, D.W.H., Cohen, Y., Emili, A., Chan, W.C.W., 2014. Protein Corona Fingerprinting Predicts the Cellular Interaction of Gold and Silver Nanoparticles. ACS Nano 8, 2439–2455. doi:10.1021/nn406018q
Walling, M.A., Novak, J.A., Shepard, J.R.E., 2009. Quantum dots for live cell and in vivo imaging. Int. J. Mol. Sci. 10, 441–491. doi:10.3390/ijms10020441
Walrant, A., Vogel, A., Correia, I., Lequin, O., Olausson, B.E.S., Desbat, B., Sagan, S., Alves, I.D., 2012. Membrane interactions of two arginine-rich peptides with different cell internalization capacities. Biochim. Biophys. Acta 1818, 1755–1763. doi:10.1016/j.bbamem.2012.02.024
Walton, C.M., Wu, C.H., Wu, G.Y., 1999. A DNA delivery system containing listeriolysin O results in enhanced hepatocyte-directed gene expression. World J. Gastroenterol. WJG 5, 465–469.
Wang, A.Z., Langer, R., Farokhzad, O.C., 2012. Nanoparticle delivery of cancer drugs. Annu. Rev. Med. 63, 185–198. doi:10.1146/annurev-med-040210-162544
Wang, D., Gao, G., 2014. State-of-the-art human gene therapy: part I. Gene delivery technologies. Discov. Med. 18, 67–77.
Wang, F., Yu, L., Monopoli, M.P., Sandin, P., Mahon, E., Salvati, A., Dawson, K.A., 2013. The biomolecular corona is retained during nanoparticle uptake and protects the cells from the damage induced by cationic nanoparticles until degraded in the lysosomes. Nanomedicine Nanotechnol. Biol. Med. doi:10.1016/j.nano.2013.04.010
Wang, M., Thanou, M., 2010. Targeting nanoparticles to cancer. Pharmacol. Res. 62, 90–99. doi:10.1016/j.phrs.2010.03.005
Wang, Y.J., Pan, M.H., Cheng, A.L., Lin, L.I., Ho, Y.S., Hsieh, C.Y., Lin, J.K., 1997. Stability of curcumin in buffer solutions and characterization of its degradation products. J. Pharm. Biomed. Anal. 15, 1867–1876.
Wang, Z.-G., Liu, S.-L., Tian, Z.-Q., Zhang, Z.-L., Tang, H.-W., Pang, D.-W., 2012. Myosin-driven intercellular transportation of wheat germ agglutinin mediated by membrane nanotubes between human lung cancer cells. ACS Nano 6, 10033–10041. doi:10.1021/nn303729r

Wang, Z., Tiruppathi, C., Minshall, R.D., Malik, A.B., 2009. Size and dynamics of caveolae studied using nanoparticles in living endothelial cells. ACS Nano 3, 4110–4116. doi:10.1021/nn9012274

Watkins, C.L., Brennan, P., Fegan, C., Takayama, K., Nakase, I., Futaki, S., Jones, A.T., 2009. Cellular uptake, distribution and cytotoxicity of the hydrophobic cell penetrating peptide sequence PFVYLI linked to the proapoptotic domain peptide PAD. J. Control. Release Off. J. Control. Release Soc. 140, 237–244. doi:10.1016/j.jconrel.2009.04.028

Watkins, C.L., Sayers, E.J., Allender, C., Barrow, D., Fegan, C., Brennan, P., Jones, A.T., 2011. Co-operative membrane disruption between cell-penetrating peptide and cargo: implications for the therapeutic use of the Bcl-2 converter peptide D-NuBCP-9-r8. Mol. Ther. J. Am. Soc. Gene Ther. 19, 2124–2132. doi:10.1038/mt.2011.175

Weissleder, R., Stark, D.D., Engelstad, B.L., Bacon, B.R., Compton, C.C., White, D.L., Jacobs, P., Lewis, J., 1989. Superparamagnetic iron oxide: pharmacokinetics and toxicity. AJR Am. J. Roentgenol. 152, 167–173. doi:10.2214/ajr.152.1.167

Wei, Y., Jana, N.R., Tan, S.J., Ying, J.Y., 2009. Surface coating directed cellular delivery of TAT-functionalized quantum dots. Bioconjug. Chem. 20, 1752–1758. doi:10.1021/bc8003777

Wellner, P., 1993. Interacting with paper on the DigitalDesk. Commun. ACM 36, 87–96.

Wilson, W.L., Szajowski, P.F., Brus, L.E., 1993. Quantum confinement in size-selected, surface-oxidized silicon nanocrystals. Science 262, 1242–1244. doi:10.1126/science.262.5137.1242

Wohlfart, S., Gelperina, S., Kreuter, J., 2012. Transport of drugs across the blood-brain barrier by nanoparticles. J. Control. Release Off. J. Control. Release Soc. 161, 264–273. doi:10.1016/j.jconrel.2011.08.017

Wu, Y., Ma, J., Woods, P.S., Chesarino, N.M., Liu, C., Lee, L.J., Nana-Sinkam, S.P., Davis, I.C., 2015. Selective targeting of alveolar type II respiratory epithelial cells by anti-surfactant protein-C antibody-conjugated lipoplexes. J. Control. Release Off. J. Control. Release Soc. doi:10.1016/j.jconrel.2015.02.016

Xiong, X.-B., Lavasanifar, A., 2011. Traceable multifunctional micellar nanocarriers for cancer-targeted co-delivery of MDR-1 siRNA and doxorubicin. ACS Nano 5, 5202–5213. doi:10.1021/nn2013707

Xu, Y., Liu, B.R., Lee, H.-J., Shannon, K.B., Winiarz, J.G., Wang, T.-C., Chiang, H.-J., Huang, Y., 2010. Nona-arginine facilitates delivery of quantum dots into cells via multiple pathways. J. Biomed. Biotechnol. 2010, 948543. doi:10.1155/2010/948543

Yallapu, M.M., Dobberpuhl, M.R., Maher, D.M., Jaggi, M., Chauhan, S.C., 2012. Design of curcumin loaded cellulose nanoparticles for prostate cancer. Curr. Drug Metab. 13, 120–128.

Yallapu, M.M., Ebeling, M.C., Khan, S., Sundram, V., Chauhan, N., Gupta, B.K., Puumala, S.E., Jaggi, M., Chauhan, S.C., 2013. Novel curcumin-loaded magnetic nanoparticles for pancreatic cancer treatment. Mol. Cancer Ther. 12, 1471–1480. doi:10.1158/1535-7163.MCT-12-1227

Yallapu, M.M., Gupta, B.K., Jaggi, M., Chauhan, S.C., 2010. Fabrication of curcumin encapsulated PLGA nanoparticles for improved therapeutic effects in metastatic cancer cells. J. Colloid Interface Sci. 351, 19–29. doi:10.1016/j.jcis.2010.05.022

Yallapu, M.M., Khan, S., Maher, D.M., Ebeling, M.C., Sundram, V., Chauhan, N., Ganju, A., Balakrishna, S., Gupta, B.K., Zafar, N., Jaggi, M., Chauhan, S.C., 2014. Anti-cancer activity of curcumin loaded nanoparticles in prostate cancer. Biomaterials 35, 8635–8648. doi:10.1016/j.biomaterials.2014.06.040

Yallapu, M.M., Othman, S.F., Curtis, E.T., Gupta, B.K., Jaggi, M., Chauhan, S.C., 2011. Multi-functional magnetic nanoparticles for magnetic resonance imaging and cancer therapy. Biomaterials 32, 1890–1905. doi:10.1016/j.biomaterials.2010.11.028

Yanes, R.E., Tarn, D., Hwang, A.A., Ferris, D.P., Sherman, S.P., Thomas, C.R., Lu, J., Pyle, A.D., Zink, J.I., Tamanoi, F., 2013. Involvement of lysosomal exocytosis in the excretion of mesoporous silica nanoparticles and enhancement of the drug delivery effect by exocytosis inhibition. Small Weinh. Bergstr. Ger. 9, 697–704. doi:10.1002/smll.201201811

Yaroslavov, A.A., Melik-Nubarov, N.S., Menger, F.M., 2006. Polymer-induced flip-flop in biomembranes. Acc. Chem. Res. 39, 702–710. doi:10.1021/ar050078q
Ylä-Herttuala, S., 2015. Glybera's Second Act: The Curtain Rises on the High Cost of Therapy. Mol. Ther. 23, 217–218. doi:10.1038/mt.2014.248
Yla-Herttuala, S., Raty, J., Lesch, H., Wirth, T., 2008. Improving Safety of Gene Therapy. Curr. Drug Saf. 3, 46–53. doi:10.2174/157488608783333925
Yoo, J.S., Won, N., Kim, H.B., Bang, J., Kim, S., Ahn, S., Soh, K.-S., 2010. In vivo imaging of cancer cells with electroporation of quantum dots and multispectral imaging. J. Appl. Phys. 107, 124702. doi:10.1063/1.3447858
Youngblood, D.S., Hatlevig, S.A., Hassinger, J.N., Iversen, P.L., Moulton, H.M., 2007. Stability of cell-penetrating peptide-morpholino oligomer conjugates in human serum and in cells. Bioconjug. Chem. 18, 50–60. doi:10.1021/bc060138s
Yue, Z.-G., Wei, W., Lv, P.-P., Yue, H., Wang, L.-Y., Su, Z.-G., Ma, G.-H., 2011. Surface charge affects cellular uptake and intracellular trafficking of chitosan-based nanoparticles. Biomacromolecules 12, 2440–2446. doi:10.1021/bm101482r
Yukawa, H., Kagami, Y., Watanabe, M., Oishi, K., Miyamoto, Y., Okamoto, Y., Tokeshi, M., Kaji, N., Noguchi, H., Ono, K., Sawada, M., Baba, Y., Hamajima, N., Hayashi, S., 2010. Quantum dots labeling using octa-arginine peptides for imaging of adipose tissue-derived stem cells. Biomaterials 31, 4094–4103. doi:10.1016/j.biomaterials.2010.01.134
Yukawa, H., Watanabe, M., Kaji, N., Okamoto, Y., Tokeshi, M., Miyamoto, Y., Noguchi, H., Baba, Y., Hayashi, S., 2012. Monitoring transplanted adipose tissue-derived stem cells combined with heparin in the liver by fluorescence imaging using quantum dots. Biomaterials 33, 2177–2186. doi:10.1016/j.biomaterials.2011.12.009
Yu, M.K., Park, J., Jon, S., 2012. Targeting Strategies for Multifunctional Nanoparticles in Cancer Imaging and Therapy. Theranostics 2, 3–44. doi:10.7150/thno.3463
Zeigerer, A., Gilleron, J., Bogorad, R.L., Marsico, G., Nonaka, H., Seifert, S., Epstein-Barash, H., Kuchimanchi, S., Peng, C.G., Ruda, V.M., Del Conte-Zerial, P., Hengstler, J.G., Kalaidzidis, Y., Koteliansky, V., Zerial, M., 2012. Rab5 is necessary for the biogenesis of the endolysosomal system in vivo. Nature 485, 465–470. doi:10.1038/nature11133
Zensi, A., Begley, D., Pontikis, C., Legros, C., Mihoreanu, L., Wagner, S., Büchel, C., von Briesen, H., Kreuter, J., 2009. Albumin nanoparticles targeted with Apo E enter the CNS by transcytosis and are delivered to neurones. J. Controlled Release 137, 78–86. doi:10.1016/j.jconrel.2009.03.002
Zhang, H., Burnum, K.E., Luna, M.L., Petritis, B.O., Kim, J.-S., Qian, W.-J., Moore, R.J., Heredia-Langner, A., Webb-Robertson, B.-J.M., Thrall, B.D., Camp, D.G., 2nd, Smith, R.D., Pounds, J.G., Liu, T., 2011. Quantitative proteomics analysis of adsorbed plasma proteins classifies nanoparticles with different surface properties and size. Proteomics 11, 4569–4577. doi:10.1002/pmic.201100037
Zhang, H., Wu, S., Tao, Y., Zang, L., Su, Z., 2010. Preparation and Characterization of Water-Soluble Chitosan Nanoparticles as Protein Delivery System. J. Nanomater. 2010, 1–5. doi:10.1155/2010/898910
Zhang, K., Fang, H., Wang, Z., Taylor, J.-S.A., Wooley, K.L., 2009. Cationic shell-crosslinked knedel-like nanoparticles for highly efficient gene and oligonucleotide transfection of mammalian cells. Biomaterials 30, 968–977. doi:10.1016/j.biomaterials.2008.10.057
Zhang, L.W., Monteiro-Riviere, N.A., 2009. Mechanisms of quantum dot nanoparticle cellular uptake. Toxicol. Sci. Off. J. Soc. Toxicol. 110, 138–155. doi:10.1093/toxsci/kfp087
Zhou, H., Beevers, C.S., Huang, S., 2011. The targets of curcumin. Curr. Drug Targets 12, 332–347.
Zhou, H., Gao, M., Skolnick, J., 2015. Comprehensive prediction of drug-protein interactions and side effects for the human proteome. Sci. Rep. 5, 11090. doi:10.1038/srep11090

Supplementary

Supplementary Chapter 4

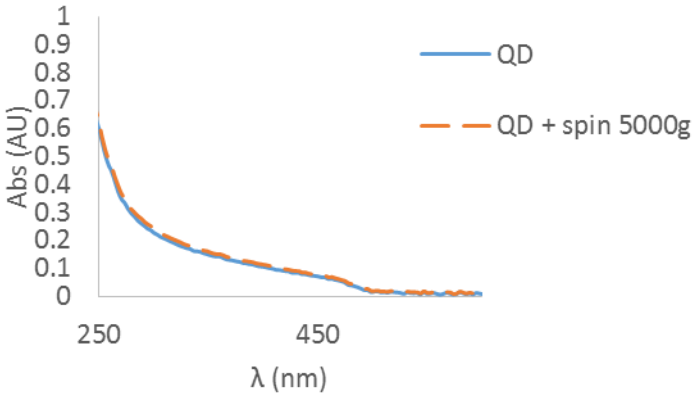

Supplementary Figure 4.1 QDs are resistant to low speed centrifugation.

Showing the absorbance spectra of 100 nM QDs before or after centrifugation at 5000 g for 5 mins. n=2.

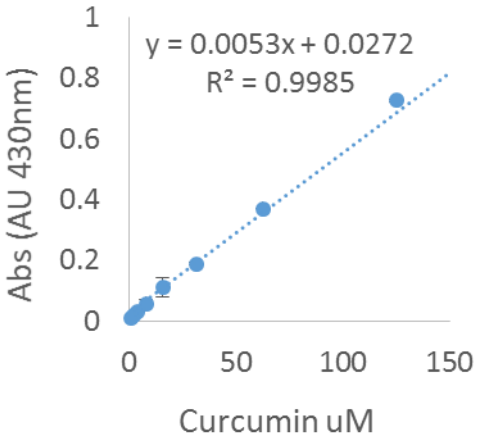

Supplementary Figure 4.2 Curcumin in DMSO standard curve.

The absorbance of curcumin at 430 nm was quantified using a serial dilution of the drug in DMSO. n = 2.

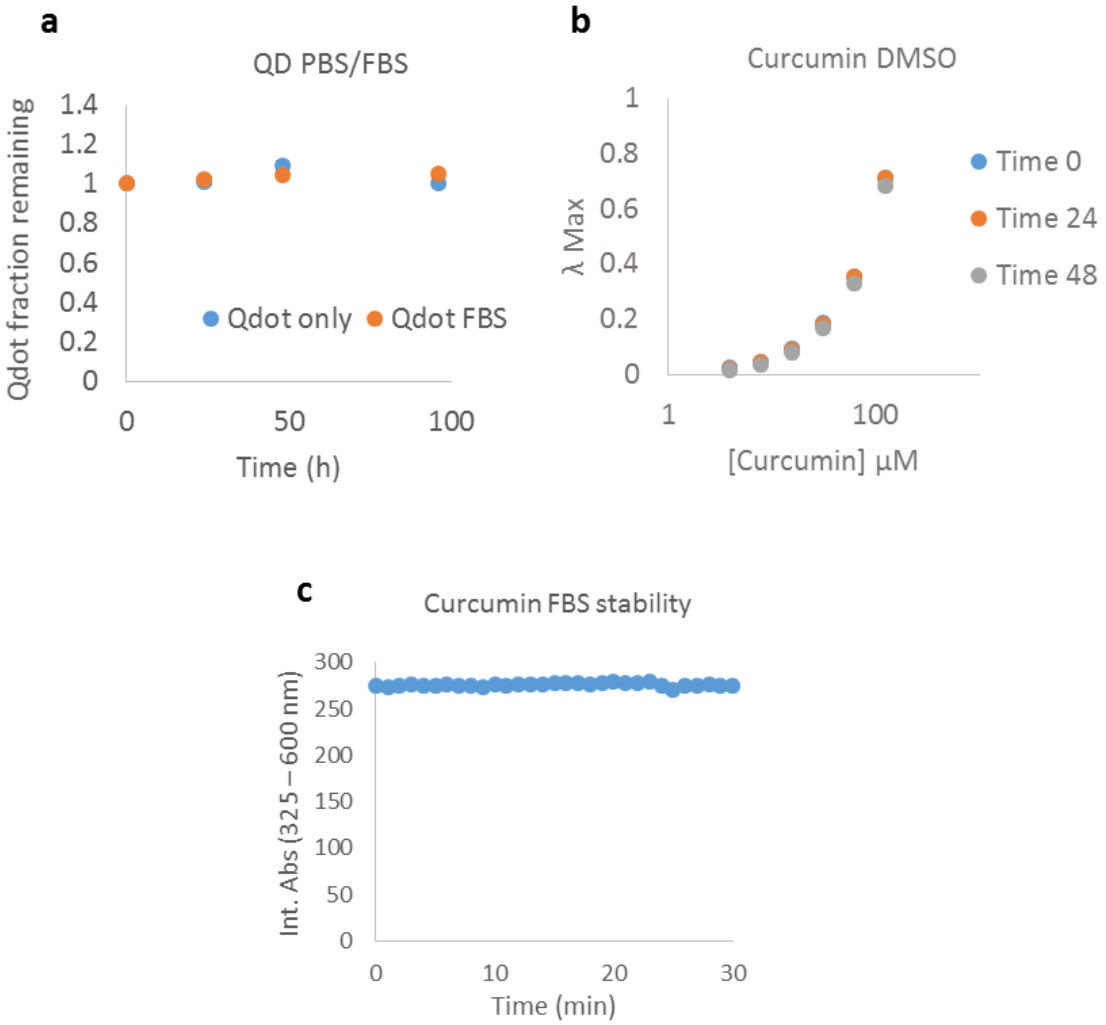

Supplementary Figure 4.3 Stability of QDs and curcumin under different buffer conditions.

The stability of 100 nM QDs in PBS alone or PBS and 10 % FBS was assessed by absorbance spectroscopy over 96 h by taking the normalized integrated absorbance between 325 – 600 nm (a, n = 2). The stability of a serial dilution of curcumin in DMSO was also assessed by taking the peak curcumin absorbance at each time point (b, n = 2). Curcumin stability in 10 % FBS was assessed over 30 min by the integrated absorbance method (c, n = 1), and indicates the stability of curcumin absorbance over a scale comparable with the binding saturation assays in this report.

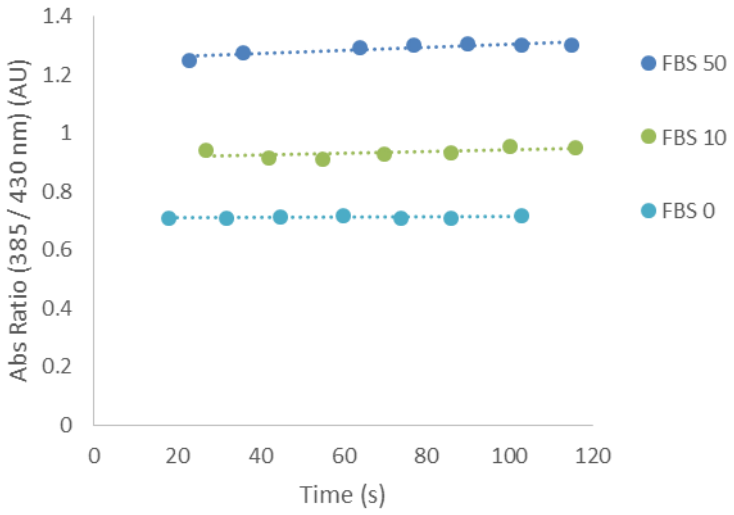

Supplementary Figure 4.4 Absorbance ratio change of curcumin:QDs when placed in FBS.

The change in the absorbance ratio at 385/430 nm of curcumin:QDs complexes as a result of being placed in 10 % FBS, was assayed from roughly 20 – 120 s by absorbance spectroscopy although the kinetics of the ratio change could not be captured by the equipment used (n = 1).

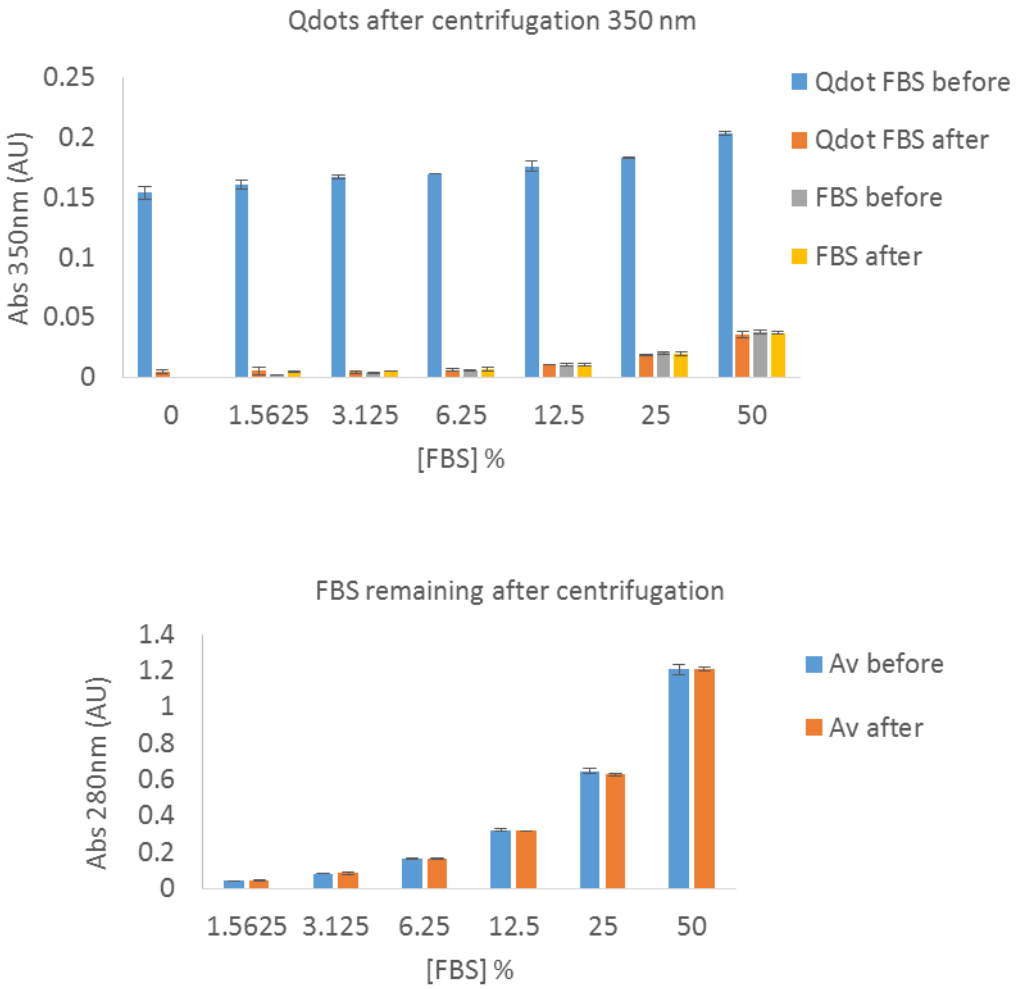

Supplementary Figure 4.5 Quantification of QDs and FBS remaining after centrifugation at 20,000g.

The volume of QDs following centrifugation was quantified by taking the absorbance at 350 nm (a). However, at this wavelength a baseline signal from FBS was also detected which was not sensitive to centrifugation (a). To assess the stability of FBS to centrifugation further, the absorbance was quantified at 280 nm which provided greater sensitivity (b).

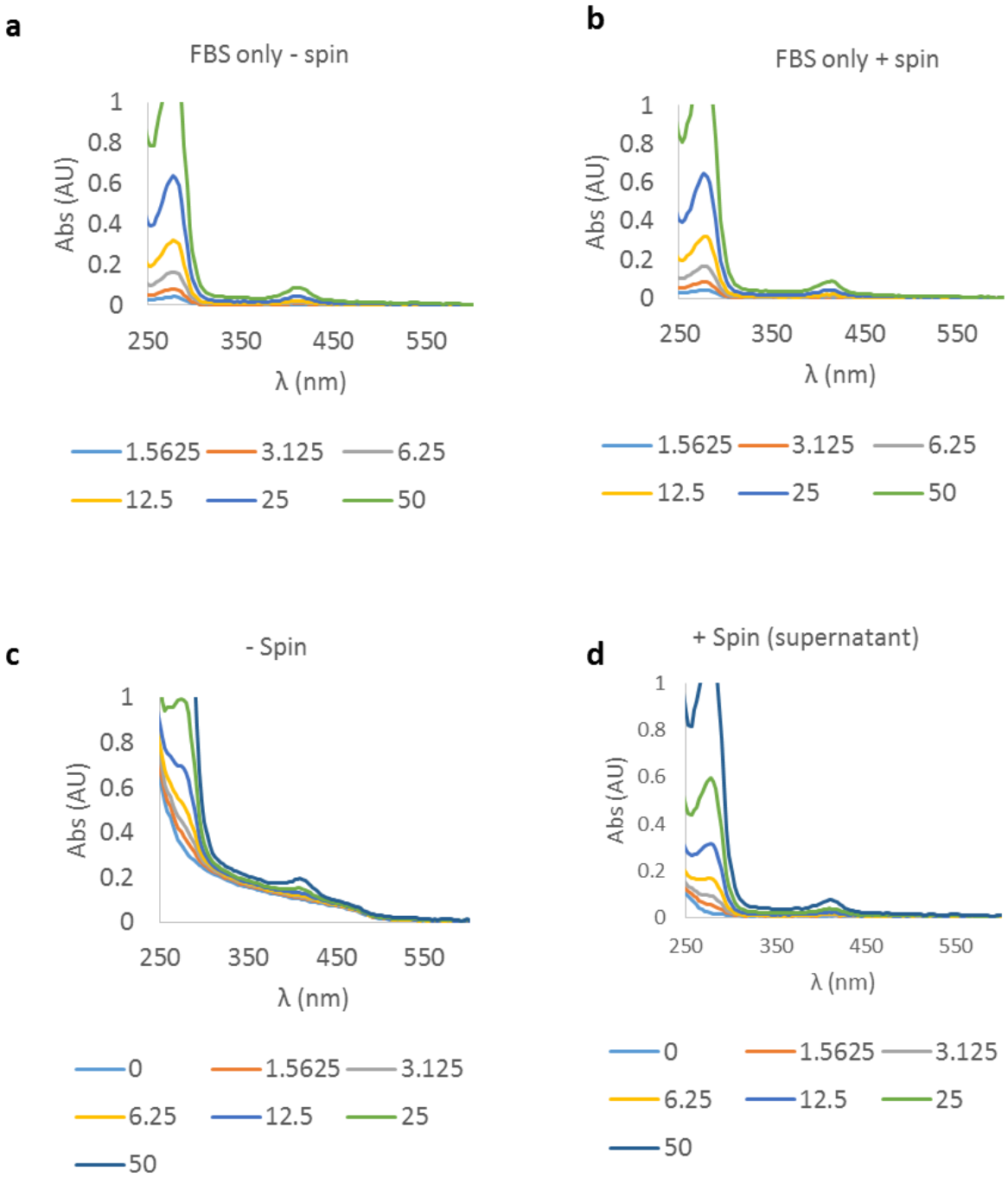

Supplementary Figure 4.6 Spectra of QD FBS following centrifugation at 20,000g.

Absorbance spectra of FBS showed little change following centrifugation (a, b). For QDs in FBS however, a large change was observed consistent with the removal of QDs from the supernatant fraction (c, d).

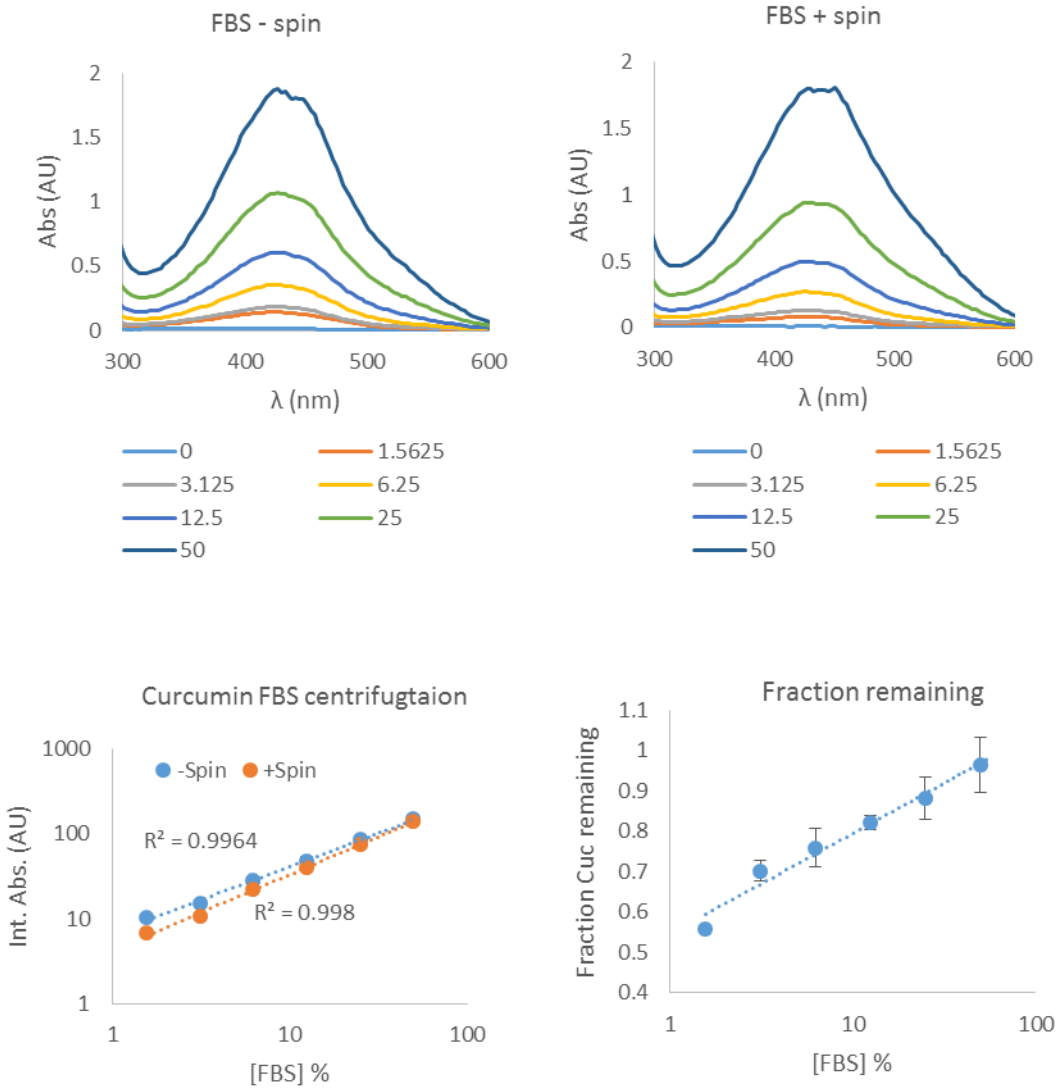

Supplementary Figure 4.7 Quantification of curcumin in FBS remaining after centrifugation at 20,000g.

The absorbance spectra of curcumin in FBS before and after centrifugation are given in a, b. The amount of curcumin in the supernatant fraction was quantified by taking the integrated absorbance between 325 – 600 nm (c) which allowed the remaining fraction of curcumin to be calculated (d).

Supplementary Chapter 5

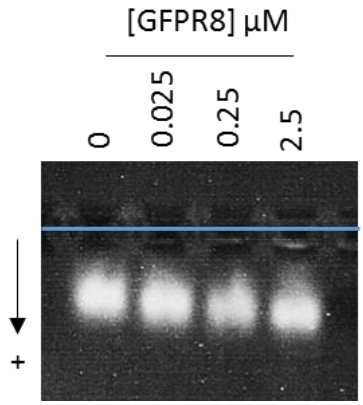

Supplementary Figure 5.1 GFPR8 does not bind aQDs.

Complexes were prepared by mixing 25nM aQDs with GFPR8 for 30 mins prior to analysis by agarose gel electrophoresis.

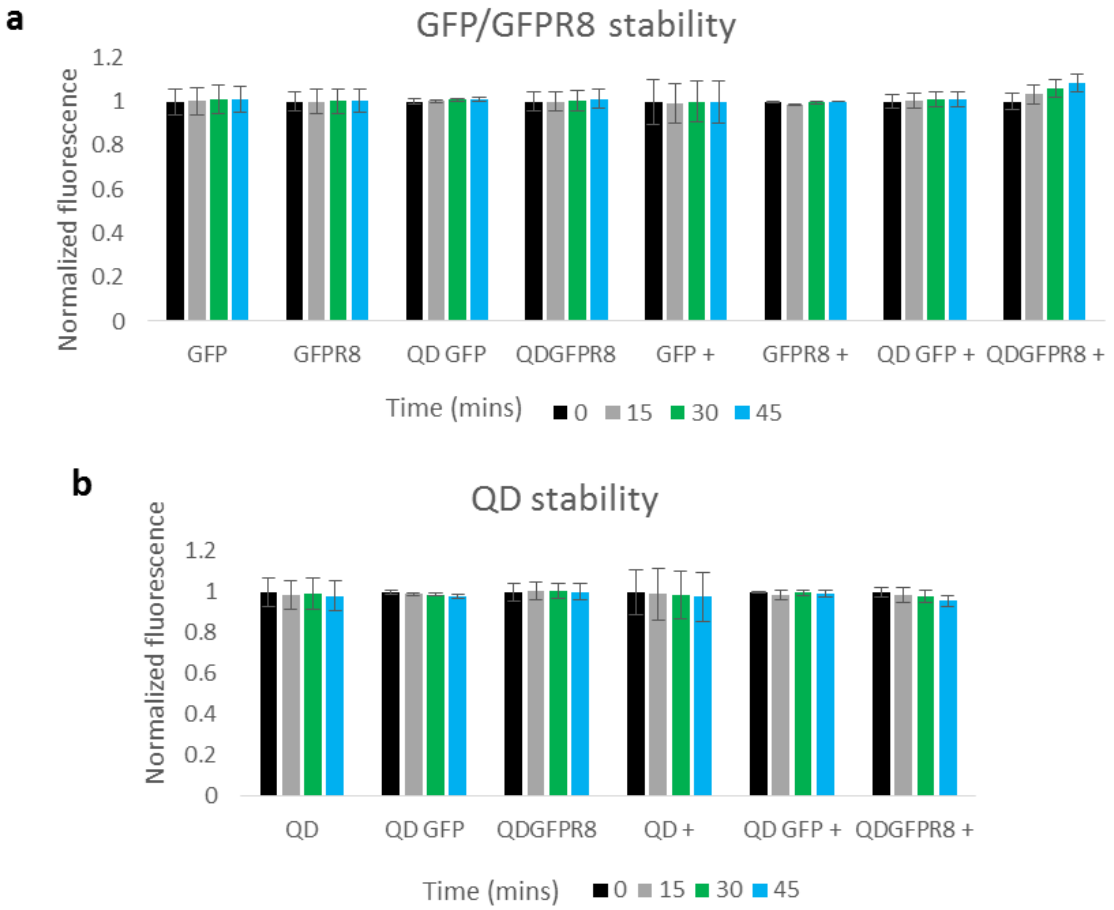

Supplementary Figure 5.2 Stability of components in the presence of serum.

GFP, GFPR8 or QDs, alone or in combination, were assayed in the absence or presence of 10 % FBS which is denoted by '+'. The normalized fluorescence in the green (a) or red channel (b) was quantified periodically over a period of 45 mins.

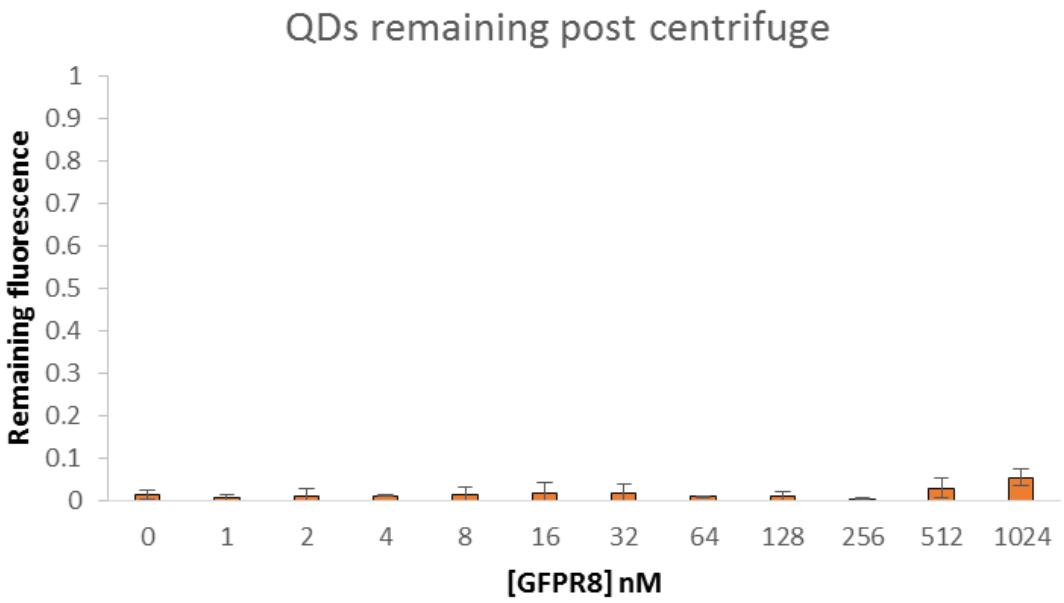

Supplementary Figure 5.3 QD centrifugation efficiency with respect to GFPR8.

QDs at 10 nM were mixed with GFPR8 for 30 mins prior to centrifugation at 20,000g for 30 mins and the remaining fluorescence in the green channel was quantified.

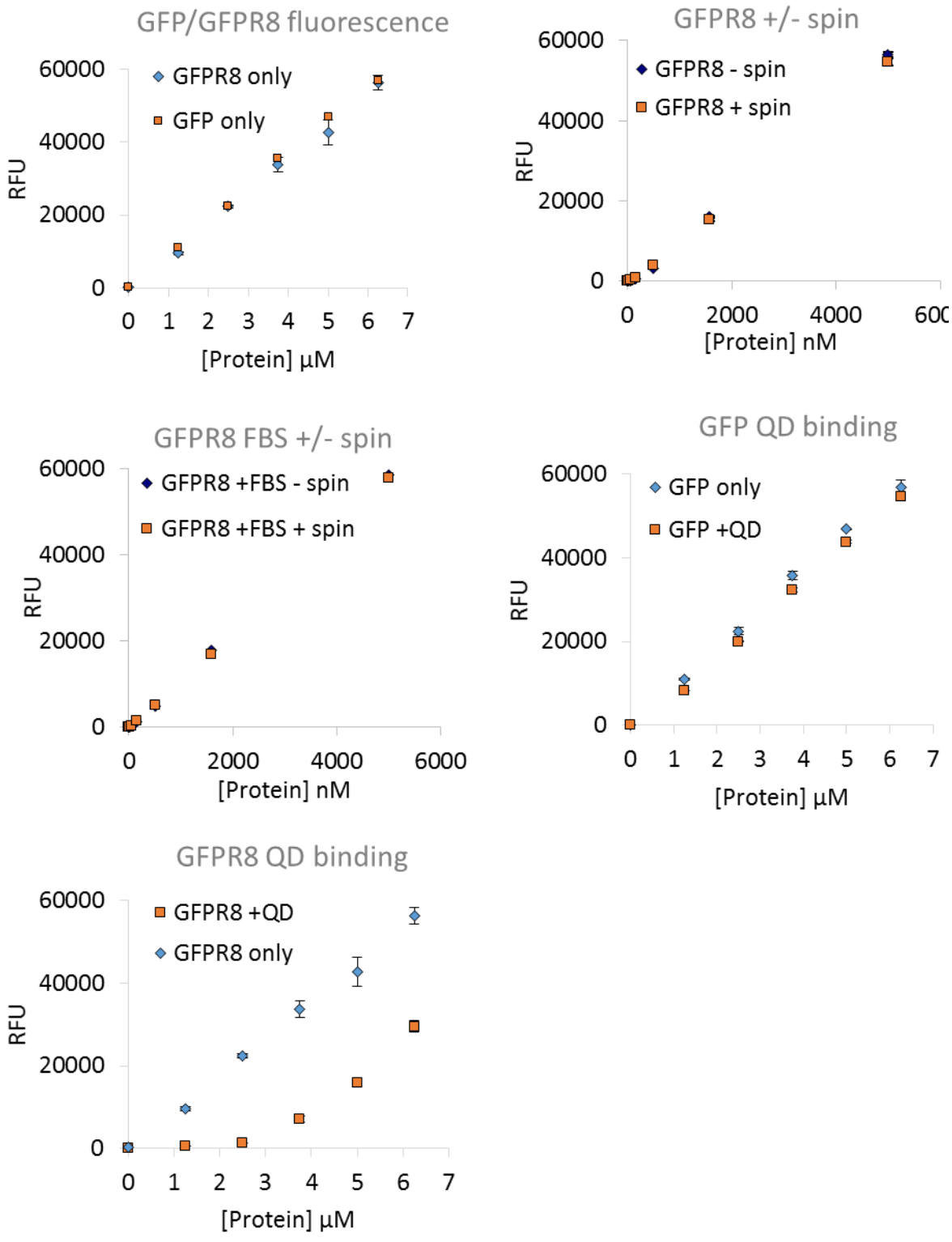

Supplementary Figure 5.4 Controls for GFPR8 QD binding.

The fluorescence of GFPR8 and GFP were equivalent in intensity (a). GFPR8 was insensitive to centrifugation at 20,000 g for 30 mins (b) even in the presence of 10 % FBS (a). The binding of GFP or GFPR8 to carboxyl QDs was quantified in d, e, by measuring the free protein component remaining in the supernatant following removal of QD complexes by centrifugation.

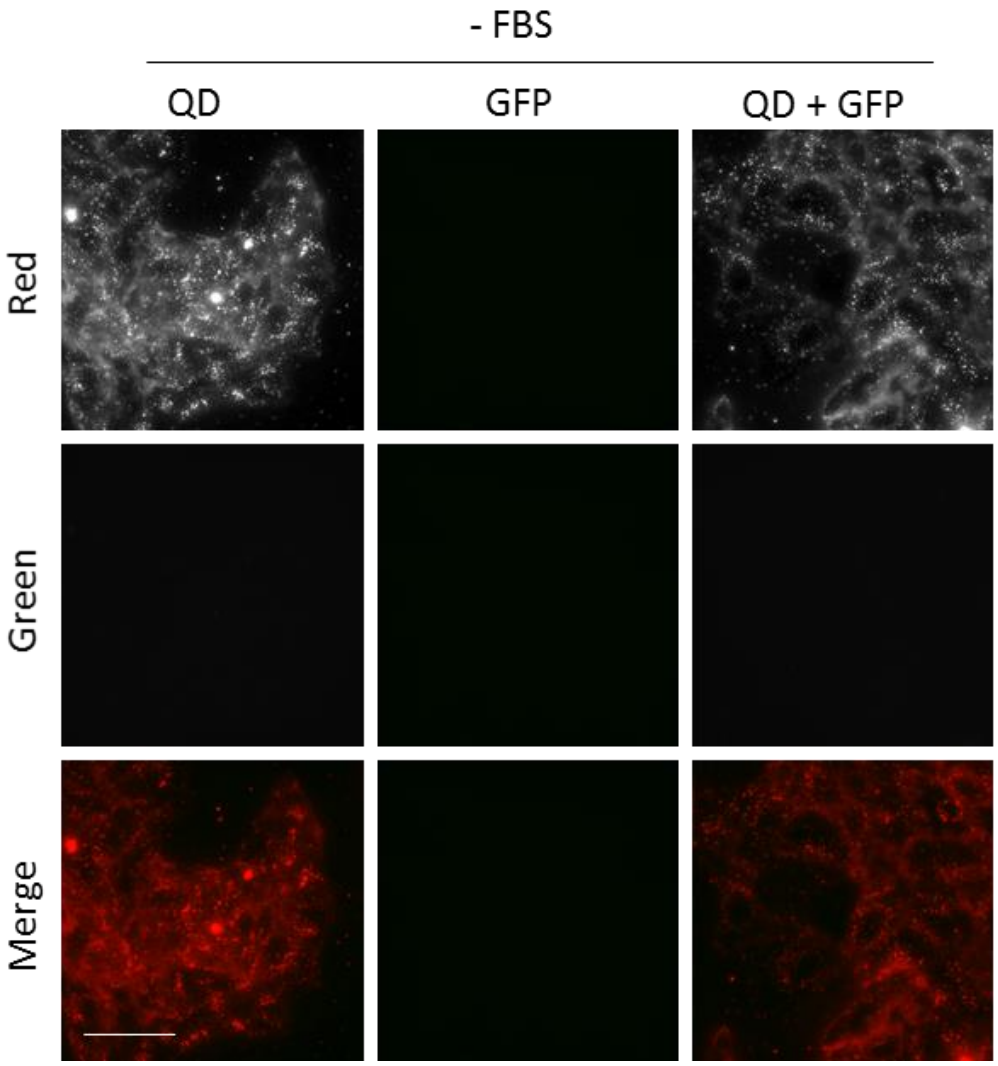

Supplementary Figure 5.5 GFP and QD uptake in the absence of FBS.

QDs at 5 nM and GFP at 500 nM, alone or following complexation were assessed for uptake in HeLa cells for 1 hour in the absence of serum. Scale bar is 100 µm.

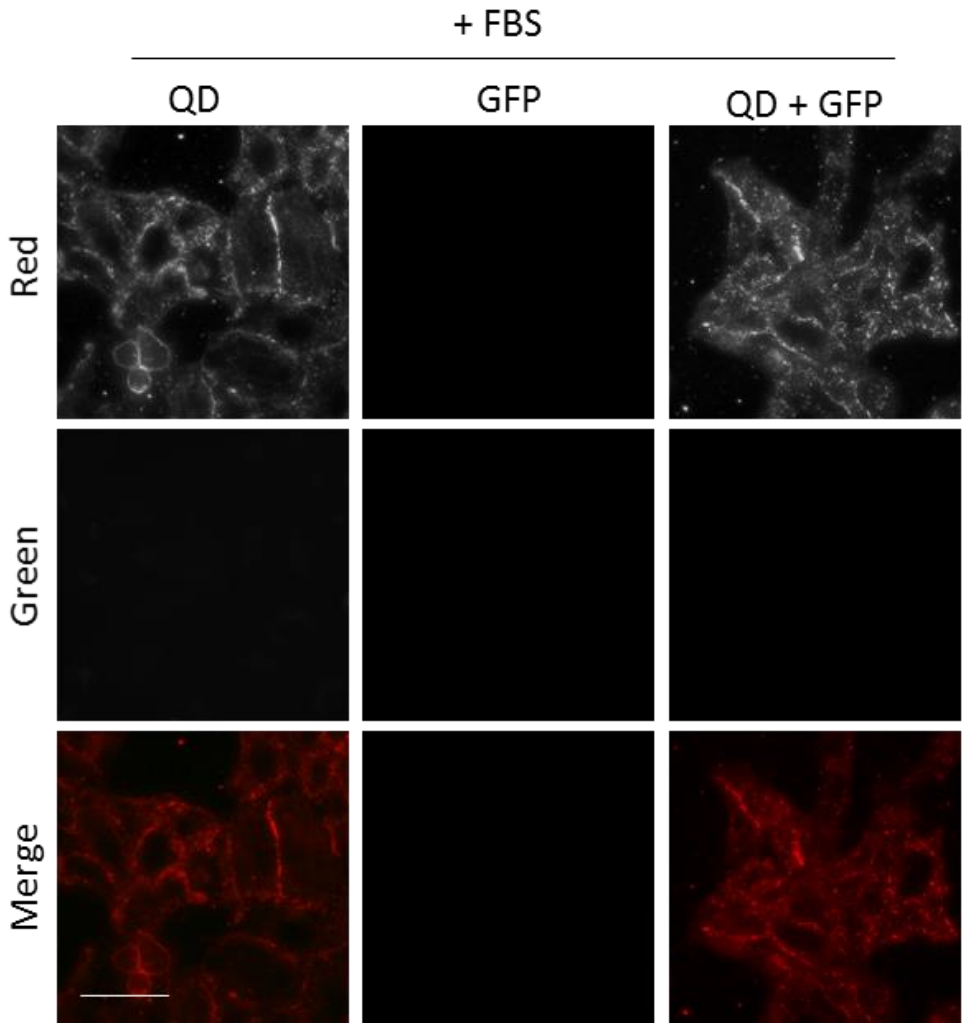

Supplementary Figure 5.6 GFP and QD uptake in the presence of FBS.

QDs at 5 nM and GFP at 500 nM, alone or following complexation were assessed for uptake in HeLa cells for 1 hour in the presence of 10 % FBS. Scale bar is 100 µm.

Supplementary Chapter 6

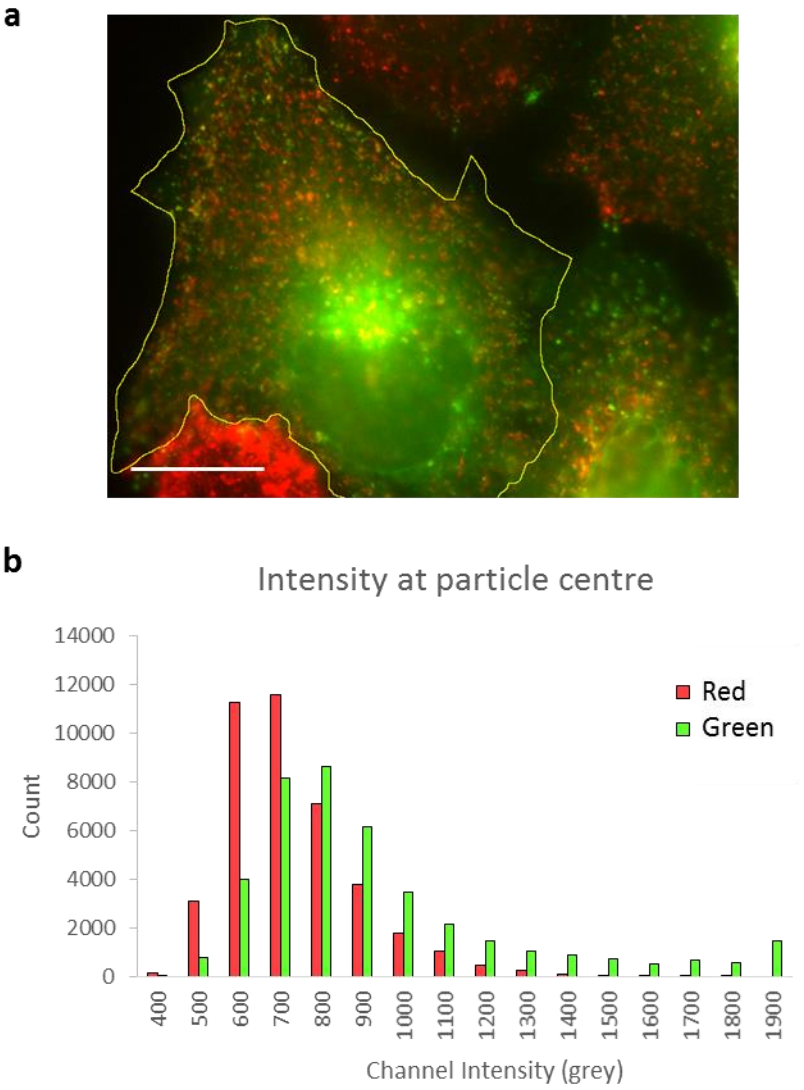

Supplementary Figure 6.1 Intensity distributions at particle centre in dual colour time lapse.

A representative HeLa cell expressing Rab21-GFP (highlighted in yellow in a) was treated with transferrin-Alexa568 for 5 mins before the green channel was subjected to single particle tracking. The intensity at the particle centre in both channels was then plotted in b to illustrate the highly analogue nature of particle intensity distributions in a live cell. Scale bar is 10 microns.

Supplementary Figure 6.2 Total event detection using ST filtering with respect to object density.

A simulation was run to investigate the effect of object density on the number of events identified using ST filtering when compared to the actual number of event occurrences. Object numbers ranged from 100 to 500 per frame with relative object radii = 3 px.

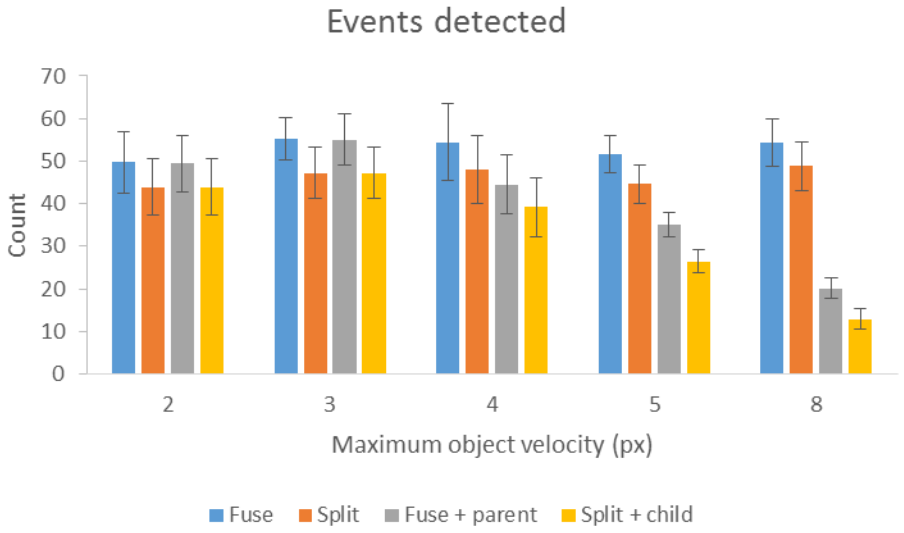

Supplementary Figure 6.3 Object parentage tracking as a function of object velocity.

An object is considered to possess a parent if the object is visible in consecutive frames at the index of a fuse or split event. Object parentage is tracked by using an overlap method which requires at least one pixel of the object to be visible in both frames. In ordered to assess the performance of object parentage tracking with respect to object velocity a simulation was run with object velocities ranging from a maximum of 2 to 8 px/frame and the number of events. As no objects disappear in the simulation all events are expected to possess parents. Total fusion and splitting events and the number of events with object parents were then quantified using the spatial temporal filter.

Methods 1

Interaction_simulator

Interaction_simulator comprises of 4 scripts. RandomEP1, endosome and particle scripts are provided below. In addition tiffile.py from Christoph Gohlke (http://www.lfd.uci.edu/~gohlke/) is required. To use Interaction_simulator, the RandomEP1 script must be run from the command-line e.g. execute by typing "python RandomEP1.py". The licence for Interaction_simulator is provided here:

"*Interaction_simulator is free software: you can redistribute it and/or modify it under the terms of the GNU General Public License as published by the Free Software Foundation, either version 3 of the License, or (at your option) any later version.*

Interaction_simulator is distributed in the hope that it will be useful, but WITHOUT ANY WARRANTY; without even the implied warranty of MERCHANTABILITY or FITNESS FOR A PARTICULAR PURPOSE. See the GNU General Public License for more details."

Further dependencies:

Numpy

Skimage

Scipy

To run Interaction_simulator, place the following scripts in a directory and run the particles.py script.

RandomEP1.py

```
"""
This file is part of Interaction_simulator

@author: Kez Cleal, ClealK@cardiff.ac.uk
"""

import endosome as E
import particles as P
import numpy as np
import tifffile
# import Image
import pandas as pd
import os
from os.path import isfile, join
import time
```

```
16.
17.
18. vids = 10
19. outputpath = 'C:\\Users\\Kez\\Desktop\\Py\\simulated data\\new\\SNR\\fp\\3'  # Ente
    r suitable path
20. bg = 20  # background level
21. sigma = 1  # stdev of background, keep this at 1
22. SNRs = [3]
23. number_particles = 100
24.
25. frames = 100
26. number = 200  # Endosomes
27. ar_size = 250
28. end_size = (3, 3)  # Range, lower and upper sizes
29. end_velocity = (5, 5)
30.
31. velocity, p_fuse, p_split, event_gap, frames = 5, 0.999999, 0.999999, 5, frames
32.
33. # ------------------------------------------------------------------------------
34.
35. def makeVids():
36.     endosomes = {}
37.     array_1 = E.ar_1(frames, ar_size)
38.     E.make_endosomes(ar_size, number, frames, end_size, end_velocity,
39.                      endosomes)
40.
41.     E.add_over_ar(endosomes, array_1)
42.
43.     def random_c():
44.         return np.random.randint(10, ar_size-10)
45.
46.     # list of dictionaries
47.     ds_all = []
48.     for i in range(number_particles):
49.         name = 'Particle' + str(i)
50.         centre = (random_c(), random_c())
51.         ds = P.make_particles(velocity, centre, p_fuse, p_split, event_gap,
52.                               frames, endosomes, name, ar_size)
53.         ds_all.append(ds)
54.
55.     array_1_P = []
56.     for frame in range(frames):
57.         array_1_P.append(np.zeros((ar_size, ar_size), dtype=np.uint16))
58.
59.     data = {'Trajectory': [], 'Frame': [], 'x': [], 'y': []}
60.
61.     number_fuse = 0
62.     number_split = 0
63.
64.     part = 0
65.     for k in ds_all:
66.         c = 0
67.         h = k['History']
68.         fuseE = k['Fuse_Events']
69.         splitE = k['Split_Events']
70.         number_fuse += fuseE
71.         number_split += splitE
72.         fr = [x for x in range(len(h))]
73.         traj = [part for y in range(len(h))]
74.         xl = []
75.         yl = []
76.         # for each frame
77.         for l in h:
78.             x = l[0]
79.             y = l[1]
80.             xl.append(x)
```

```
            yl.append(y)
            ar = array_l_P[c]
            if x > 0 and x < ar_size and y > 0 and y < ar_size:
                ar[x][y] += 1
            c += 1
        data['Trajectory'] += traj
        data['Frame'] += fr
        data['x'] += xl
        data['y'] += yl
        part += 1

    print 'Fuse events: ', number_fuse
    print 'Split events: ', number_split

    pie_out = pd.DataFrame(data)
    cols = ['Trajectory', 'Frame', 'x', 'y']
    pie_out = pie_out[cols]

    def calc_offset(bg, sigma, SNR):
                return SNR*sigma

            def add_offset(im, signal, bg):
                n = np.empty_like(im)
                n[:] = im
                n[n == 0] = bg
                n[n == 1] = bg+signal
                return n

            def add_noise(image, sigma):
                poissonNoise = np.random.poisson(sigma, image.shape).astype(float)
                p = image + poissonNoise
                p[p > 255] = 255
                return p

            def stack(SNR, sigma):
                im_l = []
                for j in range(len(array_l)):
                    signal = calc_offset(bg, sigma, SNR)
                    a = add_offset(array_l_P[j], signal, bg)
                    a = add_noise(a, sigma)

                    b = add_offset(array_l[j], signal, bg)
                    b = add_noise(b, sigma)

                    c = np.zeros((ar_size, ar_size))
                    im = np.dstack((a, b, c))
                    im = im.astype(np.uint16, copy=False)
                    im_l.append(im)
                return im_l

            def save_images(directory, images):
                binaryArrays = None
                count = 0
                for k in images:
                    k = np.expand_dims(k, axis=0)
                    if count == 0:
                        binaryArrays = k

                    else:
                        binaryArrays = np.concatenate((binaryArrays, k))
                    count += 1
                # binaryArrays = np.rollaxis(binaryArrays, 3, 1)
                filename = directory + '.tif'
                value = u'{"shape": %s}' % str(list(binaryArrays.shape))
                print value
                tifffile.imsave(filename, binaryArrays)
```

```
147.
148.            def save_result(outputpath):
149.                f = open(outputpath + 'Results.txt', 'a')
150.                f.write('Fuse events: ' + str(number_fuse) + '\n')
151.                f.write('Split events: ' + str(number_split) + '\n')
152.
153.            def save_txt(outputpath):
154.                f = open(outputpath + 'Summary.txt', 'w')
155.                f.write('Params:\n')
156.                f.write('Background: ' + str(bg) + '\n')
157.                f.write('Sigma: ' + str(sigma) + '\n')
158.                f.write('SNRs: ' + str(SNRs) + '\n')
159.                f.write('Particles: ' + str(number_particles) + '\n')
160.                f.write('Frames: ' + str(frames) + '\n')
161.                f.write('Array size: ' + str(ar_size) + '\n')
162.                f.write('Endosome number: ' + str(number) + '\n')
163.                f.write('Endosome size: ' + str(end_size) + '\n')
164.                f.write('Endosome velocity: ' + str(end_velocity) + '\n')
165.                f.write('P fusion: ' + str(p_fuse) + '\n')
166.                f.write('P splitting: ' + str(p_split) + '\n')
167.                f.write('Event gap: ' + str(event_gap) + '\n')
168.                f.write('Out: ' + 'D:\\Data\\14-07-
    29\\False positive SIM\\' + '\n')
169.
170.            print 'Fuse events: ', number_fuse
171.            print 'Split events: ', number_split
172.
173.            def checkforfile(SNR_str):
174.                onlyfiles = [f for f in os.listdir(outputpath) if
175.                             isfile(join(outputpath, f))]
176.                if any(SNR_str in s for s in onlyfiles):
177.                    return True
178.                else:
179.                    return False
180.
181.            def save_SNR(SNRs):
182.                for i in SNRs:
183.                    image_l = stack(i, sigma)
184.
185.                    SNR_str = 'Vid_' + str(i)
186.                    fileexists = checkforfile(SNR_str)
187.                    count = i + 1
188.                    while fileexists:
189.                        SNR_str = 'Vid_' + str(count)
190.                        fileexists = checkforfile(SNR_str)
191.                        count += 1
192.                    outpath = outputpath + '\\' + SNR_str
193.                    save_images(outpath, image_l)
194.                    pie_out.to_csv(outputpath + '\\' + SNR_str + '_Results.csv')
195.
196.            save_txt(outputpath)
197.            save_result(outputpath)
198.            save_SNR(SNRs)
199.
200.        time1 = time.time()
201.        for i in range(vids):
202.            print 'Video: ', i
203.            makeVids()
204.        print 'Time: ', time.time()-time1
```

endosome.py

```
1.  """
```

```
2.  This file is part of Interaction_simulator
3.
4.  @author: Kez Cleal, ClealK@cardiff.ac.uk
5.  """
6.
7.  from skimage.draw import circle
8.  import numpy as np
9.  from random import randint, uniform
10. import matplotlib as plt
11. import math
12.
13.
14. class Endosome:
15.     def __init__(self, size, velocity, centre, name):
16.         self.size = size
17.         self.velocity = velocity
18.         self.centre = centre
19.         self.history = []
20.         self.pixels = None
21.         self.fused = None
22.         self.make_circle()
23.         self.name = name
24.
25.     def print_name(self):
26.         return self.name
27.
28.     def print_props(self):
29.         self.props = {'Size': self.size, 'Velocity': self.velocity,
30.                       'Centre': self.centre, 'Pixels': self.pixels,
31.                       'History': self.history}
32.         return self.props
33.
34.     def make_circle(self):
35.         c = []
36.         for x in range(-self.size-1, self.size+1):
37.             for y in range(-self.size-1, self.size+1):
38.                 if math.ceil(math.sqrt((x) ** 2 + (y) ** 2)) < self.size:
39.                     c.append((x, y))
40.         c1 = []
41.         for i in c:
42.             c1.append(tuple(map(sum, zip(self.centre, i))))
43.         self.pixels = set(c1)
44. #        img = np.zeros((self.size*2+1, self.size*2+1), dtype=np.double)
45. #        rr, cc = circle(int(self.size), int(self.size), self.size, img.shape)
46. #        img[rr, cc] = 1
47. #        a, b = np.where(img == 1)
48. #
49. #        x = a+self.centre[0]
50. #        y = b+self.centre[1]
51. #        self.pixels = zip(x, y)
52.
53.     def update_velocity(self, new_v):
54.         self.velocity = new_v
55.
56.     def update_centre(self, coords):
57.         self.centre = coords
58.         self.history.append(self.pixels)
59.         self.update_pixels(coords)
60.
61.     def update_pixels(self, coords):
62.         c = []
63.         for i in self.pixels:
64.             c.append(tuple(map(sum, zip(coords, i))))
65.         self.pixels = set(c)
66.
67.
```

```
68. def make_blobs(tups_l, array):
69.     size = np.shape(array)
70.     for i in tups_l:
71.         if 0 < i[0] < size[0]:
72.             if 0 < i[1] < size[1]:
73.                 array[i[0]][i[1]] = 1
74.     return array
75.
76.
77. def ar_l(frames, ar_size):
78.     array_l = []
79.     for i in range(frames):
80.         a = np.zeros((ar_size, ar_size), dtype=np.uint16)
81.         array_l.append(a)
82.     return array_l
83.
84.
85. # make endosomes
86. def make_endosomes(ar_size, number, frames, end_size, end_velocity, endosomes):
87.     for i in range(number):
88.         size = randint(end_size[0], end_size[1])
89.         velocity = randint(end_velocity[0], end_velocity[1])
90.         centre_x = randint(0, ar_size)
91.         centre_y = randint(0, ar_size)
92.         string = 'End'+str(i)
93.         name = string
94.         string = Endosome(size, velocity, (centre_x, centre_y), name)
95.         # move the endosome around
96.         for j in range(frames):
97.             rx = uniform(-velocity, velocity)
98.             ry = uniform(-velocity, velocity)
99.             string.update_centre((int(rx), int(ry)))
100.                endosomes[name] = string.print_props()
101.
102.
103.        # get the particle coords
104.        def add_over_ar(endosomes, array_l):
105.            for i in range(len(endosomes)):
106.                string = 'End'+str(i)
107.                hist = endosomes.setdefault(string, {})['History']
108.                count = 0
109.                for i in hist:
110.                    make_blobs(i, array_l[count])
111.                    count += 1
112.
113.
114.        if __name__ == "__main__":
115.            frames = 100
116.            number = 250
117.            ar_size = 1000
118.            end_size = (3, 6)
119.            end_velocity = (2, 6)
120.            endosomes = {}
121.            array_l = ar_l(frames, ar_size)
122.            make_endosomes(ar_size, number, frames, end_size, end_velocity, endosome
    s)
123.            add_over_ar(endosomes, array_l)
124.
125.        #    for i in range(frames):
126.        #        plt.figure()
127.        #        plt.imshow(array_l[i], interpolation='nearest')
```

particles.py

```
1.  """
```

```
This file is part of Interaction_simulator

@author: Kez Cleal, ClealK@cardiff.ac.uk
"""

from numpy import random
from scipy import spatial


class Particle:
    def __init__(self, velocity, centre, p_fuse, p_split, event_gap, name):
        self.name = name
        self.velocity = velocity
        self.centre = centre
        self.history = []
        self.p_fuse = p_fuse
        self.p_split = p_split
        self.fused = False
        self.fusedwith = None
        self.fuse_events = 0
        self.fframe = []
        self.fusedendosomes = []
        self.split_events = 0
        self.sframe = []
        self.splitendosomes = []
        self.ori_gap = event_gap
        self.event_gap = event_gap
        self.pause = False

    def save_history(self):
        self.history.append(self.centre)

    def print_centre(self):
        return self.centre

    def print_velocity(self):
        return self.velocity

    def print_fuse(self):
        return self.fused

    def show_track(self):
        return self.history

    def print_history(self):
        self.props = {'History': self.history, 'Fuse_Events': self.fuse_events,
                      'Fuse_frames': self.fframe,
                      'Split_Events': self.split_events,
                      'Split_frames': self.sframe,
                      'Fused_with': self.fusedendosomes,
                      'Split_from': self.splitendosomes, 'Particle': self.name}
        return self.props

    def print_fused_with(self):
        return self.fusedwith

    def check_colocalization(self, one_frame_history):
        if self.centre in one_frame_history:
            return True

    def tick_gap(self):
        if self.pause:
            self.event_gap -= 1
            if self.event_gap == 0:
                self.pause = False
                self.event_gap = self.ori_gap
```

```
68.
69.     def update_fusion(self, frame, endo):
70.         if self.pause:
71.             pass
72.         else:
73.             r = random.rand()
74.             if r > self.p_fuse:
75.                 self.fused = True
76.                 self.pause = True
77.                 self.fuse_events += 1
78.                 self.fframe.append(frame)
79.                 self.fusedwith = endo
80.                 self.fusedendosomes.append(str(endo))
81.                 # print 'Fusion', str(frame), str(endo)
82.
83.     def update_splitting(self, frame):
84.         if self.pause:
85.             pass
86.         else:
87.             r = random.rand()
88.             if r > self.p_split:
89.                 self.fused = False
90.                 self.pause = True
91.                 self.split_events += 1
92.                 self.sframe.append(frame)
93.                 self.splitendosomes.append(self.fusedwith)
94.                 self.fusedwith = None
95.                 # print 'Splitting', str(frame)
96.
97.     def update_centre(self, newxy):
98.         self.centre = newxy
99.
100.
101.        def check_colocalization(centre, frame, endosomes):
102.            x = centre[0]
103.            y = centre[1]
104.            colo_with = []
105.
106.            for i in range(len(endosomes)):
107.                string = 'End'+str(i)
108.                h = endosomes.setdefault(string, {})['History']
109.                if len(h) > 0:
110.                    hframe = h[frame]
111.                    if (x, y) in hframe:
112.                        colo_with.append(string)
113.
114.            if len(colo_with) > 0:
115.                return True, colo_with
116.            else:
117.                return False, 1
118.
119.
120.        def move_random(centre, velocity):
121.            oldx = centre[0]
122.            oldy = centre[1]
123.            newx = random.uniform(-velocity, velocity) + oldx
124.            newy = random.uniform(-velocity, velocity) + oldy
125.
126.            # City block distance to move
127.            d = spatial.distance.cityblock([oldx, oldy], [newx, newy])
128.
129.            # clockwise, potential pixels to walk through
130.            pixel_walk = [0, 1, -1]
131.            new_cx = oldx
132.            new_cy = oldy
133.            for i in range(int(round(d, 0))):
```

```
                rand_x = 0
                rand_y = 0
                while (rand_x, rand_y) == (0, 0):
                    rand_x = random.choice(pixel_walk)
                    rand_y = random.choice(pixel_walk)
                new_cx += rand_x
                new_cy += rand_y
            return new_cx, new_cy


        def distance(item, target):
            '''''http://stackoverflow.com/questions/12696916/'''
            return ((item[0] - target[0]) ** 2 + (item[1] - target[1]) ** 2) ** 0.5


        def move_inside_endosome(centre, endo, velocity):
            newx, newy = None, None
            if centre in endo:
                while (newx, newy) not in endo:
                    newx, newy = move_random(centre, velocity)
                return newx, newy
            else:
                best = min(endo, key=lambda x: distance(x, centre))
                while (newx, newy) not in endo:
                    newx, newy = move_random(best, velocity)
                return newx, newy


        def make_particles(velocity, centre, p_fuse, p_split, event_gap,
                           frames, endosomes, name, ar_size):

            # create particle
            p = Particle(velocity, centre, p_fuse, p_split, event_gap, name)
            # record initial particle position
            p.save_history()
            # move particle through frames

            for i in range(frames-1):
                centre = p.print_centre()
                velocity = p.print_velocity()

                # check to see if events can occur
                p.tick_gap()

                # check to see if fused
                fuse_status = p.print_fuse()
                co, endo_col = check_colocalization(centre, i, endosomes)

                # check to see if splitting occurs
                if fuse_status:
                    endo = p.print_fused_with()
                    p.update_splitting(i)
                    endosome_tups = endosomes.setdefault(endo, {})['History'][i+1]
                    x, y = move_inside_endosome(centre, endosome_tups, velocity)
                    new_position = (x, y)
                    if x > 1 and x < ar_size-1 and y > 1 and y < ar_size-1:
                        p.update_centre(new_position)
                        p.save_history()
                    else:
                        return p.print_history()

                # check to see if colocalized, and if fusion occurs
                if not fuse_status:
                    if co:
                        p.update_fusion(i, random.choice(endo_col))
```

```
                    x, y = move_random(centre, velocity)
                    new_position = (x, y)
                    if x > 1 and x < ar_size-1 and y > 1 and y < ar_size-1:
                        p.update_centre(new_position)
                        p.save_history()
                    else:
                        return p.print_history()

            return p.print_history()


        if __name__ == '__main__':

            hist = {'History': [[(1, 1), (2, 2)], [(1, 2), (3, 2)], [(2, 1), (2, 2)]]}
            hist2 = {'History': []}

            endosomes = {'End0': hist, 'End1': hist2 }

            velocity, centre, p_fuse, p_split, event_gap, frames, name = 10, (1, 1), 0.5, 0.5, 2, 3, '1'

            array_l = []
            for i in range(frames):
                array_l.append(np.zeros((20, 20)))

            #list of dictionaries
            ds = make_particles(velocity, centre, p_fuse, p_split, event_gap, frames, endosomes, name)
            print ds
            ds_all = []
            ds_all.append(ds)

            c = 0
            for i in ds_all:
                h = ds_all[c]['History']
                # for each frame
                for i in h:
                    x = i[0]
                    y = i[1]
                    ar = array_l[c]
                    ar[x][y] += 1
                    try:
                        ends = endosomes.setdefault('End0', {})['History'][c]
                        for k in ends:
                            x1 = k[0]
                            y1 = k[1]
                            ar1 = array_l[c]
                            ar1[x1][y1] += 1
                    except:
                        pass
                    c += 1

        #         for i in array_l:
        #             plt.figure()
        #             plt.imshow(i, interpolation='nearest')
        #             plt.colorbar()
```

Methods 2

Quacker

Quacker comprises of 5 scripts. Main, file_handler, cell_process, qfilter1 and lines_draw scripts are provided below. In addition tiffile.py from Christoph Gohlke (http://www.lfd.uci.edu/~gohlke/) is required. To use Quacker, the main.py script must be run from the command-line e.g. execute by typing "python main.py". The licence for Quacker is provided here:

Further dependencies:

Numpy

Skimage

Scipy

Pandas

Image

To run Quacker, place the following scripts in a directory and run the main.py script.

main.py

```
"""
This file is part of Quacker

@author: Kez Cleal, ClealK@cardiff.ac.uk
"""

import time
import pickle
import multiprocessing as mp
import numpy as np

import file_handler as FH
import cell_process as CP
import qfilter1 as QF
import lines_draw as LD


class MultiQ(object):
    """Accepts a list of parameters to generate multiple processes. One process
```

```
    is started for each cell to a maximum of cpu cores present. The worker
    function deals with fleshing out the results for each cell. Results should
    be returned in order into self.output which can then be read later on."""
    def __init__(self, pool_parameters, pool_size):
        self.pool_parameters = pool_parameters
        self.pool_size = pool_size
        self.pool = mp.Pool(self.pool_size)
        # Sets up a results list
        self.results = \
            [self.pool.apply_async(worker, args=((self.pool_parameters[i]),),)
                for i in range(self.pool_size)]
        self.output = [r.get() for r in self.results]  # Output objects in here


def args():
    argnames = ['idir',
                'Clip_edges',
                'Clip_amount',
                'col',
                'pixel_tomicron',
                'multi_process']
    return argnames


def default_params():
    params = {'idir': 'C:\\Users\\Kez\\Desktop\\OldPC\\Thesis\\Chapter 5\\rab data\
\Rab 21\\corrected',
              'Clip_edges': False,
              'Clip_amount': 10,
              'col': 'Trajectory_Frame_x_y',
              'pixel_tomicron': False,
              'pixel_size': 0.625,
              'multi_process': True,
              'plots': False,
              'plot_frame': 0,
              'Initial_gauss': 1,
              'Gauss_size': 5,
              'Block_size': 30,
              'Offset': 40,
              'Dilate_small': False,
              'Dilate': 2,
              'Small_object_size': 15,
              'min_track_length': 10,
              'remove_short': True,
              'split_variance': 1,
              'Temporal': True,
              'Spatial': True,
              'Fuse_length': 5,
              'Split_length': 5,
              'Split_p_val': 0.05,
              'Fuse_score': 0.05,
              'Score_threshold': 1.01}
    return params


def data_list():
    data = ['results',
            'shape',
            'binary_tups_frame',
            'pie',
            'max_displacement',
            'xpdf',
            'ypdf',
            'binary_object',
            'DTrans_l',
            'pdf_normal',
```

```
            'outpath',
            'tif_f',
            'csv_f',
            'out',
            'binary_ob']
    return data


def cell_list(params, data):
    """Generate a cell list with paths and parameters to process in a pool.
    Returns tuples containing the params, and the size of the required pool
    to generate."""
    cell_list = FH.load_cells(params, data)
    pool_parameters = []
    for c in cell_list:
                pool_parameters.append((c.name, c.tifpath_d, c.csvpath_d,
                                        c.params, data))
            return pool_parameters


        def pipeline():
            return [FH.load_data,
                    CP.find_objects,
                    FH.remove_short,
                    FH.add_columns_to_csv,
                    CP.displacement,
                    CP.make_pdf_circle,
                    CP.pdf_normal,
                    CP.get_intensity1,
                    # CP.make_pdf_circle,
                    CP.find_good,
                    QF.filter_events,
                    FH.create_out_pth,
                    LD.lines,
                    FH.write_to_csv]


        def worker(object_args):
            """Function which processes information for one cell. Creates a new cell

            instance and populates it with data from multiprocessing. A new cell_
            instance has to be created because multiprocesing wont let objects be
            passed through it; a new cell object is created and populated here."""
            # Deal with files
            cell = FH.Cell(*object_args)

            for job in pipeline():
                # print str(job)  uncomment to find bugs
                job(cell)
                if job == CP.find_objects and cell.params['plots']:
                    break

            return cell.out


        def dumpout(out, params):
            dataset_event_n = {'Total_fuse': [],
                               'Fuse_i=0': [],
                               'Fuse_i>0': [],
                               'Fuse+parent': [],
                               'Total_split': [],
                               'Split+child': [],
                               'Any_events': [],
                               'Multiple': [],
                               'Coloc_only': []}
            dataset_track_n = {'Total_fuse': [],  # .copy() or dict() doesnt work!
```

```
                                'Fuse_i=0': [],
                                'Fuse_i>0': [],
                                'Fuse+parent': [],
                                'Total_split': [],
                                'Split+child': [],
                                'Any_events': [],
                                'Multiple': [],
                                'Coloc_only': []}
            for i in out:
                outstring = \
                    '{path}\\{cell}_output\\{cell}.p'.format(path=params['idir'],
                                                             cell=i['Cell'])
                # print outstring
                pickle.dump(i, open(outstring, 'wb'))
                print 'Cell ', i['Cell']

                for key, value in i.iteritems():
                    if key == 'Particle_results':
                        print 'Particle_number: ', len(value)

                        event_n = {'Total_fuse': 0,
                                   'Fuse_i=0': 0,
                                   'Fuse_i>0': 0,
                                   'Fuse+parent': 0,
                                   'Total_split': 0,
                                   'Split+child': 0,
                                   'Any_events': 0,
                                   'Multiple': 0,
                                   'Coloc_only': 0}
                        track_n = event_n.copy()
                        for i in range(len(value)):  # For each particle object
                            d = value[i].event_numbers()
                            # Adds up all the events and track numbers
                            event_n = { k: event_n.get(k) + d.get(k) for k in event_
    n}
                            track_n = { k: track_n.get(k) + bool(d.get(k)) for k in
    track_n}

                        print 'Type Event_number Tracks_number'
                        for key1, value1 in event_n.iteritems():
                            print key1, value1, track_n[key1]
                            dataset_event_n[key1].append(value1)
                            dataset_track_n[key1].append(track_n[key1])

            print 'Type, Avg_events, Avg_tracks, Std_events, Std_tracks'
            for key2, value2 in dataset_event_n.iteritems():
                a = np.array(value2)
                a1 = np.array(dataset_track_n[key2])
                print key2, np.mean(a), np.mean(a1), np.std(a), np.std(a1)


        if __name__ == '__main__':
            time1 = time.time()
            print 'Main function running'

            # Generates parameters.
            argnames = args()

            params = p.args
            if not params['idir']:
                params = default_params()
            # A list of data attributes to add to the Cell class for filling later.

            data = data_list()

```

```
212.           # Looks in the directory for files to process. Pairs .tif files with .cs
    v
213.           # files according to their names and places them in 'Cell' objects. Each

214.           # Cell is dealt with in a seperate process.
215.           pool_of_cells = cell_list(params, data)
216.           out = []
217.           if not params['multi_process'] or len(pool_of_cells) == 0:
218.               print 'Single process'
219.               for i in range(len(pool_of_cells)):
220.                   out.append(worker(pool_of_cells[i]))
221.
222.           else:
223.               print 'Multiprocess'
224.               pool_size = len(pool_of_cells)
225.               multip = MultiQ(pool_of_cells, len(pool_of_cells))
226.               for i in multip.output:
227.                   out.append(i)
228.           if not params['plots']:
229.               dumpout(out, params)
230.           print 'Time: ', time.time() - time1
```

file_handler.py

```
1.  """
2.  This file is part of Quacker
3.
4.  @author: Kez Cleal, ClealK@cardiff.ac.uk
5.  """
6.
7.  import os  # Standard library imports
8.  from csv import DictReader
9.  import numpy as np  # Other imports
10. import tifffile
11. import pandas as pd
12. import main as M
13. from itertools import groupby, izip
14. import csv
15.
16.
17. class Cell(object):
18.     def __init__(self, name, tifpath_d, csvpath_d, params, data):
19.         """Holder to deal with individual cells."""
20.         self.name = name
21.         self.tifpath_d = tifpath_d
22.         self.csvpath_d = csvpath_d
23.         self.params = params
24.         for d in data:
25.             setattr(self, d, None)
26.
27.     def __getitem__(self, key):
28.         return getattr(self, key)
29.
30.     def __setitem__(self, key, value):
31.         return setattr(self, key, value)
32.
33.
34. class Tiff_wrapper:
35.     def __init__(self, idir):
36.         """Holder for tif data for a single cell."""
37.         self.idir = idir
38.         self.channel1 = []
39.         self.channel2 = []
40.         self._channel_list()
41.
```

```
42.     def _channel_list(self):
43.         """Accepts a path string and splits tif file into two numpy
44.         channels."""
45.         try:
46.             f = tifffile.imread(self.idir)
47.         except:
48.             print 'Could not read tif file.'
49.         try:
50.             if np.shape(f)[3] < 4:
51.                 for i in range(len(f)):
52.                     self.channel1.append(f[i, :, :, 0])
53.                     self.channel2.append(f[i, :, :, 1])
54.             else:
55.                 for i in range(len(f)):
56.                     self.channel1.append(f[i, 0, :, :])
57.                     self.channel2.append(f[i, 1, :, :])
58.         except:
59.             print 'Tif file structure problem.'
60.
61.
62. class CSV_wrapper:
63.     def __init__(self, idir, col):
64.         """Holder for csv data for a single cell. Contains methods for cliping
65.         tracks and converting data to microns."""
66.         self.idir = idir
67.         self.data = {'Particles': [], 'Frame': [], 'X': [], 'Y': []}
68.         self._extractdata(col)
69.
70.     def _extractdata(self, col):
71.         """Gets data from csv file according to column."""
72.         # columns for data
73.         a = col.split('_')
74.         try:
75.             csvfile = open(self.idir)
76.             reader = DictReader(csvfile)
77.             for line in reader:
78.                 self.data['Particles'].append(int(line[a[0]]))
79.                 self.data['Frame'].append(int(line[a[1]]))
80.                 self.data['X'].append(float(line[a[2]]))
81.                 self.data['Y'].append(float(line[a[3]]))
82.         except:
83.             print 'Could not read .csv file.'
84.         if len(self.data['X']) == 0:
85.             print 'No tracks to process.'
86.             raise SystemExit
87.
88.     def clip_edges(self, minx, maxx, miny, maxy):
89.         """Accepts clip list and returns tracks contained within bounds."""
90.         try:
91.             self.data = pd.DataFrame(self.data)
92.             self.data.groupby('Particles').filter(lambda x: min(x['X']) > minx)
93.             self.data.groupby('Particles').filter(lambda x: max(x['X']) < maxx)
94.             self.data.groupby('Particles').filter(lambda x: min(x['Y']) > miny)
95.             self.data.groupby('Particles').filter(lambda x: max(x['Y']) < maxy)
96.             self.data = pd.DataFrame.to_dict(self.data, 'list')
97.         except:
98.             print 'Clip edges function failed.'
99.
100.            def to_microns(self, data, pixel_size):
101.                """Converts data to from pixels to microns if needed."""
102.                try:
103.                    self.data['X_microns'] = [x*pixel_size for x in data['X']]
104.                    self.data['Y_microns'] = [x*pixel_size for x in data['Y']]
105.                except:
106.                    print 'Conversion to microns failed.'
107.
```

```
108.
109.       def get_paths(idir, rf):
110.           """Given a directory and a file extension and returns a list of files wi
    th
111.           given extension."""
112.           rf_list = []
113.           listing = os.listdir(idir + '\\')
114.           for files in listing:
115.               if rf in files:
116.                   rf_list.append(files)
117.           return sorted(rf_list)
118.
119.
120.       def load_cells(params, data):
121.           """Takes a list of parameters and returns cell objects which contain
122.           all .csv and .tif data. This is then used for multiprocessing."""
123.           tifpath = get_paths(params['idir'], 'tif')
124.           csvpath = get_paths(params['idir'], 'csv')
125.           tifpath = [t for t in tifpath if '.txt' not in t]  # get rid of .txt fil
    es
126.           cell_list = []
127.
128.           for i in range(len(tifpath)):  # Get Tiff and CSV object for each cell
129.               tifpath_d = '{directory}\\{tiffile}'.format(directory=params['idir']
    ,
130.                                                           tiffile=tifpath[i])
131.               csvpath_d = '{directory}\\{csvfile}'.format(directory=params['idir']
    ,
132.                                                           csvfile=csvpath[i])
133.               st = tifpath[i][:-4]
134.               cell_object = Cell(st, tifpath_d, csvpath_d, params, data)
135.               cell_list.append(cell_object)
136.
137.           return cell_list
138.
139.
140.       def load_data(cell):
141.           """After cell object is initialised this method is called to populate
142.           the object with associated raw data."""
143.           # print self.name
144.           tiff_object = Tiff_wrapper(cell.tifpath_d)
145.           csv_object = CSV_wrapper(cell.csvpath_d, cell.params['col'])
146.           if cell.params['Clip_edges'] == 'True':
147.               clips = cell.params['Clip_amount']
148.               csv_object.clip_edges(clips, clips, clips, clips)
149.           if cell.params['pixel_tomicron'] == 'True':
150.               csv_object.to_microns(cell.params['pixel_size'])
151.           cell['tif_f'] = [tiff_object.channel1, tiff_object.channel2]
152.           cell['csv_f'] = csv_object.data
153.
154.
155.       def remove_short(cell):
156.           if cell.params['remove_short']:
157.               f = cell.csv_f
158.               p = f['Particles']
159.               minl = cell.params['min_track_length']
160.               for key, val in f.iteritems():
161.                   # Turn value into groups of particles
162.                   g = [list(grp) for _, grp in groupby(izip(p, val), lambda x: x[0
    ])]
163.                   g_idx = [[number for _, number in items] for items in g]
164.                   s = [i for i in g_idx if len(i) > minl]
165.                   s = [item for sublist in s for item in sublist]
166.                   f[key] = s
167.               cell.pie = f
168.           else:
```

```
            cell.pie = cell.csv_f


    def add_columns_to_csv(cell):
        columns = ['tups_l', 'Temporal', 'Spatial', 'Spatial_score',
                   'Combined_filters', 'Intensity_red',
                   'Intensity_green', 'Colocalized', 'Info', 'Score',
                   'Object_parent']
        column_length = len(cell.pie['Particles'])
        for col in columns:
            cell.pie[col] = [0 for i in range(column_length)]


    def create_out_pth(cell):
        name = cell.name
        pth = cell.params['idir']
        directory = '{p}\\{n}_output'.format(p=pth, n=name)
        if not os.path.exists(directory):
            os.makedirs(directory)
        cell.outpath = directory


    def write_to_csv(cell):
        name = cell.name
        csv_name = '{out_pth}\\{n}_out.csv'.format(out_pth=cell.outpath, n=name)

        del cell.pie['tups_l']
        with open(csv_name, 'wb') as csvfile:
            writer = csv.writer(csvfile)
            writer.writerow(cell.pie.keys())
            writer.writerows(zip(*cell.pie.values()))


    if __name__ == '__main__':
        params = {'idir': 'C:\\Users\\Kez\\Desktop\\Py\\In',
                  'Clip_edges': True,
                  'Clip_amount': 10,
                  'col': 'Trajectory_Frame_x_y',
                  'pixel_tomicron': False,
                  'pixel_size': 0.625}
        data = M.data_list()
        cell_list = load_cells(params, data)
        print cell_list
        for i in cell_list:
            load_data(i)
```

cell_process.py

```
"""
This file is part of Quacker

@author: Kez Cleal, ClealK@cardiff.ac.uk
"""

import time
import numpy as np
import matplotlib.pyplot as plt
from scipy import ndimage
from skimage.filter import threshold_adaptive
import matplotlib.mlab as mlab
from math import sqrt, cos, sin, pi
import sys
```

```
15. from itertools import groupby, izip
16.
17.
18. def timing(f):
19.     def wrap(*args):
20.         time1 = time.time()
21.         ret = f(*args)
22.         time2 = time.time()
23.         print '%s: %0.4f s' % (f.func_name, (time2-time1))
24.         sys.stdout.flush()
25.         return ret
26.     return wrap
27.
28.
29. # @timing
30. def find_objects(cell):
31.     """Uses Otsu adaptive to find blobs and then dilates them to match the
32.     original image a bit better."""
33.     cell.binary_ob = []
34.     cell.DTrans_l = []
35.     if cell.params['plots']:
36.         length = (cell.params['plot_frame'],
37.                   cell.params['plot_frame']+1)
38.     else:
39.         length = (0, len(cell.tif_f[1]))  # Channel 2 (green)
40.     cell.shape = np.shape(cell.tif_f[1][0])
41.     for i in range(*length):
42.         array = cell.tif_f[1][i]
43.         if cell.params['Initial_gauss'] > 0:
44.             gaussian = ndimage.filters.gaussian_filter(array,
45.                                                        cell.params['Initial_gauss']
    )
46.             b = threshold_adaptive(gaussian,
47.                                    int(cell.params['Block_size']),
48.                                    offset=-(int(cell.params['Offset'])),
49.                                    method='gaussian',
50.                                    param=(int(cell.params['Gauss_size'])))
51.         else:
52.             b = threshold_adaptive(array,
53.                         int(cell.params['Block_size']),
54.                         offset=-(int(cell.params['Offset'])),
55.                         method='gaussian',
56.                         param=(int(cell.params['Gauss_size'])))
57. #         b = b.astype(np.int, copy=False)
58.
59.         if cell.params['Dilate_small'] and cell.params['Dilate'] > 0:
60.             struct1 = ndimage.generate_binary_structure(2, 1)
61.             struct2 = ndimage.generate_binary_structure(2, 2)
62.             mask = b > 0
63.             label_im, nb_labels = ndimage.label(mask)
64.             sizes = ndimage.sum(mask, label_im, range(nb_labels + 1))
65.             mask_size = sizes > cell.params['Small_object_size']
66.             remove_pixel = mask_size[label_im]
67.             label_im[remove_pixel] = 0
68.             label_im[label_im > 0] = 1
69.             if cell.params['Dilate'] == 1 \
70.                     or cell.params['Dilate'] == 2:
71.                 b1 = ndimage.binary_dilation(label_im, structure=struct1,
72.                                              iterations=1)
73.                 if cell.params['Dilate'] == 2:
74.                     b1 = ndimage.binary_dilation(b1, structure=struct2,
75.                                                  iterations=1)
76.             if cell.params['Dilate'] > 2:
77.                 b1 = ndimage.binary_dilation(label_im,
78.                                              structure=struct2,
79.                                              iterations=cell.
```

```
                                                params['Dilate'])
            if cell.params['Dilate'] > 0:
                b = b1 + b
                b[b > 0] = 1

        cell.binary_ob.append(b)
        cell.DTrans_l.append(ndimage.morphology.distance_transform_edt(1 - b))

        if cell.params['plots']:
            fig = plt.figure(figsize=(14, 7), facecolor='white')

            ax1 = fig.add_subplot(121)
            im = ax1.imshow(array, interpolation='nearest')
            ax1.set_title('Original')
            ax1.title.set_color('gray')
            ax1.set_adjustable('box-forced')
            ax1.tick_params(axis='x', colors='gray')
            ax1.tick_params(axis='y', colors='gray')
            ax1.get_yaxis().set_tick_params(direction='out')
            ax1.get_xaxis().set_tick_params(direction='out')

                    #fig.subplots_adjust(right=0.8)
                    cbar_ax = fig.add_axes([0.04, 0.15, 0.02, 0.7])
                    fig.colorbar(im, cax=cbar_ax)

                    ax2 = fig.add_subplot(122, sharex=ax1, sharey=ax1)
                    ax2.imshow(b, interpolation='nearest', cmap='gray')
                    ax2.set_title('Adaptive gaussian threshold')
                    ax2.set_adjustable('box-forced')
                    ax2.title.set_color('gray')
                    ax2.set_adjustable('box-forced')
                    ax2.tick_params(axis='x', colors='gray')
                    ax2.tick_params(axis='y', colors='gray')
                    ax2.get_yaxis().set_tick_params(direction='out')
                    ax2.get_xaxis().set_tick_params(direction='out')


                    plt.show()


        # @timing
        def remove_short(cell):
            if cell.params['remove_short']:
                f = cell.csv_f
                p = f['Particles']
                minl = cell.params['min_track_length']
                for key, val in f.iteritems():
                    # Turn value into groups of particles
                    g = [list(grp) for _, grp in groupby(izip(p, val), lambda x: x[0
    ])]
                    g_idx = [[number for _, number in items] for items in g]
                    s = [i for i in g_idx if len(i) > minl]
                    s = [item for sublist in s for item in sublist]
                    f[key] = s
                cell.pie = f


        # @timing
        def displacement(cell):
            """Gets particle displacements"""
            l = len(cell.csv_f['Particles'])
            dip = [0 for i in range(l)]
            alx = cell.csv_f['X']
            aly = cell.csv_f['Y']
            alp = cell.csv_f['Particles']
            tups_l = zip(alx, aly)
```

```
            cell.pie['tups_l'] = tups_l
            for i in range(l-1):
                dx = abs(alx[i+1] - alx[i])
                dy = abs(aly[i+1] - aly[i])
                d = sqrt(dx**2 + dy**2)
                if alp[i] != alp[i+1]:
                    continue  # dip[i+1] = pylab.nan
                else:
                    dip[i+1] = d
            cell.pie['Displacement'] = dip
            cell.max_displacement = max(dip[1:])


        # @timing
        def pdf_normal(cell):
            '''''Called once to find the probability density function of a normal
            distribution centered around 0 with variance, up to a maximum of
            100px displacement.'''
            mean = 0
            variance = cell.params['split_variance']
            # sigma = np.sqrt(variance)
            x = np.linspace(0, 1000, 100000)  # 10 per pixel for 100 pixels
            a = mlab.normpdf(x, mean, variance)
            m = np.max(a)
            a = a/m
            cell.pdf_normal = a


        # @timing
        def get_intensity1(cell):
            """Takes the list of particle coords in every frame and makes a list of
            tuples for the intensity in (red, green) channels."""
            l = len(cell.pie['Particles'])
            xl = cell.pie['X']
            yl = cell.pie['Y']
            frame = cell.pie['Frame']
            for i in range(l):  # For each particle
                x = int(xl[i])
                y = int(yl[i])
                cell.pie['Intensity_red'][i] = cell.tif_f[0][frame[i]][y, x]
                cell.pie['Intensity_green'][i] = cell.tif_f[1][frame[i]][y, x]
                if cell.binary_ob[frame[i]][y, x]:
                    cell.pie['Colocalized'][i] = 1


        def circle_edge(r, samples):
            step = 360/float(samples)
            x = np.zeros((samples))
            y = np.zeros((samples))
            angle = 0
            for i in range(0, samples):
                x[i] = r*cos(angle*pi/180)
                y[i] = r*sin(angle*pi/180)
                angle += step
            return x, y


        # @timing
        def make_pdf_circle(cell, d_per_pixel=0.1):
            d = cell.max_displacement / d_per_pixel
            den = 10
            x1 = []
            y1 = []
            for i in range(int(d) + 2):
                size = float((i) * d_per_pixel)
                if size > 0:
```

```
                    samples = int(2 * pi * size * den)  # Circumpherence
                    px, py = circle_edge(size, samples)
                    x1.append(px)
                    y1.append(py)
                else:
                    x1.append(np.array([0]))
                    y1.append(np.array([0]))
            cell.xpdf = x1
            cell.ypdf = y1


        def find_ones(ar, to_check, checked, ones, p, shape):
            checked.add(p)
            px = p[0]
            py = p[1]
            if any([px < 0, py < 0, px >= shape[0], py >= shape[1]]):
                return 0
            else:
                if ar[px, py]:
                    ones.add(p)
                    looksee = ((px-1, py), (px, py-1), (px+1, py), (px, py+1))
                    for i in looksee:
                        if i not in checked:
                            to_check.add(i)


        def set_looksee(point, to_check):
            x = point[1]
            y = point[0]
            to_check.add(point)
            looksee = ((x-1, y), (x, y-1), (x+1, y), (x, y+1))
            for j in looksee:
                to_check.add(j)


        def find_connected(point, ar):
            shape = np.shape(ar)
            to_check = set()
            checked = set()
            ones = set()
            set_looksee(point, to_check)
            while len(to_check) > 0:
                p = to_check.pop()
                find_ones(ar, to_check, checked, ones, p, shape)
            return ones


        # @timing
        def find_good(cell):
            frame = cell.pie['Frame']
            col = cell.pie['Colocalized']
            tups_l = cell.pie['tups_l']
            particle = cell.pie['Particles']
            for i in range(len(tups_l)-1):
                if particle[i] != particle[i+1]:
                    continue  # Start of next particle
                # Check for parent objects for split events
                if col[i] == 1 and col[i+1] == 0:
                    # Check if region has a child from next frame
                    ar = cell.binary_ob[frame[i]]
                    ar_next = cell.binary_ob[frame[i+1]]
                    region = find_connected(tups_l[i], ar)
                    for k in region:
                        if ar_next[k[0], k[1]]:
                            cell.pie['Object_parent'][i+1] = 2
                            break
```

```
                # Check for parent objects for fuse events
                if col[i] == 0 and col[i+1] == 1:
                    # Check if region has a child from previous frame
                    ar = cell.binary_ob[frame[i+1]]
                    ar_previous = cell.binary_ob[frame[i]]
                    region = find_connected(tups_l[i+1], ar)
                    for k in region:
                        if ar_previous[k[0], k[1]]:
                            cell.pie['Object_parent'][i+1] = 1
                            break
```

qfilter1.py

```
"""
This file is part of Quacker

@author: Kez Cleal, ClealK@cardiff.ac.uk

The filters function takes a data_ref object which containes parameters for the
functions listed here, a list of arrays to work on as well as a dictionary
containing information on particle tracks. The data_ref object is altered in
place and an 'Output' dict is added which gives a basic output for printing.
"""

from itertools import groupby as groupby
from collections import Counter
import time
import sys
from scipy import stats


def timing(f):
    def wrap(*args):
        time1 = time.time()
        ret = f(*args)
        time2 = time.time()
        print '%s: %0.4f s' % (f.func_name, (time2-time1))
        sys.stdout.flush()
        return ret
    return wrap


def distance_transform_p(data_ref, tup, frame, var=1):
    '''''Performs array look ups in the distance transform array to find p_value
    for appearing outside of an object.'''
    dt = data_ref.DTrans_l[frame][int(tup[1])][int(tup[0])]
    return stats.norm.pdf(dt, scale=var)/stats.norm.pdf(0, scale=var)


def spatial_colocalized(data_ref, tup, displacement, frame, d_per_pixel=0.1):
    '''''Performs array look ups in a circle to find probability of landing in an
    object for a single track.'''
    p_value = 1
    find = round(displacement, 1)  # Round the displacement vector.

    # The binary position in the probability density function.
    position = int(find / d_per_pixel)
    # Indicies are flipped because of array format
    x_distribution = data_ref.xpdf[position] + tup[0]
    y_distribution = data_ref.ypdf[position] + tup[1]
    f0 = zip([int(xx) for xx in x_distribution],
```

```
49.             [int(yy) for yy in y_distribution])
50.
51.     f = set(f0)  # Gets all the unique pixels to look at***
52.     maxx = data_ref.shape[0]
53.     maxy = data_ref.shape[1]
54.     # All the values outside of the array bounds are removed.
55.     f1 = [(v, k) for v, k in f if v > 0 and k > 0 and v < maxx and k < maxy]
56.
57.     weights = Counter(f0)  # The number of occurances of each pixel
58.     p = 0
59.     for point in f1:
60.         y = point[0]
61.         x = point[1]
62.         weight = weights[point]
63.         if data_ref.binary_ob[frame][y][x] == 1:
64.                 p += weight
65.     p_value = float(p)/sum(weights.values())
66.
67. #    xy_dis = [list(t) for t in zip(*f1)]  # Create x and y lists
68. #    if len(xy_dis) > 0:  # Exit function if no pixels need to be checked.
69. #        x_dis = xy_dis[0]
70. #        y_dis = xy_dis[1]
71. #        p = 0
72. #        d = len(x_dis)
73. #        for j in range(d):  # For each point around the edge of the circle.
74. #            xj = int(x_dis[j])
75. #            yj = int(y_dis[j])
76. #            if data_ref.binary_ob[frame][xj][yj] == 1:
77. #                p += 1
78. #        p_value = float(p)/d
79.
80.     return p_value
81.
82.
83. def score_this_track(data_ref, z, lengths, ci):
84.     '''''Looks at a particular point in the track; looks at intensity surrounding
85.     a pixel to see if it is above the score threshold.'''
86.     green = data_ref.pie['Intensity_green']
87.     result = [False, 'Error. ']
88.     back1 = lengths[0] if lengths[0] > 3 else 3
89.     forward1 = lengths[1] if lengths[1] > 3 else 3
90.     # ci = [chunk, index, end]
91.     # See if there is enough room to look forward and back around a split site.
92.     # If not then use the length of the block either side of the event.
93.     back = ci[1] if ci[1] - back1 < 0 else ci[1] - back1
94.     forward = ci[2] if ci[1] + forward1 > ci[2] else ci[1] + forward1
95.
96.     event_idx = ci[1]
97.
98.     score_list = data_ref.pie['Score']
99.     score = float(sum(green[back:event_idx])) / sum(green[event_idx:forward])
100.            score_list[event_idx] = score
101.            if score >= data_ref.params['Score_threshold']:
102.                result = [True, 'Split event ({s}). '.format(s=round(score, 3))]
103.            elif score < data_ref.params['Score_threshold']:
104.                result[1] = 'No event ({s}). '.format(s=round(score, 3))
105.
106.            return result
107.
108.
109.        def look_fusion(data_ref, filters, z, lengths, info, ci):
110.            '''''Check for fusion events. Please see look_split for a fuller descrip
    tion.
111.            '''
112.            found = 0
113.            result = False
```

```
            if filters[0]:  # Temporal filter
                if len(ci[0]) > lengths[0]:
                    found += 1
                    data_ref.pie['Temporal'][ci[1]] = 1
                    info[ci[1]] += 'Temporal: Fuse event ({fuse_l}). '.format(fuse_l
    =len(ci[0]))
                else:
                    info[ci[1]] += 'Temporal: No event ({fuse_l}). '.format(fuse_l=l
    en(ci[0]))

            if filters[1]:  # Spatial filter
                tups_l = data_ref.pie['tups_l'][ci[1]: ci[2]]
                displacement = data_ref.pie['Displacement'][ci[1]: ci[2]]
                frames = data_ref.pie['Frame'][ci[1]: ci[2]]
                pval = 1
                for i in range(len(ci[0])):
                    if i == len(ci[0]) - 1:
                        info[ci[1]] += 'Spatial: No event ({s}). '.format(s=pval)
                        break
                    # Process to end of block, stop if event is found
                    val = spatial_colocalized(data_ref, tups_l[i],
                                              displacement[i + 1], frames[i + 1])
                    pval *= val  # Keeps tally of cumulative p score

                    if pval < data_ref.params['Fuse_score']:
                        found += 1
                        data_ref.pie['Spatial'][ci[1]] = 1
                        data_ref.pie['Spatial_score'][ci[1]] = pval
                        info[ci[1]] += 'Spatial: Fuse event ({s}). '.format(s=pval)

                        break

            if found == 2:  # If both filters agree
                data_ref.pie['Combined_filters'][ci[1]] = 1  # Add to both result
                info[ci[1]] += 'Both filters agree. '
                result = True

            if sum(filters) == 1 and found == 1:
                info[ci[1]] += 'Single filter sucess. '
                result = True  # If both filters agree, or single filter success

            return result


        def look_split(data_ref, filters, z, lengths, info, ci):
            '''''Checks for splitting. The data_ref object must contain the followin
    g:
            - A reference to information on the particle track with data columns:
            Frame, tups_l, Spatial, Combined_filters, Temporal.
            - Parameters required in the data_ref.params dict are 'Split_p_val'.
            Other params are fuse and split lengths which are contained in the list
            'lengths'.
            - The data_ref object must also have binary image arrays and distance
            transform arrays.
            - z is the particle number which the data dict should be sorted by.
            - The ci parameter is a list which contains a block generated by
            'chunk_track', and the index and end points of this block within the tra
    ck.
            - info is an empty list of strings as in
            ['' for i in range(length_of_track)], which is updated to provide a
            legible readout.
            - Out is a dict to store some useful numberf for output.'''
            found = 0
            result = False
            var = data_ref.params['split_variance']
            if filters[0]:  # Temporal filter
```

```
175.                 if len(ci[0]) > lengths[1]:
176.                     found += 1
177.                     data_ref.pie['Temporal'][ci[1]] = 2
178.                     info[ci[1]] += 'Temporal: Split event ({l}). '.format(l=len(ci[0
    ]))
179.                 else:
180.                     info[ci[1]] += 'Temporal: No event ({l}). '.format(l=len(ci[0]))
181.
182.             if filters[1]:  # Spatial filter
183.                 pval = 1
184.                 frames = data_ref.pie['Frame'][ci[1]:ci[2]]
185.                 tups_l = data_ref.pie['tups_l'][ci[1]:ci[2]]
186.                 for i in range(len(ci[0])):
187.                     pval *= distance_transform_p(data_ref, tups_l[i], frames[i], var
    )
188.                     if pval < data_ref.params['Split_p_val']:
189.                         found += 1
190.                         data_ref.pie['Spatial'][ci[1]] = 2
191.                         data_ref.pie['Spatial_score'][ci[1]] = pval
192.                         info[ci[1]] += 'Spatial: Split event ({s}). '.format(s=pval)
193.                         break
194.                     if i == len(ci[0]):
195.                         info[ci[1]] += 'Spatial: No event ({s}). '.format(s=pval)
196.             if found == 2:  # If both filters agree
197.                 data_ref.pie['Combined_filters'][ci[1]] = 2  # Add to both result
198.                 info[ci[1]] += 'Both filters agree. '
199.                 result = True
200.             if sum(filters) == 1 and found == 1:
201.                 info[ci[1]] += 'Single filter sucess. '
202.                 result = True  # If both filters agree, or single filter success
203.
204.             return result
205.
206.
207.         def chunk_track(c):
208.             '''''Takes a list of colocalization data and returns a nested list of
209.             continous blocks.'''
210.             return [list(g) for k, g in groupby(c)]
211.
212.
213.         def accumu(lis):
214.             total = 0
215.             for x in lis:
216.                 total += x
217.                 yield total
218.
219.
220.         def particle_idx(pl):
221.             '''''Returns a list with the indexes of the end of every particle.'''
222.             parts = [list(g) for k, g in groupby(pl)]
223.             sizes = [len(x) for x in parts]
224.             return list(accumu(sizes))
225.
226.
227.         class ParticleResult(object):
228.             def __init__(self, name, length, index):
229.                 self.name = name
230.                 self.length = length
231.                 self.index = index  # This is absolute index in csv file
232.                 self.anyevents = False  # Set to true if events occur
233.                 self.coloconly = False
234.                 self.multiple = False
235.                 self.fcount = 0
236.                 self.fzero = 0
```

```
237.                self.foverzero = 0
238.                self.scount = 0
239.                self.fparents = 0
240.                self.sparents = 0
241.                self.fusions = []
242.                self.splits = []
243.
244.            def event_numbers(self):
245.                return {'Total_fuse': self.fcount,
246.                        'Fuse_i=0': self.fzero,
247.                        'Fuse_i>0': self.foverzero,
248.                        'Fuse+parent': self.fparents,
249.                        'Total_split': self.scount,
250.                        'Split+child': self.sparents,
251.                        'Any_events': self.anyevents,
252.                        'Multiple': self.multiple,
253.                        'Coloc_only': self.coloconly}
254.
255.
256.        def setup(data_ref):
257.            '''''Makes an output dict to record results. Also calibrates fuse and sp
    lit
258.            lengths according to input parameters. 'filters' is a convenience
259.            variable which shows what filters to use.'''
260.            if data_ref.params['Temporal']:
261.                lengths = (data_ref.params['Fuse_length'],
262.                           data_ref.params['Split_length'])
263.            else:
264.                lengths = (3, 3)  # Arbitraty number to generate a score
265.            filters = (data_ref.params['Temporal'], data_ref.params['Spatial'])
266.            return lengths, filters
267.
268.
269.        def filter_events(data_ref):
270.            '''''Applys filter functions to particle tracks.'''
271.            lengths, filters = setup(data_ref)
272.
273.            out1 = {'Cell': data_ref.name, 'Particle_results': []}
274.
275.            info = ['' for i in data_ref.pie['Info']]
276.
277.            # Get the index of the start and end points of all tracks:
278.            end_idxs = particle_idx(data_ref.pie['Particles'])
279.            start_idxs = end_idxs[:]
280.            start_idxs.insert(0, 0)  # [i-end_idxs[0] for i in end_idxs]
281.            del start_idxs[-1]
282.
283.            count = 0
284.            for z in range(len(start_idxs)):  # For each particle
285.                particle = data_ref.pie['Particles'][start_idxs[count]]
286.                particle_len = end_idxs[count] - start_idxs[count]
287.
288.                ev = 0
289.                P = ParticleResult(particle, particle_len, start_idxs[count])
290.
291.                c = data_ref.pie['Colocalized'][start_idxs[count]:end_idxs[count]]
292.
293.                if sum(c) == 0:  # Skip track if no colocalization
294.                    # info[0] += 'No colocalization: Track skipped. '
295.                    out1['Particle_results'].append(P)
296.                    count += 1
297.                    continue
298.                # Gets data in blocks
299.                all_chunks = chunk_track(c)
300.                index = start_idxs[count]  # This is the index within the track
301.                fused = False
```

```
302.
303.                 for chunk in all_chunks:
304.                     block_end = index + len(chunk)
305.                     ci = [chunk, index, block_end]
306.
307.                     if not fused and chunk[0] == 0:  # Skip block if no colocalizati
    on
308.                         # info[index] += 'No colocalization: Block skipped. '
309.                         index += len(chunk)
310.                         continue  # Skip to look for colocalization
311.
312.                     elif chunk[0] == 1 and not fused:  # Look for fusion
313.                         fusion = look_fusion(data_ref, filters, z, lengths, info,
314.                                              ci)
315.                         if fusion:
316.                             P.fcount += 1
317.                             P.fusions.append(index)
318.                             P.anyevents = True
319.                             fused = True
320.                             # info[index] += 'Looking for splitting'
321.         #                     if len(chunk) == particle_len:
322.         #                         # The whole track is colocalized
323.         #                         P.coloconly = True
324.                             # Check for fusion at start of tracks
325.                             if index == start_idxs[count]:
326.                                 P.fzero += 1
327.                             else:
328.                                 ev += 1  # Counts true fusion events
329.                                 P.foverzero += 1  # Fuse over zero
330.
331.                             if data_ref.pie['Object_parent'][index] == 1:
332.                                 # This only checks away from track start, index > 0

333.                                 P.fparents += 1
334.
335.                     elif chunk[0] == 0 and fused:  # Look for splitting
336.                         scored = score_this_track(data_ref, z, lengths, ci)
337.                         # info[index] += 'Intensity score: {s}'.format(s=scored[1])

338.                         if scored[0]:
339.                             split = look_split(data_ref, filters, z, lengths, info,

340.                                                ci)
341.                             if split:
342.                                 P.scount += 1
343.                                 P.splits.append(index)
344.                                 ev += 1
345.                                 fused = False
346.                                 # info[index] += 'Looking for fusion'
347.                                 if data_ref.pie['Object_parent'][index] == 2:
348.                                     P.sparents += 1
349.
350.                     index += len(chunk)
351.
352.                 if ev > 1:
353.                     P.multiple = True
354.                 if P.fzero and not P.scount:
355.                     P.coloconly = True
356.
357.                 out1['Particle_results'].append(P)
358.                 count += 1
359.
360.             # data_ref.pie['Info'] = info
361.             data_ref['out'] = out1  # Provides a basic analysis output
```

lines_draw.py

```
"""
This file is part of Quacker

@author: Kez Cleal, ClealK@cardiff.ac.uk
"""

import numpy as np
import Image
import ImageDraw
import tifffile
from qfilter import particle_idx
from itertools import groupby, izip


def draw_stuff(frame, lines, boxes, array):
    draw = ImageDraw.Draw(array)
    for li in lines[frame]:
        draw.line(li, 'white')
    if len(boxes[frame]) > 0:
        for bo in boxes[frame]:
            x, y = bo[1], bo[0]  # From tuple coordinate
            draw.rectangle([(y-10, x-10), (y+10, x+10)], outline='white')


def binary_tups_frame(data_ref):
    all_frames = [i for i in range(max(data_ref.pie['Frame']))]
    tupf = dict.fromkeys(all_frames)

    zs = sorted(zip(data_ref.pie['Frame'], data_ref.pie['tups_l']))
    zs = [list(t) for t in zip(*zs)]
    f = zs[0]
    t = zs[1]
    groups = [list(grp) for _, grp in groupby(izip(f, t), lambda x: x[0])]
    tup_groups = [[n for _, n in items] for items in groups]

    setf = list(set(f))
    for i in range(len(setf)):
        frame = setf[i]
        tupg = tup_groups[i]
        tupf[frame] = tupg
    return tupf


def make_binary_r(data_ref, tup_in_frame):
    r = np.zeros(data_ref.shape, dtype=np.uint16)
    for i in tup_in_frame:
        x = i[0]
        y = i[1]
        r[y, x] = 1
    return r * 16535


def draw_frame(data_ref, lines, boxes):
    tupf = binary_tups_frame(data_ref)
    binaryArrays = None
    for i in range(max(data_ref.pie['Frame'])+1):
        blue = np.zeros(data_ref.shape, dtype=np.uint8)
        blue_im = Image.fromarray(blue)
        draw_stuff(i, lines, boxes, blue_im)

```

```
        r = make_binary_r(data_ref, tupf[i])
        g = np.array(data_ref.binary_ob[i], dtype=np.uint16)*16535
        b = np.array(blue_im, dtype=np.uint16)*16535

        rgb = np.dstack((r, g, b))
        rgb = np.expand_dims(rgb, axis=0)
        if i == 0:
            binaryArrays = rgb
        else:
            binaryArrays = np.concatenate((binaryArrays, rgb))
    p = '{o}\\{n}_Binary.tif'.format(o=data_ref.outpath, n=data_ref.name)
    tifffile.imsave(p, binaryArrays)


def which_col(data_ref):
    if data_ref.params['Temporal'] and data_ref.params['Spatial']:
        column = 'Combined_filters'
    elif data_ref.params['Temporal']:
        column = 'Temporal'
    elif data_ref.params['Spatial']:
        column = 'Spatial'
    return column


def lines(data_ref, column=None):
    if not column:
        column = which_col(data_ref)
    result_column = data_ref.pie[column]
    max_frames = max(data_ref.pie['Frame'])

    lines = {i: [] for i in range(max_frames+1)}
    boxes = {i: [] for i in range(max_frames+1)}

    end_idxs = particle_idx(data_ref.pie['Particles'])

    start_idxs = end_idxs[:]
    start_idxs.insert(0, 0)  # [i-end_idxs[0] for i in end_idxs]
    del start_idxs[-1]

            for z in range(len(start_idxs)):  # For each particle in dict
                if sum(result_column[start_idxs[z]:end_idxs[z]]) == 0:
                    continue  # Skip tracks with no events
                else:
                    # Loop through each track
                    for j in range(start_idxs[z], end_idxs[z]-1):
                        if j == start_idxs[z]:
                            continue  # No lines on first frame
                        else:
                            frame = data_ref.pie['Frame'][j]
                            l = data_ref.pie['tups_l'][start_idxs[z]:j+1]
                            lines[frame].append(l)
                            # Draw box if split event
                            if result_column[j] == 2:
                                b = data_ref.pie['tups_l'][j]
                                boxes[frame].append(b)
            draw_frame(data_ref, lines, boxes)
```